

“EVIDENCE FOR ELECTRON NEUTRINO FLAVOR CHANGE THROUGH  
MEASUREMENT OF THE  ${}^8\text{B}$  SOLAR NEUTRINO FLUX AT THE SUDBURY  
NEUTRINO OBSERVATORY”

Mark Stephen Neubauer

A DISSERTATION

in

Physics and Astronomy

Presented to the Faculties of the University of Pennsylvania in Partial Fulfillment of  
the Requirements for the Degree of Doctor of Philosophy

2001

---

Eugene W. Beier

Supervisor of Dissertation

---

Randall D. Kamien

Graduate Group Chairperson

COPYRIGHT

Mark Stephen Neubauer

2001

*To my parents*

## Acknowledgements

I have many people to thank for helping me along the way to completion of this thesis. I would first like to thank my advisor, Gene Beier, for his guidance and patience during my time at Penn. His great level of physics understanding has given me something to strive for in my career. I have worked more closely with Josh Klein than anyone else during my time as a graduate student. I owe him a debt of gratitude for all the time and effort he has spent on my development over the years. Essentially every part of this thesis bears his influence, and his contagious enthusiasm kept me going throughout.

There are many others in the Penn SNO group which deserve my gratitude. Richard Van de Water for those early days of hardware development and detector commissioning, and for someone always ready to throw back a few in Sudbury. Because of him, I will never forget the importance of paddle cards in high energy physics. Bill Frati and Doug Cowen for many useful discussions which always seem to lead to a better understanding of a particular problem. My fellow “old phase” graduate students Doug McDonald and Peter Wittich who suffered with me through the all ups and downs that have come to define my SNO graduate student career at Penn. I have learned a great deal from both of you over the years. Vadim Rusu deserves special thanks for handling the production data processing at Penn for which my analysis has greatly benefited (“where’s my data?”). He has also been a great friend both inside and outside of work where he has proven from experiments done at Buzzy’s to be quite a powerful “winger” adversary. Thanks to Scott Oser for useful discussions on signal extraction and systematic uncertainties. Bill Heintzelman for his correlation  $\chi^2$  statistic used in this thesis.

It cannot be stressed enough that my hardware contributions to SNO could not

have been possible without the help of others in the Penn electronics group. Rick Van Berg and Mitch Newcomer were a constant source of guidance during the entire process and their vast knowledge of electronics proved invaluable. Chuck Alexander (“Chucka”) for all his technical skill on the electronics and the fun times we have had in Sudbury. Godwin Mayers, Ron Pearce, and Jim Cook for the wonderful job they have done to make the SNO electronics a working reality.

Ignacio Taboada and Kael Hanson of the AMANDA group have been great SNO office mates that have provided a fresh perspective on neutrino physics and life outside of SNO. I would also like to thank Paul Keener for his computing support and work on the SNO data acquisition system. Dave Wark, Rich Helmer, Steve Biller, Neil McCauley, Gordon McGregor, and Kate Frame are fellow members of the TOXENN analysis group which deserve my thanks for useful discussions and help with the analysis. Andrew Hime for pointing out the flavor analysis which represents the most important conclusions of this thesis.

I cannot thank my parents enough for all the support they have given me in this and other endeavors in my life. This thesis is dedicated to them. Thanks to my sister, Lisa, for her support and strength in holding things together for her little brother over the years. Finally, I would like to thank Ellena for all her love and seemingly endless patience as I worked on this thesis. She has contributed more than she knows to its completion by giving me a future that I can look forward to.

## ABSTRACT

# EVIDENCE FOR ELECTRON NEUTRINO FLAVOR CHANGE THROUGH MEASUREMENT OF THE ${}^8\text{B}$ SOLAR NEUTRINO FLUX AT THE SUDBURY NEUTRINO OBSERVATORY

Mark S. Neubauer

Eugene W. Beier

The Sudbury Neutrino Observatory (SNO) is a water Cerenkov detector designed to study solar neutrinos. Using 1 kiloton of heavy water as the target and detection medium, SNO is able to separately determine the flux of electron neutrinos ( $\nu_e$ ) and the flux of all active neutrinos from the Sun by measuring the rate of charged current (CC) and neutral current (NC) interactions with deuterons. A comparison of these interaction rates allows for direct observation of solar neutrino oscillations. SNO can also search for oscillations by comparing the rate of CC and neutrino-electron elastic scattering (ES) events, since ES has both charged current and neutral current sensitivity.

In this thesis, we present measurement of the  ${}^8\text{B}$  solar  $\nu_e$  flux of  $1.78^{+0.13}_{-0.14}$  (stat+syst)  $\times 10^6 \text{cm}^{-2} \text{s}^{-1}$  (35% BP2000 SSM) through measurement of the CC rate over 169.3 days of livetime. We have also measured the  ${}^8\text{B}$  flux from the ES reaction to be  $2.56^{+0.48}_{-0.45}$  (stat+syst), consistent with measurements by previous water Cerenkov experiments. A flavor analysis comparing the CC measured flux with that determined through ES by SuperKamiokande yields a non- $\nu_e$  active neutrino flux from  ${}^8\text{B}$  of  $3.62^{+1.06}_{-1.08} \times 10^6 \text{cm}^{-2} \text{s}^{-1}$ , providing evidence for  $\nu_e \rightarrow \nu_{\mu,\tau}$  oscillations as a solution to the solar neutrino problem. This result excludes pure solar  $\nu_e \rightarrow \nu_s$  oscillations at greater than the 99.7% C.I. The total active  ${}^8\text{B}$  neutrino flux has been measured to

be  $5.39^{+1.07}_{-1.09} \times 10^6 \text{cm}^{-2}\text{s}^{-1}$ , consistent with BP2000 SSM predictions. First analyses of the CC ( $N_{\text{Hit}}$ ) spectrum and *hep* flux in SNO are presented. The CC spectrum is found to be a good fit to expectations from an undistorted  ${}^8\text{B}$  spectrum, and global best fit vacuum oscillation solutions are disfavored over the other solutions by the data. Through observations near the  ${}^8\text{B}$  endpoint with consideration of energy systematics, *hep* flux limits of 4.1 (90% C.I.) and 6.9 (99% C.I.) times SSM expectations are obtained. A statistical fit for the *hep* flux signal yields a  $3\sigma$  upper limit of 3.2 times the SSM expected flux.

# Contents

<b>1</b>	<b>Introduction</b>	<b>1</b>
1.1	Neutrinos in Particle Astrophysics . . . . .	1
1.2	Organization of this Thesis . . . . .	2
<b>2</b>	<b>Solar Neutrinos</b>	<b>4</b>
2.1	Neutrino Physics in the Standard Model . . . . .	4
2.2	The Standard Solar Model . . . . .	6
2.3	The Solar Neutrino Problem . . . . .	9
2.3.1	Radiochemical Experiments . . . . .	9
2.3.2	Light Water Cerenkov Experiments . . . . .	12
2.3.3	Comparison of Results with Expected Rates . . . . .	13
2.3.4	Possible Solutions to the Solar Neutrino Problem . . . . .	13
2.4	Oscillations of Massive Neutrinos . . . . .	16
2.4.1	Neutrino Oscillations in Vacuum . . . . .	16
2.4.2	Neutrino Oscillations in Matter . . . . .	18
2.4.3	Limits on Oscillation Parameters . . . . .	20
2.4.4	Oscillation Signatures . . . . .	23
2.5	The SNO Experiment . . . . .	24

2.5.1	Overview	24
2.5.2	Interaction and Detection of Neutrinos in SNO	27
2.6	Summary	28
<b>3</b>	<b>The SNO Detector</b>	<b>29</b>
3.1	Acrylic Vessel	29
3.2	Water Systems	30
3.2.1	Heavy Water ( $D_2O$ ) System	31
3.2.2	Light Water ( $H_2O$ ) System	31
3.2.3	Cover Gas System	32
3.3	Photomultiplier Tubes and Support Structure	32
3.4	Front-End Electronics	34
3.4.1	PMT Interface and High Voltage Supply System	36
3.4.2	PMT Signal Processing	36
3.5	Trigger System	38
3.5.1	Design Criteria	38
3.5.2	System Overview	41
3.5.3	Global Trigger Generation Logic	44
3.5.4	Global Trigger and Clock Counter Arrays	48
3.5.5	Memory	49
3.5.6	Calibration Pulser	50
3.5.7	Signal Fanout	52
3.5.8	Trigger Utility Board	52
3.5.9	Interface to Global Positioning Satellite (GPS) System	53
3.5.10	Physical Design	55

3.6	Data Acquisition Hardware and Software . . . . .	56
3.7	Monte Carlo Detector Simulation (SNOMAN) . . . . .	57
3.8	Summary . . . . .	58
<b>4</b>	<b>Event Reconstruction</b>	<b>59</b>
4.1	Overview . . . . .	60
4.2	The Pre-Existing Fitters . . . . .	61
4.2.1	Time Fitter . . . . .	61
4.2.2	Quad Fitter . . . . .	63
4.2.3	Grid Fitter . . . . .	64
4.2.4	Elastic Fitter . . . . .	65
4.3	A New Fitter: The Path Fitter . . . . .	66
4.3.1	General Fitter Considerations . . . . .	67
4.3.2	Use of Time and Angle Information in Reconstruction . . . . .	74
4.3.3	Fitter Development - A Brief History of Time and Angle . . . . .	82
4.3.4	The SNOMAN Path Fitter . . . . .	87
4.3.5	Goodness-of-Fit Criteria . . . . .	92
4.3.6	Performance . . . . .	98
4.4	Summary . . . . .	107
<b>5</b>	<b>Detector Calibrations</b>	<b>108</b>
5.1	Electronics Calibrations . . . . .	109
5.1.1	Validation Information . . . . .	110
5.1.2	Time-Since-Last-Hit (TSLH) Correction . . . . .	110
5.2	PMT Calibrations . . . . .	111
5.3	Optical Calibrations . . . . .	112

5.3.1	Optical Model Used in this Thesis . . . . .	113
5.3.2	Alternative “Extreme” Optical Parameter Sets . . . . .	114
5.4	Energy Calibrations . . . . .	115
5.4.1	$N_{\text{Hit}}$ as Primary Energy Variable . . . . .	116
5.4.2	Energy Scale and Resolution . . . . .	121
5.5	Reconstruction Characteristics . . . . .	142
5.5.1	Vertex Resolution and Shift . . . . .	143
5.5.2	Angular Resolution . . . . .	154
5.6	Trigger Efficiency . . . . .	157
5.6.1	Introduction . . . . .	157
5.6.2	Trigger Efficiency and Acceptance . . . . .	161
5.6.3	Sources of inefficiency . . . . .	162
5.6.4	Method of Measurement . . . . .	167
5.6.5	Results . . . . .	171
5.7	Summary . . . . .	176
<b>6</b>	<b>Data Reduction</b>	<b>177</b>
6.1	Run Selection . . . . .	178
6.2	Removal of Instrumental Backgrounds . . . . .	179
6.2.1	Zoology of the SNO Instrumental Backgrounds . . . . .	180
6.2.2	Approach to Instrumental Background Removal . . . . .	187
6.2.3	Junk Cut . . . . .	187
6.2.4	Burst Cuts . . . . .	188
6.2.5	Charge Cuts . . . . .	188
6.2.6	Hit Geometry Cuts . . . . .	189

6.2.7	Time Spread Cuts	190
6.3	Vertex and Direction Goodness-of-Fit Cuts	194
6.3.1	Azimuthal Angular Symmetry Cut	195
6.3.2	2-D Angular ( $\cos \alpha, \psi$ ) Distribution Cut	195
6.4	Post-reconstruction Cerenkov Signal Cuts	196
6.4.1	Angular Correlation Cut: The Correlation $\chi^2$	197
6.4.2	In-time Ratio (ITR) Cut	197
6.5	Muon Follower Cut	198
6.6	Signal Acceptance of Combined Cuts	198
6.7	Fiducial Volume and $N_{hit}$ cuts	199
6.8	Application of Cuts to Selected Data Set	204
6.9	Summary	204
<b>7</b>	<b>Background Estimation</b>	<b>206</b>
7.1	Low Energy Backgrounds	206
7.2	High Energy $\gamma$ -ray Backgrounds	210
7.2.1	Description of the Method	212
7.2.2	Application of Method to Neutrino Data Set	214
7.3	Non-Cerenkov Backgrounds	218
7.4	Summary	219
<b>8</b>	<b>Results</b>	<b>221</b>
8.1	General Analysis Approach	221
8.2	Signal Extraction Techniques	224
8.2.1	CC and ES Extraction - NHIT Constrained	225
8.2.2	Parameterized PDFs	226

8.2.3	CC $N_{\text{Hit}}$ Spectrum Extraction	231
8.3	Extracted Solar Neutrino Signals	233
8.3.1	CC and ES - $N_{\text{hit}}$ Constrained Fit	233
8.3.2	CC $N_{\text{Hit}}$ Spectrum	236
8.4	CC and ES Fluxes Compared to SSM Predictions	236
8.5	Systematic Errors	240
8.5.1	Sources of Systematic Uncertainty	240
8.5.2	Systematic Error Summary	246
8.6	Sanity Checks	248
8.6.1	Dependence on Fiducial Volume	248
8.6.2	Dependence on Energy Threshold	250
8.6.3	Removal of Muon Follower Cut	251
8.7	CC $N_{\text{Hit}}$ Spectrum Compared to SSM	252
8.8	<i>hep</i> Neutrino Flux	255
8.8.1	Observations Near ${}^8\text{B}$ Endpoint	256
8.8.2	Fitting for the <i>hep</i> Signal	264
8.9	Summary	264
<b>9</b>	<b>Conclusions and Discussion</b>	<b>266</b>
9.1	CC and ES Rates	266
9.1.1	Neutrino Flavor Content of ${}^8\text{B}$ Flux	268
9.1.2	MSW Analysis of the CC Rate	272
9.2	CC Spectrum	273
9.3	<i>hep</i> Flux	278
9.4	Final Remarks	278

<b>A The Path Fitter: Future Development</b>	<b>280</b>
A.1 Suggestions for Future Work . . . . .	280
A.2 The 'Paths' Approach . . . . .	281
A.3 Spherical Specular Reflections . . . . .	283
A.3.1 Introduction . . . . .	284
A.3.2 Reflection Paths Given Source Point and Direction . . . . .	285
A.3.3 Reflection Paths Given Source and Sink Points . . . . .	290
A.4 Uniform Scattering . . . . .	300
<b>B Energy Scale Interpolation</b>	<b>305</b>
B.1 Preparing the Grid . . . . .	305
B.2 Using the Grid . . . . .	308
B.3 Effect of Applying Response Corrections to Grid Data . . . . .	310
B.4 Fitter Dependence . . . . .	310
<b>C Trigger Efficiency Follow-up</b>	<b>314</b>
C.1 Checks and Systematics . . . . .	314
C.2 Effect of Missing Channels on Trigger Efficiency . . . . .	318

# List of Figures

2.1	Nuclear reactions involved in the proton-proton ( $pp$ ) chain. . . . .	7
2.2	Bahcall-Pinsonneault Standard Solar Model (BP2000) neutrino energy spectra . . . . .	10
2.3	Graphical representation of solar neutrino flux measurements . . . . .	14
2.4	Correlations between the measured ${}^8B$ and ${}^7Be$ flux ratios for standard and various non-standard solar models . . . . .	15
2.5	Allowed regions in the $\Delta m^2$ - $\tan^2 \theta$ plane at various confidence levels for oscillation to active ( $\nu_\mu$ , $\nu_\tau$ ) and sterile neutrinos . . . . .	21
2.6	Survival probability versus neutrino energy for the allowed solutions shown in Figure 2.5 . . . . .	22
2.7	Schematic drawing of the SNO detector . . . . .	26
3.1	Schematic diagram of the Hamamatsu R1408 PMT . . . . .	33
3.2	Schematic diagram of PMT and concentrator assembly . . . . .	34
3.3	Diagram of the SNO electronics and data acquisition hardware . . . .	35
3.4	Block diagram of the the SNO trigger system . . . . .	40
3.5	Schematic diagram of the trigger latching and global trigger generation logic involved in the digital trigger system . . . . .	44

3.6	Diagram showing the coincidence window involved in trigger word latching . . . . .	47
3.7	Schematic diagram of the GPS synchronization system logic . . . . .	54
3.8	Simplified diagram of the DAQ system and data flow . . . . .	57
4.1	Distribution of energies for generated and detected photons produced by electrons in the D <sub>2</sub> O . . . . .	71
4.2	Photon speed distributions of detected photons for electrons generated uniformly and isotropic in the D <sub>2</sub> O and H <sub>2</sub> O regions . . . . .	73
4.3	Distribution of fit positions in 2D world and a typical fit example for “electrons” generated at the center in the +x direction . . . . .	77
4.4	Likelihood contour for 2D fits using time only and angle only . . . . .	78
4.5	$x_{fit}$ distributions of events generated at the center of 2D world with 1.5 ns PMT time jitter and 20 ns jitter, when time only is used and time and angular is used in the fitting . . . . .	79
4.6	Distribution of fit positions for electrons generated at the center of 3D world in the +x direction when SNOMAN EGS4 and the same distribution is used to generate and fit the events . . . . .	81
4.7	Drive distribution for events generated uniformly and isotropically in the D <sub>2</sub> O when SNOMAN EGS4 and the same distribution is used to generate and fit the events . . . . .	82
4.8	Diagram showing the general flow of the Path Fitter algorithm . . . . .	87
4.9	Time and angle probability functions used in Path Fitter reconstruction	90
4.10	Path Fitter drive versus $M_{gen}$ and $M_{fit}$ . . . . .	93

4.11 Example of azimuthal symmetry KS test for fit quality applied to a 5 MeV MC electron and a PMT flasher event . . . . .	95
4.12 Example of 2D angular distribution KS test for fit quality applied to a 5 MeV MC electron and a PMT flasher event . . . . .	97
4.13 Distribution of $x_{fit}$ residuals for CC electrons generated uniformly inside the D <sub>2</sub> O and isotropic in direction . . . . .	99
4.14 $R_{dev}$ distribution for CC electrons generated uniformly inside the D <sub>2</sub> O and isotropic in direction . . . . .	100
4.15 Comparison of drive for CC electrons generated uniformly inside the D <sub>2</sub> O and isotropic in direction . . . . .	102
4.16 Sensitivity of Path Fitter drive to scattering in the MC, via the TOXENN extreme optical parameter sets . . . . .	103
4.17 Distribution of the cosine of the angle between the fit direction and initial direction of the MC CC electron for the different fitters . . . .	105
4.18 $\cos \theta_{\odot}$ distribution of MC ES events for the different fitters . . . .	106
5.1 Monte Carlo $N_{\text{Hit}}$ distribution for a series of electron energies from 4-20 MeV . . . . .	123
5.2 Monte Carlo predictions for energy scale and resolution as a function of electron energy . . . . .	124
5.3 Comparison of energy scale between <sup>16</sup> N calibration data and source MC as a function of days since production data taking . . . . .	127
5.4 Fractional difference in energy scale between <sup>16</sup> N calibration data and source MC as a function of days since production data taking . . . .	128

5.5	Poisson mean $N_{\text{Hit}}$ versus run number from fits to PULSE_GT triggered data collected in tandem with neutrino data . . . . .	129
5.6	$N_{\text{Hit}}$ distributions for two $^{16}\text{N}$ calibration source runs near the center of the detector with different trigger rate . . . . .	131
5.7	Energy scale with and without energy interpolation for the Dec99 $^{16}\text{N}$ yz-scan using the Path Fitter. . . . .	133
5.8	Energy scale with and without energy interpolation for the Jan01 $^{16}\text{N}$ x-axis scan using the Path Fitter . . . . .	135
5.9	Fractional error in interpolation corrected $N_{\text{Hit}}$ versus source radius from source Monte Carlo when compared to the January 2001 x,y, and z-axis scan data . . . . .	136
5.10	Comparison between $^{252}\text{Cf}$ data and interpolation corrected source MC energy scale for August 2000 and November 2000 neutron source runs	138
5.11	$N_{\text{Hit}}$ distribution of pT source run 15172 at the center of the detector after data cleaning and high level cuts. Overlayed is the interpolation corrected MC of the pT source . . . . .	140
5.12	Energy resolution for x-axis and z-axis scans of the $^{16}\text{N}$ calibration source compared to source Monte Carlo . . . . .	142
5.13	The electron source distributions used to extract $\sigma$ and $\mu$ from $^{16}\text{N}$ and $^8\text{Li}$ along with example fits to the calibration data. . . . .	145
5.14	Comparison of vertex resolution from $^{16}\text{N}$ source MC and data as a function of source z-position . . . . .	145
5.15	Comparison of vertex resolution from $^8\text{Li}$ source MC and data as a function of source z-position . . . . .	146

5.16 Comparison of vertex resolution from $^{16}\text{N}$ and $^8\text{Li}$ calibration data as a function of source z-position . . . . .	147
5.17 Comparison of vertex resolution from $^{16}\text{N}$ source MC and data as a function of NHIT . . . . .	148
5.18 Comparison of vertex resolution from $^8\text{Li}$ source MC and data as a function of NHIT . . . . .	149
5.19 Comparison of vertex resolution from $^{16}\text{N}$ and $^8\text{Li}$ calibration data as a function of NHIT . . . . .	150
5.20 Comparison of $^{16}\text{N}$ and $^8\text{Li}$ $N_{\text{Hit}}$ distribution for source at the center of the detector . . . . .	151
5.21 Scatter plot of reconstructed vertex for four different $^8\text{Li}$ source positions	152
5.22 Comparison of x and y vertex shift from $^8\text{Li}$ and $^{16}\text{N}$ source MC and data as a function of source z-position . . . . .	153
5.23 Comparison of z vertex shift from $^8\text{Li}$ and $^{16}\text{N}$ source MC and data as a function of source z-position . . . . .	154
5.24 Diagram showing vectors involved in measurement of angular resolution using the $^{16}\text{N}$ $\gamma$ -ray calibration source . . . . .	156
5.25 Comparison of the $\cos\theta$ distributions between $^{16}\text{N}$ calibration data at the center of the detector and source Monte Carlo for events reconstructing more than 1.5 m from the source . . . . .	158
5.26 Log-scale version of Figure 5.25 showing that the angular resolution tail from $^{16}\text{N}$ is also in good agreement with Monte Carlo . . . . .	159
5.27 Dramatization of how the various sources of trigger inefficiencies can alter the trigger efficiency curve in an ideal system. . . . .	163

5.28	Exaggerated diagram of the effects of analog pulse shape on trigger efficiency. . . . .	164
5.29	Block diagram of trigger efficiency measurement method using the laserball with the FEC/D as the trigger latch . . . . .	169
5.30	Measured trigger efficiency using the laserball at the center with the FEC/D as the trigger latch . . . . .	172
5.31	Measured trigger efficiency using the laserball at $z = -5$ m with the FEC/D as the trigger latch . . . . .	173
6.1	Flasher rate over 160 hrs of neutrino livetime around the beginning of production running . . . . .	182
6.2	Distribution of $\delta t$ for hit PMT pairs with $ \vec{r}_i - \vec{r}_j  < 2$ m in $^{16}\text{N}$ calibration data at the center and flasher events where cluster tubes are ignored . . . . .	191
6.3	Distribution of median $\delta t$ calculated from hit PMT pairs with $ \vec{r}_i - \vec{r}_j  < 2$ m in $^{16}\text{N}$ calibration data at the center and flasher events where cluster tubes are ignored . . . . .	192
6.4	Distribution of ITC ratio for $^{16}\text{N}$ calibration data and events in run 10700 before and during the flat-TAC burst . . . . .	193
6.5	Sacrifice versus source radius obtained from x and z-axis scans of the $^{16}\text{N}$ source and z-axis scan of the $^8\text{Li}$ source . . . . .	200
6.6	Fitter-related cut sacrifice stability over time, probed by comparing the sacrifice from $^{16}\text{N}$ calibration data taken nearly a year apart . . .	201
6.7	$R_{fit}^3$ distribution of events after data cleaning for 45, 55, and 65 $N_{\text{Hit}}$ thresholds	203

6.8	Effect of reduction cuts on the neutrino data $N_{\text{Hit}}$ distribution above 30 $N_{\text{Hit}}$	205
7.1	$N_{\text{Hit}}$ distribution for cleaned data showing the analysis threshold relative to the exponential wall from low energy radioactive backgrounds	208
7.2	Pictorial description of the method used to estimate the amount of high energy $\gamma$ background reconstructing into the fiducial volume. . . . .	213
7.3	$\hat{u} \cdot \hat{r}$ versus $R^3$ distribution for tagged events from $^{16}\text{N}$ run 13980 where the source was 853.7 cm (-586, 208, 585 cm) . . . . .	216
7.4	$\hat{u} \cdot \hat{r}$ versus $R^3$ distribution for the cleaned, reconstructed 169.3 day neutrino data set above 50 $N_{\text{Hit}}$ . . . . .	217
7.5	Non-Cerenkov contamination inside a 6 m fiducial volume as a function of $N_{\text{Hit}}$ threshold . . . . .	220
8.1	Monte Carlo CC distribution in $N_{\text{Hit}}$ and $R^3$ for 10xSSM (BP00) over the neutrino data livetime . . . . .	227
8.2	Monte Carlo CC distribution in $\cos \theta_{\odot}$ for 10xSSM (BP00) over the neutrino data livetime . . . . .	228
8.3	Monte Carlo ES distribution in $N_{\text{Hit}}$ and $R^3$ for 50xSSM (BP00) over the neutrino data livetime . . . . .	228
8.4	Monte Carlo ES distribution in $\cos \theta_{\odot}$ for 50xSSM (BP00) over the neutrino data livetime . . . . .	229
8.5	Monte Carlo NC distribution in $N_{\text{Hit}}$ and $R^3$ for 50xSSM (BP00) over the neutrino data livetime . . . . .	230
8.6	Mean $N_{\text{Hit}}$ versus electron energy for Monte Carlo CC electrons generated uniform and isotropic inside the $\text{D}_2\text{O}$ volume . . . . .	232

8.7	$N_{\text{Hit}}$ and $R^3$ distributions for the 169.3 day neutrino data set with the $N_{\text{Hit}}$ signal PDFs scaled to the number of extracted CC, ES, and “NC” signal events superimposed . . . . .	234
8.8	$\cos \theta_{\odot}$ distribution for the 169.3 day neutrino data set with the $\cos \theta_{\odot}$ signal PDFs scaled to the number of extracted CC, ES, and “NC” signal events superimposed . . . . .	235
8.9	Extracted CC $N_{\text{Hit}}$ spectrum for the 169.3 day neutrino data set . . . . .	237
8.10	CC and ES flux measurements relative BP2000 SSM predictions as a function of fiducial volume cut . . . . .	249
8.11	CC and ES flux measurements relative SSM predictions as a function of $N_{\text{Hit}}$ threshold . . . . .	250
8.12	Comparison of the extracted CC $N_{\text{Hit}}$ spectrum (169.3 days) with BP2000 SSM predictions . . . . .	253
8.13	Ratio of extracted CC $N_{\text{Hit}}$ spectrum (169.3 days) to BP2000 SSM predictions . . . . .	254
8.14	Combined CC+ES $N_{\text{Hit}}$ distributions obtained from Monte Carlo of 100 and 4000 times the BP2000 SSM over our livetime for ${}^8\text{B}$ and <i>hep</i> neutrinos, respectively . . . . .	257
8.15	Total number of events expected in the 169.3 day data set as a function of $N_{\text{Hit}}$ threshold for ${}^8\text{B}$ and <i>hep</i> neutrinos . . . . .	258
8.16	Distribution of $N_{\text{Hit}}$ thresholds with the best expected sensitivity to a <i>hep</i> signal based on Monte Carlo signal ( <i>hep</i> CC+ES) and background ( ${}^8\text{B}$ CC+ES) distributions . . . . .	260
8.17	Event display of <i>hep</i> neutrino candidate event found at 168 $N_{\text{Hit}}$ . . . . .	261

8.18 ITR versus $\chi^2_{corr}$ for selected events comprising the reduced data set, which shows that the <i>hep</i> neutrino candidate event lies near the corner of the Cerenkov signal box . . . . .	263
8.19 Monte Carlo <i>hep</i> CC+ES distribution in $N_{\text{Hit}}$ for 4000xSSM (BP00) over the neutrino data livetime . . . . .	265
9.1 Measurement of the non-electron active neutrino component of the ${}^8\text{B}$ flux though comparison of SNO CC and Superkamiokande ES flux results	270
9.2 Measurement of the total active ${}^8\text{B}$ neutrino flux though comparison of SNO CC and Superkamiokande ES flux results . . . . .	271
9.3 Allowed MSW regions at 95.4% and 99% confidence for CC flux measurement presented in this thesis, relative to BP2000 SSM predictions	274
9.4 Comparison between the extracted CC $N_{\text{Hit}}$ spectrum and global best fit MSW solutions for active neutrino oscillations . . . . .	275
9.5 Comparison between the extracted CC $N_{\text{Hit}}$ spectrum and global best fit MSW solutions for sterile neutrino oscillations . . . . .	276
A.1 Schematic pictures of the different photon path considered in the Path Fitter PDF calculations . . . . .	282
A.2 Reflection problem defined by source point G and photon direction $\hat{d}_\gamma$	285
A.3 Reflection paths off concentric spheres of radius 850 and 600cm for an initial photon at (0,500) in the (-1,0) direction . . . . .	291
A.4 Reflection problem defined by source point E and sink point P . . . .	292
A.5 Geometry involved in near and far reflection solutions . . . . .	293
A.6 Diagram showing successive rotation of a arbitrary vector . . . . .	295

A.7	Photon direction cosines for antipodal and non-antipodal source and sink points . . . . .	298
A.8	Plots of the transcendental equations in the near and far regions for non-antipodal source and sink points . . . . .	299
A.9	Figure showing the vectors involved in the scattering problem . . . . .	302
B.1	Figure showing the grid used in energy scale interpolation . . . . .	306
B.2	Figure showing grid points with enough statistics to use in the energy scale interpolation scheme . . . . .	309
B.3	Energy scale before and after energy interpolation for the Dec99 $^{16}\text{N}$ x-scan using the Time Fitter . . . . .	311
B.4	Energy scale before and after energy interpolation for the Dec99 $^{16}\text{N}$ x-scan using the Path Fitter . . . . .	312
B.5	Energy scale before and after energy interpolation for the Dec99 $^{16}\text{N}$ z-scan using the Path Fitter. . . . .	313
C.1	Measured trigger efficiency using the laserball at the center with the MTC/D as the trigger latch . . . . .	315
C.2	Measured trigger efficiency using the NHIT triggered data from standard neutrino runs. . . . .	317
C.3	Reduction in efficiency versus the fraction of newly disabled trigger channels for $\tilde{N}_o = 18$ and $\tilde{N}_o = 23$ . . . . .	320

# List of Tables

2.1	Bahcall-Pinsonneault Standard Solar Model (BP2000) neutrino fluxes at one astronomical unit . . . . .	9
2.2	Solar neutrino experiments along with measured flux relative to BP2000 (modified) SSM predictions . . . . .	13
3.1	The 26 raw trigger types of the SNO trigger system . . . . .	45
3.2	The Digital Master Tigger Card (MTC/D) Memory Map . . . . .	50
4.1	Summary of vertex reconstruction performance comparisons for CC electrons generated uniformly inside the D <sub>2</sub> O and isotropic in direction	101
5.1	Sources used for Energy Calibration in SNO . . . . .	116
5.2	Energy scale uncertainties for the alternate optics sets from comparison of the neutron source data and MC . . . . .	138
5.3	Trigger efficiency results near full efficiency for the N100MED threshold using FEC/D latch method. . . . .	175
6.1	Progression of data reduction cuts . . . . .	204
7.1	Summary of U/Th contamination in D <sub>2</sub> O , H <sub>2</sub> O , and AV regions . . .	209

8.1	Number of extracted signal events from the 169.3 day data set . . . . .	234
8.2	Number of expected signal events over the 169.3 day data set from ${}^8\text{B}$ assuming BP2000 SSM . . . . .	238
8.3	Summary of systematic errors . . . . .	247
8.4	Summary of <i>hep</i> results using observations near the ${}^8\text{B}$ endpoint . . . . .	262
9.1	Global best fit MSW solutions with the $\chi^2$ and GOF obtained from CC spectrum measurement shown for each solution . . . . .	277
A.1	Results for the non-antipodal pair: source pt at $(0.905R, 0, 0.095R)$ and sink pt at $= (0, 0, 1)$ implementing the algorithms described in section A.3.2 and section A.3.3 . . . . .	300

# Chapter 1

## Introduction

### 1.1 Neutrinos in Particle Astrophysics

Neutrinos play an important role in our understanding of both particle physics and astrophysics. The fact that neutrinos interact very weakly with ordinary matter allows one to gain insight into neutrino producing astrophysical processes over the information obtained with more traditional carriers of astrophysical information (photons, cosmic rays) that can be obscured by interactions with intervening matter. While this weakly interacting nature of neutrino interactions represents a blessing for directly probing otherwise inaccessible regions of the cosmos, it poses real technical challenges for neutrino detection. Neutrino detectors must have very large interaction masses and even then are only sensitive to sources which produce a large flux of neutrinos incident at the detector location.

Because of these difficulties, many fundamental properties of neutrinos are not well known. In fact, the neutrino associated with heaviest charged lepton - the tau neutrino - has only been directly observed through its interactions recently [1]. Neutrino

masses are of particularly fundamental interest to particle physics and astrophysics. Neutrinos are assumed massless in the Standard Model, yet long-standing hints from the observed deficit of solar electron neutrinos and the strong evidence in favor of neutrino mass from observations of atmospheric neutrinos by the Kamiokande and SuperKamiokande experiments has established that this description of nature is incomplete. Extensions to the Standard Model, such as those implicit in some Grand Unified Theories and more exotic scenarios like extra dimensions, naturally incorporate neutrino mass into their theoretical framework. It is likely that further study of neutrino properties such as masses and mixing parameters will play a critical role in determining which, if any, of these theories are correct models of new physics. Neutrinos are also very important for cosmology, as even small masses can yield a substantial contribution to the overall mass of the universe. In this context, massive neutrinos have been proposed as possible hot dark matter candidates. Nucleosynthesis models and supernova dynamics are also affected by neutrino masses and the lepton number violation implied by oscillations.

The main focus of this thesis is to present an analysis of data collected by the Sudbury Neutrino Observatory (SNO) in an attempt to answer some of these questions through study of neutrinos produced by the Sun.

## 1.2 Organization of this Thesis

This thesis has two main goals. One goal is to present to the reader an analysis of the existing SNO data performed by the author along with conclusions that can be drawn from the obtained results. The other goal is to provide a high-level documentation base for specific items worked on by the author that are of lasting importance for the

experiment. More detailed information on these items can be found elsewhere in the references.

The organization of this thesis is as follows. Chapter 2 describes solar neutrinos and presents the motivation for doing an experiment like SNO. The SNO detector is described in Chapter 3. Event reconstruction is described Chapter 4, with emphasis placed on a reconstruction method developed by the author that is used for the analysis presented in this thesis. Calibration of the detector elements is described in Chapter 5. The start of the analysis of calibrated and reconstructed neutrino data is Chapter 6, where data reduction is described. Chapters 8 and 9 then present the experimental results and the physics conclusions that can be drawn from these results. Finally, three appendices describe in more detail some proposed future directions for the reconstruction method developed by the author, present a method for improving energy scale uncertainties through explicit use of calibration data to correct Monte Carlo, and follow-up the discussion of trigger efficiency in Chapter 5.

# Chapter 2

## Solar Neutrinos

In this chapter, we touch upon the very rich subject of neutrino physics and investigate what can be learned from studying solar neutrinos. This naturally leads into a discussion of the Sudbury Neutrino Observatory, which has great potential for definitively solving the long-standing problem of an observed deficit of solar electron neutrinos observed by previous experiments.

### 2.1 Neutrino Physics in the Standard Model

Wolfgang Pauli postulated the existence of the neutrino in 1930 to explain the continuous electron energy spectrum observed in nuclear beta decay. Since then, all three neutrino types ( $\nu_e$ ,  $\nu_\mu$ ,  $\nu_\tau$ ) thought to exist in the standard paradigm have been directly observed through their interactions with other matter. Many interesting properties of neutrinos have been uncovered - neutrino helicity, weak neutral currents, direct mass limits. These and many other important discoveries in particle physics have allowed a consistent theory of particles and their electromagnetic, strong

and weak interactions to be developed. The continued success of this theory despite intense experimental scrutiny continues to amaze and, for the same reasons, frustrate those involved in particle physics research.

In the Standard Model of particle physics describing the electroweak and strong interactions, neutrinos have some rather unique properties that set them aside from the other fundamental particles. Unlike the other fundamental fermions in the Standard Model, neutrinos *only* experience the weak interaction - that is, neutrinos carry no electric or color charges - and are assumed to be massless. This latter assumption is intimately tied to observation that only left-handed (right-handed) neutrinos (anti-neutrinos) participate in weak interactions. The fact that neutrinos only participate in the weak interactions is what makes neutrinos so difficult to detect and study because these forces - mediated by massive  $W^\pm$  and  $Z^0$  bosons - are so weak compared to the other forces<sup>1</sup>. All fermionic particles feel the weak force, but this interaction is typically masked by the dominance of electromagnetic and strong forces experienced by the quarks and charged leptons.

Despite the continued success of Standard Model predictions, it is generally accepted to be an incomplete description of nature in need of generalization. For example, it is not at all clear how to incorporate gravity into the theory. In fact, the Standard Model in its present form runs into difficulties at gravitational mass scales where quantum effects become important (hierarchy problem). The theory also does not make direct predictions of fermion masses nor does it explain why there are three generations of fermions.

Another potential problem for the Standard Model is the assumption of massless neutrinos related to the observation of neutrinos in only one helicity state (left-

---

<sup>1</sup>except for gravity, which is weakest of all the forces.

handed). There is a growing body of evidence in strong favor of neutrino mass, particularly from observations of solar (described in Section 2.3) and atmospheric neutrinos. If neutrinos do indeed have mass, then the smallness of their masses compared to their charged lepton counterparts could be an indication of some underlying symmetry, or may at least yield some important clues as to how to construct a more general theory. Incorporating neutrino mass into the existing framework may also tell us something interesting about neutrino properties themselves, such as whether neutrinos are Dirac or Majorana (i.e. their own antiparticles) particles unlike the other fermions or whether they mix with other neutrino states (i.e. oscillations). It is the possibility of elucidating new physics which makes the study of neutrinos currently such an interesting field of particle physics research.

## 2.2 The Standard Solar Model

The Sun is a source of neutrinos. This has been established by water Cerenkov experiments - the SNO experiment included [2, 3] - which have sensitivity to incident neutrino direction. The question one now wants to ask is how well the measured rate and energy spectrum of solar neutrinos agree with expectations from our understanding of how the Sun works. To answer this question, one first needs a model of the Sun which predicts the neutrino flux. The Standard Solar Model (SSM) is briefly described in this section - see [4, 5] for a more complete description. Solar neutrino measurements from existing experiments are presented in Section 2.3.

The Sun is powered by nuclear fusion reactions which convert hydrogen into helium deep inside the solar core. Electron-type neutrinos are produced as a byproduct of

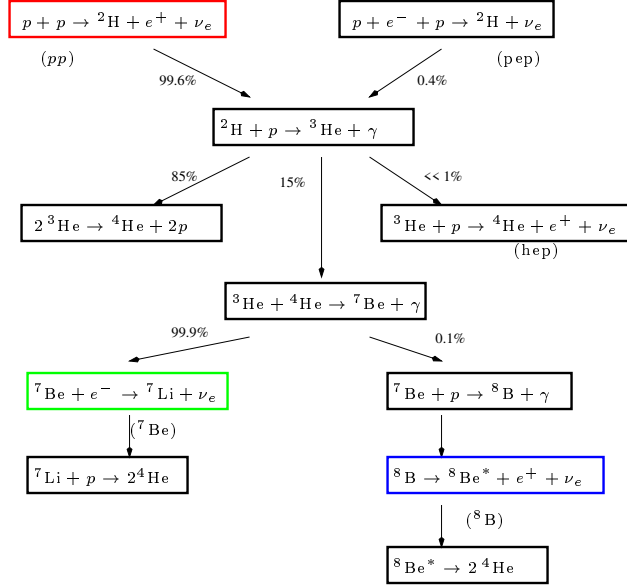


Figure 2.1: Nuclear reactions involved in the *pp* chain. From [4].

these fusion reactions. The dominant overall reaction<sup>2</sup>.

$$4p + 2e^- \rightarrow ^4\text{He} + 2\nu_e + 26.7 \text{ MeV} \quad (2.1)$$

proceeds through a set of nuclear reactions called the *pp* chain. The majority ( $\sim 97\%$ ) of the 26.7 MeV is released in the form of photons, with the remainder going into kinetic energy of the neutrinos (and heavy particles) produced. The photon energy is transported to the surface of the Sun where it is emitted as sunlight. Figure 2.1 shows the nuclear reactions involved in the *pp* chain, with the neutrino-producing reactions labeled in parentheses.

Solar model calculations are used to calculate, among other solar quantities, the flux of neutrinos produced by the Sun. It is important to note that the *energy spec-*

<sup>2</sup>>98% of the solar luminosity and neutrino flux is produced by this reaction. A sub-dominant chain called the *CNO* cycle representing the fusion of four protons makes up the remainder.

*trum* of neutrinos produced by each of the reactions shown in Figure 2.1 is almost entirely dictated by nuclear physics rather than details of the solar model. The solar model calculations simply determine the overall and relative normalizations of the neutrino fluxes produced in these reactions. Detailed calculations which make accurate predictions are notoriously difficult to perform for astrophysical systems, however, certain characteristics of the Sun afford an opportunity to use the Sun as a reliable neutrino source. The Sun is a main sequence star, the implications being that it burns its nuclear fuel without rapid evolution or change<sup>3</sup>. This greatly simplifies solar model calculations, because the Sun can be considered to evolve from one hydrostatic equilibrium state to another while on the main sequence. Also, solar parameters such as mass, radius, surface composition, photon luminosity and spectrum are known to much higher accuracy than for other stars.

In SSM model calculations, the Sun is assumed to have started at some distant time with a homogeneous composition largely comprised of hydrogen. Hydrogen burns deep inside the solar interior and consequently the chemical composition slowly changes as the Sun evolves. Energy is transported from the solar interior to exterior regions which are at lower temperatures by photon diffusion and convective motions. Using the solar equation of state relating pressure, temperature and density and the transport equations, the Sun is evolved quasistatically to its present age ( $4.6 \times 10^9$  years). In practice, an iterative process of refining input parameters and recalculation is performed until the calculated model agrees at some level with the current measured solar properties.

The calculated total neutrino fluxes from the Bahcall-Pinsonneault (BP2000) standard solar model are shown in Table 2.1. The calculated neutrino energy spectra are

---

<sup>3</sup>for which life on earth is very grateful

Source	Flux ( $10^{10} \text{cm}^{-2}\text{s}^{-1}$ )
pp	$5.96 (1.00^{+0.01}_{-0.01})$
pep	$1.40 \times 10^{-2} (1.00^{+0.015}_{-0.015})$
$^7\text{Be}$	$4.77 \times 10^{-1} (1.00^{+0.10}_{-0.10})$
$^8\text{B}$	$5.05 \times 10^{-4} (1.00^{+0.20}_{-0.16})$
hep	$9.3 \times 10^{-7}$
$^{13}\text{N}$	$5.48 \times 10^{-2} (1.00^{+0.21}_{-0.17})$
$^{15}\text{O}$	$4.80 \times 10^{-2} (1.00^{+0.25}_{-0.19})$
$^{17}\text{F}$	$5.63 \times 10^{-4} (1.00^{+0.25}_{-0.25})$

Table 2.1: BP2000 (modified) SSM neutrino fluxes at one astronomical unit from [5].

shown in Figure 2.2. Along with the neutrino fluxes shown in Table 2.1, the BP2000 SSM also predicts solar evolution and density profile. The BP2000 SSM predictions have been shown to agree with helioseismological data on the observed surface vibration modes to better than 0.1% at all solar radii, giving confidence in the model used to predict the solar neutrino fluxes.

## 2.3 The Solar Neutrino Problem

Several experiments have tested SSM neutrino flux predictions by directly measuring various regions of the spectra shown in Figure 2.2. The existing experiments fall into two classes related to their neutrino detection technique - radiochemical and water Cerenkov. Other experiments using novel detection techniques are either coming online (e.g. Borexino) or in development.

### 2.3.1 Radiochemical Experiments

The first solar neutrino observations were from a radiochemical experiment (Homestake). In this type of experiment, large volumes of material containing target nuclei

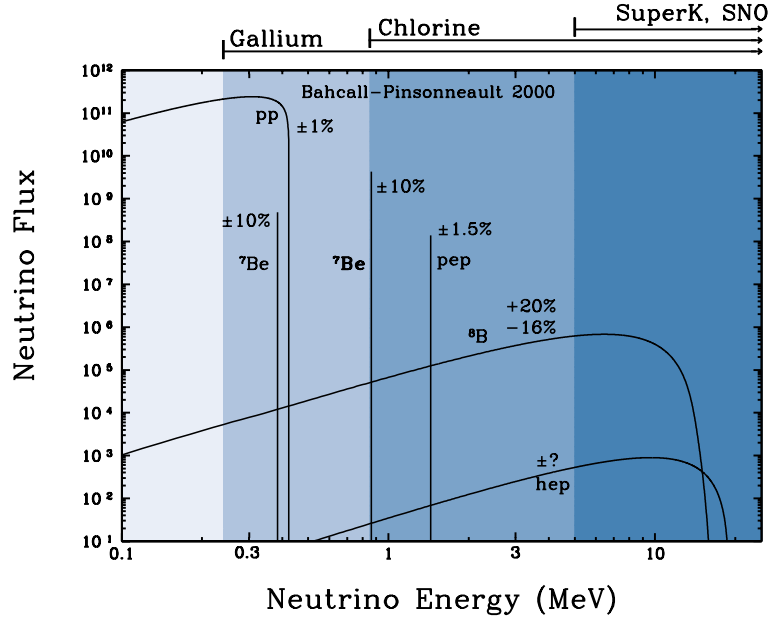


Figure 2.2: BP2000 SSM neutrino energy spectra from [6]. Also shown (top of figure) are the energy thresholds for the various types of solar neutrino experiments.

that are changed into some other nuclei by electron neutrino charge-current (CC) interactions are employed. After some exposure time, the number of neutrino-induced reactions is inferred from the extracted number of nuclei produced from target nuclei. No directional or time information is obtained and the only energy information comes from the threshold for transmutation of the target nuclei.

### The Homestake Chlorine Experiment

First detection of solar neutrinos was by Ray Davis Jr. in his pioneering  $^{37}\text{Cl}$  radiochemical experiment [7] located inside the Homestake gold mine in Lead, South Dakota. This experiment uses  $3.8 \times 10^5 \text{ l}$  of  $\text{C}_2\text{Cl}_4$  as a neutrino target.  $^{37}\text{Cl}$  undergoes the following reaction



for neutrinos above 0.8 MeV. This means that the Homestake experiment is sensitive to all solar neutrinos except for the lower  ${}^7\text{Be}$  line and  $pp$  neutrinos. The  ${}^{37}\text{Ar}$  atoms produced in the  $\text{C}_2\text{Cl}_4$  solutions are extracted and counted at regular intervals to arrive at a measured neutrino flux at the experiment.

### **Gallium Experiments: SAGE, GALLEX, and GNO**

Other radiochemical experiments using gallium instead of chlorine have been performed. The advantage of using gallium is the very low energy threshold (0.233 MeV) for electron neutrino reaction on  ${}^{71}\text{Ga}$



which gives sensitivity to neutrinos from the important  $pp$  reaction. The  $pp$  neutrinos represent by far the largest solar neutrino flux. More importantly, the uncertainty on their flux ( $\sim 1\%$ ) is small compared to other solar neutrino sources because their flux is tied to the solar luminosity which is known to high accuracy. The gallium experiments that have been performed - SAGE, GALLEX, and GNO - are similar in principle to the chlorine experiment in that the number of neutrino-induced reactions are counted after some period of exposure. In practice, the extraction techniques are very different, however. The experiments differ largely in the form of gallium used. The SAGE experiment [8] used 55 tons of gallium metal as their target, while GALLEX [9] and more recently GNO [10] experiments use a 100 ton gallium chloride target solution.

### 2.3.2 Light Water Cerenkov Experiments

Water Cerenkov experiments use large volumes of water and sensitive light detectors (photomultiplier tubes or PMTs) to detect neutrino interactions in real time. In traditional light water experiments, energetic electrons are produced by neutrinos scattering on atomic electrons. Electrons which are energetic enough to travel faster than the speed of light in water ( $\sim 23$  cm/nanosecond) will produce Cerenkov light that can be detected by a surrounding PMT array. The first such experiment to be performed was the Kamiokande II experiment [11] located in the Kamioka mine in Kamioka, Japan. Following the success of the Kamiokande II experiment, a much larger experiment called SuperKamiokande was built and continues to collect neutrino data [12] [13].

There are a few important points to be made about light water Cerenkov experiments. These experiments operate at significantly higher energy thresholds than the radiochemical experiments because of backgrounds at low energy from naturally occurring radioactivity. This limits water Cerenkov experimental sensitivity to  $^8\text{B}$  and  $\text{hep}$  neutrinos. Water Cerenkov experiments also have sensitivity to neutrino direction through forward scattering of the electrons, enabling Kamiokande II to be the first experiment to establish the Sun as a source of neutrinos. Light water Cerenkov experiments also have mixed sensitivity to all neutrino flavors due to the neutral current component of neutrino-electron scattering. At solar neutrino energies, the cross section for  $\nu_e$  scattering on electrons is  $\sim 6$  times that of  $\nu_\mu$  and  $\nu_\tau$ . The relative fractions of neutrino types contributing to the observed elastic scattering rate cannot be determined by these experiments alone, however. As we will see, this neutral current sensitivity is important to interpreting early results from the SNO experiment.

Experiment	Detection Reaction	Threshold	$\nu$ Sensitivity	Flux/SSM
Homestake	$\nu_e + {}^{37}\text{Cl} \rightarrow e^- + {}^{37}\text{Ar}$	0.8 MeV	${}^7\text{Be}, {}^8\text{B}$	$0.34 \pm 0.06$
Kamiokande	$\nu_{e,(\mu,\tau)} + e \rightarrow \nu_{e,(\mu,\tau)} + e$	7.3 MeV	${}^8\text{B}$	$0.55 \pm 0.13$
SAGE	$\nu_e + {}^{71}\text{Ga} \rightarrow e^+ + {}^{71}\text{Ge}$	0.23 MeV	$pp, {}^7\text{Be}, {}^8\text{B}$	$0.59 \pm 0.07$
GALLEX/GNO	$\nu_e + {}^{71}\text{Ga} \rightarrow e^+ + {}^{71}\text{Ge}$	0.23 MeV	$pp, {}^7\text{Be}, {}^8\text{B}$	$0.58 \pm 0.07$
SuperK	$\nu_{e,(\mu,\tau)} + e \rightarrow \nu_{e,(\mu,\tau)} + e$	5 MeV	${}^8\text{B}$	$0.46 \pm 0.09$

Table 2.2: Solar neutrino experiments along with measured flux relative to BP2000 (modified) SSM predictions [5].

### 2.3.3 Comparison of Results with Expected Rates

The solar neutrino flux measured by each of the experiments is summarized in Table 2.2 and shown diagrammatically in Figure 2.3.

Notice that all experiments to date measure a solar neutrino rate of between 30-60% relative to the SSM predictions. This measured deficit, called the “solar neutrino problem”, has existed for more than 30 years without definitive resolution. If one considers the measured deficit in the context of the various experimental sensitivities to the solar neutrino energy spectrum, an interesting feature emerges. The flux suppression is larger for the Homestake experiment than it is for the water Cerenkov experiments which have a larger average neutrino energy threshold. It therefore appears as if the solar neutrino spectrum where the  ${}^7\text{Be}$  line resides between the Homestake experimental threshold (0.8 MeV) and 5 MeV is more suppressed than the higher energy neutrinos.

### 2.3.4 Possible Solutions to the Solar Neutrino Problem

What are possible explanations for the observed deficits of solar neutrinos? One possibility is that one or more of the experiments could be wrong. This seems very

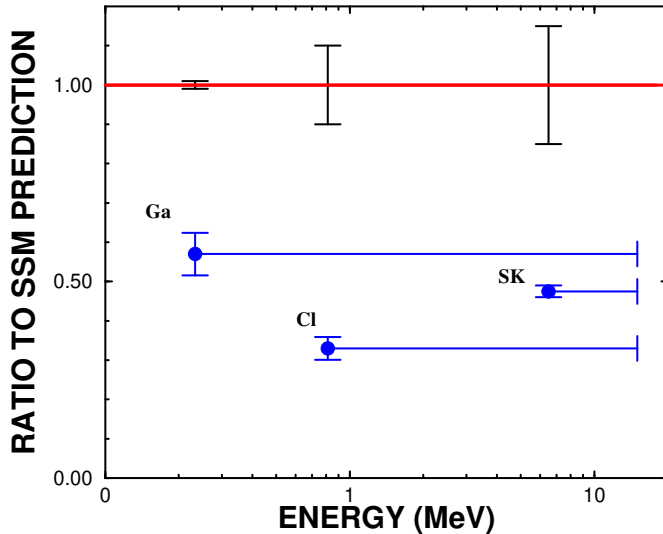


Figure 2.3: Graphical representation of solar neutrino flux measurements, shown as a function of the average neutrino energy sensitivity for type of experiment.

unlikely, as six different experiments have now confirmed the substantial deficit of solar neutrinos. The water Cerenkov, Ga, and Cl experiments all use very different detection methods and have very different systematics.

It is possible that the solar neutrino problem is simply due to some inadequacies in the SSM description of the Sun. It actually turns out to be very difficult if not impossible to construct alternative models of the Sun that agree with all the existing solar data and the observed neutrino fluxes. As previously mentioned, the excellent agreement between SSM predictions and helioseismology is an often quoted triumph of the SSM which constrains the degree to which solar model parameters can be tweaked to agree with neutrino observations. The importance of the gallium experiments also cannot be overstated in this context, because the  $pp$  neutrino flux is highly constrained by the observed solar luminosity. It is also very difficult to

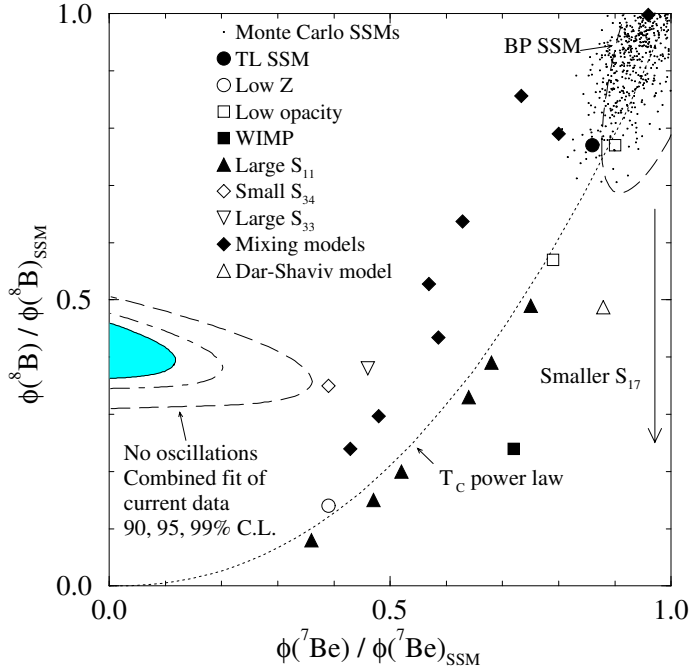


Figure 2.4: Correlations between the measured  ${}^8\text{B}$  and  ${}^7\text{Be}$  flux ratios for standard and various non-standard solar models. See [14, 15] for a complete description.

account for the larger suppression of  ${}^7\text{Be}$  relative to  ${}^8\text{B}$  neutrinos. This is because  ${}^8\text{B}$  neutrinos are from decay of  ${}^8\text{B}$  that is produced from the same  ${}^7\text{Be}$  responsible for the  ${}^7\text{Be}$  neutrino line (recall Figure 2.1). It therefore seems difficult to suppress  ${}^7\text{Be}$  without also suppressing  ${}^8\text{B}$  by the same amount. The difficulty in constructing alternative “non-standard” solar models that can describe the solar neutrino problem and, in particular, the correlations between  ${}^7\text{Be}$  and  ${}^8\text{B}$  deficits is summed up nicely in Figure 2.4 and described in [14, 15].

A third possibility is that the Sun is producing the number of electron neutrinos predicted by the SSM and the observed deficit is due to some non-standard neutrino physics. Many of these scenarios invoke neutrino mass, and therefore involve new physics beyond the Standard Model. By far, the most favored particle physics solution

to solar neutrino problem is neutrino oscillations, described in Section 2.4. There are also several other so-called “exotic” solutions to the solar neutrino problem which get less serious consideration but nevertheless can fit the observed solar neutrino data [16, 17]. Examples include neutrino decay, violation of the equivalence principle, resonant spin-flavor precession, and flavor changing neutral currents.

## 2.4 Oscillations of Massive Neutrinos

Neutrino oscillations (i.e. conversion of one neutrino type into another) can provide a natural explanation of the solar neutrino problem. Neutrino oscillations require at least one of the neutrinos to have nonzero mass and for the weak (i.e. flavor) eigenstates to be mixtures of neutrino states with definite mass. The idea is that a  $\nu_e$  produced by weak interaction in the Sun has some probability of being converted through oscillations into a different neutrino flavor<sup>4</sup> by the time it reaches the earth. The measured solar neutrino deficit is therefore due to oscillations and the fact the prior experiments have been primarily sensitive only to electron neutrinos.

### 2.4.1 Neutrino Oscillations in Vacuum

If neutrinos have mass and their weak eigenstates differ from the eigenstates of the free particle Hamiltonian (mass eigenstates), then a neutrino produced in a weak eigenstate can oscillate between flavors simply by propagation through free space. For simplicity, we consider vacuum oscillations between two neutrino flavors,  $\alpha$  and  $\beta$  ( $\alpha, \beta = e, \mu, \tau$ ). Mass eigenstates  $|\nu_1\rangle, |\nu_2\rangle$  are related to the weak eigenstates through

---

<sup>4</sup>or possibly a *sterile* neutrino which has no standard electroweak interactions.

a unitary transformation,

$$\begin{pmatrix} |\nu_\alpha\rangle \\ |\nu_\beta\rangle \end{pmatrix} = U \begin{pmatrix} |\nu_1\rangle \\ |\nu_2\rangle \end{pmatrix} = \begin{pmatrix} \cos \theta & \sin \theta \\ -\sin \theta & \cos \theta \end{pmatrix} \begin{pmatrix} |\nu_1\rangle \\ |\nu_2\rangle \end{pmatrix} \quad (2.4)$$

where  $U$  is the unitary mixing matrix and  $\theta$  is the vacuum mixing angle (analogous to the Cabibbo angle  $\theta_c$  in quark mixing). A given mass eigenstate  $|\nu_i\rangle$  ( $i = 1, 2$ ) at time  $t = 0$  with energy  $E_i$  propagating through free space will evolve at some later time  $t$  as

$$|\nu_i(t)\rangle = e^{-iE_i t} |\nu_i(0)\rangle \quad (2.5)$$

where

$$E_i = \sqrt{p^2 + m_i^2} \simeq p + \frac{m_i^2}{2p} \quad (2.6)$$

for common neutrino momentum  $p$  and  $p \gg m_i$ .

Imagine that a neutrino of flavor  $\alpha$  is produced in a weak interaction at some time  $t = 0$ . According to 2.4, this weak eigenstate  $|\nu_\alpha(0)\rangle$  is produced in a superposition of mass eigenstates given by

$$|\nu_\alpha(0)\rangle = \cos \theta |\nu_1(0)\rangle + \sin \theta |\nu_2(0)\rangle \quad (2.7)$$

At some later time  $t$ , this state evolves because of different phases acquired by the mass eigenstates  $|\nu_1\rangle$ ,  $|\nu_2\rangle$  as the neutrino propagates through the vacuum and is given by

$$|\nu_\alpha(0)\rangle = \cos \theta e^{-iE_1 t} |\nu_1(0)\rangle + \sin \theta e^{-iE_2 t} |\nu_2(0)\rangle \quad (2.8)$$

From this relation and 2.6, it can be readily shown that the probability for the neutrino

flavor  $\alpha$  with energy  $E$  in MeV to remain flavor  $\alpha$  after some distance  $L$  in meters is given by

$$P(\nu_\alpha \rightarrow \nu_\alpha) = 1 - \sin^2 2\theta \sin^2 \left( \frac{1.27 \Delta m^2 L}{E} \right) \quad (2.9)$$

using  $t = L/c$  and  $\Delta m^2 \equiv m_2^2 - m_1^2$  in  $\text{eV}^2$ . This relation is also sometimes re-written in terms of a “vacuum oscillation length”,  $L_v$ , defined as

$$L_v = \frac{4\pi E}{\Delta m^2} \quad (2.10)$$

Notice from 2.9 that this “survival probability” can be less than unity (oscillations) after the neutrino propagates some distance. For a given  $\theta$ , the maximum sensitivity to vacuum oscillations occurs when  $\Delta m^2 \sim E/L$ . This means that solar neutrinos ( $L \sim 1.5 \times 10^{11} \text{ m}$ ,  $E \sim 10 \text{ MeV}$ ) can probe mass-squared differences between  $10^{-10}$  and  $10^{-11} \text{ eV}^2$ , far smaller than can be probed with terrestrial neutrino sources.

## 2.4.2 Neutrino Oscillations in Matter

It was pointed out by Wolfenstein [18] that neutrino oscillation phenomena can change in very interesting ways when neutrinos propagate through ordinary matter. These matter effects were later applied to the Sun by Mikheyev and Smirnov [19] and are called MSW effects. Details about the MSW effect can be found in many references (see [20], for example). Therefore, only the main points are included in this section.

While all neutrino flavors scatter electrons via  $Z^0$  exchange (neutral current), only electron neutrinos have CC interactions ( $W^\pm$  exchange) with matter at solar neutrino energies (few MeV). This additional interaction leads to different forward scattering amplitude for  $\nu_e$ ’s relative to the other neutrino flavors. The effect of this additional

potential is to add off-diagonal terms, proportional to the electron number density,  $n_e$ , to the Hamiltonian governing the propagation of vacuum mass eigenstates through matter. The mixing between neutrino flavors is now different than the vacuum case because the Hamiltonian is diagonalized by effective mass eigenstates that depend on the electron density. The flavor eigenstates are related to the effective mass eigenstates by a unitary form similar to Equation 2.4 except that the vacuum mixing angle  $\theta$  is replaced by an effective mass mixing angle  $\theta_m$  given by

$$\tan 2\theta_m = \frac{\tan 2\theta}{1 - (L_v/L_e) \sec 2\theta} \quad (2.11)$$

where  $L_e = \sqrt{2\pi}/G_F n_e$  and  $G_F$  is the Fermi constant. A resonance condition exists if  $L_v = L_e \cos 2\theta$  where  $\theta_m$  becomes maximal ( $\theta_m = 45^\circ$ ) independent of the vacuum mixing angle  $\theta$ . In terms of  $\Delta m^2$  and  $\theta$ , the resonance condition is satisfied if

$$\Delta m^2 \cos 2\theta = 2\sqrt{2}G_F n_e E \quad (\text{resonance condition}) \quad (2.12)$$

The fact that large mixing can be attained without a large vacuum mixing angle was initially very attractive because people were generally wary of the requirement in vacuum mixing for the neutrino mixing angle to be much larger than that in quark mixing. The demonstration of maximal mixing in atmospheric neutrinos has made this less of issue, however.

Consider a  $\nu_e$  produced in a high density region near the center of the Sun where the nuclear fusion reactions take place. If  $E \gg \Delta m^2 \cos 2\theta/G_F n_e$ , then  $\theta_m \simeq \frac{\pi}{2}$  and  $\nu_e$  is almost completely in the heavier mass eigenstate  $\nu_2$ . As the neutrino propagates to the solar surface where  $n_e = 0$ , it will pass through a resonance region where mixing

is maximal ( $\theta_m = 45^\circ$ ). If the density is slowly varying so that the change in  $n_e$  per unit oscillation length is small, the neutrino will remain a  $\nu_2$  state throughout its propagation through the Sun. If this *adiabatic* condition is satisfied and the vacuum mixing angle is small, nearly complete conversion of  $\nu_e$  to the other flavor eigenstate when it exits the Sun will occur. In the other case of *non-adiabatic* conversion, there is a certain probability for  $\nu_2$  to “jump” to the  $\nu_1$  eigenstate near resonance (where the eigenstates are closest) and emerge from the Sun as a  $\nu_e$ . This will increase the  $\nu_e$  survival probability relative to the adiabatic case.

It should be noted that for certain regions of parameter space, the  $\nu_e$  survival probability is strongly dependent on neutrino energy, allowing for the possibility of experiments with spectral sensitivity to observe distortions from the primary neutrino energy spectrum. This is particularly true for vacuum mixing and MSW small-angle mixing where the oscillation pattern is “imprinted” in the neutrino energy spectrum. Also, matter effects from neutrinos propagating through the earth can be significant for certain regions of parameter space. In this case,  $\nu_e$ ’s can be regenerated in the earth which leads to an enhancement of detected  $\nu_e$ ’s at night compared to the day (where  $\nu$ ’s essentially propagate directly to a given detector). An observed day-night asymmetry in the solar neutrino flux would represent very strong evidence for oscillations.

### 2.4.3 Limits on Oscillation Parameters

Under the assumption of neutrino oscillations as a solution to the solar neutrino problem, limits on the neutrino parameters ( $\Delta m^2$ ,  $\theta$ ) can be determined through analysis of the existing data. Allowed regions in the  $\Delta m^2$ - $\tan^2 \theta$  plane at various

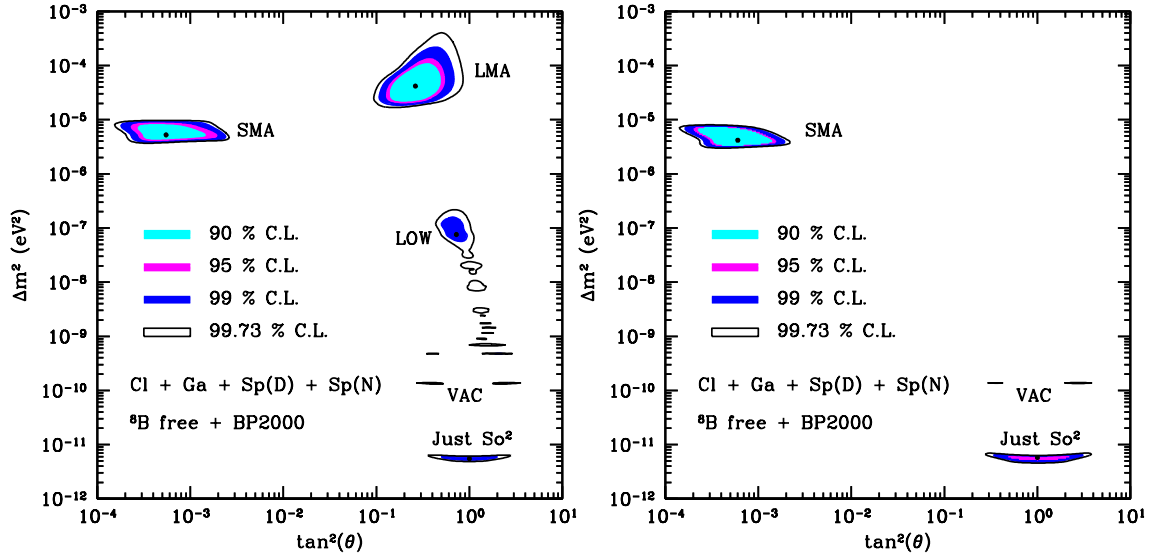


Figure 2.5: Allowed regions in the  $\Delta m^2$ - $\tan^2 \theta$  plane at various confidence levels for oscillation to (left) active ( $\nu_\mu$ ,  $\nu_\tau$ ) and (right) sterile neutrinos. From [21].

confidence levels for oscillation to active ( $\nu_\mu$ ,  $\nu_\tau$ ) and sterile neutrinos are shown in Figure 2.5. For the analysis [21] producing these allowed regions, the  ${}^8\text{B}$  and *hep* fluxes were fit as free parameters to directly test the oscillation hypothesis without constraints from the solar model.

For oscillation to active neutrinos, three MSW solutions exist (SMA, LMA, and LOW solutions) and two vacuum (VAC, Just So<sup>2</sup>) solutions. The energy dependence of the neutrino survival probability for these solutions is shown in Figure 2.6. The only possible MSW solution for oscillation of solar neutrinos to a sterile state is the SMA. In addition to the total observed neutrino fluxes, several other oscillation characteristics contribute to the allowed regions shown in Figure 2.5. The lack of a significant day-night asymmetry or spectral distortions observed by SuperKamiokande significantly contributes to the exclusion of certain regions in the  $\Delta m^2$ - $\tan^2 \theta$  plane (see [22] for a nice recent discussion of global neutrino analyses).

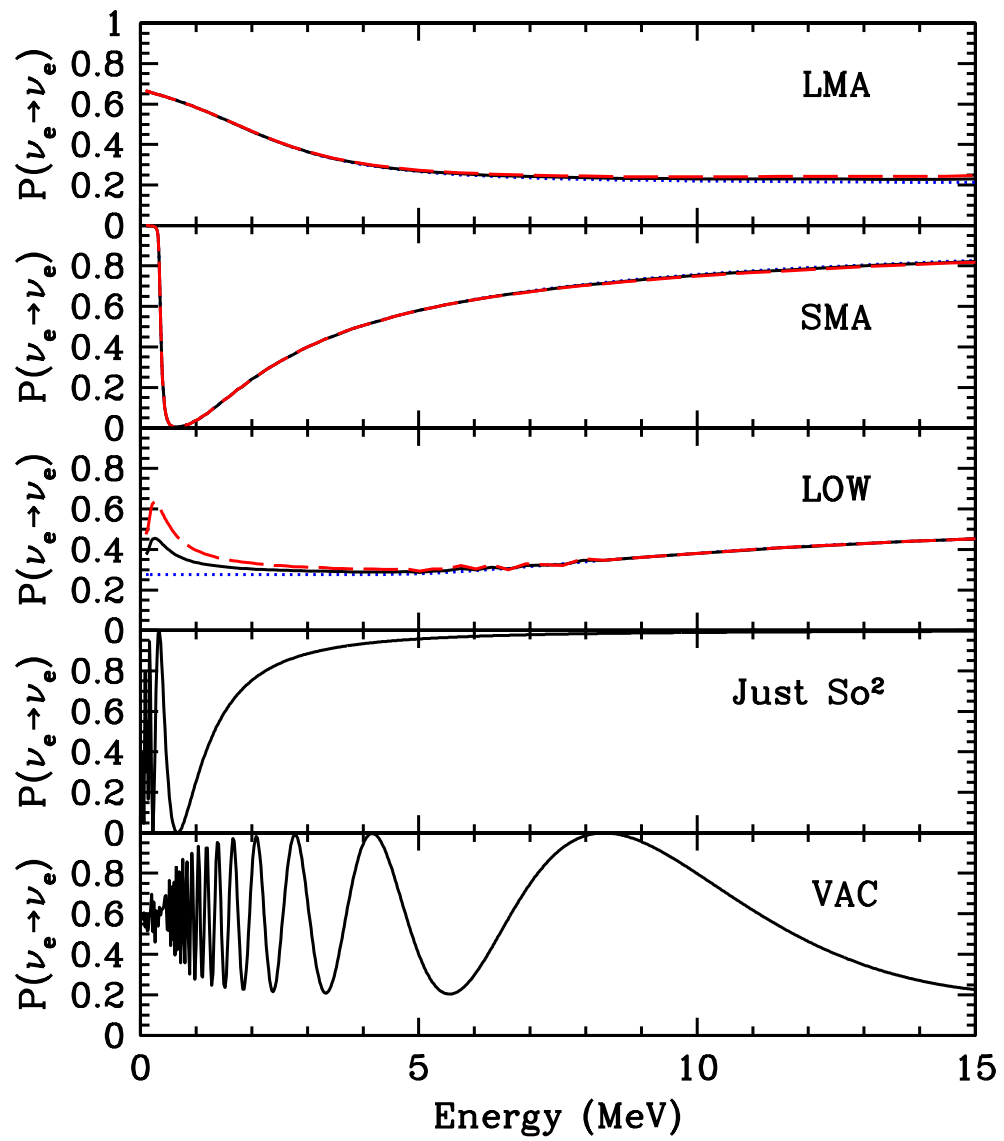


Figure 2.6: Survival probability versus neutrino energy for the allowed solutions shown in Figure 2.5. The solid line represents an average over earth regeneration effects. The dotted line is for daytime without regeneration and the dashed line includes regeneration at night. From [21].

#### 2.4.4 Oscillation Signatures

Measurements of solar neutrino fluxes are inconsistent with any standard solar model. This has lead us to consider neutrino oscillations as a possible explanation of the solar neutrino problem. It was shown that neutrino oscillations (vacuum and/or matter) are consistent with all solar neutrino data for certain values of  $\Delta m^2$  and  $\tan^2 \theta$ . For oscillations to other active neutrino flavors, the SMA region is most favored when only total experimental rates (flux) are considered. Inclusion of energy spectrum and day-night information changes the favored solution to within the LMA region. For oscillations to sterile neutrinos, only the SMA and vacuum solutions (VAC, Just So<sup>2</sup>) are consistent with the data.

Although neutrino oscillations can explain the solar neutrino data, we are still in need of “smoking-gun” evidence that oscillations are occurring for solar neutrinos. We would like separate measurement of the  $\nu_e$  flux and the total (active) neutrino flux in one experiment. If active neutrino oscillations are occurring, then the deficit in the former measurement will not be seen in the latter. An observable distortion of the  ${}^8\text{B}$  neutrino energy spectrum would be strong evidence for neutrino oscillations. Observation of temporal modulations (after accounting for the Earth’s orbital eccentricity) such as a difference in event rate between day and night would demonstrate Earth matter effects that are very difficult (if not impossible) to explain without introducing oscillations.

The next section describes the SNO experiment which is designed to directly search for these oscillation signals.

## 2.5 The SNO Experiment

In Section 2.3.3, it was shown that all solar neutrino experiments to date measure a deficit of  $\nu_e$  coming from the Sun. It was strongly suggested that an explanation of this deficit lies in physics beyond the standard electroweak model (e.g. oscillations) rather than new solar models or systematic problems with the experiments. This is an exciting prospect, indeed. New experimental information is needed to further constrain the possible new physics interpretations and definitively demonstrate neutrino oscillations, if this is indeed a resolution of the solar neutrino problem.

### 2.5.1 Overview

All previous radiochemical solar neutrino experiments were sensitive to only electron neutrinos. The light water Cerenkov experiments (Kamiokande and Super-Kamiokande) have additional sensitivity to other active neutrino flavors ( $\nu_\mu$ ,  $\nu_\tau$ ) through the neutral current component to neutrino-electron elastic scattering. The sensitivity to other neutrino flavors is weak compared to  $\nu_e$  ( $\sigma_{\nu_e} \sim 6\sigma_{\nu_\mu, \nu_\tau}$ ) and neutral current interactions cannot be separated from dominant  $\nu_e$  charged current interactions. Without additional information on flavor content of solar neutrinos, a direct determination of whether the neutrino deficit is due to a simple suppression (fewer  $\nu_e$ 's produced in the Sun or  $\nu_e \rightarrow \nu_s$  oscillations) or active flavor neutrino oscillations ( $\nu_e \rightarrow \nu_\mu, \nu_\tau$ ) remains elusive.

The importance of an experiment having both charged current *and* neutral current sensitivity in directly resolving the solar neutrino problem was stressed in 1985 by H. Chen [23]. He further pointed out that a heavy water Cerenkov detector could be used for such an experiment, provided stringent background requirements inherent to the

use of  $D_2O$  could be achieved. Neutral current breakup of the deuteron is independent of neutrino flavor, consequently the observed rate gives a measurement of the total solar neutrino flux that is unaffected by oscillations<sup>5</sup>. At solar neutrino energies, the charged current interaction of neutrinos on deuterium results in an electron that is detected through its Cerenkov light. Since this reaction only occurs for electron-type neutrinos, the charged current rate gives a measurement of the total solar  $\nu_e$  flux. Comparison of the charged current and neutral current rates provides a direct test of the neutrino oscillation hypothesis as a solution of the solar neutrino problem for active  $\nu$ 's.

The Sudbury Neutrino Observatory (SNO) is a second generation water Cerenkov detector which uses 1 kt of  $D_2O$  as the interaction and detection medium. The detector is located near Sudbury, Ontario, Canada at the 6800 ft level of an active nickel mine operated by Inco Limited. SNO is the deepest solar neutrino experiment, with more than 6000 meters water equivalent (m.w.e) of overburden limiting the rate of cosmic ray components to  $\sim 70$  muons per day. The cavity in which the detector resides is 22 m  $\times$  30 m in diameter. The detector itself consists of a 12 m diameter acrylic vessel that contains the heavy water and a 17 m diameter support structure holding 9438 inward-looking PMTs used to detect the Cerenkov light produced in neutrino interactions. The remaining volume is filled with ultra-pure light water to act as a shield for naturally occurring radioactivity from the construction materials and the cavity walls. A schematic picture of the SNO detector is shown in Figure 2.7.

---

<sup>5</sup>This is only true for oscillation into other active neutrino flavors. Oscillation into *sterile* neutrinos which do not participate in weak interactions would reduce the observed neutral current rate relative to solar model predictions.

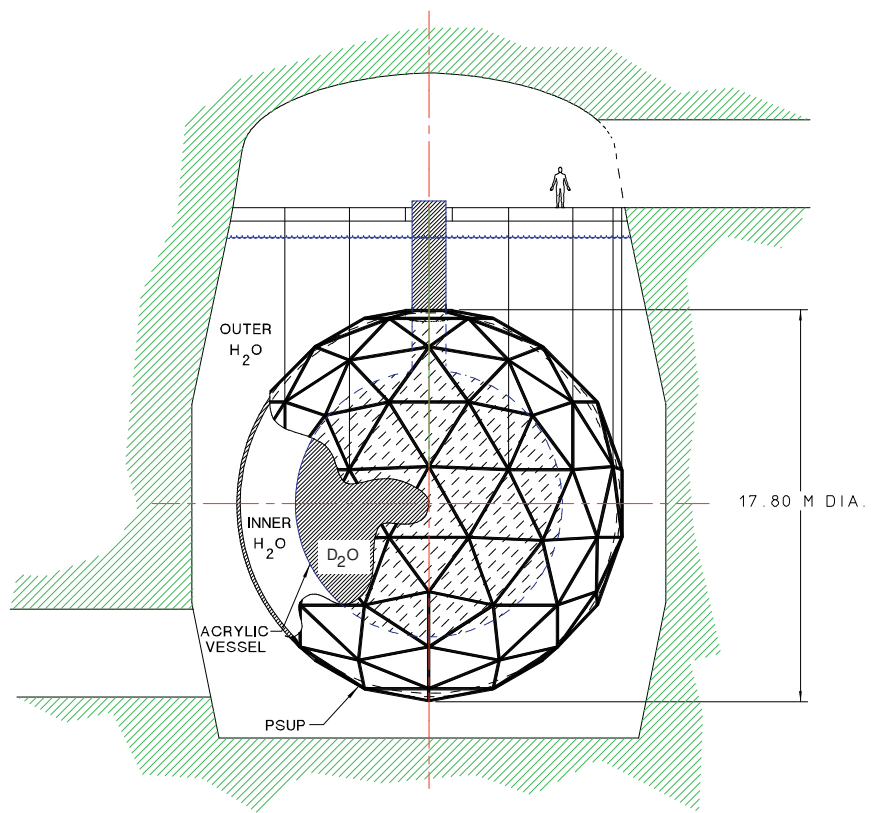
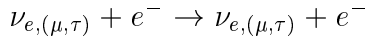


Figure 2.7: Schematic drawing of the SNO detector. Taken from [24].

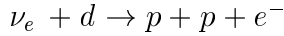
### 2.5.2 Interaction and Detection of Neutrinos in SNO

Neutrinos in the solar neutrino energy range interact in the detector through three different reactions. Neutrinos can elastically scatter electrons in the D<sub>2</sub>O and H<sub>2</sub>O regions to produce relativistic electrons that are detected through Cerenkov light they produce. This elastic scattering (ES) reaction,



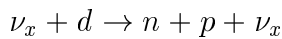
is the method of solar neutrino detection used in previous water Cerenkov experiments. The angular distribution of the scattered electron is forward-peaked in the direction of the incident neutrino, which is important for establishing the sun as the source of observed neutrino events. The ES reaction also allows for direct comparison with other water Cerenkov experiments (e.g. SuperKamiokande).

Neutrinos interact with deuterons through two different reactions. There is the charged current (CC) reaction,



which only occurs for electron neutrinos with energy greater than 1.44 MeV. The electron direction is slightly forward/backward asymmetric having a  $1 - 0.340 \cos \theta_{e\nu}$  angular distribution, where  $\theta_{e\nu}$  is the angle between the incident neutrino direction and the initial direction of the electron. The energy of CC electrons is much more closely related to the neutrino energy than the ES reaction, which has a flat distribution in energy up to the kinematic limit.

Neutrinos can also break up the deuteron through the neutral current (NC) reaction,



where  $\nu_x = \nu_e$ ,  $\nu_\mu$ , or  $\nu_\tau$ . This reaction occurs at the same rate independent of neutrino flavor. The threshold for the NC reactions 2.2 MeV. In contrast to the ES and CC reactions, the NC reaction results in a free neutron and the subsequent signal does not provide any angular or energy information (aside from the production threshold). In the pure D<sub>2</sub>O phase of the experiment upon which this thesis is based, the neutron is detected through its capture on deuterium which produces a 6.25 MeV  $\gamma$ -ray that generates Cerenkov light via Compton scattering. In later phases of the experiment, the neutron signal is enhanced by the addition of chlorine-based salt and <sup>3</sup>He proportional counters to the D<sub>2</sub>O .

## 2.6 Summary

In this chapter, it was shown that all solar neutrino experiments measure a deficit of neutrinos from the Sun. It was argued that a resolution of this problem is likely to involve non-standard neutrino properties like neutrino mass rather than more mundane (from a particle physicist's perspective!) astrophysical or unknown experimental systematics explanations. This is truly an exciting time in neutrino physics, as many new experiments are either in operation or will be operating in the near future. SNO is one such experiment which is now operating that will test the neutrino oscillation hypothesis directly. The detector which has been built to achieve this goal is described in the next chapter.

# Chapter 3

## The SNO Detector

This chapter provides a description of the SNO detector. Particular emphasis is placed on the SNO trigger system, for which the author held primary responsibility for digital design and commissioning. A more detailed description of the other detector elements can be found in [24].

### 3.1 Acrylic Vessel

The spherical vessel used to contain the D<sub>2</sub>O is comprised of 122 UVT (UV transmitting) 5.6 cm thick acrylic panels. These acrylic panels had to be transported underground and bonded together *in-situ* into a sphere without comprising stringent cleanliness requirements.

The UVT acrylic comprising the acrylic vessel (AV) was chosen for several reasons. Acrylic is a simple hydrocarbon that is readily available and can be made low in radioactivity ( $< 1.1 \times 10^{-12}$  g/g U/Th). It can be molded together with bond strengths close to the bulk material. Also, the light transmission of UVT acrylic

closely matches the spectral response of the SNO PMTs. In contrast, UV absorbing acrylic is used in the neck of the vessel to reduce light being piped into the inner detector which could be mis-reconstructed into the fiducial volume.

## 3.2 Water Systems

The heavy and light water regions are maintained using two separate water treatment systems in continual operation. These systems are responsible for delivering the D<sub>2</sub>O and H<sub>2</sub>O volumes during the initial fill as well as maintaining their integrity throughout the life of the experiment.

Achieving and maintaining low levels of radioactive contaminants in the light and heavy water is critical for the experiment. The background low energy “wall” of Cerenkov light produced by  $e^-$  and  $\gamma$ ’s from radioactive decay of contaminates (predominately U, Th, and K decay chains) ultimately puts a lower limit on the energy above which data from the detector can be accurately analyzed. More troublesome is deuteron photodisintigration by  $\gamma$ -rays above 2.2 MeV which mimics the neutral current neutrino signal by producing a free neutron. There are two decays in the U/Th chain that produce such  $\gamma$ -rays: <sup>208</sup>Tl (2.615 MeV  $\gamma$ ) and <sup>214</sup>Bi (2.445 MeV  $\gamma$ ). The goal for radioactive backgrounds is for photodisintegration to represent less than 5% of the SSM expected neutral current signal. This corresponds to  $4.5 \times 10^{-14}$  g/g <sup>222</sup>Rn,  $3.7 \times 10^{-15}$  g/g <sup>224</sup>Ra, and  $4.5 \times 10^{-14}$  g/g <sup>226</sup>Ra in the D<sub>2</sub>O. For the H<sub>2</sub>O, the goals are to  $4.5 \times 10^{-13}$  g/g <sup>222</sup>Rn,  $3.7 \times 10^{-14}$  g/g <sup>224</sup>Ra, and  $4.5 \times 10^{-13}$  g/g <sup>226</sup>Ra. Assay techniques for U/Th decay chain nuclei such as Th, Ra, Pb, and Rn have been developed to determine levels of U and Th in the water volume. Based on these techniques, the radioactivity goals have been achieved and the backgrounds are small

enough to permit an accurate NC measurement in future phases of the experiment.

### 3.2.1 Heavy Water ( $D_2O$ ) System

The availability of 1 kt of heavy water for loan from Atomic Energy of Canada (AECL) is what makes an experiment like SNO feasible. The heavy water system is responsible for purifying the  $D_2O$  upon delivery and maintaining the required levels of radioactive impurities for the experiment. The system must do this without compromising the high isotopic purity ( $> 99.9\%$ ) of the  $D_2O$ .

The full  $D_2O$  volume can be circulated at a rate of  $\sim 150$  l/min. The heavy water is passed through ultra-filtration membranes and a reverse osmosis (RO) system which filter out impurities to very low levels. The  $D_2O$  is also degassed before going into the detector to reduce radon levels in the water. The heavy water system must also facilitate the addition and removal of chlorine-base salt used in the current phase of the experiment to enhance the NC signal.

### 3.2.2 Light Water ( $H_2O$ ) System

Input to the light water system is purified water from the surface of the mine. The water is first de-aerated to remove dissolved  $O_2$  and  $N_2$ . The  $H_2O$  then enters a series of successively finer membranes to filter out particulate matter and passes through an RO system to achieve ultra-filtration. The water is then degassed, passed through a UV unit consisting of mercury lamps to kill bacteria, and cooled to 10 degrees Celsius before being put into the detector. The light water is continually circulated through the system to maintain high purity levels.

While the light water is degassed to remove radon and  $O_2$  which facilitates bio-

logical growth, it is regassed with pure  $N_2$  before being introduced into the detector. Maintaining atmospheric levels of  $^2N$  gas in the light water is used as a workaround for a potentially serious problem with high-voltage (HV) breakdown encountered [25] during early commissioning of the SNO detector. Marginal design of the PMT HV connectors resulted in gaps within the inner connector insulation region that exhibited breakdown when “pumped down” by the degassed water originally used. Nitrogenated water increases air gap pressures within the connectors that raises the HV breakdown voltage so that the detector can be operated without significant problems from breakdown.

### 3.2.3 Cover Gas System

Although the heavy and light water are degassed in the recirculation systems, radon-rich mine air can still enter the water from leaks in the deck and glovebox hardware<sup>1</sup>, for example. To isolate the  $D_2O$  and  $H_2O$  from laboratory air, a cover gas system has been developed. Nitrogen gas boiled off from a liquid nitrogen dewar is used as a physical barrier between the detector water volume and laboratory air to maintain radon in the water at acceptable levels.

## 3.3 Photomultiplier Tubes and Support Structure

Cerenkov light from the inner part of the detector is collected by 9438 inward-facing Hamamatsu R1408 photomultiplier tubes (PMTs) fixed to a 17 m diameter geodesic support structure (PSUP). Figure 3.1 shows a diagram of the Hamamatsu R1408

---

<sup>1</sup>The “glovebox” envelops the top of the AV neck in the central deck clean room. It provides an interface for calibration source deployment into the detector.

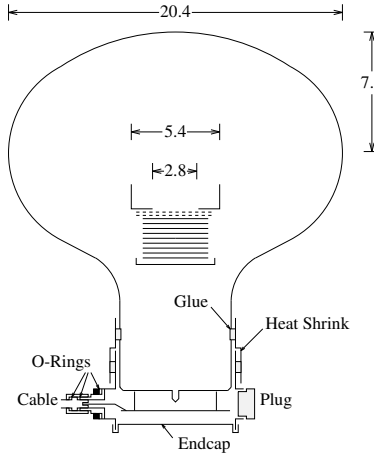


Figure 3.1: Schematic diagram of the Hamamatsu R1408 PMT. Taken from [24].

PMT. The glass bulbs of the SNO PMTs are made of a special low radioactivity (U, Th, K) borosilicate glass (Schott 8246) by Schott Glaswerke. The PMTs are 20 cm in diameter, providing a photocathode coverage of 31%. Light Concentrating reflectors 27 cm in diameter are fitted around the PMTs to increase light collection, which increases the effective photocathode coverage to 59%<sup>2</sup>. Figure 3.2 shows a diagram of the PMT and concentrator assembly. To further increase the light collection efficiency of the PMTs, the vertical component of the geomagnetic field in the detector is approximately canceled with 14 horizontal field-compensation coils embedded in the cavity walls. In addition to the inward-facing PMTs, 91 PMTs without concentrators are mounted on the PSUP facing outward. These PMTs are used to identify muons and other sources of light in the exterior region of the detector.

The PMTs are operated at a positive HV of approximately 2 kV and  $10^7$  gain<sup>3</sup> with a dark current noise rate of  $\sim 600$  Hz in the detector. They have a transit

---

<sup>2</sup>This reduces to  $\sim 54\%$  when concentrator reflectivity is included

<sup>3</sup>Forty-nine “low gain” PMTs have a dynode tap before the final stage that increases their charge dynamic range by a factor of  $\sim 100$ .

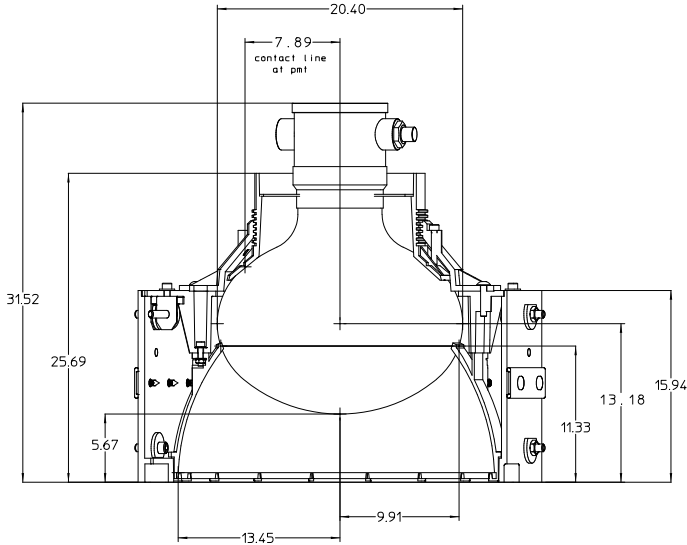


Figure 3.2: Schematic diagram of PMT and concentrator assembly. Taken from [24].

time spread of 1.6 ns which, along with the low noise rate, allows for accurate vertex reconstruction. A base circuit made of Kapton is potted within the rear of each PMT. An RG59/U-type cable carrying supply HV and the capacitively coupled anode signal to the PMT interface electronics is connected to the PMT base.

### 3.4 Front-End Electronics

The SNO electronics system is responsible for performing and storing PMT time and charge measurements when there is a potentially interesting occurrence in the detector. The determination of when to store PMT information is made by the central trigger system, which is described in Section 3.5. The PMT information is read out by the DAQ hardware and merged with trigger information to form the event data stream that is eventually archived to tape. The data acquisition hardware is described in Section 3.6. Figure 3.3 depicts an overview of the SNO electronics and

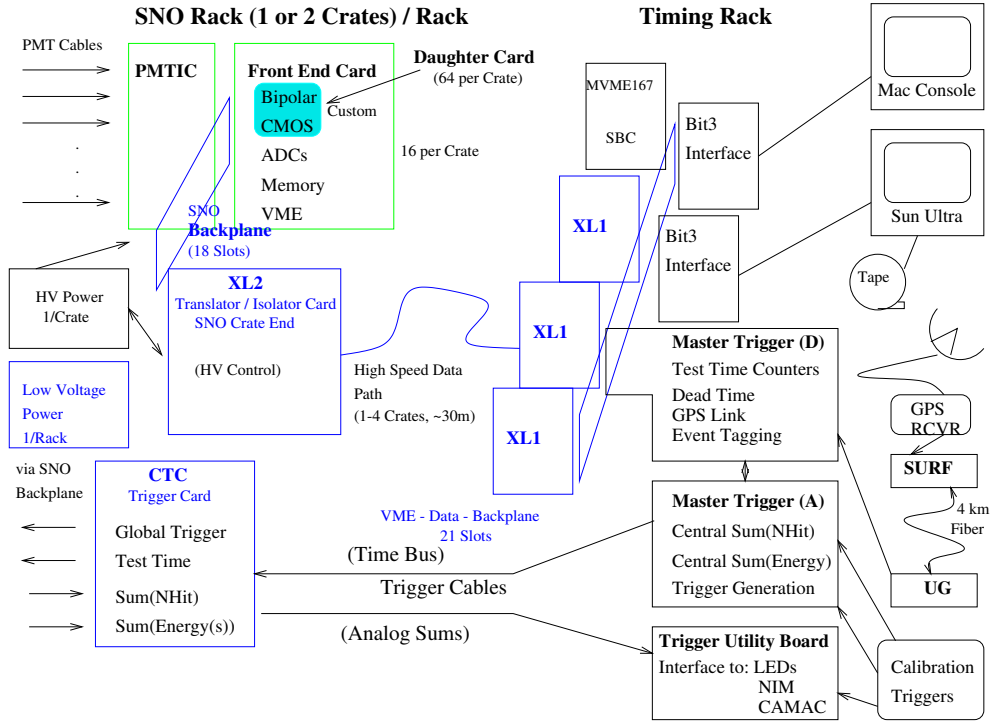


Figure 3.3: Diagram of the SNO electronics and data acquisition hardware. The front-end system responsible for PMT signal processing is shown in the left part of the figure. Components of the central trigger system and VME-SNOBUS interface electronics reside in the central timing rack shown on the right. Also shown on the right part of the figure are the fiber optics boards (SURF and UG) which negotiate communication between the surface GPS and detector electronics.

data acquisition hardware.

The PMT interface and signal processing tasks which make up the front-end electronics are briefly described in Sections 3.4.1 and 3.4.2, respectively. More information about these systems can be found in [2, 24, 26–29].

### 3.4.1 PMT Interface and High Voltage Supply System

Each PMT in the detector is connected through 32 m of  $75\Omega$  RG59/U-type cable to one channel<sup>4</sup> of an eight channel paddle card. Four paddle cards plug into one 32-channel PMT interface card (PMTIC). Each electronics crate contains 16 PMTICs corresponding to 512 channels per crate. The system is comprised of 19 crates that make up the 9728 electronics channels available for use. Each PMTIC connects to both a custom high voltage backplane (HVBP) used for HV distribution and a 32-channel Front-end Card (FEC) to which HV decoupled PMT signals are passed for processing. Each crate of electronics is supplied by one HV supply that delivers  $\sim 70\text{mA}$  total DC current to the PMTs in a crate. The PMT Interface System also protects against over-voltage and HV breakdown, provides coarse read-back of PMT currents, and contains charge injection circuitry for diagnostics purposes.

### 3.4.2 PMT Signal Processing

PMT signals from the PMTICs are terminated and processed on FEC's. The majority of analog signal processing is done by three custom, application specific integrated circuits (ASICs) which physically reside on each of four daughter boards (DBs) plugged into each FEC. A PMT signal received onto a DB is fed to a custom four-channel fast discriminator chip (SNOD) which is triggered on the crossing of a preset threshold.<sup>5</sup> The PMT current is also split in the approximate ratio of 1:16 and sent to two separate inputs - one low gain and one high gain - of a custom four-channel integrator chip (SNOINT) that integrates these signals.

The channel cycle is started on the firing of a SNOD and ends when a global

---

<sup>4</sup>Some PMTs have been removed over time due to irreparable wet-end problems.

<sup>5</sup>On average, SNOD thresholds are  $\sim \frac{1}{4}$  of the mean single photoelectron charge per channel.

trigger (GT) is received from the central trigger or the channel times out after a time (GTVALID) of  $\sim 400$  ns. The SNOD sends timing signals to the SNOINT that determine the total integration time and the times at which the integrals are to be sampled. The high gain integration is sampled at two times relative to the start of integration. This provides a “short” integration (QHS) of a few tens of ns and a “long” integration (QHL) of a little more than 100 ns. The low gain integration can be set to either short or long (QLX). The QHS measurement is used to make a time slewing correction on a given PMT hit time (to be discussed in Section 5.2). The QHL measurement provides some information about the amount of late light for possible inclusion in energy calibration. The firing of a SNOD also signals the QUSN7 ASIC (or “CMOS” chip) to start a time-to-amplitude converter (TAC) ramp which is stopped on a GT or a channel time-out if no GT is received. Since the GT stop time is common to all channels in the system, the TAC voltage of each channel is directly related to the time that each PMT fires relative to the global trigger.

For each event, the analog time and charge measurements (TAC, QHS, QHL, and QLX) are stored in a 16 cell analog storage array within each CMOS chip. An FPGA-based sequencer then controls the digitization of these signals by a commercial ADC and subsequent storage into the 4 MB of on-board DRAM. A FIFO controller signals to the DAQ hardware that the particular FEC has data available for read-out. Communication between FECs and the DAQ hardware is achieved through SNOBUS<sup>6</sup>↔VME translation by two translator boards - XL1 and XL2.

---

<sup>6</sup>SNOBUS refers to the GTL-based custom interface protocol used to access the front-end electronics.

## 3.5 Trigger System

This section contains a general description of the SNO trigger system. For an exhaustive description, see [30]. The author held primary responsibility for design, simulation, board layout, and commissioning of the digital trigger system. In addition, the author designed and commissioned the fiber optic interface to the GPS system used to keep absolute time in SNO<sup>7</sup>. Much of this section is rather technical, therefore the casual reader may want to skip to Section 3.6 after reading Sections 3.5.1 and 3.5.2.

### 3.5.1 Design Criteria

The trigger system design is dictated by the particular physics one wishes to study with the detector. SNO is primarily a solar neutrino detector, but the system also needs to facilitate detection of other signals such as supernovae neutrinos, anti-neutrinos, and atmospheric neutrino-induced muons and electrons. The trigger system must also allow for the study of backgrounds from naturally occurring radioactivity and instrumental effects.

To achieve these goals, the SNO trigger system must be capable of the following:

- Deciding when a potentially interesting event has occurred in the detector based on the PMT information. This decision should be made as quickly as possible and a global trigger distributed to the front-end electronics within a time comparable to time required for the PMTs to collect the majority of light from the event.

---

<sup>7</sup>For a general discussion of time keeping in SNO, see [31].

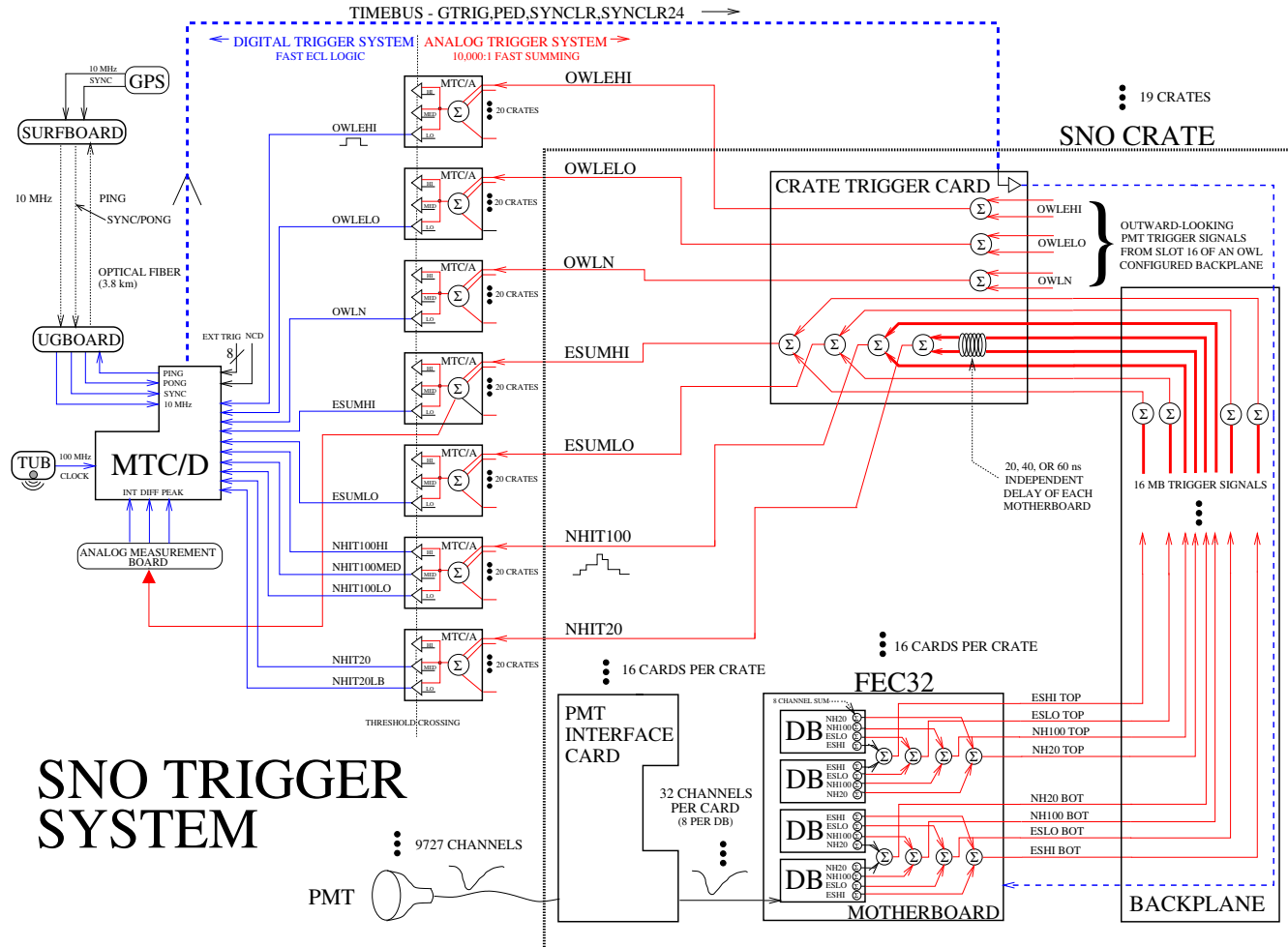
- Operating asynchronously with little or no dead time so that the system is ready to issue another global trigger on the next event of interest.
- Maintaining a large trigger rate dynamic range from Hz during neutrino data collection to MHz rates possible during supernovae bursts.
- Keeping good inter-event and absolute timing of events.
- Providing unique event IDs within a run and maintaining the synchronization of these IDs for all the channels in the system.

In addition, the trigger system should be able to accommodate calibration sources and non-PMT detector subsystems such as the neutral current detectors (NCDs). Specifically, the system should also provide the following:

- A set of calibration pulses to the front-end electronics for channel-level calibration of pedestals, charge slopes, and time slopes.
- External trigger inputs for calibration devices and non-PMT detector subsystems.
- A unique tag for each external or internal trigger type firing in an event and a means to trigger the detector on logical combinations of these trigger types.
- Utilities for interfacing with calibration devices or other systems. Examples include logic level translations, analog pulse discrimination, and signal fanout.

The remainder of this section describes the hardware that was developed to achieve these goals for the SNO detector.

Figure 3.4: Block diagram of the the SNO trigger system. Shown is the full summing chain of the analog trigger primitives starting within the SNO crate and summed to a single point on the MTC/A. Also shown are the components of the digital trigger system which contain the global generation logic (MTC/D), GPS fiber optic interface electronics (Surf/UG Boards), and trigger utility board (TUB).



### 3.5.2 System Overview

A diagram of the trigger system is shown in Figure 3.4. The main role of the trigger system is to determine when a potentially interesting event has occurred in the detector and then signal the front-end electronics to store any PMT data they may have accumulated. This determination is nominally based on the total number of coincident PMT hits (NHIT), but can also involve total coincident PMT charge or possibly non-PMT detector subsystems such as the neutral current detectors (NCDs). The system also triggers the detector at a regular rate of 5 Hz in the current detector configuration. This “PULSE\\_GT” trigger has proven extremely useful for studying detector activity (e.g. PMT noise rates) in an unbiased way.

In addition to global trigger generation, the trigger also handles many other important system tasks. It provides a set of programmable calibration pulses for measurement of front-end charge/time pedestals and slopes. This is implemented using an on-board pulser and precision delay circuitry which is programmable through the data acquisition system (DAQ). In addition, the trigger system provides a user interface to the detector for calibration sources by including a number of external trigger inputs as well as a utility board for analog pulse discrimination.

The trigger system is also responsible for maintaining and recording trigger-related event information such as relative event timing, absolute event time, global trigger ID number, and information regarding which trigger types fired during an event. The inter-event timing is recorded by latching a 50 MHz counter that is sourced by a local 100 MHz ECL oscillator. Absolute time is maintained for correlating SNO events with astronomical observations by interfacing the system to a GPS receiver on the surface. This interfacing is handled by two fiber optic transceiver boards - one on

the surface and one underground - which transmit a 10 MHz GPS clock as well as a synchronization signal from the GPS receiver to the trigger system hardware over roughly 4 km of fiber. These interface boards also “ping-pong” the synchronization signal between surface and the detector underground to allow measurement and monitoring of the synchronization delay. For global trigger identification, a 24-bit counter is latched and incremented on each event so that the count represents a unique event ID (up to roughly 16 million triggers) for a particular run. Each front-end channel also has a similar counter to allow association of PMT and trigger related data for building events, so the trigger system is also responsible for keeping these channel-level counters in synchronization with the central trigger counter. This is accomplished by sending a synchronization pulse to each channel on 16-bit roll-overs of the central global trigger counter (i.e. every 65536 events), setting an error flag on out-of-sync channels as well as synchronizing them to the central counter.

As depicted in Figure 3.4, the trigger system is naturally divided into analog and digital subsystems. The crossing of a channel-level discriminator threshold (e.g. in response to a PMT signal) initiates two equal amplitude current pulses of different duration - 20 ns and 100 ns - to enter independent analog summing networks. Shaped versions of the actual PMT signals are also separately summed, which represents an energy-sum (“ESUM”) trigger for the detector. While neutrino interactions do not typically fire the ESUM trigger, this trigger has proved extremely important for low-level detector monitoring as well the rejection of instrumental background such as PMT flashers<sup>8</sup>.

The trigger primitives of all channels in the system are summed together to form

---

<sup>8</sup>These refer to events caused by spontaneous emission of light by a PMT which will be discussed in more detail in Section 6.2.

a final analog “NHIT” sum in the central trigger crate. In practice, however, the final sum is current limited to about two crates worth of hits (1024 channels). This final sum is then fed into a current mirror which produces four identical copies of the analog sum. One copy is used for monitoring and the other three go to independent comparators for discrimination. Each comparator fires if its respective copy of the analog sum exceeds a threshold voltage set by a 12-bit digital-to-analog converter (DAC). Therefore, the analog system begins with the firing of channel-level analog trigger primitives that are subsequently summed together and ends with comparison of the final NHIT sum to three different DAQ-programmable thresholds for discrimination.

The front-end to the digital trigger system is the input of ECL trigger pulses on to the digital Master Trigger Card (MTC/D). These are sometimes referred to as “raw” trigger pulses, since they are candidate pulses for initiating a global trigger (i.e. generating an event in the detector). The output of the three comparators discriminating the 100 ns NHIT analog sum, called the N100LO, N100MED, and N100HI triggers, are examples of raw triggers that make up the “physics triggers” of the detector. While these three are the main physics triggers for the detector, others include the 20 ns NHIT thresholds, low and high gain ESUM triggers, and a set of outward-looking PMT triggers. There are also a number of external raw trigger inputs for calibration devices and other systems requiring absolute time tagging (e.g. GPS synchronization signals, NCDs, hydrophone). In addition, there are a number of trigger signals internal to the MTC/D that are treated in the same way as the external raw trigger signals in terms of their global trigger generation and latching. These include the PULSE\_GT trigger already mentioned as well a PEDESTAL calibration trigger, a PRESCALE of the N100LO physics trigger, a DAQ-initiated “software trigger” (SOFT\_GT), and a special trigger (SPECIAL\_RAW) which fires on a programmable logical combination

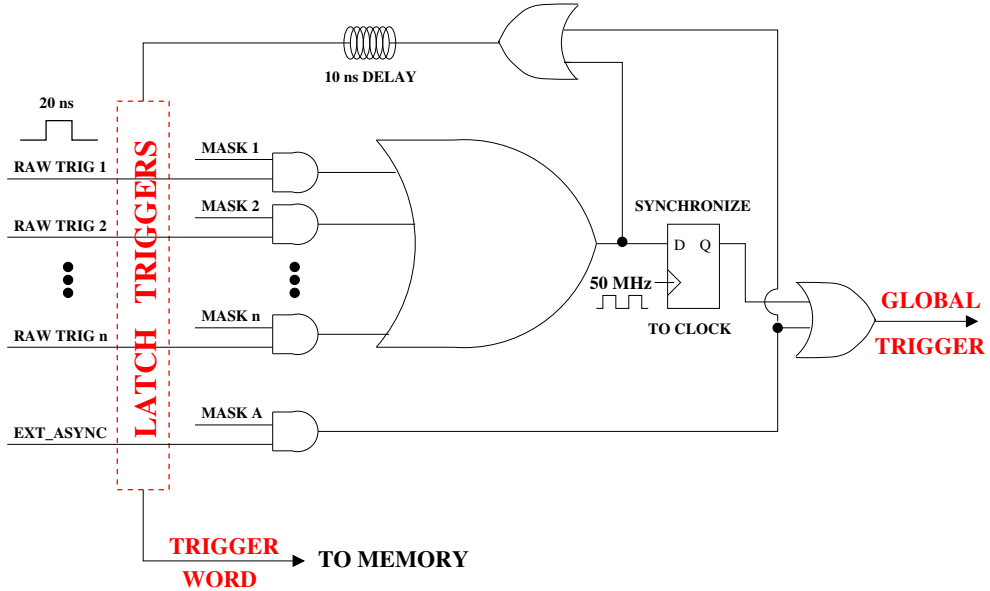


Figure 3.5: Schematic diagram of the trigger latching and global trigger generation logic involved in the digital trigger system. This figure is meant to depict logic flow and should not be interpreted as a literal schematic of discrete logic elements in the trigger electronics.

of nine pre-selected physics and external raw triggers. Table 3.1 contains a complete list of the 26 raw trigger types implemented in the SNO trigger system.

### 3.5.3 Global Trigger Generation Logic

Figure 3.5 shows a schematic diagram of the trigger latching and global trigger generation logic involved in the digital trigger system. The way that the *digital* trigger system decides when to trigger the detector is actually quite simple. A set of 20 ns ECL raw trigger pulses (see Table 3.1) are input to the global trigger generation logic. Each raw trigger encounters a DAQ-programmable mask bit that determines whether or not any signal from that trigger input will continue on to the rest of the generation logic. As such, only masked in raw trigger types are permitted to initiate

Mask bit	Raw trigger	GT?	Type	Raw trigger description
0	N100LO		External	Low threshold 100 ns
1	N100MED	✓	External	Med threshold 100 ns
2	N100HI	✓	External	High threshold 100 ns
3	N20	✓	External	Normal 20 ns
4	N20LB		External	Low threshold 20 ns
5	ESUMLO		External	Low-gain energy sum
6	ESUMHI	✓	External	High-gain energy sum
7	OWLN	✓	External	OWL PMT 100 ns
8	OWLELO		External	OWL PMT low-gain energy sum
9	OWLEHI	✓	External	OWL PMT high-gain energy sum
10	PULSE_GT	✓	Internal	Pulser generated
11	PRESCALE	✓	Internal	Prescaled N100LO
12	PEDESTAL		Internal	Pedestal calibration
13	PONG	✓	External	GPS synchronization delay
14	SYNC	✓	External	GPS synchronization
15	EXT_ASYNC		External	Ext not sync'd to 50MHz clock
16..22	EXT2..8		External	External generic input
23	SPECIAL_RAW		Internal	Special logic programmable
24	NCD		External	Neutral-current detector input
25	SOFT_GT	✓	Internal	DAQ-initiated trigger

Table 3.1: The 26 raw trigger types of the SNO trigger system. A global trigger resulting from any of these signals, except for the EXT\_ASYNC external input, is synchronized to the 50 MHz system clock. A ✓ in the third column indicates the raw trigger types that are masked in for global trigger generation during production neutrino data taking. The type (external, internal) indicates whether the corresponding trigger is externally input to the MTC/D or is generated on the board (through the DAQ or otherwise).

events in the detector. The signals from all masked in *synchronous* triggers (i.e. all except EXT\_ASYNC) are **OR**'d together and a valid output of this **OR** initiates a global trigger on the next rising edge of the 50 MHz clock. This synchronization of the global trigger to the system clock is important for maintaining robust digital operation of the MTC/D (for latching of counters, memory, etc.) and also leads to the so-called “20 ns jitter” of the PMT times event-to-event. It is important to note that since the front-end time measurement is operated as a common-stop system (i.e. each TAC ramp is started when the channel fires and stopped on a common global trigger, this synchronization only jitters the overall time offset of each event relative to other events and *does not* smear the individual PMT times relative to each other (like the 1.6 ns jitter inherent to SNO PMTs) within an event.

It is sometimes useful to sum up a large number of events and have the summed PMT time spectrum remain sharp, without smearing due to the global trigger synchronization. An example of such an application is laserball calibration of the PMT cable delays (phototube calibration is described in Section 5.2). Therefore, to accommodate these types of applications, an alternative trigger path (EXT\_ASYNC) is provided for asynchronous global trigger generation (see Figure 3.5).

Aside from depicting the global trigger generation logic, Figure 3.5 also shows how information is stored about which triggers fired in a particular event. When one or more masked in raw trigger fires, the **OR** of these signals is not only synchronized to the system clock for global trigger generation but also acts as a latch of any valid raw triggers. This latch signal is delayed  $\sim 10$  ns (adjustable with an RC circuit) before sending a “snapshot” of the state of *all* raw triggers to the on-board memory for storage. This snapshot of the raw trigger inputs along with a “missed trigger” status bit (to be described later) make up what is referred to as the “trigger word” of

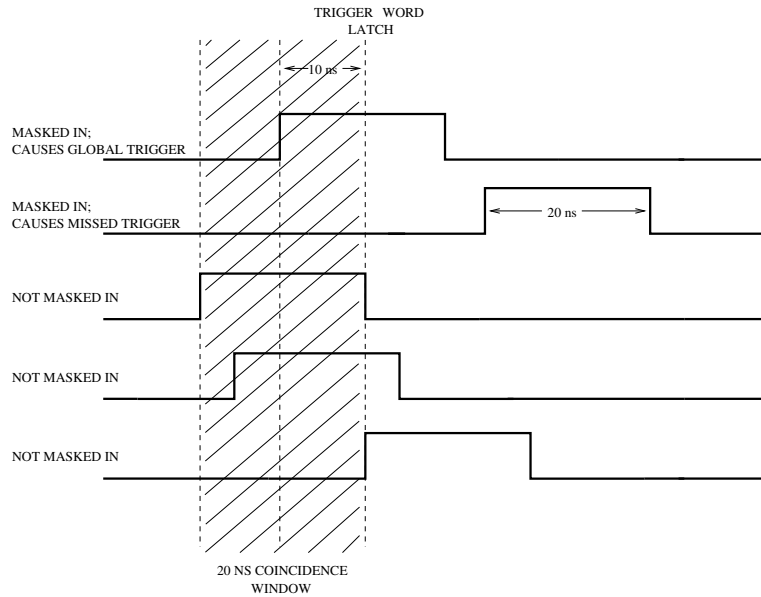


Figure 3.6: Diagram showing the coincidence window involved in trigger word latching. Each pulse represents a different raw trigger signal arriving at the global trigger generation logic. Note that raw triggers arriving within  $\pm 10$  ns of the raw trigger that initiates the global trigger are latched into the trigger word. Also shown is how a masked in raw trigger arriving after the latching time during the trigger cycle causes the “missed trigger” bit to be set in the trigger word.

the event. Note the important fact that on each event, the trigger system latches *all* 26 raw triggers, independent of their mask state and whether they are synchronous or asynchronous triggers.

The coincidence window for raw triggers to be latched together into the trigger word is determined by their pulse width and the latch delay, as well as their timing relative to the earliest masked in raw trigger which fires (i.e. the raw trigger that initiates the global trigger and determines the trigger timing). Figure 3.6 shows a diagram of the coincidence window involved in trigger word latching. Note that in an ideal sense, all raw triggers arriving within  $\pm 10$  ns of the earliest masked in raw trigger are latched into the trigger word, as well as the raw trigger that initiated

the global trigger itself. In actuality, variations in the raw trigger pulse width as well as differences in signal propagation times to the latching logic slightly change the condition for coincident triggers at the point they are externally input to the MTC/D. In addition to bits corresponding to the state of each raw trigger at latching time, the trigger word also contains a “missed trigger” status bit. This bit is set if any *masked in* raw trigger arrives after the latching time but before the end of the trigger cycle ( $\sim 420$  ns), as shown in Figure 3.6.

### 3.5.4 Global Trigger and Clock Counter Arrays

The global trigger ID, 50 MHz clock, and GPS 10 MHz clock are maintained in the central trigger using three independent counter arrays on the MTC/D.

The 50 MHz clock is used for inter-event timing and consists of a 43-bit counter array that is sourced by an external oscillator. At 50 MHz, the counter rolls over approximately every 2 days of continuous operation. The choice of external sourcing allows the system to incorporate as sophisticated an oscillator as one desires without any additional on-board circuitry. The MTC/D provides for standard BNC single-ended ECL input or a twinx connector for differential ECL clock input.

A 53-bit counter holds Universal Coordinated Time (UTC) time which is used to keep absolute time in SNO. This counter is incremented by a 10 MHz clock signal that is transmitted from a surface GPS receiver to the underground detector. It provides times for up to 28 years without rolling over - well beyond the expected lifetime of the experiment.<sup>9</sup> Details about how the GPS clock signal is transmitted to the trigger system and how SNO keeps synchronized to the GPS receiver are described

---

<sup>9</sup>although nearly 3.5 of those years ticked away by the time SNO began commissioning data taking since  $t_0$  is defined as midnight Jan 1, 1996.

in Section 3.5.9.

Each event is assigned a unique global trigger ID within a run. This ID is stored in a 24-bit counter on the MTC/D which is incremented every time the trigger system issues a global trigger. Aside from this global trigger ID counter, each front-end channel also has its own independent counter which needs to be kept synchronized to the central counter. The details of how this accomplished is actually rather involved (see [30] for a detailed description), and complications arising from this synchronization cause some IDs to be skipped as the counter increments through a run. Therefore, the actual number of allowed global trigger IDs is slightly less than  $2^{24} = 16,777,216$  implied by the size of the counter.

### 3.5.5 Memory

The MTC/D stores 192 bits of trigger-related information on each event, shown in Table 3.2. This information is read out by the DAQ and associated with PMT data by global trigger ID.

The memory front end consists of 24 1Kx9 FIFOs which act to buffer the incoming 192 bits of data before going to commercial memory modules. All of the FIFOs are written to in parallel at the end of a trigger cycle during which time no other global triggers can be issued. The FIFOs then remove their empty flags, signaling to the memory controller that they have data. At this time the controller will attempt to move the data from the FIFOs to the DRAM SIMMs as long as the FIFOs still have data and the memory controller is not currently servicing a VME read request. There are six 32-bit 4MB SIMMs which are written to in parallel at a maximum rate inversely related to the trigger cycle time, corresponding to  $\sim 60$  MBytes/sec.

SIMM(s)	Bit(s)	Description
0,1	0..31,0..20	10 MHz count (53 bits)
1,2	21..31,0..31	50 MHz count (43 bits)
3	0..23	Global Trigger count (24 bits)
3,4	24..31,0..17	Trigger Word (26 bits)
4	18	Missed Trigger
4	19..28	NHIT peak after crossing threshold
4,5	29..31,0..6	NHIT slope after crossing threshold
5	7..16	NHIT integral near threshold crossing
5	17	GT counter testmode status
5	18	50MHz counter testmode status
5	19	10MHz counter testmode status
5	20	Memory testmode 1 status
5	21	Memory testmode 2 status
5	22	SYNCLR16 sent
5	23	SYNCLR16 sent w/o counter 16-bit rollover
5	24	SYNCLR24 sent
5	25	SYNCLR24 sent w/o counter 24-bit rollover
5	26	FIFOs do not all have the same empty status
5	27	FIFOs do not all have the same full status
5	28	FIFOs are full
5	29..31	Not used

Table 3.2: The Digital Master Tigger Card (MTC/D) Memory Map.

### 3.5.6 Calibration Pulser

As mentioned in Section 3.5.1, the trigger system has the responsibility of generating calibration pulses for front-end channel timing and charge. These pulses are referred to as ‘Pedestal’ or just ‘PED’ pulses because firing the channel discriminators in the absence of charge is the main way in which the front-end electronics uses these pulses. The PED pulses generated by the MTC/D are also used to perform charge slope measurements, as the width of the PED pulse is used to set total charge injected into the integrators from calibration circuitry. In addition, the PED pulse in combination with

a programmable delay global trigger pulse is used to perform time slope calibrations of the front-end Time-to-Analog Converters (TACs).

The pulsed global trigger is produced from an internal trigger signal (PULSE\\_GT) and can be either asynchronous or synchronous to the 50 MHz clock, depending on the bit set in the trigger mask. The PED and PULSE\\_GT pulses can be generated in a number of ways. The first and simplest way is to use the on-board pulser which can generate PED and global trigger pulses at a programmable rate between 390 kHz and 0.04 Hz. On the other hand, if a precise number of PED events is desired, the MTC/D can use software initiated pulses (SOFT\\_GTs) in place of the pulser. If one wants ultimate flexibility in PED generation, the MTC/D also has an external pedestal input (EXT\\_PED) where pedestal events can be generated by an external source such as a pulser.

As previously mentioned, control over the pulse width and relative delay of pedestal event pulses is required for charge injection and TAC slope measurements. In the case of charge injection, the total amount of charge injected by the PMTIC is proportional to the PED width. This width is programmable in 5 ns increments from 5 ns to 1.275  $\mu$ s. The relative delay between PED and the internal trigger signal PULSE\\_GT can be varied using a coarse 10 ns delay relying on the 50 MHz clock and a fine delay in  $\sim$  100 ps increments using a programmable delay chip. If the GT is generated asynchronously, then it will have the full 100 ps delay resolution of the PULSE\\_GT pulses. However, if the GT is generated synchronously, it can only be delayed in 20 ns increments but will be synchronous to the 50 MHz clock. The relative delay is programmable between 24 ns and 2574 ns, with the 24 ns offset resulting from gate and trace delays inherent to the board. Both PED and GT can be independently delayed with cables that plug directly into the front panel, so any desired offset can

be attained. The MTC/D can also be used to generate double PED pulses by feeding the GT output of a spare fanout connector (trigger signal fanout is described in Section 3.5.7) back into the EXT\_PED input. This double pulsing is used to calibrate the width of a front-end timing signal GTVALID, which sets the amount of time a channel waits for a global trigger before resetting. The relative delay between the two PED pulses is then controlled by varying the coarse and fine delay settings as in the PED/GT delay.

### 3.5.7 Signal Fanout

The trigger system returns four signals to the front-end electronics - pedestal, global trigger, and two global trigger counter synchronization signals (one for the lower 16 bits and one for the upper 8 bits). The front-end electronics are arranged into 19 separate crates, and so the central trigger fans out the signals through one cable per crate connected to the MTC/D. The signals are driven as differential ECL, so these cables are comprised of four sets of twisted pair wires.

The PED and global trigger signals can be sent separately to any combination of crates through a DAQ programmable mask register. This is very useful for calibrating a subset of the electronics or masking out particular crates from taking data. The synchronization signals are always driven to all crates of front-end electronics to avoid mistakenly masking out certain crates, which would wreak havoc on data collection.

### 3.5.8 Trigger Utility Board

The Trigger Utility Board (TUB) holds many special-purpose circuits which have proved useful during the debugging and operating of the trigger system, as well as for

general purpose interface to the electronics as a whole (e.g. for calibration devices).

Aside from being generally useful, the TUB provides one necessary service in that it contains the local oscillator which feeds the 50 MHz clock on the MTC/D. It also contains a speaker and circuitry to drive the speaker with either PED or global trigger pulses. This speaker signal is then transmitted to the surface control room and makes up one of the most useful pieces of low-level monitoring information for sensing changes in detector operation.

Below is just a brief list of other TUB features (see [30] for more information):

- Logic level translations (ECL $\leftrightarrow$ TTL, NIM $\leftrightarrow$ ECL)
- Dual polarity analog pulse discrimination with retriggering capability
- TTL Pulse LED indicator
- DAQ programmable 32-bit serial register array with output connectors
- Drive circuitry for individual firing of PSUP LEDs
- Connector type “translations” (BNC $\leftrightarrow$ SMB)
- 10:1 ECL signal fanout

### 3.5.9 Interface to Global Positioning Satellite (GPS) System

A commercial GPS receiver and custom interface electronics are used to keep absolute time in SNO. The GPS receiver drives a 10 MHz sine wave signal whose frequency is continuously modulated to remain in synchronization with clocks on-board the GPS satellites. There is also a TTL synchronization signal (“SYNC”) output which can be driven by the receiver at a user-defined UTC.

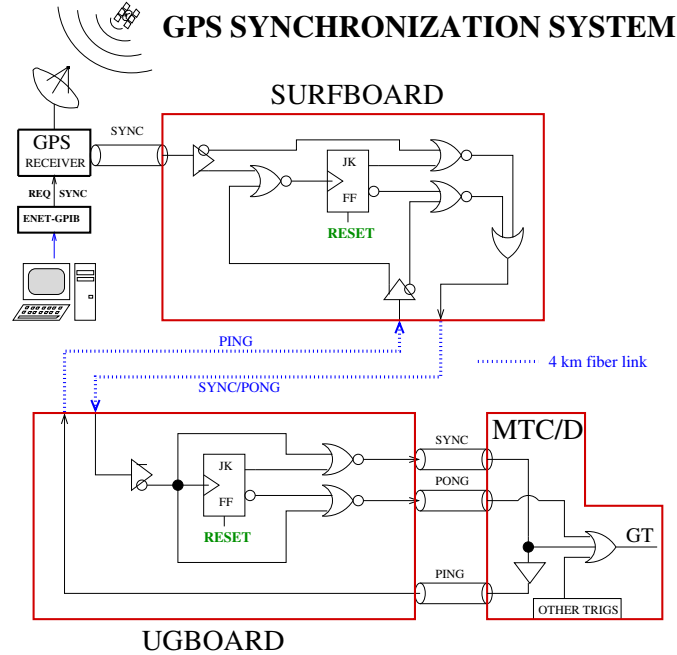


Figure 3.7: Schematic diagram of the GPS synchronization system logic.

Signals between the surface GPS receiver and the SNO detector electronics underground are passed along 4 km fiber optic cables. The translation to and from electrical and optical signals is performed by two separate custom fiber optic translator PCBs - one on surface (the “SurfBoard”) and one underground (“the UGBoard”). These boards use commercial point-to-point optical ports made by Hewlett Packard which are infrared ( $\lambda \sim 1300$  nm) LED transmitter (HFBR-1312T) and PIN diode receiver (HFBR-2316T) pairs. The GPS 10 MHz clock signal is continually transmitted to the underground system by the SurfBoard. The UGBoard receives this signal and sends it to the MTC/D 10 MHz counter as an ECL clock signal.

Synchronization of the MTC/D 10 MHz counter with the GPS receiver (hence UTC) is kept using the receiver’s synchronization output and the logic shown in Figure 3.7. A preset future time (i.e. count) is loaded into a shift register at the

front-end of the MTC/D 10 MHz counter and is also loaded into the GPS receiver's synchronization circuitry. When the time according to the GPS receiver reaches this preset time, a SYNC pulse is sent from the GPS receiver to the MTC/D via the Surf/UGBoard combination. The MTC/D does three things with this pulse - loads the 10 MHz counter with the preset time, generates a SYNC tagged GT, and drives the signal (now called "PING") back to the UGBoard. The PING pulse is sent to the SurfBoard where it is electrically "reflected" back through the UGBoard to a "PONG" input on the MTC/D which generates a PONG tagged GT. The round trip synchronization delay is simply the time difference between SYNC and PONG triggers based on the 50 MHz clock.

Synchronization of SNO to the GPS receiver is checked by the DAQ instructing the GPS to send SYNC pulses once per hour and inspecting the SYNC/PONG triggers in the data stream. This monitoring suggests that absolute time is kept to within 100 ns (i.e. one 10 MHz clock tick) with hour sampling over periods of months. There have been some interruptions - not always related to the GPS hardware - but overall the system has performed stably over time.

### 3.5.10 Physical Design

Layout of the MTC/D and TUB designs into printed circuit boards (PCBs) was carried out by the author. The TUB is a simple two-layer board with a bottom ground layer and essentially all signal and power routing constrained to the top layer. The MTC/D was a much more difficult design to physically implement due to comparatively large and complex capabilities. The MTC/D PCB is a ten-layer, 9U board with a corner removed so that it fits inside a 6U VME crate. The design logic was

implemented as a mixture of fast TTL and ECL (both standard ECL and Motorola ECLinPS). While much of the ECL and TTL logic was packaged into discrete logic elements (i.e. discrete commercial ICs for AND gates, OR gate, etc.), a significant fraction of the board logic was implemented in Xilinx FPGAs (**Field Programmable Gate Arrays**). The use of FPGAs - along with very extensive simulations of the design carried out by the author using Verilog digital logic simulation language - drastically reduced the total board debugging time since a new logic design can be loaded into FPGAs “on the fly” without any re-manufacture. In fact, the MTC/D currently running in the detector is the first and only manufactured version (with some inconspicuous physical modifications), despite containing more than 1300 components and 7300 interconnections.

### 3.6 Data Acquisition Hardware and Software

The primary role of the DAQ system is to read out accumulated PMT and trigger data, and merge this information into complete events which are archived to tape for off-line processing. The DAQ system also provides the necessary configuration control of the detector hardware and online monitoring of low-level data integrity.

Figure 3.8 shows a simplified diagram of the DAQ system and data flow. The FECs in each crate of electronics are read out through the XL1/XL2 interface by a single Motorola 68040 single-board computer (eCPU) residing in a central VME crate. The eCPU also reads out MTC data and passes the MTC and FEC data to separate circular buffers in the dual-port memory (DPM) of an SBUS-VME interface card. This DPM is directly accessed by a Sun Ultra-1 workstation running a program designed to sort PMT and FEC data and build the event data stream. This stream

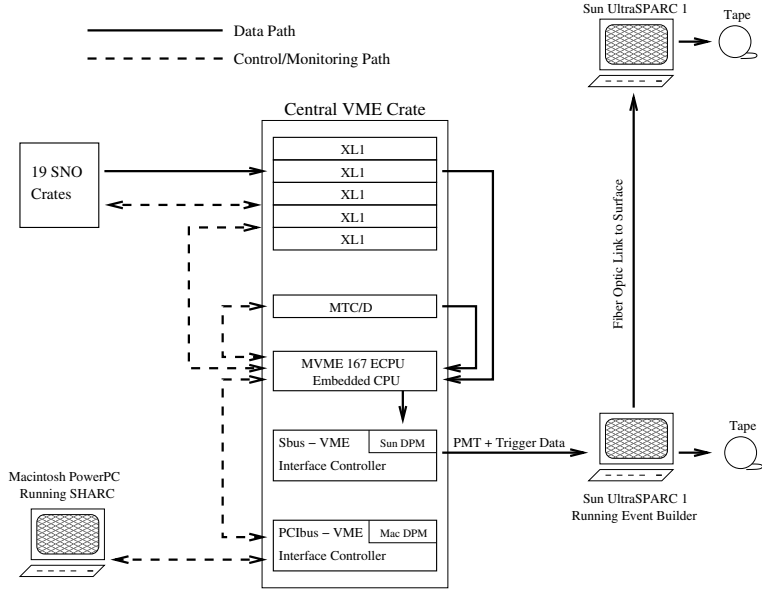


Figure 3.8: Simplified diagram of the DAQ system and data flow.

is written to local disk on the Sun and subsequently written to tape via a DLT drive connected to the computer. The data is also transferred via Ethernet to a Sun on the surface and again written to tape. The surface system also broadcasts a sampled data stream to authorized clients via a Dispatcher program for near-line monitoring.

Hardware control is performed by the user through an interface program called “SHARC” running on a Macintosh PowerPC (PPC). Access to the front-end and trigger hardware is done through the eCPU using DPM on a PCIBus-VME interface card connected to the PPC.

### 3.7 Monte Carlo Detector Simulation (SNOMAN)

Analysis of raw data from tape and physics/detector simulation use the SNOMAN (SNO Monte Carlo and Analysis) software package [32,33]. SNOMAN can simulate

the production and transport of many types of particles (e.g.  $e^-$ ,  $\gamma$ ,  $n$ ) and radioactive decay of many nuclei relevant for SNO (e.g.  $^{208}\text{Tl}$ ,  $^{214}\text{Bi}$ ). Transport of  $e^\pm$  and  $\gamma$ s including the production of Cerenkov light is handled using the EGS4 Electron Gamma Shower Code. SNOMAN includes models of the full detector geometry, optical properties, electronics and data acquisition system so that the software can simulate the detector response as accurately as possible.

Constants used for detector simulation and calibration of raw data are derived from calibration data that is stored in a data base (SNODB [34]) based on the CERNLIB HEPDB software package [35]. When an event is read into SNOMAN after being unpacked from the raw data, the software applies calibration constants which are valid for the particular event. The Monte Carlo will also access SNODB to get information such as which PMTs were available for data collection (DQXX banks) during the simulated time period for proper modeling of the detector response.

## 3.8 Summary

In this chapter, the SNO detector was described in some detail. It is clear that numerous complex detector subsystems are required to work together for an experiment like SNO to achieve its physics goals. In a similar way, analysis tools which work well together must be developed to maximize the physics content that can be extracted from the data stream. In the next chapter, one such critical analysis tool - event reconstruction - is presented.

# Chapter 4

## Event Reconstruction

In the previous chapter, a description of the detector designed and built to study solar neutrinos was presented. The raw data stream which reflects the richness and complexity of the detector must now be properly interpreted. Extensive calibration of detector elements and overall response is obviously an important step in interpreting the data. Calibrations are discussed in Chapter 5. Another important component to any attempt at understanding the data is estimating the location and direction<sup>1</sup> of events in the detector and evaluating the quality of this estimation. This chapter describes the methods of event reconstruction used in SNO. Emphasis is placed on a reconstruction method recently developed by the author that has become part of the official SNOMAN distribution.

All reconstruction methods rely somewhat on calibrations (e.g. PMT times *times*), so it might seem peculiar to discuss event reconstruction at this point. The reason for discussing reconstruction before calibration is because some of the higher-order

---

<sup>1</sup>That is, the initial or average position and direction of the charged particle under the hypothesis of Cerenkov light.

calibrations used for this thesis (e.g. energy calibration) use one or more of the reconstruction methods described in this chapter. Also, reconstruction properties themselves (e.g. vertex resolution) need to be calibrated. The reader dissatisfied with a discussion involving calibrated PMT times and charges without first knowing how these are determined should read Sections 5.1 and 5.2 on electronics and PMT calibrations before proceeding.

## 4.1 Overview

Reconstruction is one of the most important components of solar neutrino analyses in SNO. This is because many solar neutrino backgrounds originate, by design, in the outer regions of the detector. In many cases, the only way to remove such backgrounds is by their location in the detector<sup>2</sup>. This includes both Cerenkov light not initiated by neutrinos and other sources of light - from the instrumentation itself, for example. For the latter, one would expect to be able to reject a large fraction of these non-Cerenkov backgrounds using reconstruction because the quality of their fit under the Cerenkov hypothesis should be poor, regardless of where the fit is in the detector. In addition, good reconstruction of signal events is very important for preserving distributions that distinguish the signal types. This has direct consequences for signal extraction techniques (described in Chapter 8) which rely critically on distinctions in event observables between the signals being extracted. For example, strong correlation with solar direction is largely what distinguishes ES from CC events in the detector, so a fitter with poor direction reconstruction will smear out these distributions and

---

<sup>2</sup>and direction to a lesser extent. This is because events are not actually *cut* based on their direction in this analysis. However, direction can sometimes be used to identify a detector background source if it is more pronounced in detector rather than solar direction coordinate system.

consequently increase covariance between these signals.

Many reconstruction methods have been developed for SNO over the years. These make up a diverse set of algorithms which all try come up with clever (and sometimes rather elaborate) ways to best estimate the position and direction of events occurring in the detector. It may seem peculiar that there are so many reconstruction methods in SNO given that the information one gets out of the detector is so simple - time (relative to the trigger) and integrated charge for each hit PMT. It is, however, this relatively small amount of event information which makes reconstruction challenging in SNO, as fitters need to determine the best way to use all of the existing information in events to get the best possible reconstruction performance.

This chapter begins with a brief description of the existing fitters traditionally used for analysis. The development of a new fitter is motivated through studies of the benefits of using both PMT time *and* angular information in reconstruction. Finally, the “Path Fitter”, which implements some of these ideas and is now distributed as a standard fitter for use by the collaboration, is described in detail.

## 4.2 The Pre-Existing Fitters

This section briefly describes the relevant fitters for solar neutrino analyses that are distributed to the collaboration as standard code<sup>3</sup>.

### 4.2.1 Time Fitter

The Time Fitter is conceptually the simplest of all standard fitters and is also the least CPU intensive. This latter property makes the Time Fitter a very useful fitter

---

<sup>3</sup>before SNOMAN development release 4.0083.

for large data sets (e.g. calibrations) and applications where speed is preferred over accuracy (e.g. as a vertex seed for other fitters). The Time Fitter returns the vertex<sup>4</sup>,  $\vec{r}_{fit}$ , and time,  $t_{fit}$ , which minimizes the  $\chi^2$  function,

$$\chi^2(\vec{r}_{fit}, t_{fit}) = \sum_{i=1}^N \left[ \frac{t_i^{res}(\vec{r}_{fit}, t_{fit})}{\sigma_i} \right]^2 \quad (4.1)$$

where the sum is over hit PMTs in the event,  $\sigma_i$  is the time jitter of  $i^{th}$  hit PMT, and  $t_i^{res}(\vec{r}_{fit}, t_{fit})$  is given by

$$t_i^{res}(\vec{r}_{fit}, t_{fit}) = t_{fit} - \left( t_i - \frac{|\vec{r}_{fit} - \vec{r}_i|}{\bar{c}} \right) \quad (4.2)$$

where  $\bar{c}$  is the mean speed of light, and  $t_i$  and  $\vec{r}_i$  are recorded time and known position of the  $i^{th}$  hit PMT, respectively. PMT time jitter is the spread in signal arrival times at the PMT anode primarily due to the spread in arrival time of a given photoelectron at the first dynode. In practice, a single mean PMT time jitter resulting from calibrations discussed in Section 5.2 is used in the fitter algorithm. Notice that an implicit assumption in the Time Fitter algorithm is that all hits are due to “direct” light - photons propagating directly from a Cerenkov source to the PMTs. This assumption is actually quite a poor one, since a sizable fraction (10-20%) of hits are not from direct Cerenkov light but rather reflections, scattering, or random PMT noise coincidences. These hits produce significant tails in the  $\chi^2$  distribution and also break down the approximation of using PMT jitter as the time error for each hit since this error is now non-Gaussian. The Time Fitter attempts to circumvent this problem by selectively throwing out hits in the events and re-doing

---

<sup>4</sup>In this thesis, the term “vertex” is used interchangeably with “position”, in the context of event reconstruction.

the  $\chi^2$  minimization.

The Time Fitter also returns a direction “fit” which is simply the mean PMT unit vector calculated from the fit vertex to the hit PMTs. This provides a rough estimation of the mean charged particle direction for Cerenkov light production when direct light hits are properly selected. Even if only true direct light hits are considered, Poisson fluctuations in the angular distribution of generated photons can skew the mean direction. A better approach to direction fitting is to use the actual angular distribution of Cerenkov light relative to the mean or initial charged particle direction to estimate the direction. Direction reconstruction using this angular information is discussed in Sections 4.2.4 and 4.3.

### 4.2.2 Quad Fitter

The Quad Fitter [36, 37] uses equation 4.1, but in a very different way from the Time Fitter. Equation 4.1 applied to a single PMT hit ( $N=1$ ) yields one equation with four unknowns ( $\vec{r}_{fit}, t_{fit}$ ). Therefore, four hit PMTs result in a set of four equations which can be solved for the four unknowns. To use all available information in the event, the solutions corresponding to all possible combinations of four hit PMTs are obtained and make up a “Quad cloud” of solutions in a 4D space. The fit vertex and time is the region of the Quad cloud found to have the highest density<sup>5</sup>. An advantage of this fitting method is that one no longer has to throw out hits because the global Quad cloud maximum density is relatively insensitive to non-direct hits which in many cases do not contribute real solutions to the Quad cloud.

---

<sup>5</sup>The first work done by the author for SNO was application of simulated annealing techniques to find this maximum density. Simulated annealing is discussed later in this chapter.

### 4.2.3 Grid Fitter

The Grid Fitter [38] is a maximum likelihood fitter which uses a normalized distribution of PMT hit time residuals derived from Monte Carlo as the probability density function (PDF),  $\mathcal{P}(t_i^{res}; \vec{r}_{gen}, t_{gen})$ . The time residual function  $t_i^{res}$  is the same as in Equation 4.2, and  $\vec{r}_{gen}, t_{gen}$  are the position vector and time of a generated Monte Carlo event, respectively. The Monte Carlo events used to generate the PDF were  $^{208}\text{Tl}$  decays in the AV and PMT regions. The PDF used in the Grid Fitter is a fit to the average of the resulting  $t_i^{res}$  distributions from these simulations.

The fit vertex and time is the vector  $\vec{r}_{fit}$  and time  $t_{fit}$  that minimizes the negative log likelihood function,

$$-\log \mathcal{L}(\vec{r}_{fit}, t_{fit}) = -\sum_{i=1}^N \log [\mathcal{P}(t_i^{res}; \vec{r}_{fit}, t_{fit})] \quad (4.3)$$

In practice, the  $-\log \mathcal{L}$  function shown Equation 4.3 is minimized in two steps. The function is minimized at each point in a 3D position grid within the detector volume. This is a set of  $N_g$  1D minimizations in the variable  $t_{fit}$ , where  $N_g$  is the total number of grid points. The  $\vec{r}_{fit}$  and  $t_{fit}$  corresponding to the grid point with largest log-likelihood is used to seed a 4D minimization of the function in 4.3 by the CERNLIB MINUIT minimization package.

Various attempts at improving the vertex reconstruction performance of the Grid Fitter have been implemented along with the addition of a separate fit for direction using the angular distribution of Cerenkov photons generated by electrons in Monte Carlo simulations [39].

#### 4.2.4 Elastic Fitter

The Elastic Fitter [40] is a reconstruction method which fits events for vertex and direction by minimizing separate position and angular residual functions. What separates the Elastic Fitter from the previously discussed fitters (and gives the fitter its name) is the rather elegant method used to discard “bad” (i.e. non-direct) hits during the fitting process. The algorithm used to discard hits during the fit is quite similar to the method of simulated annealing<sup>6</sup> which has proved useful in solving global minimization problems. The basic idea of the Elastic Fitter is to weight each hit PMT’s contribution to the sum of squared residuals to be minimized by an amount related to a “temperature” parameter that is slowly reduced during the fit. In the early stages of the fitting process (highest temperature), the true vertex or direction is usually more poorly estimated than in the latter stages, so the fitter is more forgiving of hits with bad residuals. As the fit progresses, however, the error presumably decreases by the fitting process so hits with poor residuals are weighted much closer to zero - effectively throwing them out of the fit.

While the detailed scheme used by the Elastic Fitter to weight the individual squared residual terms in the sum is rather involved, the residual functions are comparatively straightforward. The residual function for the vertex fit is essentially just Equation 4.1 multiplied through by  $\bar{c}$  to make it a position residual,  $R_i^{pos}$ , given by

$$R_i^{res}(\vec{r}_{fit}, t_{fit}) = \bar{c}(t_{fit} - t_i) + |\vec{r}_{fit} - \vec{r}_i| - \delta^{pos} \quad (4.4)$$

where  $\delta^{pos}$  is an added term to compensate for skew in the mean of  $R_i^{res}$  caused by

---

<sup>6</sup>The method of simulated annealing is discussed in Section 4.3 related to its use in the Path Fitter reconstruction method.

late light from reflections and scattering. A fit for direction is done separately<sup>7</sup> by minimizing the weighted sum of squared angular residual functions for each PMT. The angular residual function is the sine of the angle between a hit PMT vector and a vector from the fit position to the point on the “Cerenkov cone” closest to the hit PMT. In this context, the “Cerenkov cone” refers to the set of all rays from the fit position such that the angle between a given ray and the fit direction is equal to the Cerenkov angle,  $\theta_c$ , in the medium ( $\theta_c \sim 42^\circ$  in water).

### 4.3 A New Fitter: The Path Fitter

A new reconstruction method [41] has been developed by the author in an attempt to improve vertex reconstruction performance of time-only based fitters by simultaneously including PMT angular information along with hit PMT time information in fitting events. This fitter builds upon earlier work [42] on the use of time and angle information in maximum likelihood (ML) based fitters for SNO.

This new fitter is called the “Path Fitter” because the original approach was to construct a different PDF that is a sum of all possible photon paths from the electron vertex to a given PMT, properly weighted by the relative probability of each path. The fit position, direction, and time are then the set of these parameters which maximize the likelihood function for the event. This turned out to be quite an ambitious undertaking, largely because of the difficulty of determining the late light component to events for which there is currently no calibration<sup>8</sup>. As a result, the

---

<sup>7</sup>The vertex and direction fits are completely independent except that the direction fit uses PMT weighting information from the vertex fit.

<sup>8</sup>The optical calibrations described in Section 5.3 are for *prompt light* only and consequently, no calibration of reflected or scattered light currently exists.

fitter used in this thesis and distributed for use by the collaboration<sup>9</sup> implements a scaled-down version of original Path Fitter principles which attempts to incorporate the best parts of the method with simplifying assumptions about late light. Based on vertex and direction reconstruction performance, the Path Fitter has been chosen by the SNO collaboration as the current primary fitter used for solar neutrino analyses.

This section describing the Path Fitter is organized in the following way. In Section 4.3.1, some general issues related to reconstructing events in SNO are discussed in the context of constructing the Path Fitter. These include the motivation for using signal-based PDFs, discarding PMT hits during the fitting process, and speed-of-light issues. The use of PMT time and angular information in vertex reconstruction is discussed in Section 4.3.2, where studies under ideal Monte Carlo conditions that demonstrate some interesting effects of using angular information are presented. This naturally leads into a description of the Path Fitter approach to vertex and direction reconstruction in Section 4.3.3 along with a description in Section 4.3.4 of the actual fitter implemented in SNOMAN and used in this thesis. The interested reader is referred to [41] and [42] for more detailed information regarding the Path Fitter and time and angle fitting.

### 4.3.1 General Fitter Considerations

This section contains a discussion of some general issues relevant for developing a reconstruction method such as the Path Fitter.

---

<sup>9</sup>SNOMAN versions 4.0083 and later.

## Signal PDFs

The explicit approach used to fit events with the Path Fitter is to use as much information about the signals one is trying to reconstruct as possible to estimate the most likely position, direction, and time of the event. The reconstruction is performed under the hypothesis that the event was initiated by a single relativistic electron. For CC and ES signals, this is a valid hypothesis. A given neutron signal event may involve several Compton-scattered electrons from the capture  $\gamma$ . We are fortunate to have copious amounts of calibration data<sup>10</sup> very near the capture  $\gamma$  energy to test how well these reconstruct under the single electron hypothesis. After a particular fit is completed, the consistency of this hypothesis with the observed time and angular distribution of hits in the event is tested. Reconstructed events which are inconsistent with this hypothesis (at some level) are rejected. Aside from rejecting Cerenkov events (e.g. external  $\beta - \gamma$ s) that are poorly reconstructed in either position or direction, this approach has the added advantage of rejecting non-Cerenkov backgrounds from instrumental sources of light, for example.

## Discarding Hits During the Fit

Most fitters use some sort of algorithm to discard PMTs during the fit in an effort to improve vertex reconstruction. As described in Section 4.2.4, the Elastic Fitter uses a particularly elegant method of de-weighting hits that is closely analogous to the method of simulated annealing. The idea is that only PMT hits from *direct* Cerenkov light are well understood through calibrations, therefore other PMT hits should be ignored because they add no useful information to the fit. A simple example of a

---

<sup>10</sup>from the  $^{16}\text{N}$  calibration source to be discussed in Chapter 5.

fitter that follows this procedure is the SNOMAN Time Fitter that was discussed in Section 4.2.1. An implicit assumption in the Time Fitter algorithm is that hits are due to direct light - photons propagating directly from a Cerenkov source to the PMTs. However, a sizable fraction of hits are not from direct Cerenkov light but rather reflections, scattering, or random PMT noise coincidences. The Time Fitter attempts to circumvent this problem by selectively throwing out hits in the events and re-doing the  $\chi^2$  minimization.

Any method of selecting direct light hits is non-ideal and can lead to vertex reconstruction tails when non-direct light hits remain in the fit. This may be particularly serious at low energies where it is more difficult to distinguish direct light from other types of PMT hits. There is also an unavoidable loss of direct light hits in the process, which degrades the vertex resolution by throwing out information that is valid under the fitter hypothesis. In the Path Fitter, all PMTs which pass the full timing calibration are used in the fit<sup>11</sup>. The maximum likelihood method allows one to incorporate any type of information into the PDF. For example, a hit far out of time with the prompt time peak (determined by the hypothesized electron position) has a certain probability of being random noise which is incorporated as a uniform probability distribution in time and angle with relative magnitude related to the average PMT noise rate in the detector and occupancy of the event.

Of course, a PDF is only as good as the information that goes into it. One might argue that it is better to simply throw out late hits rather than assign them probabilities because of the difficulty of determining an accurate PDF. This may be true, although in the end it is a trade-off between the dangers of properly selecting

---

<sup>11</sup>Eventually, channel property information from ANXX banks should be used to ignore hits from bad channels.

only direct hits and the dangers of assigning non-direct hits the wrong probability. In the Path Fitter, the choice of using all the hits in the event is made and the late light component is modeled in a very simple way as a step function at the prompt time  $\Theta(t_i - t_{prompt})$ .

## Speed of Light

Choosing the speed of light to be used in fitters designed for SNO is a non-trivial matter due to the acrylic vessel. The reason is that the group velocity,  $v_g$ , of Cerenkov light depends on wavelength in a dispersive medium like water and AV absorption is wavelength dependent (shorter wavelengths are preferentially absorbed). Also, the AV has a larger index of refraction than water ( $\sim 1.5$  for acrylic compared to 1.33 for water) so the speed of light from source to PMT depends on the amount of acrylic traversed, even neglecting the wavelength dependence of  $v_g$ . A path-dependent speed of light can be naturally incorporated into the Path Fitter framework.

For Cerenkov light, the total energy deposited per unit angular frequency,  $\omega$ , per unit track length,  $x$ , is given by [43],

$$\frac{d^2E}{dxd\omega} = \left(\frac{ze}{c}\right)^2 \omega \left(1 - \frac{1}{\beta^2 n^2(\omega)}\right) \quad (4.5)$$

where  $ze$  is the particle charge,  $\beta = v/c$  is the particle velocity relative to the speed of light in vacuum, and  $n(\omega)$  is the index of refraction. The integral of Equation 4.5 over all wavelengths remains finite because of the asymptotic behavior of  $n$  and medium absorption at very long and short wavelengths. In addition, Equation 4.5 need only be integrated over the wavelength range imposed by the PMT response ( $\sim 300 - 600$  nm). In this range,  $n$  is not a strong function of  $\omega$ , although it does increase slightly

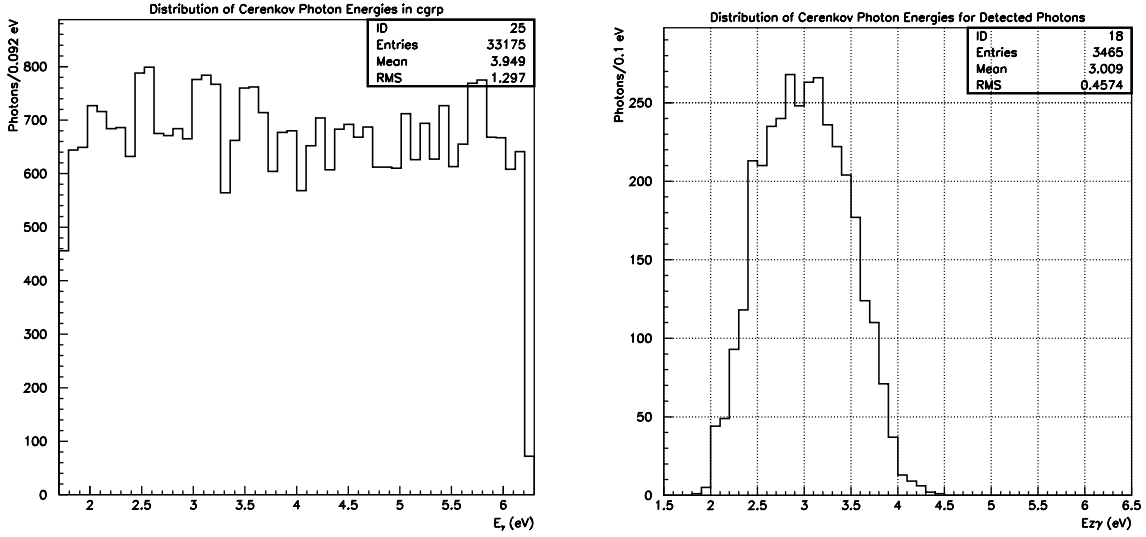


Figure 4.1: Distribution of energies for (left) generated and (right) detected photons produced by electrons in the D<sub>2</sub>O. For reference, 2 eV photons correspond to  $\sim 600$  nm wavelength and 4 eV corresponds to  $\sim 300$  nm. Figures courtesy of J.R. Klein.

from 300 nm to 600 nm.

It follows that if  $n$  is approximately independent of  $\omega$  over the range of interest (i.e. PMT wavelength response), then the number of Cerenkov photons generated,  $dN_\gamma$ , over a track length,  $L$ , where the particle energy is above Cerenkov threshold, is independent of photon energy ( $E_\gamma = \hbar\omega$ ),

$$\frac{dN_\gamma}{dE_\gamma} = L \left( \frac{ze}{\hbar c} \right)^2 \left( 1 - \frac{1}{\beta^2 n^2} \right) \quad (4.6)$$

Note that Equation 4.6 implies that Cerenkov photons will be generated provided  $\beta^2 n^2 > 1$ , or in terms of total electron energy,

$$E > mc^2 \frac{n}{\sqrt{n^2 - 1}} = 0.78 \text{ MeV (in water)}$$

Figure 4.1 shows the energy distribution of detected photons for electrons generated inside the D<sub>2</sub>O region. The flat photon energy distribution is “altered” by acceptance

effects of both the acrylic vessel, which absorbs predominantly short wavelengths, and the PMT wavelength response.

As previously mentioned, the group velocity of light depends on wavelength in a dispersive medium. Specifically, the group velocity is given by

$$v_g = \frac{d\omega}{dk} \quad (4.7)$$

where  $k$  is the wave number. Equation 4.7 can re-written as

$$\frac{1}{v_g} = \frac{n}{c} + \frac{\omega}{c} \frac{dn}{d\omega} \quad (4.8)$$

using the relation between  $k$ ,  $\omega$ , and  $c$ ,  $k = \frac{n\omega}{c}$ . Note that while  $v_g$  equals the phase velocity,  $v_p = \frac{c}{n}$ , in a non-dispersive medium (e.g. vacuum), in a normally dispersive medium like water where  $n(\omega)$  is a monotonically increasing function of  $\omega$  ( $\frac{dn}{d\omega} > 0$ ) the group velocity gets *smaller* as the photon energy *increases*. Therefore, the proper speed of light to use in a fitter which considers path-dependent probabilities (like the Path Fitter) is a distribution of speeds that is a convolution of the group velocity  $v_g(\omega)$ , the attenuation length of the medium at a distance  $x$  from the source,  $\lambda(x, \omega)$ , and the PMT response,  $R(\omega)$ ,

$$P(v_g) \sim \int \int v_g(\omega) R(\omega) e^{\frac{-x}{\lambda(x, \omega)}} dx d\omega \quad (4.9)$$

where variation of the PMT angular response with wavelength is ignored and recalling that the Cerenkov photon energy distribution is approximately constant over the angular frequency range of interest.

As an example of these effects, compare the photon speed distributions shown

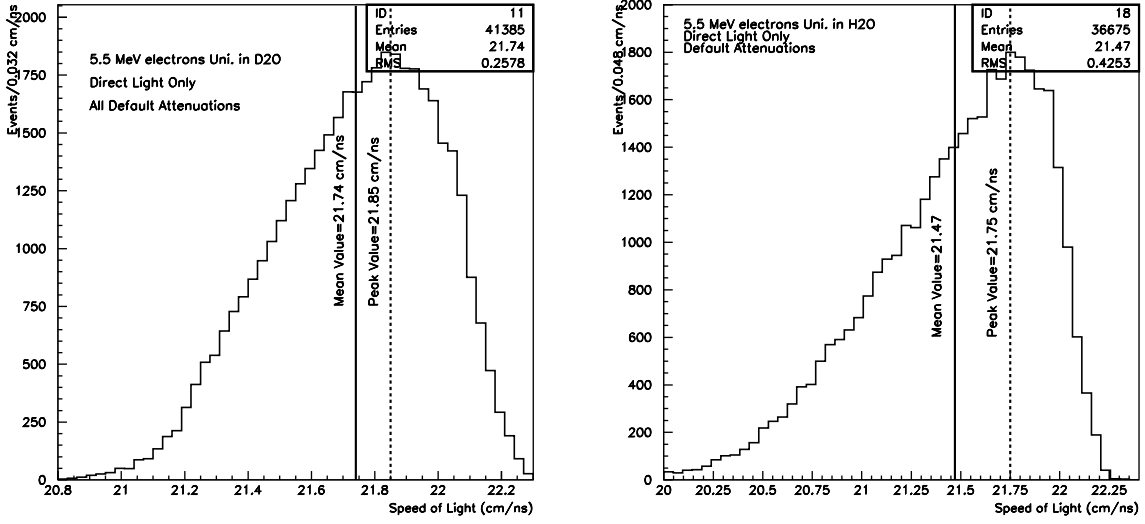


Figure 4.2: Photon speed distributions of detected photons for electrons generated uniform and isotropic in the (left)  $\text{D}_2\text{O}$  and (right)  $\text{H}_2\text{O}$  regions. Figures courtesy of J.R. Klein.

in Figure 4.2 of detected photons for Monte Carlo electrons generated uniform and isotropic in the heavy water and light water regions. A given detected photon speed is simply the distance from source to PMT divided by the photon time-of-flight. Note that the mean and most probable (peak or mode) speeds are larger for events from the  $\text{D}_2\text{O}$ . The reason is that because of solid angle considerations, the majority of photons from the light water travel directly to the PMTs without traversing the acrylic vessel. Recall that acrylic attenuates higher energy photons which are slower in water. Therefore, the more acrylic that is traversed, the larger the speed of light on average. This is why the mean and mode speeds are larger for events originating in the heavy water than events from the light water. Note also that the photon speed distribution is *broader* for light water events, owing to the fact that light water photons can traverse either zero or two AV thicknesses, while detected photons from the heavy water always cross the AV exactly once.

While inclusion of a path-dependent speed of light in the Path Fitter is straightforward and should improve performance, the effects are probably quite small according to the distributions shown in Figure 4.2. Therefore, the Path Fitter uses the average of the modes of the heavy water and light water distributions (21.8 cm/ns) as the speed of light in reconstructing events.

### 4.3.2 Use of Time and Angle Information in Reconstruction

All previous standard fitters in SNO use only PMT timing (distance-corrected) information in vertex reconstruction<sup>12</sup>. However, there is information in the pattern of PMT hits which is related to the angular distribution of Cerenkov light from relativistic electrons which initiate the events we are interested in analyzing. This section describes some studies that were done to understand how inclusion of this information affects the quality of vertex reconstruction.

A well-known effect in time-only based fitters is the so-called “drive” - the vertex fit is systematically displaced from the true position along the initial electron direction. This reason for this effect is that the azimuthal symmetry of Cerenkov light provides a poor constraint on the vertex along the axis of symmetry<sup>13</sup>. For a perfect Cerenkov cone imaged as a ring on the PSUP, the vertex is completely unconstrained along this axis, since one can always move the vertex and not degrade the direct light hypothesis if one also adjusts the electron time in kind. If one adds a PMT hit from a direct photon which does not lie on this ring, the fitter will chose a particular point on the along the ring axis for the fix vertex. What happens to the fit if this additional hit

---

<sup>12</sup>Although not a standard fitter included in the SNOMAN distribution, Bill Frati at Penn has developed a fitter that uses angular information for vertex reconstruction.

<sup>13</sup>and this axis is closely related to the initial direction of the electron if one considers that multiple electron scattering is forward-peaked in a Cerenkov photon-weighted sense.

is not direct, but rather comes at a time earlier or later than the direct light time? In a nice treatment of this problem shown in Appendix C of [44], it was shown that an early hit inside (outside) the ring drives the fit forward (backward) and a late hit inside (outside) the ring drives the fit backward (forward). The drive displayed in time-residual based fitters is a consequence of more light being late (scattering, reflections) than early and of late hits being predominantly outside the ring produced by Cerenkov light.

Since the source of the drive in time-based fitters is related to the symmetry of hit patterns resulting from Cerenkov light, it seems natural that explicit inclusion of this angular information should mitigate this systematic effect. However, when time and angular information were used together in vertex reconstruction on MC electrons in SNOMAN, it was observed that the drive actually gets substantially worse! Studies that were done to try to understand this rather disappointing fact under ideal MC situations are discussed in the remainder of this section. It is found that proper use of angular information is much more subtle than originally believed.

### Fitting in 2D “Perfect World”

To study vertex fitting using angular information, the simplest non-trivial “world” was created where events could be generated through Monte Carlo techniques and fit using an angular distribution representative of Cerenkov light from a multiply scattered electron. This angular distribution is discussed in Section 4.3.4, however all one needs to know for this discussion is that the largest probability is at the Cerenkov angle ( $\sim 42^\circ$ ) relative to the initial electron direction. The world created for study is a 2D world where the ‘PMTs’ are simply represented as  $N_{pmt}$  equal angular regions on a circle that give full coverage and have unit quantum efficiency. In addition, there

are no optical or other effects that would alter a generated photon's trajectory so that a generated Cerenkov photon is always detected by exactly one PMT.

Since this ideal 2D world has perfect photocathode coverage and efficiency, an “electron” that generates  $N_\gamma$  Cerenkov photons will result in an event with  $N_{\text{Hit}} = N_\gamma$  PMT hits, although some PMTs may be hit more than once. The probability,  $\mathcal{P}$ , of observing  $r$  hits in the  $i^{\text{th}}$  PMT has a Poisson probability distribution,

$$\mathcal{P}_i(r; \vec{r}_e, \hat{d}_e) = \frac{1}{r!} \lambda_i^r e^{-\lambda_i} \quad (4.10)$$

where

$$\lambda_i \equiv N_\gamma \rho_i = \frac{N_{\text{Hit}}}{2} \int_{\alpha_{i1}}^{\alpha_{i2}} g(\alpha) d\alpha \quad (4.11)$$

where  $\alpha$  is the angle between the electron direction vector  $\hat{d}_e$  and the vector from the electron position  $\vec{r}_e$  to a point on the PMT, and  $g(\alpha)$  is the angular distribution of Cerenkov photons relative to the initial electron direction. The probability is divided by two as shown in Equation 4.11 because of the azimuthal symmetry of Cerenkov light. Projected into 2D, this symmetry means that there are always two points on the circle which have the same  $\alpha$  and, consequently, the same probability. The fit electron position and direction are the vectors which maximize the likelihood function for the event,

$$\mathcal{L}(\vec{r}_e, \hat{d}_e) = \prod_{i=1}^{N_{\text{pmt}}} \mathcal{P}_i(r; \vec{r}_e, \hat{d}_e) \quad (4.12)$$

where the product is over all PMTs on the circle.

The distribution of fit positions for “electrons” generated at the center in the  $+x$  direction is shown in Figure 4.3 along with a display of a typical event and fit. The drive is clearly evident here, as the mean fit position along the initial electron

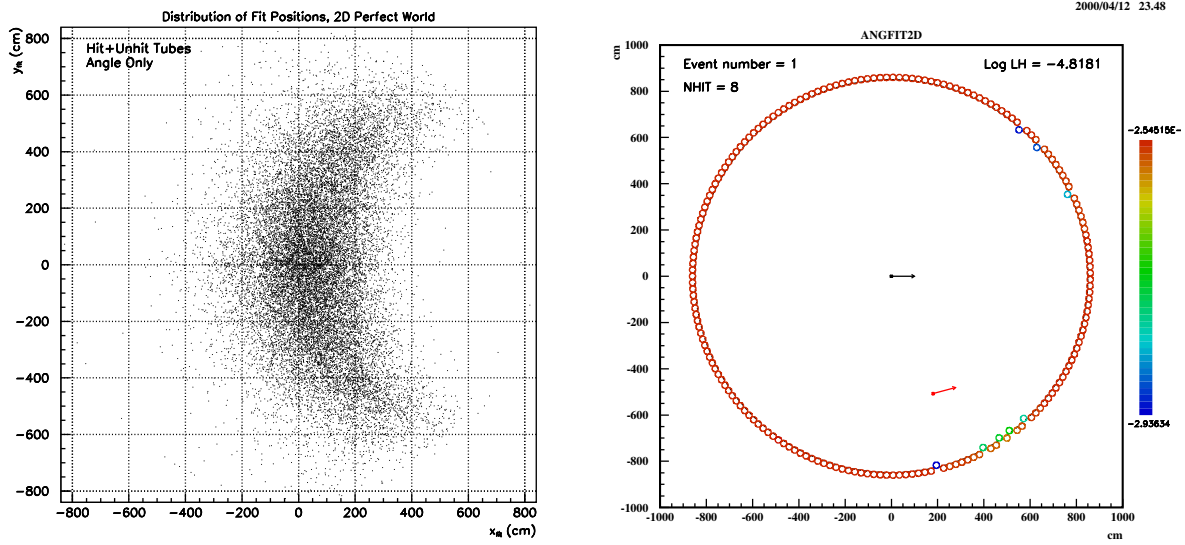


Figure 4.3: (left) Distribution of fit positions in 2D world for “electrons” generated at the center in the  $+x$  direction. (right) An event display of a fit showing the “swirl” effect.

direction ( $+x$ ) is positive. The reason for this crescent shaped distribution is that the likelihood can be increased by moving the fit position off axis and forward if the direction is also altered so that the hit PMTs remain near the Cerenkov angle. This so-called “swirled” position has a larger likelihood than the center because of the increased solid angle contribution gained by moving closer to the PMTs with little penalty in the angular distribution because the fit direction is simultaneously adjusted to compensate<sup>14</sup>. This argument is based on the consideration of hit tubes, but what about unhit PMTs which are also included in the likelihood? It was originally thought that unhit tube probabilities would cancel swirl effects that lead to drive. The reason is that although swirling toward hit tubes increases their hit probability (and thus increases the overall event likelihood), it *reduces* the probability that unhit tubes

<sup>14</sup>the reason one side of the crescent is chosen over the other is because of Poisson fluctuations that leave more hits on one side than the other. Larger solid angle gains can be made by moving closer to more hit tubes at the expense of reducing solid angle for fewer tubes.

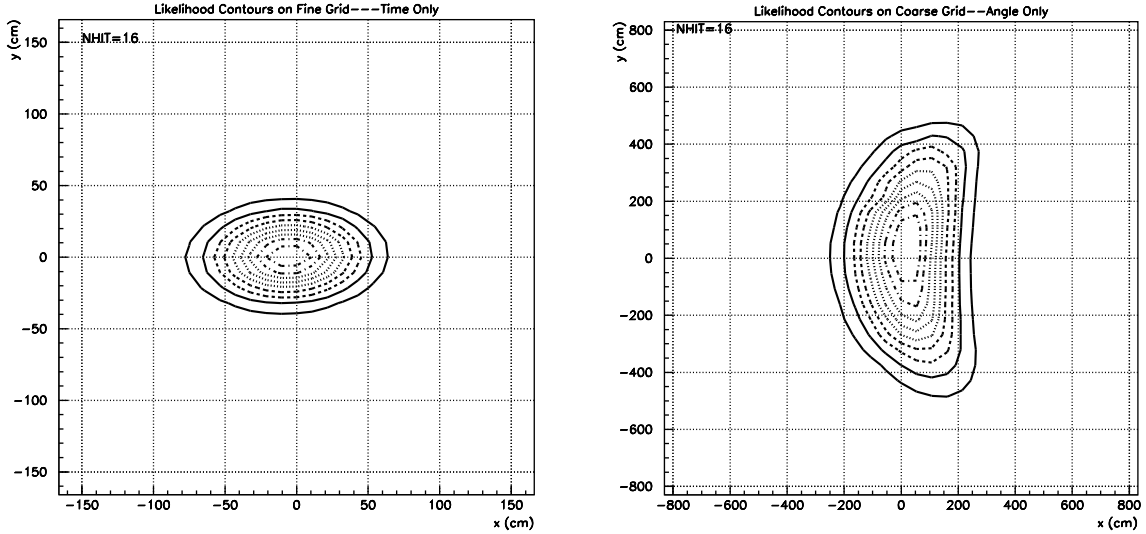


Figure 4.4: Likelihood contour for 2D fits using (left) time only and (right) angle only. Events were generated at the center of 2D world in the  $+x$  direction. Figures courtesy of J.R. Klein.

in the vicinity of the hit tubes are unhit, thus reducing their contribution to the likelihood. These unhit tube effects are at work in the fitting process, but their effect is too small to fully cancel the swirl.

The question still to be answered is whether angular information helps in vertex reconstruction. Specifically, is fitting using time and angle better than fitting using time information only? The answer turns out to be “yes” in this simple 2D world. Figure 4.4 shows contour plots of the likelihood space for fits using only time information and fits using only angular information. Note the the time and angle contours are complementary in terms of their constraints on the vertex. As previously discussed, the time information provides a poor constraint along the electron direction, as can be seen from the comparatively gradual likelihood slope in the  $+x$  direction. However, as the angular likelihood contour in Figure 4.4 shows, this is exactly the direction which is best constrained by the Cerenkov angular information. Therefore

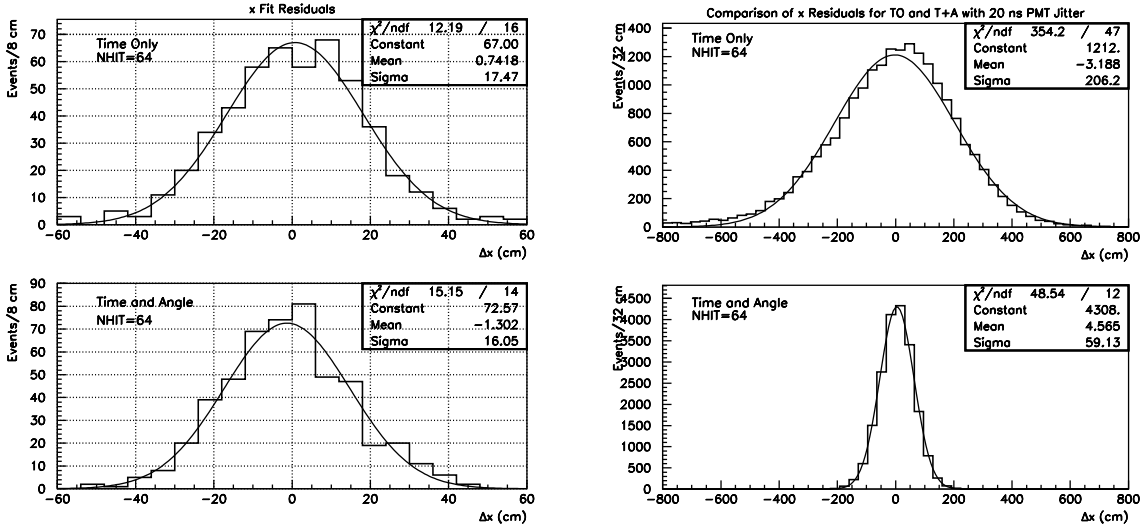


Figure 4.5:  $x_{fit}$  distributions of events generated at the center of 2D world with (left) 1.5 ns PMT time jitter and (right) 20 ns jitter, when time only is used and time and angle are used in the fitting. Figures courtesy of J.R. Klein.

one would expect that the combination of time and angle would constrain the vertex better than either piece of information alone.

Figure 4.5 shows  $x_{fit}$  distributions of events generated at the center of the 2D world, when time only is used and when both time and angular information are used in the fitting. Note that for a nominal PMT time jitter of 1.5 ns, the simultaneous use of time and angle information narrows the fit residual distribution. The improvement is much more dramatic when the timing information is bad, which is demonstrated in Figure 4.5 with 20 ns PMT jitter. This suggests that angular information may be useful in reducing ill effects on vertex reconstruction from bad channel timing, speed of light variations (recall Section 4.3.1), etc.

## Fitting in 3D

It was shown in the previous section that angular information helps vertex determination in 2D. It was also shown that angular information, while providing a strong constraint on the vertex along the initial electron direction, provides a poor constraint along a crescent-shape contour when the direction is allowed to vary. How do these effects change when we consider 3D dimensional fitting?

For these studies, it was easiest to simply use the Monte Carlo machinery that exists in SNOMAN. To make the SNOMAN 3D world as ideal as possible so that useful comparisons to 2D results could be made, all the effects which make photon propagation and detection different were disabled - reflections, scattering, speed of light variations, etc. The fit positions for electrons generated at the center of this “ideal” 3D world in the  $+x$  direction exhibit a forward drive which is larger and very different in character than the 2D case. It was pointed out [45] that a difference between the 2D and 3D worlds was the way that Cerenkov photons were generated. In the 2D world, photons were generated by directly from the Cerenkov photon distributions, both in polar and azimuthal angles. The polar distribution was obtained from the distribution of photon angles relative to the initial electron direction obtained by EGS4 simulation of many electron events in SNOMAN. The azimuthal distribution in the 2D world is a uniform distribution, and therefore all events are azimuthally symmetric. In 3D world, however, events are generated by the EGS4 code. This subtle difference turns out to have quite a large effect on the fit vertex distribution in terms of drive (See Figure 4.6). In this case, the fit results look exactly like what one expects from a 3D-rotated version of Figure 4.3 when the same Cerenkov photons distributions are used to generate and fit the events. It can also be seen in Figure 4.7

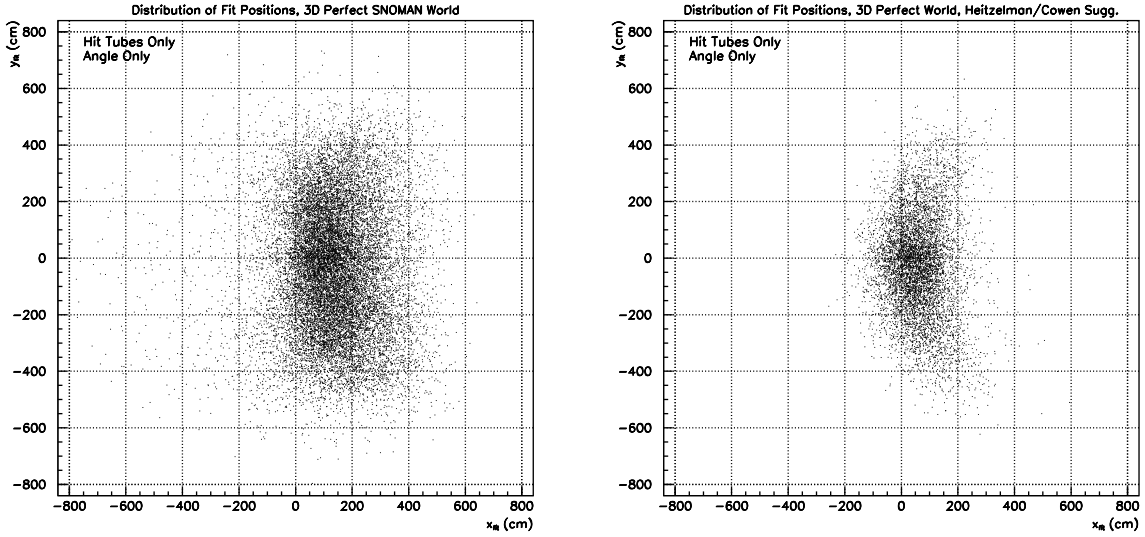


Figure 4.6: Distribution of fit positions for electrons generated at the center of 3D world in the  $+x$  direction when (left) SNOMAN EGS4 is used to generate and (right) the same distribution is used to generate and fit the events. Figures courtesy of J.R. Klein.

that the drive is greatly reduced when the same distribution is used to generate and fit the events as opposed to using EGS4 generation.

What does all this mean for 3D fitting using angular information? It was suggested [46] that the assumption of azimuthal symmetry in the PDF might be related to the additional drive seen in 3D when trying to fit events from realistic photon generation by EGS4. The studies just presented certainly demonstrate that there is a big difference between fitting EGS4 generated events and events generated from the average distribution. It also makes sense that azimuthal symmetry is not the proper individual event hypothesis for typical events when one considers the generation of Cerenkov light from a multiply scattered electron. In the simplest example, azimuthal symmetry is maximally violated in an event where the electron generates light over one straight track along its initial direction, scatters at large angle, and then generates light along this track until it drops below Cerenkov threshold. It may be that

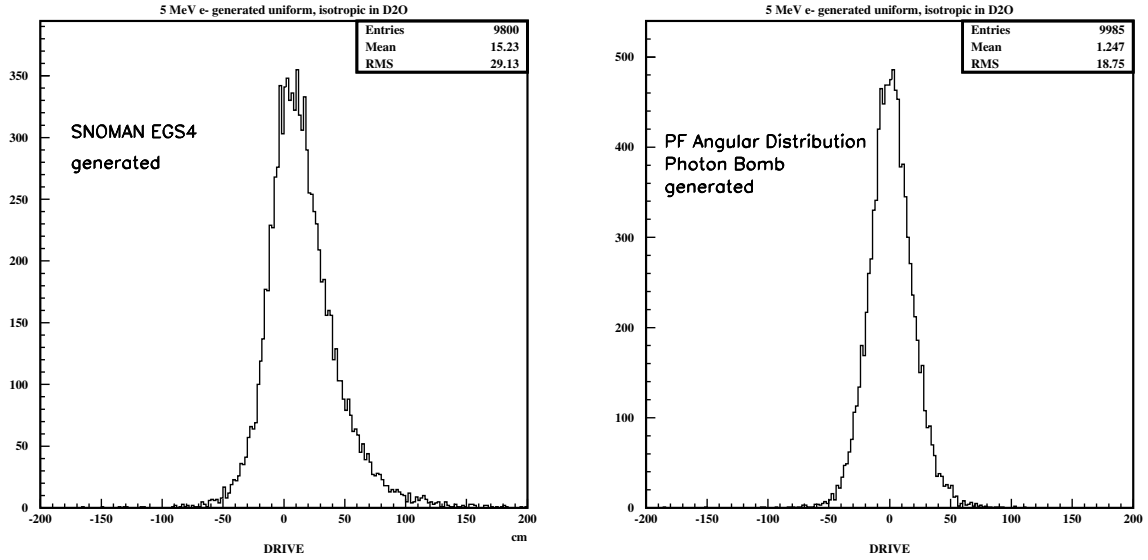


Figure 4.7: Drive distribution for events generated uniformly and isotropically in the D<sub>2</sub>O when (left) SNOMAN EGS4 is used to generate and (right) the same distribution is used to generate and fit the events.

a more accurate PDF would be one which deals with the probabilities of individual electron scattering trajectories, including scatter-to-scatter correlations in direction. This is not an easy task by any means, but it is brought up as possible direction for improvement of the existing Path Fitter in SNOMAN. As we will see, even fitting without a strictly ideal angular PDF has advantages over the existing time-only based fitters in SNO.

The next section outlines development of the Path Fitter which naturally leads into a discussion of the fitter implemented in SNOMAN and used in this thesis.

### 4.3.3 Fitter Development - A Brief History of Time and Angle

Initial work by the author on reconstruction started with the idea of using Monte Carlo simulation on a event-by-event basis to determine the PDF used for fitting events. The main point was that an ideal fitter in terms of using all available infor-

mation would be a maximum likelihood fitter that employs the full MC to determine the probability density for a given PMT to record a given charge and time. In practice, the PDF for a given hypothesized electron position, direction, time, and energy would be determined by simulating this electron many times (an infinite number, in principle) and noting the relative number of times that each PMT records a given time and charge.

In practice, there are several problems with such a fitter. The MC does not perfectly simulate the physics nor the detector response. A more serious difficulty is that simulating the large number of events required to get a statistically significant PDF and re-doing this many times as the minimization routine searches the phase space of possibilities requires an impracticable amount of CPU power. An attempt was made to speed up the MC PDF determination by preprocessing the Cerenkov photon production in terms of the angular distribution of light produced by the electron. This is possible because while PDF determination by the previously described method involves summing over many events, one can just use the angular distribution of Cerenkov light to get the PDF by simply generating one event having a very large number of photons. The MC is then used to simply propagate the photons and simulate the detector response. Such a fitter - called the “bomb” fitter since a large photon bomb with Cerenkov angular distribution is used to estimate the PDF at each minimization step - was attempted and abandoned because of the impracticable amount of CPU time required to fit events.

In the Path Fitter, a different approach is taken to estimating the PDF. In principle, the SNOMAN MC is simply using Monte Carlo techniques to do a set of integrals - albeit a very complicated set of integrals containing many different parts that reflect the richness and complexity of the detector. It may be possible to simply calculate the

most important of these integrals to get PDFs which are reasonable approximations of the “true” PDFs resulting from the full MC calculations.

The challenge in calculating a reasonably accurate PDF is to properly reproduce correlations between timing and angular distributions of hit PMTs. The principle approach of the Path Fitter is to break the PDF into a sum of terms, each of which represents the probability for a given PMT to be hit at a certain time if the Cerenkov photon causing the hit follows a particular type of path (e.g. direct light, scattering, reflections). Each of the terms then has the proper correlation between time and angle that can, in principle, be calculated. Therefore, we have the following estimate for the PDF,

$$\mathcal{P}_i(n_i, t_i; \vec{r}_e, \hat{d}_e, t_e, E) = \sum_{j \text{ paths}} P_{ij}(n_i, t_i; \vec{r}_e, \hat{d}_e, t_e, E) \quad (4.13)$$

where  $P_{ij}$  is the probability density corresponding to the  $j^{th}$  path type for the  $i^{th}$  PMT to be hit  $n_i$  times and record a time  $t_i$ , given an electron initially at  $\vec{r}_e$ ,  $t_e$  in the direction  $\hat{d}_e$ . Note that higher order terms (e.g. paths corresponding to scatter + reflection or scatter + scatter) are left out of the PDF calculation.

The path-dependent density functions  $P_{ij}$  separate into the product of time and angle parts,

$$P_{ij} \sim P_{ij}^{TIM}(n_i, t_i) P_{ij}^{ANG}(n_i) \quad (4.14)$$

The reason this is not shown as an equality is because the calculation for each of the path types actually involves integration of this functional form. For example, the scattering term involves integration over all scatterers in the detector, and there are several paths that a reflected photon can take into a given phototube. Note that  $n_i$  is included in the time function to suggest the possibility of including multi-photon effects in the time PDF. The time function  $P_{ij}^{TIM}$  would then have the same form

(e.g. Gaussian PMT jitter) for each of the paths, differing only in the photon path distance. The angular part is the Poisson probability for a given PMT to be hit  $n_i$  times,

$$P_{ij}^{ANG}(n_i) = \frac{1}{n_i!} \lambda_{ij}^{n_i} e^{-\lambda_{ij}} \quad \lambda_{ij} \equiv N_\gamma \rho_{ij} \quad (4.15)$$

where  $N_\gamma$  is the number of Cerenkov photons generated by the electron (can be roughly estimated from  $N_{\text{Hit}}$  and the overall PMT efficiency + coverage), and  $\rho_{ij}$  is the probability for a Cerenkov photon generated by the electron to be detected by the  $i^{\text{th}}$  PMT. The probability  $\rho_{ij}$  depends on the angular distribution of Cerenkov photons from the electron, the solid angle subtended by the  $i^{\text{th}}$  PMT from the electron position, and optical effects such as attenuation and reflectivity.

The main disadvantage of using calculated rather than Monte Carlo generated PDFs in a fitter is the difficultly of properly estimating contributions from reflections and scattering. In terms of reflections, only the dominant PSUP reflections were included in PDF calculations and the PSUP was approximated as a spherical mirror with uniform reflectivity. Scattering was considered by assuming a uniform distribution of scatterers in the detector volume, which scatter light isotropically with a probability related to the scattering length of the medium.

While PDFs generated from modeling reflections and scattering in this way qualitatively match the Monte Carlo results, there are several problems with this approach. From a practical standpoint, a typical fit requires many such calculations to be performed, since the PDF needs to be recalculated at each electron phase space point. The scattering component to this calculation is particularly CPU intensive, since it involves mult-dimensional integration for each hit PMT to add up contributions from all scatterers in the detector volume. In addition, modeling of the PSUP as a spherical

mirror is too simplistic, as there are substantial non-specular PSUP reflections which need to be included. Appendix A contains some notes on calculation of reflections and scattering for the interested reader.

## PDF Normalization

Since a different PDF is used for each electron position  $\vec{r}_e$ , time  $t_e$  and direction  $\hat{d}_e$ , one needs to worry about the relative normalization of the PDFs<sup>15</sup>. If one ignores multi-photon effects and considers a signal photon path in the sum, the normalization is trivial

$$\sum_{n_i=0}^{\infty} \int_{-\infty}^{\infty} P_{ij}(n_i, t_i; \vec{r}_e, \hat{d}_e, t_e) dt_i = \sum_{n_i=0}^{\infty} \frac{1}{n_i!} \lambda_{ij}^{n_i} e^{-\lambda_{ij}} \int_{-\infty}^{\infty} P_{ij}^{TIM}(t_i) dt_i = 1 \quad (4.16)$$

if  $P_{ij}^{TIM}$  is itself normalized. The fact that the normalization is independent of  $\vec{r}_e$ ,  $t_e$ , and  $\hat{d}_e$  greatly simplifies the fitting procedure. If one now considers multiple photon paths, there are additional multiplicative terms that reflect the relative probabilities of photon paths. For example, if there were only direct and reflected light in the detector, the reflection term would be multiplied by the fractional amount of reflected light (related to the mean reflection coefficient) and the direct term would be preceded one minus this probability to normalize the overall PDF.

In the interest of implementing a fitter which incorporates the basic Path Fitter approach but avoids the difficulties of calculating reflections and scattering, a simplified Path Fitter has been installed in SNOMAN. This fitter is described in the next section.

---

<sup>15</sup>Technically, each PDF also needs to be normalized to one for proper interpretation of the likelihood.

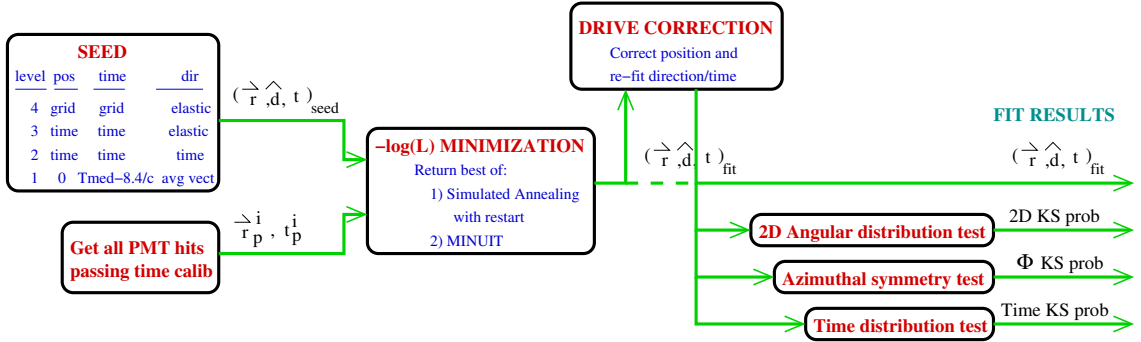


Figure 4.8: Diagram showing the general flow of the Path Fitter algorithm.

#### 4.3.4 The SNOMAN Path Fitter

The Path Fitter implemented in SNOMAN fits events by maximizing the likelihood function

$$\mathcal{L} = \prod_{i=1}^{N_{HIT}} \mathcal{P}_i(n_i = 1, t_i; \vec{r}_e, \hat{d}_e, t_e) \quad (4.17)$$

where  $\mathcal{P}_i$  is the probability density function for the  $i^{th}$  PMT which is described in Section 4.3.4. In practice, the  $-\log \mathcal{L}$  function is minimized to get the fit position, direction, and time. Note that only hit PMTs are included in the likelihood function. Unhit PMTs add information into the fit (and fit naturally into the maximum likelihood framework) and their exclusion is only because of the extra CPU time required at the occupancies relevant for solar neutrino events.

The general flow of the Path Fitter algorithm is shown in Figure 4.8. The initial ingredients of the fit are the set of PMTs used in the fit and a seed electron phase space point for the minimization routines. All hit PMTs which pass the full timing<sup>16</sup> calibrations are used in the fit. The seed point for the fit depends on the user specified seed level and the results of the other fitters (Grid, Elastic, and Time fitters). For ex-

<sup>16</sup>i.e. Channel (ECA) and PMT timing (PCA) calibrations to be discussed in Chapter 5.

ample, if the user specifies a seed level of 4 (the default), then the initial position/time are from the Grid fitter and the initial direction is the Elastic fitter direction, unless either of these fitters fail or the position fit is outside the PSUP region. In the latter scenarios, the fitter enters the next lowest seed level and continues, unless this lower seed level is below the minimum seed level specified by the user, in which case the fitter fails. Details regarding the other seed levels are shown in Figure 4.8.

The  $-\log \mathcal{L}$  function minimization proceeds through several steps. First, the function is minimized using the method of simulated annealing (specifically using the Numerical Recipes [47] routine *ameobsa*). This method has proven effective in global minimization problems when local function minima exist. The basic idea is that an  $n+1$  dimensional simplex ( $n$  is the number variables in  $\mathcal{L}$ ) randomly samples the function at very large values of a parameter  $T$  (called the “temperature”), but at very low temperatures the simplex follows the downhill simplex method of Nedler and Mead. At intermediate temperatures, the downhill simplex method is followed except that each vertex of the simplex has a non-zero probability of taking an *uphill* step from function value  $F_1$  to  $F_2$  ( $F_2 > F_1$ ) given by

$$P_{up} \sim e^{\frac{-(F_2 - F_1)}{T}} \quad (4.18)$$

where  $F$  is the value of the function at the given simplex point. The minimization proceeds by lowering the temperature from an initial value ( $T_o$ ) which is large compared to typical changes in the log-likelihood to a smaller temperature according to the “scheduling function”

$$T_i = T_o \left(1 - \frac{i}{I}\right)^\alpha \quad (4.19)$$

where  $i$  is the step index,  $I$  is the total number of temperature steps, and  $\alpha = 4$  (default). The phase space point with the lowest function value ( $-\log \mathcal{L}$ ) is then returned.

The overall minimization strategy is to first get the best point (i.e. electron phase space point with the lowest  $-\log \mathcal{L}$ ) from simulated annealing using the initial seed point from the seed levels. The simulated annealing is then performed again using the previous best point as a seed. Finally, MIUNIT (using “MINIMIZE” strategy) is called using the current best point as the seed. The best point from the three minimization stages is returned as the fit electron position, direction, and time.

After the fit is complete, the user has the option of applying a drive correction to the fit point and calculating several goodness-of-fit (GOF) criteria. The drive correction and GOF criteria are described in Section 4.3.4 and Section 4.3.5, respectively.

### The Path Fitter PDF

In the simplified version of the Path Fitter implemented in SNOMAN, all PMT hits are assumed to come from two separate photon paths - direct light and “other light”, which represents all non-direct types such as reflections, scattering, and random PMT noise. Specifically, the probability density function for the  $i$ th PMT to be hit once at time  $t_i$  given an electron initially at  $\vec{r}_e$ ,  $t_e$  in direction  $\hat{d}_e$  is given by

$$\mathcal{P}_i(n_i = 1, t_i; \vec{r}_e, \hat{d}_e, t_e) = f_{direct} \mathcal{P}_{direct}^{TIM}(t_i) \mathcal{P}_{direct}^{ANG}(1) + f_{other} \mathcal{P}_{other}^{TIM}(t_i) \mathcal{P}_{other}^{ANG}(1) \quad (4.20)$$

where  $\mathcal{P}_{direct}^{TIM}(\mathcal{P}_{direct}^{ANG})$  and  $\mathcal{P}_{other}^{TIM}(\mathcal{P}_{other}^{ANG})$  are the time (angular) probability density functions for direct and other light, respectively, and  $f_{direct} = 0.879$  and  $f_{other} = 0.121$  are the respective light fractions based on fits to laserball data.

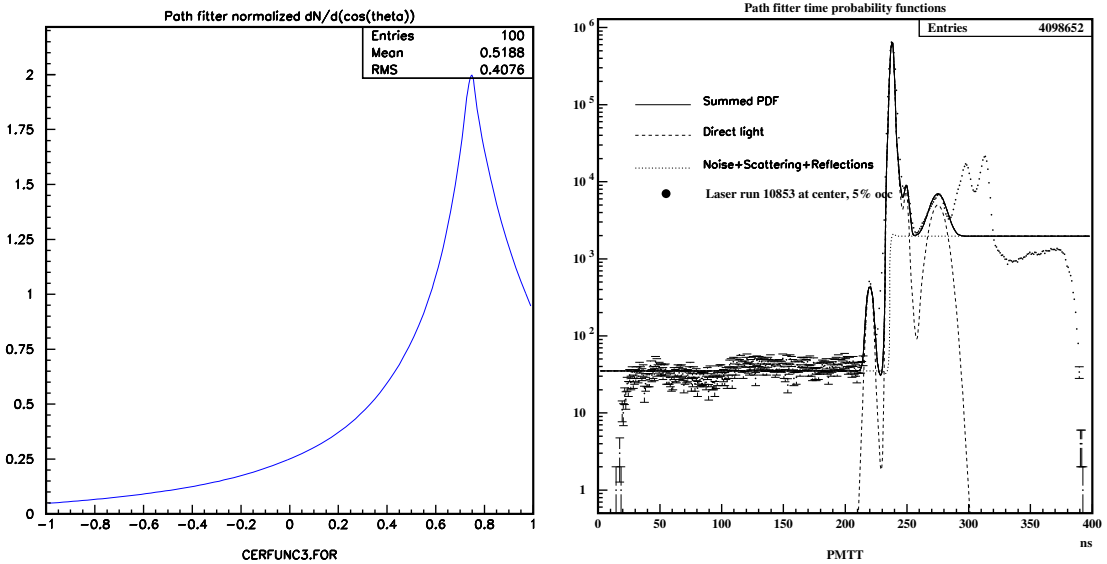


Figure 4.9: (left) Angular distribution of Cerenkov photons relative to the initial direction of a Monte Carlo 5 MeV electron. (right) Hit PMT time distributions which make up the direct light (dashed) and “other” light (dotted) time probability density functions. The solid dots correspond to hit PMT times from laserball run 10853 at the center of the detector.

The time probability density functions are derived from fits to laserball data at the center of the detector (see Figure 4.9). For direct light, the time PDF is a sum of four Gaussian functions corresponding to prompt, pre-pulse, late-pulse, and after-pulse PMT hits, where the time offset is determined by the direct time-of-flight to the PMT. The time PDF for hits from other sources is modeled as the sum of a flat PMT noise distribution and  $\Theta(t_i - t_{prompt})$  for late light from reflections and scattering.

The angular PDF for non-direct light is a normalized uniform distribution. Therefore, no attempt is made to use angular information in scattered or reflected light as was the case in the original Path Fitter, and the only time information which is used is the simple fact that the majority of hits outside the prompt peak are late. The direct light angular PDF used in the Path Fitter includes the angular distribution of Cerenkov photons from a multiply scattered electron and the solid angle subtended

by the PMT in question. Specifically, the angular PDF is the Poisson probability for a single hit of the  $i^{th}$  PMT is given by

$$\mathcal{P}_{direct}^{ANG} = N_\gamma \rho_i e^{-N_\gamma \rho_i} \quad (4.21)$$

where  $N_\gamma = \frac{N_{HIT}}{0.55}$  is used as a rough estimate of the number of emitted Cerenkov photons and

$$\rho_i = \frac{1}{2\pi} g(\cos \alpha_i) \Omega_i \quad (4.22)$$

where  $g(\cos \alpha)$  is the angular distribution of Cerenkov photons relative to the initial direction of a 5 MeV electron according to the SNOMAN implementation of EGS4 code (see Figure 4.9),  $\alpha_i$  is the angle of the  $i^{th}$  PMT relative to the hypothesized electron direction from the electron position, and  $\Omega_i$  is the solid angle of the  $i^{th}$  PMT viewed from the electron position given by

$$\Omega_i = \frac{\pi r_c^2}{d_i^2} \hat{d}_i \cdot \hat{r}_i \quad (4.23)$$

where  $r_c$  is the concentrator radius,  $\hat{r}_i$  is the unit position vector of the  $i^{th}$  PMT, and  $\vec{d}_i$  is the vector connecting the electron position and the position of the  $i^{th}$  PMT. The angular distribution,  $g(\cos \alpha)$ , is fit to the SNOMAN results as piece-wise continuous function consisting of two 10<sup>th</sup>-degree polynomials (one for each side of the Cerenkov angle) and Gaussian centered on the (cosine) of the Cerenkov angle.

## Drive Correction

It was determined through Monte Carlo studies that the Path Fitter, much like other fitters in SNOMAN, contains a systematic “drive” in the vertex fitting which causes

the mean fit residual along the initial electron direction to be positive. The drive was discussed in Section 4.3.2 in the context of time and angle fitting. While many interesting things were learned about the drive (e.g. it seems to be related to the assumption of  $\phi$  symmetry in each event), no analytical fix is currently implemented in the Path Fitter. The approach taken to improve the Path Fitter was to empirically study the effect in Monte Carlo and allow the user to apply a correction to the vertex based on the results of these studies.

It was determined that the magnitude of the drive is related to the distance,  $M_{gen}$ , along the generated direction from the generated position to the PSUP, but correlation with the distance,  $M_{fit}$ , along the *fit* direction from the *fit* position to the PSUP is small for events generated inside the D<sub>2</sub>O (see Figure 4.10). Therefore, when the drive correction option is enabled by the user (default), the position returned by the fitter is pulled back in a direction *opposite* the fit direction by an amount determined from empirical studies of the average amount of drive (15.27 cm). After this correction is applied, the direction and time are re-fit at the drive corrected position.

#### 4.3.5 Goodness-of-Fit Criteria

The Path Fitter can be requested by the user to return GOF information to assess the quality of the fit. The GOF information is in terms of a KS probability for each of three quality tests - two angular tests and one time test - each of which is related to the consistency between the event expectations based on properties of Cerenkov light and the detector response.

Two of the GOF tests evaluate the angular distribution hit PMTs to determine the fit quality. For these tests,  $(\cos \alpha, \psi)$  of each PMT is first determined, where  $\alpha$

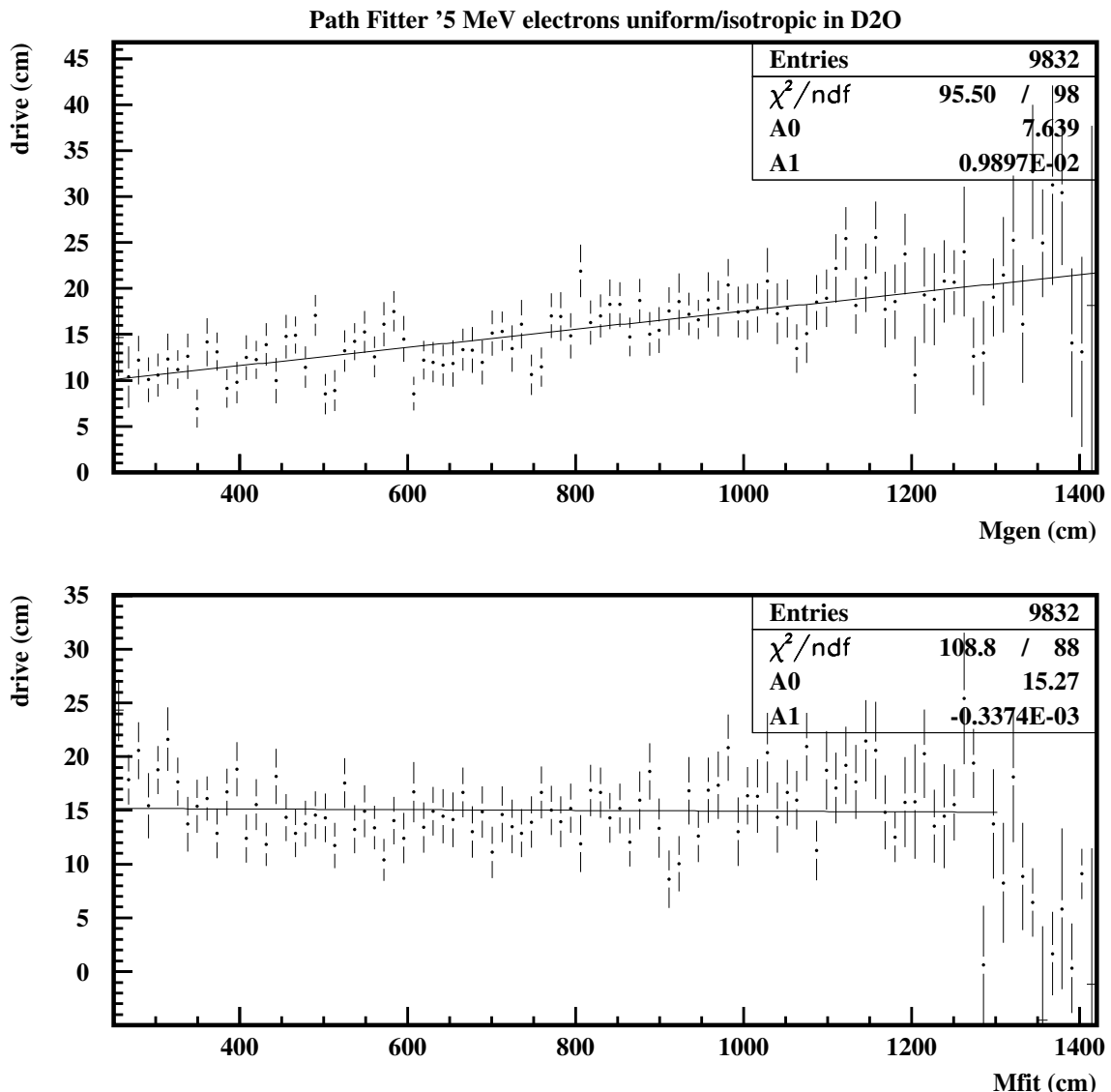


Figure 4.10: Path Fitter drive (cm) versus (a)  $M_{gen}$  and (b)  $M_{fit}$ .  $M_{gen(fit)}$  is the distance along the generated (fit) direction from the generated (fit) position to the PSUP.

and  $\psi$  are the polar and azimuthal angles of a given hit PMT's position vector in a coordinate system that is centered on the fit position with the z-axis along the fit direction and an x-y orientation chosen at random. One of the angular tests - the “azimuthal symmetry test” - returns the KS probability for the  $\psi$  distribution to be flat, using the fact that Cerenkov light is produced azimuthally symmetric about the (instantaneous) electron direction. The other angular test compares the 2D  $\cos\alpha, \psi$  distribution with the hit PMT angular probability density function for Cerenkov light. The 2D angular test statistic is the 2D KS probability for the PMT hits in the event to be drawn from the expected  $\cos\alpha, \psi$  probability distribution for Cerenkov light generated by an electron at the fit vertex with initial direction along the fit direction.

As an example of the angular tests, consider two events which have been fit well inside the D<sub>2</sub>O - a Monte Carlo 5 MeV electron fitting near its generated position/direction and an example of an instrumental background source of light - a PMT “flasher” event<sup>17</sup>. Figure 4.11 shows the  $\psi$  distribution for both events and the calculated probability density function taking into account the Cerenkov photon angular distribution, PMT solid angle, etc. Note the dip in each distribution caused by missing PMTs in the neck region. As previously mentioned, the PMT  $\psi$  distribution is simply compared to a uniform distribution, and the KS probability is calculated. For this particular example, the MC and flasher events have azimuthal symmetry KS probabilities of 0.7 and 0.03, respectively. Note that while the flasher event looks like it has a less uniform  $\psi$  distribution and has a low KS probability value, it is probably not enough to reject this event based on the azimuthal symmetry test alone. However, when one considers both the  $\cos\alpha$  and  $\psi$  together as in the 2D angular test, the two events are much more distinct (see Figure 4.12). The MC and flasher events have 2D

---

<sup>17</sup>This is when an event is initiated by the spontaneous emission of light by a PMT.

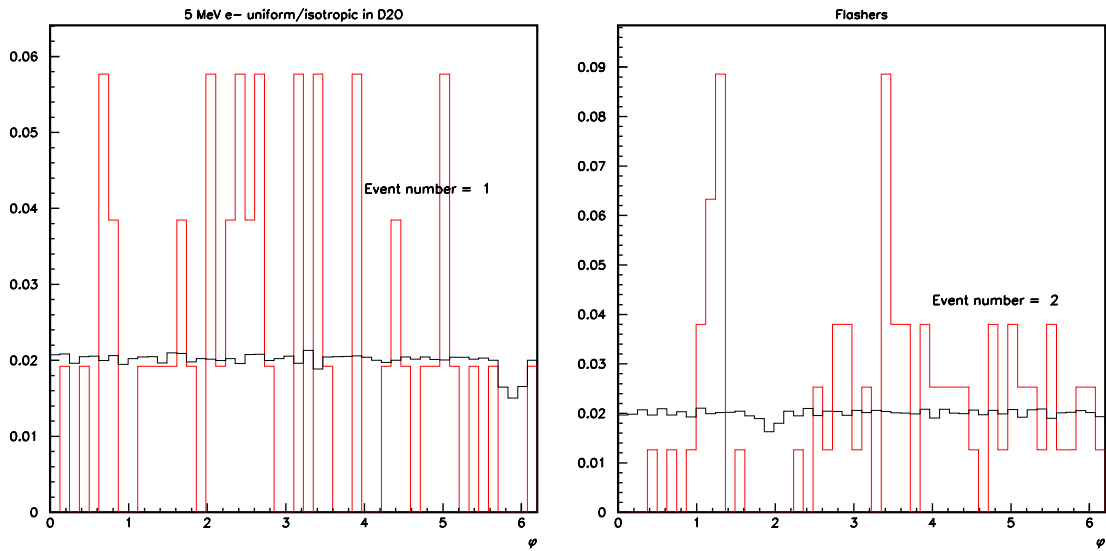


Figure 4.11: Example of azimuthal symmetry KS test for fit quality applied to (a) a 5 MeV MC electron and (b) a PMT flasher event. The solid line intersecting the y-axis near 0.02 is the  $\psi$  distribution for all PMTs relative to the fit position. The dip in the distribution is from the missing PMTs in the neck region. The other distribution corresponds to the hit PMT only. The KS probability for the hit PMT distribution to be drawn from a uniform distribution is calculated to be 0.7 for the MC electron event and 0.03 for the flasher event.

angular KS probabilities of 0.4 and  $10^{-5}$ , respectively.

The angular GOF tests have different strengths and weaknesses. The azimuthal symmetry test hinges on a simple assumption about the symmetry of Cerenkov light and should be relatively independent of electron energy. However, it does not take into account PMT solid angle effects (although this could be put in) which breaks the azimuthal symmetry of the PMT hits even from a symmetric photon distribution. This only becomes a problem near the PSUP, as the effects of PMT solid angle on the symmetry of the hit PMT distribution are small inside the D<sub>2</sub>O. On the other hand, the 2-D angular test includes PMT solid angle and in some sense is a generalization of the azimuthal symmetry test, so one might expect this test to have a smaller radial bias. The downside of the 2-D angular test, aside from the longer time it takes to perform the test due to the extra dimension in the KS test, is that the polar distribution depends on energy due to differences in the electron scattering.

An elaborate time KS test is implemented in SNOMAN along with the two angular tests just described. The time test involves calculating the expected PMT time spectrum after a fit and comparing this to the observed hit PMT time in the event. This calculation involves the direct light PDF and the reflected times computed by the specular reflection code discussed in Appendix A (scattering could be included as well). The performance of the time test were disappointing at best. This is not really unexpected. It is one thing to fit under simplifying assumptions about late light, but it is another thing altogether to test the quality of a fit based on these assumptions if they are not a particularly good model. Its possible that when further knowledge of late light is determined in SNO in the future such a test might be made useful, but for now use of this test is not recommended. In practice, one is better off using a more “blunt” test for consistency with Cerenkov light such as the fractional number

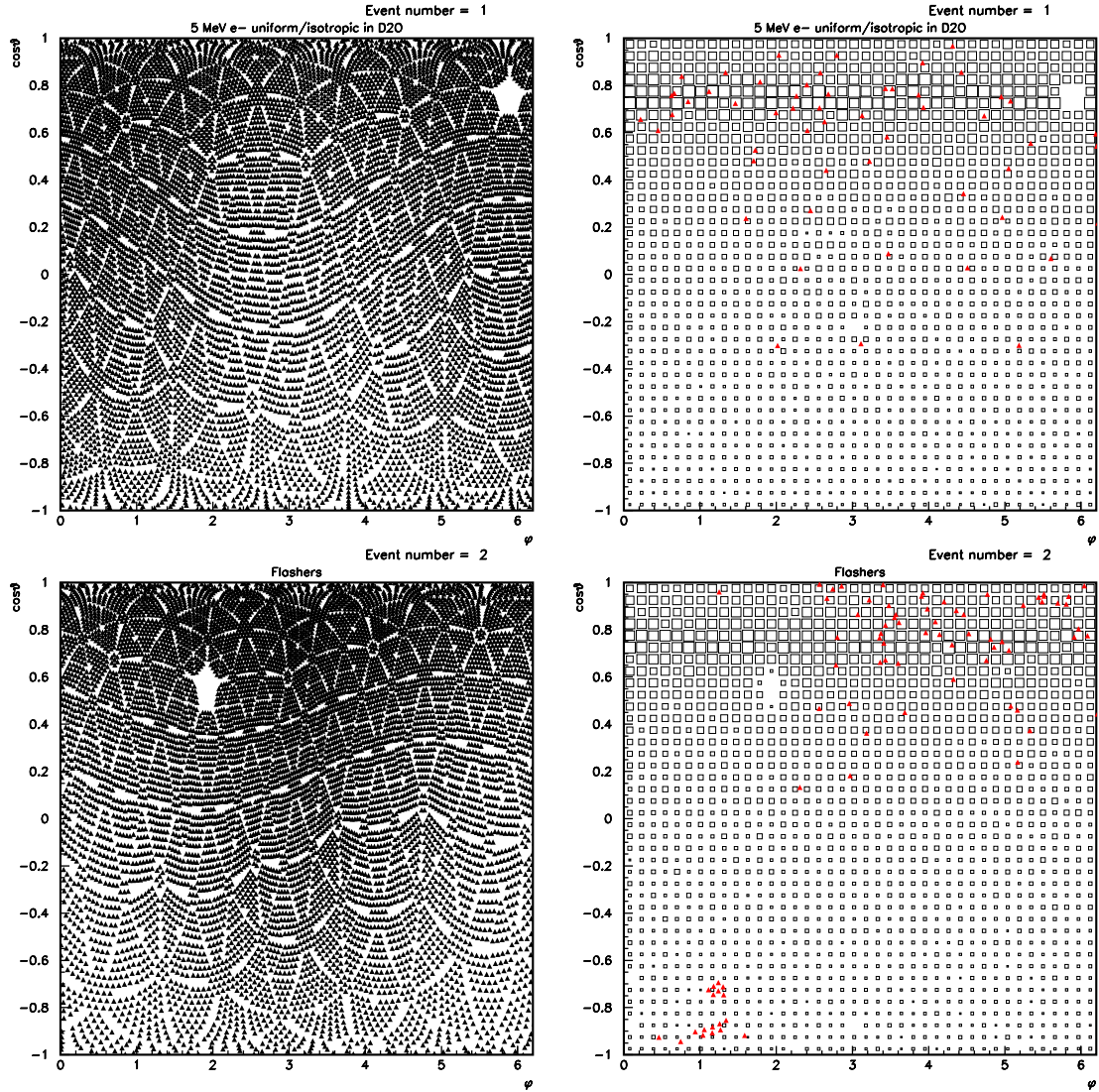


Figure 4.12: Example of 2D angular distribution KS test for fit quality applied to (top) a 5 MeV MC electron and (bottom) a PMT flasher event. The two plots on the left show the  $\cos \alpha$  and  $\psi$  of each PMT in the detector as viewed at the fit position. Notice the missing PMTs in the neck region and the solid angle effects which cluster and make sparse certain tubes. The right plots are box plots of the 2D PMT probability distributions for each event. Notice that maximum probability (largest boxes) is at the Cerenkov angle and azimuthal probability is essentially uniform. The MC and flasher events have 2D angular KS probabilities of 0.4 and  $10^{-5}$ , respectively.

of hits inside a prompt time window, like the ITR variable [48] developed by Vadim Rusu.

#### 4.3.6 Performance

In this section, performance of the Path Fitter vertex and angular reconstruction on signal MC is presented, which some comparison made to the Grid, Elastic and Time Fitters. Much work on Path Fitter characterization has been done, looking at performance on MC, calibration sources, and various types of instrumental backgrounds. Fitter performance on calibration data that are relevant to the analysis in this thesis will be presented in Section 5.5, however this section serves to give the reader a feeling for how the Path Fitter performs on MC relative to the other standard fitters.

##### Vertex Reconstruction

In this section, vertex reconstruction performance of the Path Fitter is compared to the Time and Grid Fitters. Comparisons based on vertex reconstruction characteristics of simulated CC electrons generated uniformly inside the D<sub>2</sub>O and isotropic in direction are presented.

Figure 4.13 shows the fit residual distribution along the x-axis for Time, Grid, and Path Fitters. Fit residual distributions for y and z are essentially identical to Figure 4.13. Notice that the Path Fitter has smaller tails than either of the other fitters and is narrower in width (resolution), which can also be seen in the distributions shown in Figure 4.14 of  $R_{dev}$ , the fit distance from the generated position.

Recall from the discussion in Sections 4.3.2 and 4.3.4 about fitter drive that most fitters - including the Path Fitter - possess a systematic pull of fit position in the

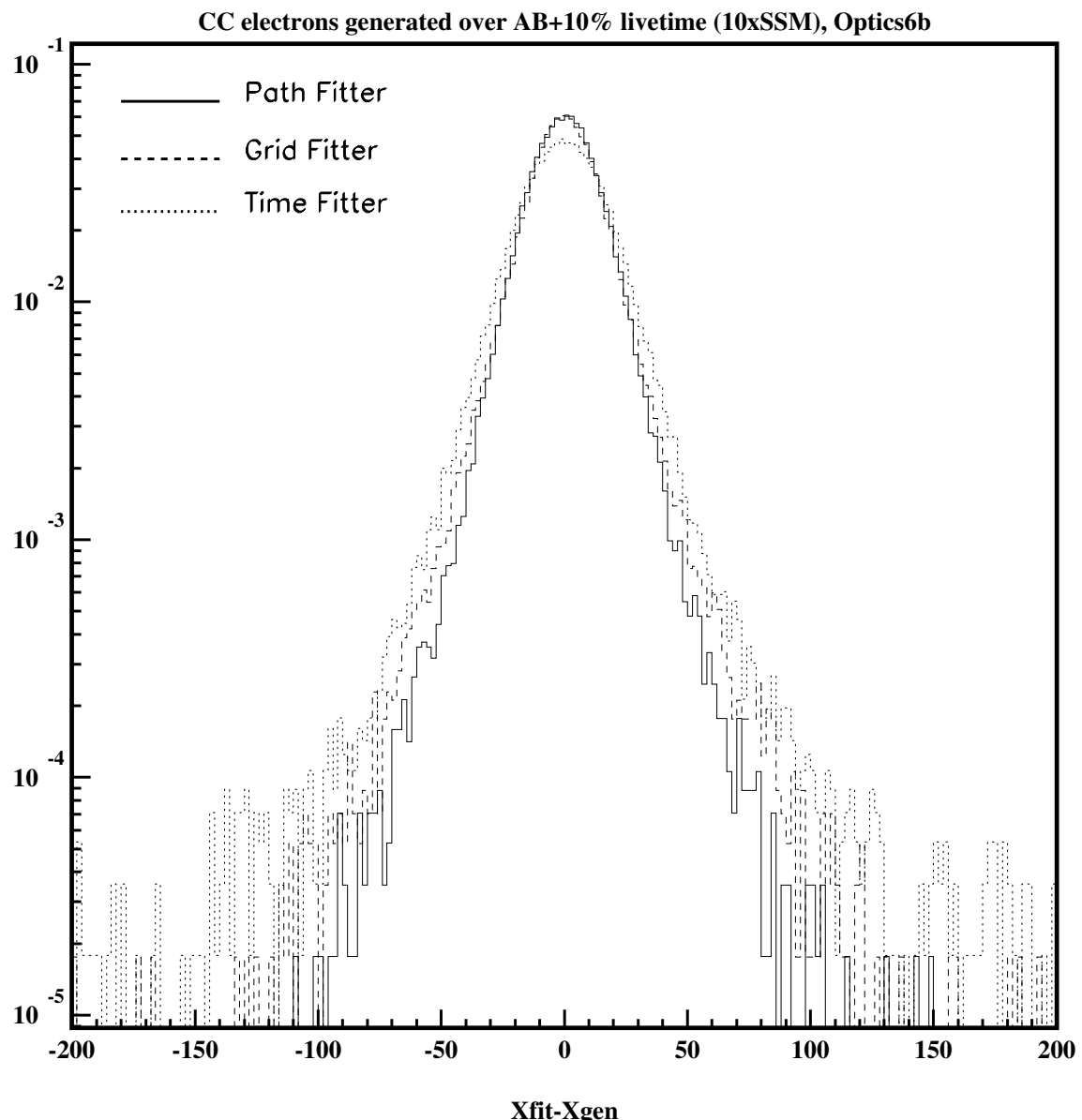


Figure 4.13: Distribution of  $x_{fit}$  residuals for CC electrons generated uniformly inside the D<sub>2</sub>O and isotropic in direction. Shown are the distributions for Path, Grid, and Time Fitters.

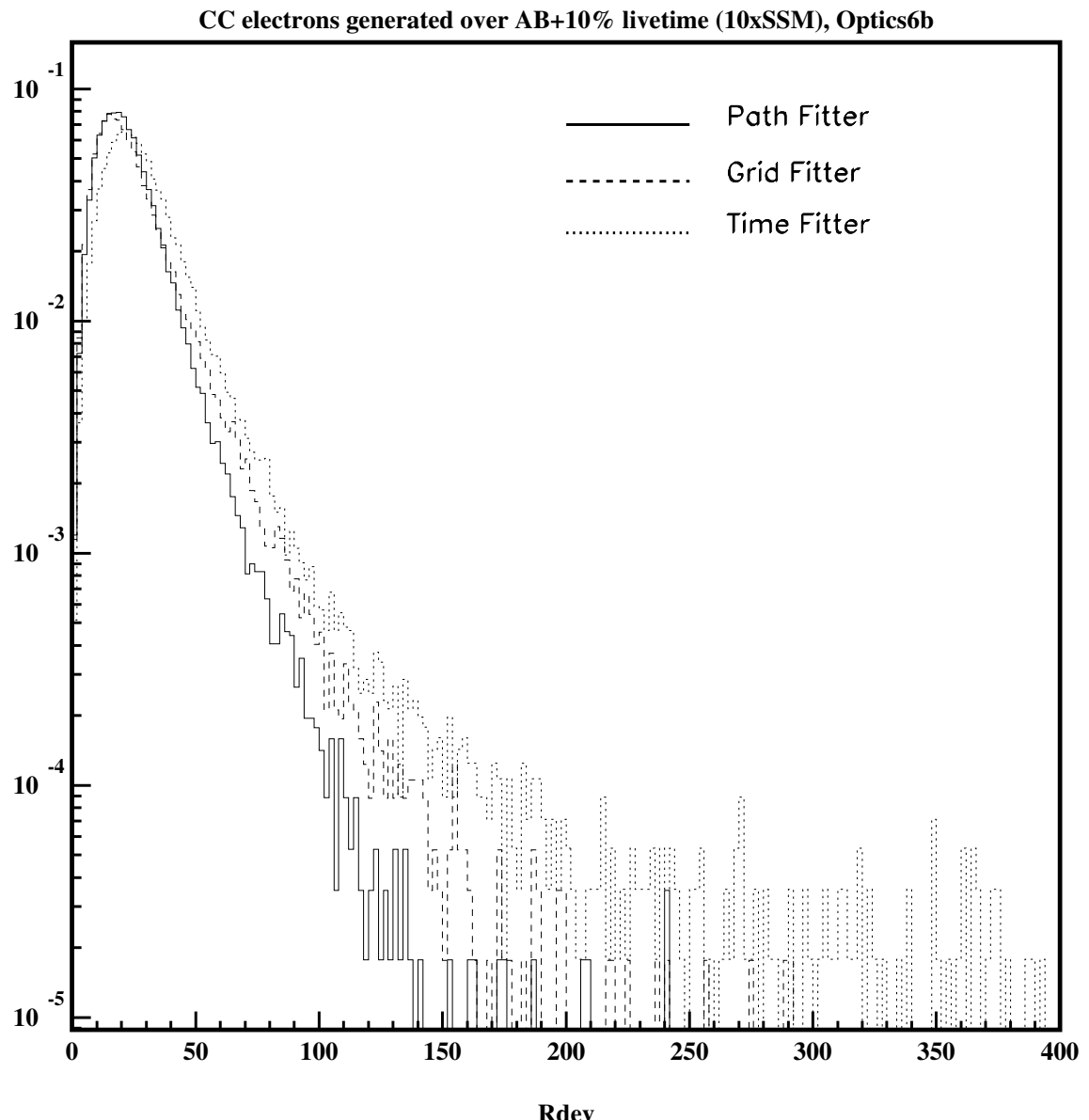


Figure 4.14:  $R_{dev}$  distribution for CC electrons generated uniformly inside the D<sub>2</sub>O and isotropic in direction.  $R_{dev}$  is the fit distance from the true MC position. Shown are the distributions for Path, Grid, and Time Fitters.

	Time Fitter	Grid Fitter	Path Fitter
X resolution (cm, Gaussian Fit)	$17.59 \pm 0.07$	$14.19 \pm 0.06$	$13.87 \pm 0.05$
X Raw $\sigma$ (cm)	21.06	17.00	15.17
Y resolution (cm, Gaussian Fit)	$17.64 \pm 0.07$	$14.22 \pm 0.06$	$13.87 \pm 0.05$
Y Raw $\sigma$ (cm)	21.18	17.12	15.22
Z resolution (cm, Gaussian Fit)	$17.50 \pm 0.07$	$14.17 \pm 0.06$	$13.96 \pm 0.05$
Z Raw $\sigma$ (cm)	20.81	16.90	15.20
$R_{dev}$ peak position (cm)	21	15	15
$R_{dev}$ mean (cm)	30.22	24.43	22.85
$R_{dev}$ $\sigma$ (cm)	22.34	16.59	13.11
Drive mean (cm)	6.41	8.50	0.45
Drive sigma (cm)	27.51	22.37	19.85

Table 4.1: Summary of vertex reconstruction performance comparisons for CC electrons generated uniformly inside the D<sub>2</sub>O and isotropic in direction.

direction of the initial electron direction. Section 4.3.4, in particular, discussed how the Path Fitter can be instructed to apply an empirical MC-based correction for this drive. Figure 4.15 shows drive distributions for the three different fitters. It is evident that while the other fitters possess this systematic pull, the correction has removed this systematic effect from the Path Fitter (according to MC). Also, notice that with the Path Fitter the drive distribution is narrower overall.

Since the drive correction was determined based on MC studies, one may wonder how sensitive the Path Fitter drive is to changes in the optical model in the MC. For example, is the correction fine-tuned to the particular amount of scattering in the MC at the time that the drive was studied? The Path Fitter drive is actually quite robust to large changes in scattering, as Figure 4.16 demonstrates with so-called “extreme” optical parameter sets to be described in Section 5.3.

Vertex reconstruction performance is summarized in Table 4.1.

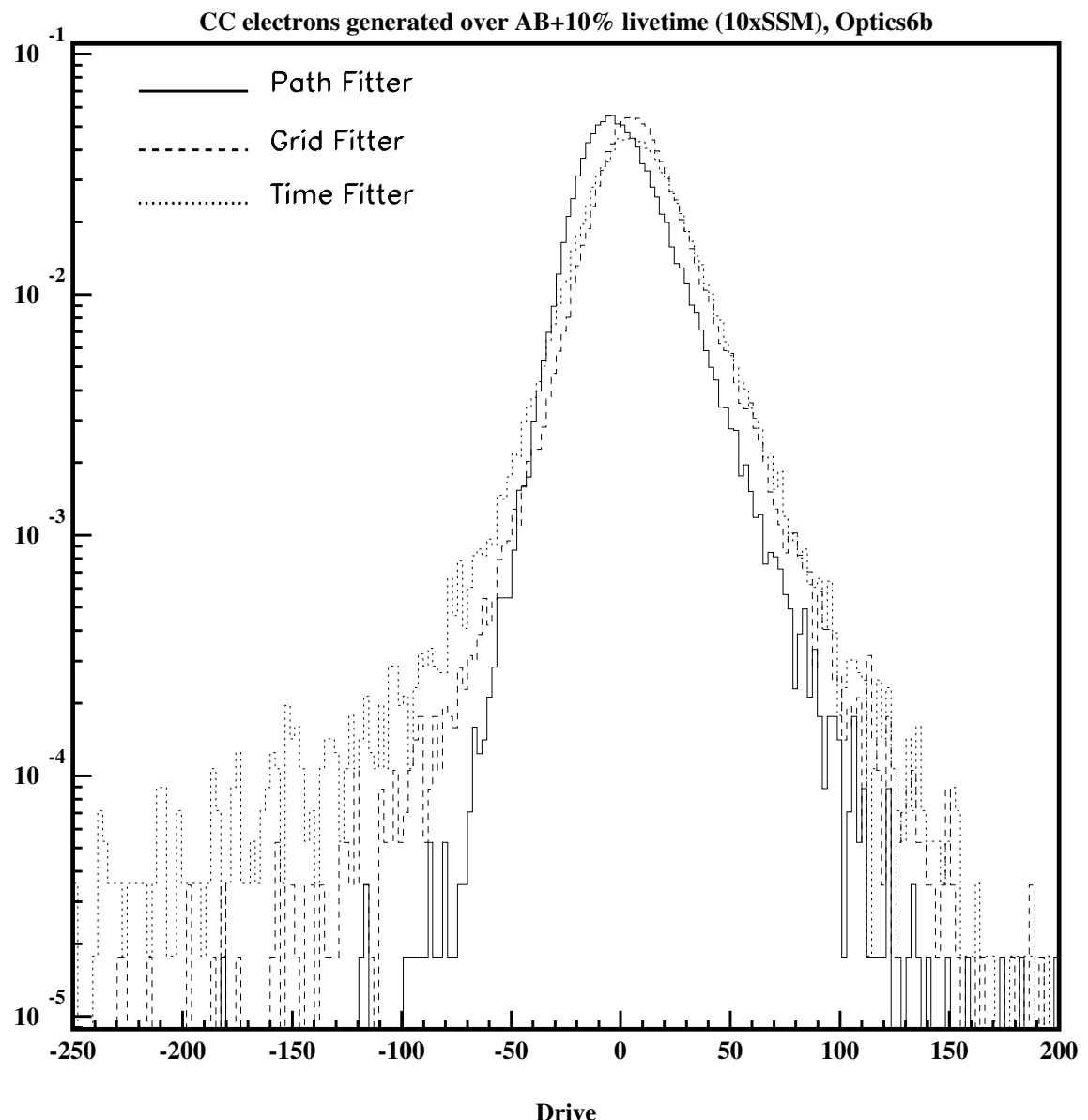


Figure 4.15: Comparison of drive for CC electrons generated uniformly inside the D<sub>2</sub>O and isotropic in direction. Shown are the distributions for Path, Grid, and Time Fitters.

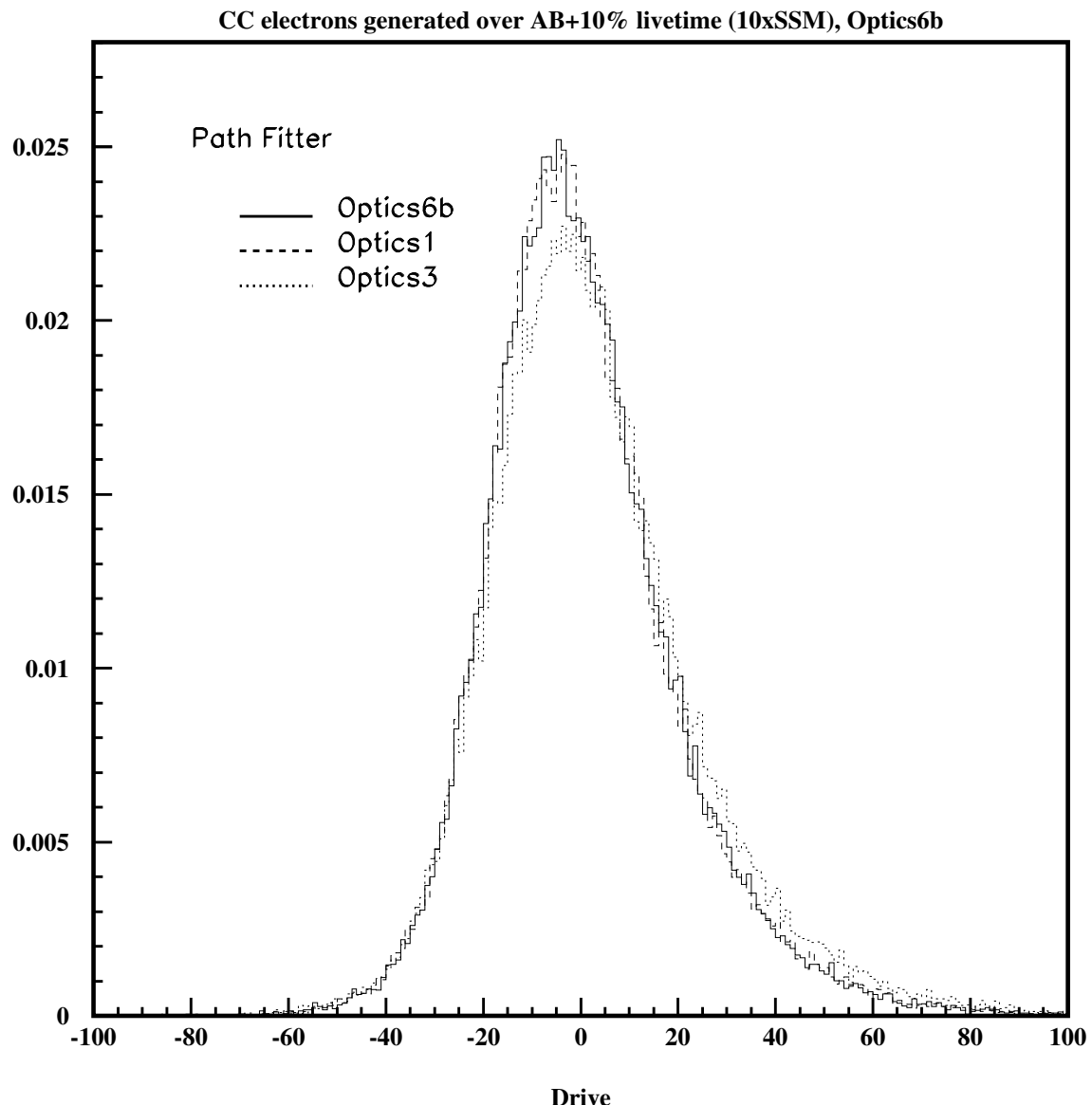


Figure 4.16: Sensitivity of Path Fitter drive to scattering in the MC, via “extreme” optical parameter sets. Optics 1 and 3 are believed to represent best and worst case scattering in the detector. Optics 6b incorporates the current best measurements from the optical calibration program.

## Angular Reconstruction

In this section, the angular reconstruction performance of the Path Fitter on MC CC and ES electrons is presented, with comparisons made to the Elastic Fitter. The direction “fit” returned by the Time Fitter is simply the mean PMT vector relative to the fit position. As a result, the angular reconstruction quality is poor and therefore comparisons are not all that useful. The “Improved” Grid Fitter [39] has the capability of doing a separate fit for direction after the vertex is determined, but this feature has not been tested in the analysis comprising this thesis. It is believed that the angular reconstruction performance is quite similar to the Elastic Fitter, so comparison to the Elastic Fitter should suffice until direct comparisons can be made.

Figure 4.17 shows a comparison between the Path and Elastic Fitters for reconstruction quality of the initial CC electron direction. Specifically, this shows distributions of the cosine of the angle between the fit direction and initial direction of the MC CC electron for the different fitters, shown on both a linear and log scale so one can see the tails. Note that angular reconstruction is quite similar for the two fitters, both in terms of the forward peak and the tails. However, one might argue from these plots that the Path Fitter is a bit sharper in the extreme forward part of the fit and that it also has a smaller tail of poorly reconstructed directions.

Figure 4.18 shows a plot similar to Figure 4.17, except this time for the  $\cos \theta_{\odot}$  distribution of MC ES electrons. In this case, it looks like the Elastic Fitter puts slightly more events into the ES peak, while the Path Fitter shows a smaller tail on the ES  $\cos \theta_{\odot}$  distribution.

CC electrons generated over AB+10% livetime (10xSSM), Optics6b

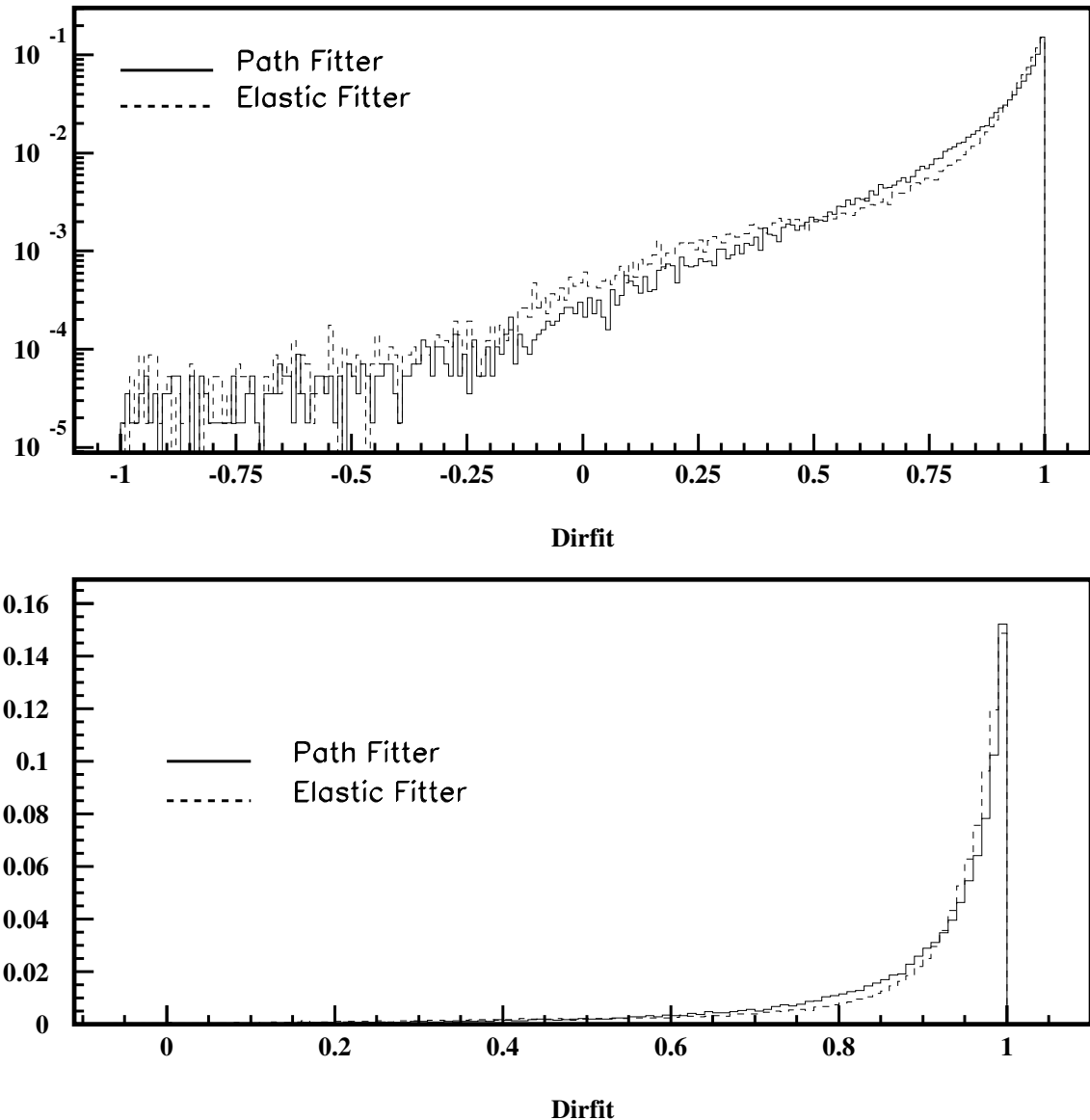


Figure 4.17: Distribution of the cosine of the angle between the fit direction and initial direction of the MC CC electron for the different fitters.

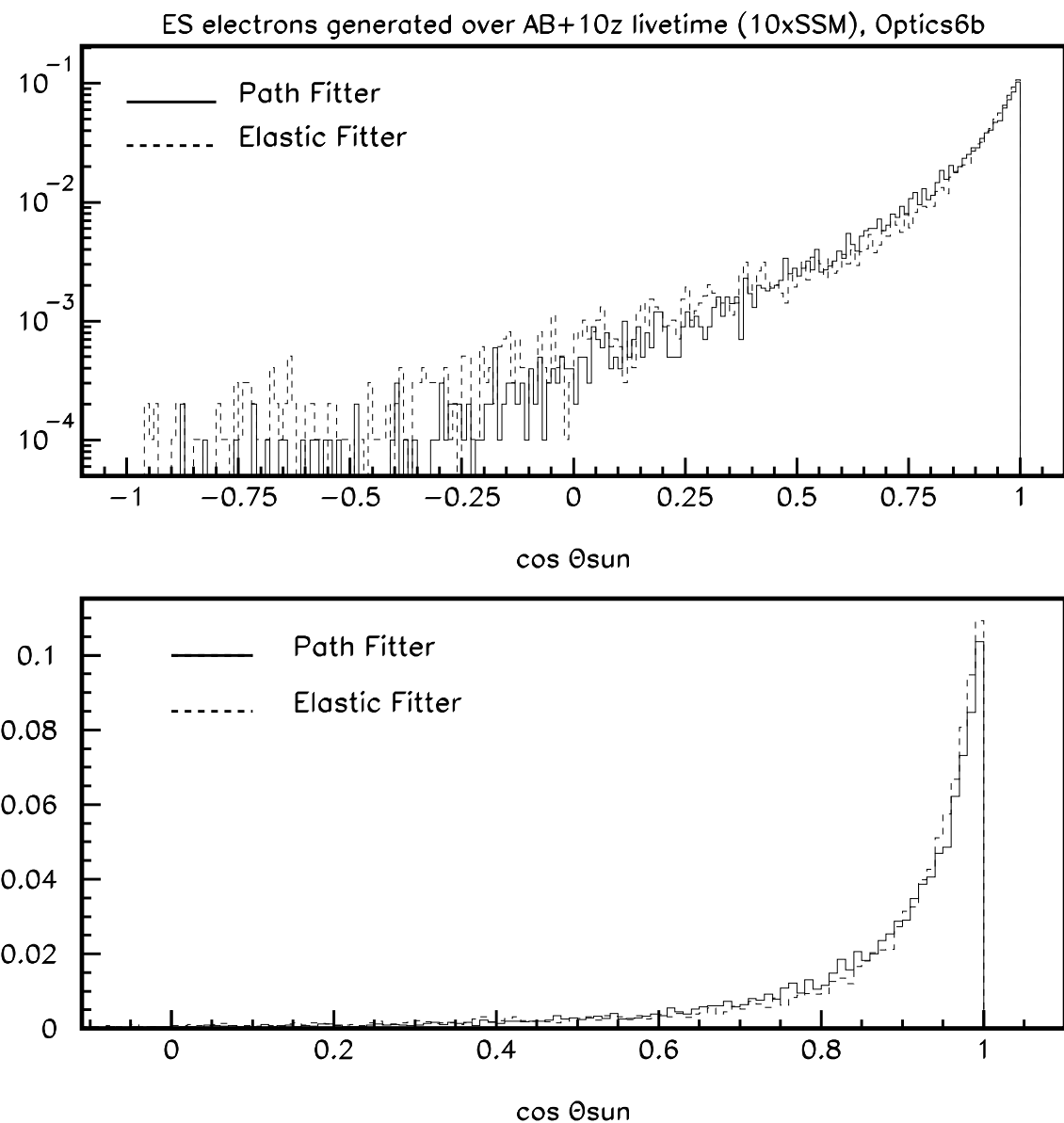


Figure 4.18:  $\cos \theta_{\odot}$  distribution of MC ES events for the different fitters.

## 4.4 Summary

In this chapter, standard reconstruction methods for use in solar neutrino analyses were discussed. This included a new maximum likelihood reconstruction method - the “Path Fitter” - which fits events by considering the relative probability of photon paths from a hypothesized electron source to each hit (and unhit, in principle) PMT in the event. Unlike other standard fitters, the Path Fitter uses both PMT time *and* angular information in *vertex* determination. This fitter has been shown to perform better on MC signal vertex reconstruction than all other fitters, with comparable or better direction reconstruction.

Perhaps the most important point, however, is not how well the Path Fitter currently performs but how much better it can yet be. It is strongly argued that the Path Fitter provides a strong foundation upon which to improve reconstruction in SNO. Although suggestions for such improvements have been hinted at in the text, an appendix (Appendix A) has been included which outlines some suggestions and contains some calculations related to simple toy models of the detector late light. As a more accurate and complete description of the detector is obtained in the future, the information gained can be naturally incorporated into the maximum likelihood framework of photon path probabilities.

# Chapter 5

## Detector Calibrations

In this chapter, calibration of the SNO detector for solar neutrino analyses is discussed. Thorough and accurate calibration of the detector is crucial to the success of an experiment like SNO where the signals of interest represent such a small fraction of the total data set. A poorly understood detector will degrade the quality of the measurements one is trying make and ultimately compromise the physics impact of the experiment. Even worse, a significant misunderstanding about how the detector responds to Cerenkov light can lead to improperly determined systematic errors or backgrounds which make the results simply wrong.

The first three sections present the low-level calibrations performed to convert channel ADC values into PMT hit times/charges and to measure optical properties of the detector. Sections 5.4 and 5.5 describe calibration of energy and reconstruction properties which enter into systematic errors more directly and at a higher level than channel, PMT, and optical calibrations since they themselves depend on these properties. Finally, measurement of the SNO trigger efficiency, for which the author held primary responsibility, is discussed in some detail in Section 5.6.

## 5.1 Electronics Calibrations

To properly interpret the digitized PMT information contained in the data stream, the front-end electronics described in Section 3.4 need to be calibrated. The hardware necessary to perform this electronics calibration (ECA) is contained within the system itself - that is, the trigger hardware previously described in Section 3.5.6. The ability to self-calibrate through DAQ control is one of the many nice features of the SNO electronics system.

Calibration of the front-end electronics consists of determining the baseline digitizations or “pedestals” for charge/time measurement - QHS, QHL, QLX, and TAC - and the TAC slopes (digitization/ns). Recall that each channel has 16 cells of analog storage and there are  $19 \text{ crates} \times 512 \text{ channels/crate} = 9728 \text{ channels}$  in the system. So, for example, there are 622,592 pedestal constants ( $9728 \text{ channels} \times 4 \text{ measurements/channel} \times 16 \text{ cells/per measurement}$ ) which need to be measured and stored for a given calibration.

Pedestal calibration is begun by instructing the trigger system to send “pedestal” and global trigger pulses to each front-end channel in the system. The channels are configured with “pedestal enable” to fire the discriminator when a pedestal pulse is received, independent of the charge on its input. The resulting data is collected and the pedestal digitization distributions are used to generate constants for each cell.

Time slope calibrations proceed in the same way, except that the time delay between pedestal and GT pulses is swept through a controlled range of times. Recall from Section 3.5.6 that the trigger system can deliver these pulses with sub-nanosecond timing accuracy, so the TAC slope can be very accurately determined. The resulting digitization values for each time delay are stored and used to calibrate

the channel timing by interpolation between the measurements.

See [49] for a complete description of generation and use of ECA constants.

### 5.1.1 Validation Information

In addition to generation of ECA constants, much recent work [49] has been done to provide information about the quality of the constants put into the database for use by the collaboration. There is a status word for each channel that contains information which can be used to validate the calibration of neutrino (or other) data based on the performance of channels during the most recent ECA runs. For example, if a channel had an abnormally wide pedestal distribution during the previous ECA or the mean value changed significantly between the previous two ECA runs, a bit is set in each case indicating the channel calibration may be suspect.

While this information is expected to be extremely useful in future SNO analyses, the information is in the process of being generated and the best way to use this information is still being determined. Therefore, ECA validation banks are not used in this thesis. The number of bad calibrations appears to be small enough as to not have a large effect the results, however this should be verified in future work.

### 5.1.2 Time-Since-Last-Hit (TSLH) Correction

It was discovered that the quality of neutrino data vertex reconstruction (based on Time Fitter  $\chi^2_{fit}$ ) was poor relative to reconstruction of high rate ( $\sim 100$  Hz)  $\gamma$ -ray ( $^{16}\text{N}$ ) source data. Subsequent study of this effect uncovered a rate dependence where the recorded TAC value for a given channel hit relative to the global trigger depends on the time since it was last hit (TSLH) and received a global trigger. The shift

in recorded TAC as function of TSLH can be mapped out for each channel using pedestal calibration data (see Section 5.1) taken at different repetition rates. This mapping is used as an additional channel calibration applied to all hit PMT times. The calibration adjusts the channel times using this mapping and stored information about the time each channel was last hit and recorded an event. Full documentation of this calibration - often referred to as the “HCA” calibration - will be available in the near future [50].

## 5.2 PMT Calibrations

Phototube calibrations (PCA) are performed to characterize the response of each PMT to Cerenkov light in both time and charge. Diffused laser light from a  $^2\text{N}$ -dye laser system [24,51] is used for PCA calibration. The laser and diffuser system - called the “laserball” system - can deliver  $< 1$  ns width pulses of adjustable monochromatic light at a repetition rate of up to  $\sim 40$  Hz.

There are several components to the PMT timing calibration. The first is a slew correction (sometimes referred to as walk) for the PMT hit time. This is due to the fact that time recorded by the channel is the time relative to threshold crossing on the PMT charge pulse and therefore different amplitude PMT pulses will record different times even if the photon struck the photocathode at exactly the same time. A correction for this effect can be made for each channel through calibration of the correlation between TAC and QHS charge. The PCA calibration also determines the relative transit time delay and spread for each PMT. Different transit time delays between PMTs are due to variations in cable lengths, electronic trace delays, and capacitances in electronics components and traces. This is calibrated by placing the

laserball at the center of the detector and looking for residual time difference between PMT times after the walk correction has been applied. The PMT time jitter is determined again from laserball data at the center and looking at the distribution of PMT times for each PMT over many laser triggers. This jitter is measured to be  $\sim 1.6$  ns on average. In addition to the laserball, it has also been measured using a sonoluminescent source developed at Penn by Doug McDonald [29].

In addition to PMT timing calibrations, the PCA provides a calibration of the relative gain of the tubes. The laser system can adjust the amplitude of the light output in a controlled way so that the charge slope can be determined (integrated charge  $\rightarrow$  photoelectrons). In this way, multi-photoelectron effects can be studied as well<sup>1</sup>.

### 5.3 Optical Calibrations

Proper calibration of detector optical properties is critical for solar neutrino analyses in SNO. Optical effects such as attenuation, scattering, and reflections directly affect energy and reconstruction response. Ideally, one would like to determine these bulk properties for each relevant medium in the detector ( $D_2O$ ,  $H_2O$ , acrylic vessel panels, PMT glass) as a function of wavelength since Cerenkov light is broad-band (recall Section 4.3.1). The results of these calibrations are then used within SNOMAN as a model of the optical properties to simulate the detector response to Cerenkov light.

The approach currently taken in SNO is to make *in situ* measurements of the  $D_2O$  and combined  $H_2O +$ acrylic extinction lengths,  $\lambda_{D_2O}$  and  $\lambda_{H_2O+acr}$ , respectively,

---

<sup>1</sup>For example, since the channel fires on the *earliest* threshold crossing, the recorded time get earlier on average as light produces more photoelectrons in the PMT.

at several wavelengths between 337 nm and 620 nm by scanning the laserball source through the D<sub>2</sub>O region. These extinction lengths are measured by analyzing how the event occupancies (i.e. the relative number of hit PMTs) within a narrow time window change as a function of source position. The time window is used to exclude a large fraction of hits that are not from prompt photons, but rather from scattering or reflections. Of course small angle scattered light can still be present in any time window, so one needs to demonstrate robustness to changes in this window. It appears through these studies that a modification of the PMT+concentrator angular response from *ex-situ* measurements is required to get a good fit to the laserball data. A global fit to the laserball data is used to extract  $\lambda_{D_2O}$ ,  $\lambda_{H_2O+acr}$ , and parameters characterizing the PMT angular response<sup>2</sup>.

The most recent results of these studies and details regarding the analysis methods can be found in [52].

### 5.3.1 Optical Model Used in this Thesis

The optical model used in this thesis as part of the detector simulation is based on optical constants generated by Bryce Moffat at Queens University in January 2001 along with a modification of the full 3D PMT simulation by Kate Frame at Oxford University to include the Moffat PMT angular response results. The optical constants are derived using a PMT model which makes no attempt at getting late light (i.e. reflections) correct but should be an accurate model of prompt light. The approach is then to use this prompt light angular response in the more realistic 3D PMT model for reflections and photons propagating in the PMTs. This optical model

---

<sup>2</sup>The angular distribution of the laserball light is not completely isotropic, so a parameterization of this response is fit out as well.

also incorporates additional components of the detector geometry available in the Monte Carlo that have consequences for energy and reconstruction such as the AV belly plates and acrylic panels/bonds. The scattering used in the model is what one expects for simple Rayleigh scattering in the various media.

### 5.3.2 Alternative “Extreme” Optical Parameter Sets

The optical model described in Section 5.3.1, referred to as “Optics 6b” for historical reasons, represents the most up-to-date results from optical calibration at the time the analysis was performed for this thesis. The optical measurements comprising this model did not have finalized uncertainties and were not fully reviewed by the collaboration, therefore no systematic uncertainties due to these parameters could be credibly assigned. As a result, a different approach to estimating the effect of our lack of knowledge of the optics has been taken, which is to determine the *sensitivity* of our results to presumed *extreme* ranges in the optical constants. In particular, several sets of alternate parameter sets have been developed by Steve Biller at Oxford University and Scott Oser at Penn for this purpose. These sets, designed to probe the sensitivity of energy and reconstruction characteristics to a few presumed best and worse case scenarios in terms of attenuation and scattering, are described below:

- “Optics 1”: No attenuation and nominal Rayleigh scattering in  $D_2O$ ;  $H_2O$  has nominal Rayleigh scattering and the attenuation length is 50 m at each wavelength, or the default attenuation length, whichever is shorter.
- “Optics 2”:  $D_2O$  has 50 m attenuation length at all wavelengths and nominal Rayleigh scattering;  $H_2O$  has default attenuation with 3 times nominal Rayleigh scattering.

- “Optics 3”: No attenuation and 3 times nominal Rayleigh scattering in  $D_2O$ ;  
 $H_2O$  has default attenuation with 3 times nominal Rayleigh scattering.

For example, Optics 1 and Optics 3 are designed to represent best and worst cases for reconstruction.

The approach taken to use of the alternative optics is to probe the sensitivity of our ability to model the detector by studying the agreement of these models with calibration data. Ideally, one would also like to probe the sensitivity of model predictions in the places that lack calibration data, noting that the primary purpose of the Monte Carlo is to interpolate and, if need be, extrapolate the detector response away from calibration data points (energy, position, etc). If the variation in model predictions over presumed extreme optical conditions is smaller than actual variations observed in calibration data, one could confidently conclude that contributions from these uncertainties are small compared to other uncertainties present in the measurements. If this is not the case, it indicates a degree of sensitivity to these uncertainties which implies that the optics need to be better understood before proceeding unless analysis techniques that reduce this sensitivity are developed.

## 5.4 Energy Calibrations

In this section, energy calibrations relevant for this analysis are presented. Energy calibration is one of the most important calibrations for solar neutrino analyses in a water Cerenkov experiment because one ultimately needs to apply an energy threshold cut to move away from radioactive backgrounds that dominate at low energy. Lack of knowledge of the detector energy response will cause one to overestimate or un-

Name	Primary Source	Relevant Reaction	Triggered?
$^{16}\text{N}$	6.13 MeV $\gamma$ s	$^{16}\text{N} \rightarrow ^{16}\text{O}^* + \beta^- + \bar{\nu}_e$ , $^{16}\text{O}^* \rightarrow ^{16}\text{O} + \gamma$	x
$^{252}\text{Cf}$	neutrons	$^{252}\text{Cf} \rightarrow$ fission fragments + neutrons	
$^8\text{Li}$	$\beta^-$ (13 MeV endpoint)	$^8\text{Li} \rightarrow ^8\text{Be}^* + \beta^- + \bar{\nu}_e$ , $^8\text{Be}^* \rightarrow 2\alpha$	x
pT	19.8 MeV $\gamma$ s	$^3\text{H}(\text{p},\gamma)^4\text{He}$	

Table 5.1: Sources used for Energy Calibration in SNO.

derestimate the number of neutrino events one expects above the analysis threshold<sup>3</sup>, for example.

The approach to energy calibration is to measure the detector response to Cerenkov light in as many places and at as many energies as possible. The sources used for energy calibration are summarized in Table 5.1 and discussed in more detail in this section. For the analyses upon which this thesis is based, measurements are made relative to Monte Carlo predictions for the neutrino signals of interest (e.g. CC events from  $^8\text{B}$  neutrinos). This approach will be described in more detail in Chapter 8. Therefore, systematic errors enter into the analysis as discrepancies between Monte Carlo model predictions and calibration data. This section demonstrates the level at which the Monte Carlo energy response agrees with calibration source data. Analogous comparisons for reconstruction characteristics will be made in Section 5.5.

### 5.4.1 $N_{\text{Hit}}$ as Primary Energy Variable

From an energy standpoint, the detector responds to Cerenkov light by recording a certain amount of integrated PMT charge. At energies relevant for solar neutrinos interacting inside the  $\text{D}_2\text{O}$  region, the vast majority of PMTs involved in an event are

---

<sup>3</sup>Systematic energy uncertainties also effect the *shapes* of distributions used to extract signals, but this is often sub-dominant to acceptance errors when cuts are imposed.

hit by a single photon of light. Therefore, to good approximation one can consider a simple count of the number of hit PMTs in an event ( $N_{\text{Hit}}$ ) as an energy estimator for the relativistic charged particle initiating the event since the number of produced Cerenkov photons is proportional to the particle energy<sup>4</sup>.

### RSP versus Forward-fitting Approach

In actuality,  $N_{\text{Hit}}$  is a rather poor estimator of electron energy. This is because  $N_{\text{Hit}}$  depends not just on electron energy but also depends on the position and direction of a given electron in the detector. The *way* in which the  $N_{\text{Hit}}$  distribution changes is in principle calculable if one knows the *actual* position and direction of the source, detector optics, and PMT response. For given event, the position and direction are *estimated* through reconstruction, so effects which change the  $N_{\text{Hit}}$  distribution of events with this location and direction from some normalizing point - say, the center of the detector - can be removed. Once these position and direction dependent effects on the  $N_{\text{Hit}}$  distribution have been removed, the energy of the event is estimated using a Monte Carlo derived scaling relation between energy and  $N_{\text{Hit}}$  for electrons at the center of the detector. This procedure (called “RSP” in SNO) then gives the most likely electron energy for an event with the *observed*  $N_{\text{Hit}}$ <sup>5</sup> and *estimated* position and direction in the detector.

This method of estimating electron energy on an event-by-event basis has the desirable feature of reporting the data in terms of energy which is convenient for

---

<sup>4</sup>This relation is actually quite linear away from Cerenkov threshold and up to the point where multi-photon effects of significant due to the linear relation with track length (recall Section 4.3.1, Equation 4.6).

<sup>5</sup>To be more precise, RSP operates on the number of hit PMTs within a prompt time window, corrected for PMT noise rather than total  $N_{\text{Hit}}$ . Only channels considered to be giving reliable time and charges are considered. See [53] for a complete description.

others in the physics community to interpret. This is because (aside from energy resolution) it removes the complicated response function of the detector - the details of which are typically only at the disposal of the experimentalists themselves. But does this approach produce the best results for neutrino hypothesis testing? In other words, if we already have some knowledge of the detector response (which is required for the aforementioned procedure), is a particular neutrino hypothesis (e.g. neutrino oscillations) better tested by first removing this response from the data and then using expected electron energy distributions in extracting signals (RSP approach) or fitting the data after this response is folded in with the expected electron energy distributions (“forward fitting” approach)?

In RSP, one is assigning an event energy based (partly) on its reconstructed position and direction. Reconstruction is not perfect, however, so one needs to consider what happens to events that are very poorly reconstructed. In the RSP approach, these events will be assigned the *wrong* energy even if the response function is perfect, and subsequently can be assigned the wrong signal type (e.g. CC  $\Leftrightarrow$  ES) upon applying signal extraction. In the forward fitting approach, the detector response function from the full Monte Carlo is convolved with position and direction distribution of events to generate PDFs used to fit the data. If a single PDF in reconstructed radius ( $R_{fit}^3$ ), direction ( $\cos \theta_{\odot}$ ), and  $N_{\text{Hit}}$  possessing all the correlations between these variables is used for each signal type to extract signals from the data, then the same problems with reconstruction tails inherent to RSP fitting will exist for the forward-fitting approach for identical response functions. This is because a poorly reconstructed event will be given the wrong joint probability of having the observed  $N_{\text{Hit}}$ , and therefore events can be mis-assigned in the same way by the signal extraction process.

These effects can be eliminated in the forward-fitting approach by factorizing the PDF into a product of the individual PDFs, effectively averaging over correlations in the MC-derived response at the true electron positions. Therefore, the probability of having an observed  $N_{\text{Hit}}$  in the data is unaltered by the reconstructed position or direction. Of course, information is thrown away in the averaging process and it remains a quantitative question as to whether better results are obtained by including the extra information contained in the correlations or averaging out this information to reduce the bad effects of mis-reconstruction tails. Some of these issues are raised again in Chapter 8 in the context of signal extraction. The forward-fitting approach using factorized PDFs in  $N_{\text{Hit}}$ ,  $R^3$ , and  $\cos \theta_{\odot}$  is used for the analysis presented in this thesis.

### **Total versus Prompt $N_{\text{Hit}}$**

For the analysis upon which this thesis is based, the energy variable used to extract signal events is total  $N_{\text{Hit}}$ . It was previously mentioned that  $N_{\text{Hit}}$  is a poor energy *estimator*, so this may seem contradictory. However,  $N_{\text{Hit}}$  is not used to estimate the energy of a given event or even an energy distribution, but rather is used in extracting signals as a variable related to electron energy. The Monte Carlo is used to generate the expected  $N_{\text{Hit}}$  distribution by convolving a given signal spectrum (e.g. electrons from SSM  ${}^8\text{B}$  neutrinos interacting uniformly within the detector volume) with a detailed model of the detector response. This  $N_{\text{Hit}}$  distribution used as a PDF in signal extraction is then the proper distribution underlying the signal events in the data if the Monte Carlo contains an accurate description of the detector response<sup>6</sup>. The actual level of agreement is sampled at different energies and positions with the

---

<sup>6</sup>and physics underlying neutrino interactions and Cerenkov light generation.

various calibration sources at SNO’s disposal.

It may seem dangerous to use *total*  $N_{\text{Hit}}$  as a energy variable given that only *prompt* light optical properties have been calibrated (recall Section 5.3). Why not then use prompt  $N_{\text{Hit}}$  instead, as the optically calibrated Monte Carlo is bound to be a better model of prompt  $N_{\text{Hit}}$  than total  $N_{\text{Hit}}$ . This is certainly true, however, prompt  $N_{\text{Hit}}$  has some shortcomings which make total  $N_{\text{Hit}}$  a more robust energy variable in the view of the author.

Recall from Section 5.3 that optical calibrations were restricted to looking at prompt light occupancies so that extinctions lengths and PMT angular response could be globally fit from the laserball calibration data. Contributions from late light components like reflections and scattering to the relative occupancy was minimized by only accepting hits within a time window placed around the prompt peak on the distance-corrected-time ( $\text{DCT} \equiv t_i - d/c$ , where  $t_i$  is a hit PMT time and  $d$  is the distance between the source and the PMT) distribution. The effects of placing this window (on various amounts of scattering, for example) can be studied in a fairly straightforward manner because the source position is known to reasonably high accuracy (few cm). The use of a similar prompt time window for neutrino data is not nearly as straightforward because the source position is not known but rather *estimated* through reconstruction. One cannot simply use the same prompt time window as was used for optical calibration and assume that energy response is well understood because the Monte Carlo prompt light model is correct. This is because late light and reconstructed position are inescapably interconnected - the same prompt light calibrated Monte Carlo will give different reconstructed vertex distributions for different late light optics. Therefore, *any prompt time cut on neutrino data will accept different amounts of direct, scattered, and reflected light for different amounts and/or*

*composition of late light.*

Using total  $N_{\text{Hit}}$  does not immunize one to the problems of changing detector optics, but rather it reduces the *sensitivity* of the energy variable to these changes over the use of prompt  $N_{\text{Hit}}$ . The use of a prompt time window introduces an additional correlation between reconstruction and energy above the position and direction dependence which already exists. It is argued that simply using the number of hits within the timing window imposed by the detector hardware ( $N_{\text{Hit}}$ ) as the primary energy variable - independent of reconstruction - is more robust than prompt  $N_{\text{Hit}}$ . These two approaches (total  $N_{\text{Hit}}$  and prompt  $N_{\text{Hit}}$ ) become equivalent for a sufficiently large prompt time window, of course.

### 5.4.2 Energy Scale and Resolution

In this section, uncertainties on energy scale and resolution using total  $N_{\text{Hit}}$  as the primary energy variable are presented. The energy scale in this analysis refers to the mean of a Gaussian fit to the  $N_{\text{Hit}}$  distribution resulting from an electron with a given position, direction, and energy in the detector. The standard deviation of this fit is referred to as energy resolution. If the detector response and Cerenkov light generation are correctly handled in the Monte Carlo, then one expects the MC energy scale to match the true energy scale in the detector. In practice, this agreement is only expected up to an overall scale factor to account for the absolute PMT and channel efficiencies which are difficult to model, so an overall scaling is applied to the MC to match calibrations at some radial position in the detector. After this overall scaling, it is expected that the energy, position, and direction dependence of energy scale should be well represented by the Monte Carlo if it represents a good model of

the detector. The degree to which this is true is tested by comparing calibration data to Monte Carlo simulation of the source deployed at various positions in the detector.

Figure 5.1 shows the Monte Carlo  $N_{\text{Hit}}$  distribution for a series of electron energies from 4-20 MeV. The electrons were generated uniformly inside the  $\text{D}_2\text{O}$  with isotropic directions. Figure 5.2 shows the Monte Carlo predictions for energy scale and resolution as a function of electron energy. It can be seen from these two figures that energy scale is a linear function of electron energy inside the  $\text{D}_2\text{O}$ , while energy resolution scales more like  $\sqrt{E}$  from Cerenkov photon statistics.

### Energy Scale Interpolation

As a refinement to the overall normalization procedure used to bring the Monte Carlo into agreement with calibration source data at one radial position, a method of energy scale interpolation has been developed by the author. The main idea is to use extensive scans of the detector with the  $^{16}\text{N}$   $\gamma$ -ray source to determine and subsequently correct for discrepancies between MC and observed energy scale. The scans are used to create a detector position grid for each of several direction bins<sup>7</sup> which contains the scale difference ( $\overline{N_{\text{Hit}}}^{MC} - \overline{N_{\text{Hit}}}^{data}$ ) at each grid point. The  $N_{\text{Hit}}$  of a given Monte Carlo event is adjusted based on the interpolated difference in scale determined from the neighboring grid points<sup>8</sup>, where the particular grid is chosen based on the reconstructed direction of the event. Scaling to energies away from the mean electron energy produced by the  $^{16}\text{N}$  6.13 MeV  $\gamma$  is performed under the assumption that the apparent scale discrepancies scale with the number of Cerenkov photons generated in the event relative to mean number generated by  $^{16}\text{N}$ . This is a

---

<sup>7</sup>The position and direction are determined from reconstruction.

<sup>8</sup>In practice, a bicubic spline function fit to the overall grid is used for this interpolation.

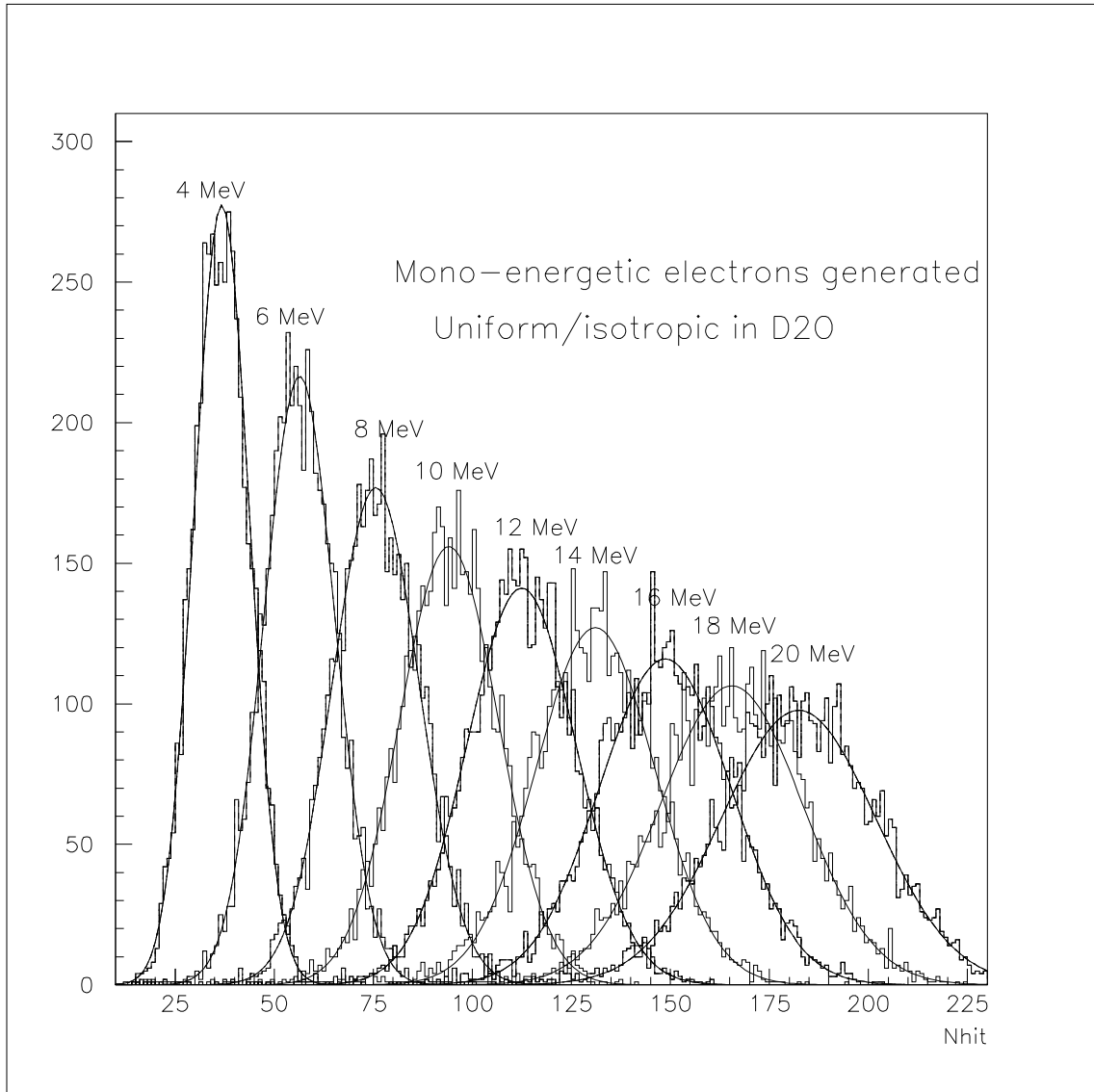


Figure 5.1: Monte Carlo  $N_{\text{Hit}}$  distribution for a series of electron energies from 4-20 MeV. The electrons were generated uniformly inside the D<sub>2</sub>O with isotropic directions.

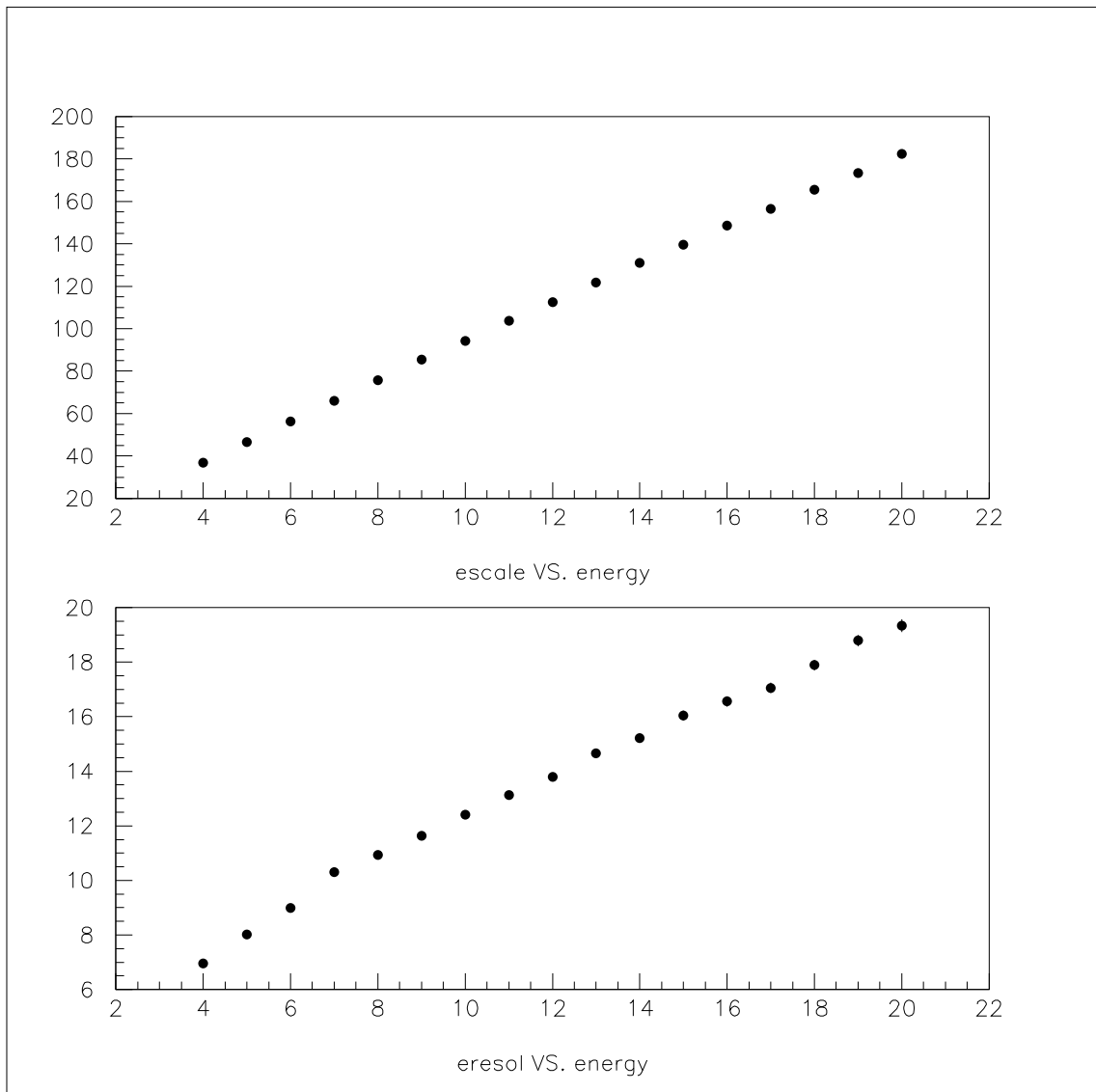


Figure 5.2: Monte Carlo predictions for (top) energy scale and (bottom) resolution as a function of electron energy.

valid assumption if the energy scale discrepancies are dominated by inaccuracies of the propagation and/or detection of light in the MC model. If, however, the discrepancies are unrelated to Cerenkov light (e.g. PMT noise, electronics noise/pickup) then this scaling is incorrect, although its hard to come up with anything but Cerenkov light-related sources of error which would have the observed position and direction dependence.

Energy scale interpolation is described in detail in Appendix B along with a discussion of performance on correcting the calibration data upon which it is based -  $^{16}\text{N}$  xz-plane scans taken in December 1999. The original motivation for using energy interpolation was to allow use of the alternate optical parameter sets described in Section 5.3.2 to probe the sensitivity of the final results to “extreme” ranges in the optical inputs to the Monte Carlo. Without energy interpolation, these sets would yield a large spread in the CC and ES flux results, for example. Given the discussion in Section 5.3.2 on the proper role of these optics sets in the analysis chain, it may seem that energy interpolation is not very useful. However, it is explicitly based on empirical calibration data, and as a result should significantly decrease the sensitivity of energy scale to optical uncertainties if the Monte Carlo model is not in gross error. In addition, even if the optical model is acceptably good in terms of energy scale, energy interpolation offer a refinement of the model to better agree with calibrations.

### **Energy Scale Stability Over Time**

In order to monitor the energy scale stability of the detector,  $^{16}\text{N}$  calibration runs at numerous times over our neutrino data livetime were taken at the center of the detector. The energy scales obtained in the data were compared to  $^{16}\text{N}$  source Monte Carlo generated at the center for each run. Figure 5.3 shows the resulting energy

scale as a function of days since the start of production neutrino data taking (run 10000, November 1999). It can be seen that while the Optics6b MC energy scale is approximately 2.5% higher than the earliest source run at the center of the detector, this is completely corrected by energy interpolation (these  $^{16}\text{N}$  runs were actually part of the scan used to generate the interpolation grids). Notice also that there are large (up to  $\sim 4\%$ ) fluctuations in energy scale between runs which are tracked by the Monte Carlo. These fluctuations in the source MC scale are due to the disabling of channels in the simulation which were actually disabled during the calibration source run (e.g. for maintenance), via DQXX banks that contain this information.

It is apparent from Figure 5.3 that much of the Monte Carlo scale trend is followed by the actual energy scale from source data, but not all. Figure 5.4 shows the fractional difference in energy scale between MC and data. Note that the MC over-predicts the energy scale as time increases in a way consistent with a linear 2.6% per year trend in both  $N_{\text{Hit}}$  and interpolation corrected  $N_{\text{Hit}}$ . The exact reasons for the observed trend are not completely understood at the time of writing this thesis. One significant component ( $\sim 0.9\%$ ) of the scale drift is understood to be due a drift in average PMT rates as determined from PULSE-GT triggered data (See Figure 5.5) since constant PMT noise of 600 Hz was used for all Monte Carlo simulations. Stability studies by others in the collaboration looking at prompt  $N_{\text{Hit}}$ ,  $^{16}\text{N}$  source systematics, and PMT charge cuts have shown that while the character of the trend shown Figure 5.5 can be changed with various types of cuts, nothing conclusive about the cause of the energy scale time variations has been found.

Although the source of roughly 1.7% of the energy scale drift is currently not known, the fact such a drift is evident from the calibration data begs the question of exactly how to handle it in the analysis. Rather than simply absorb the full

## Energy Scale Stability

N16 at Center of Detector; Optics 6b MC

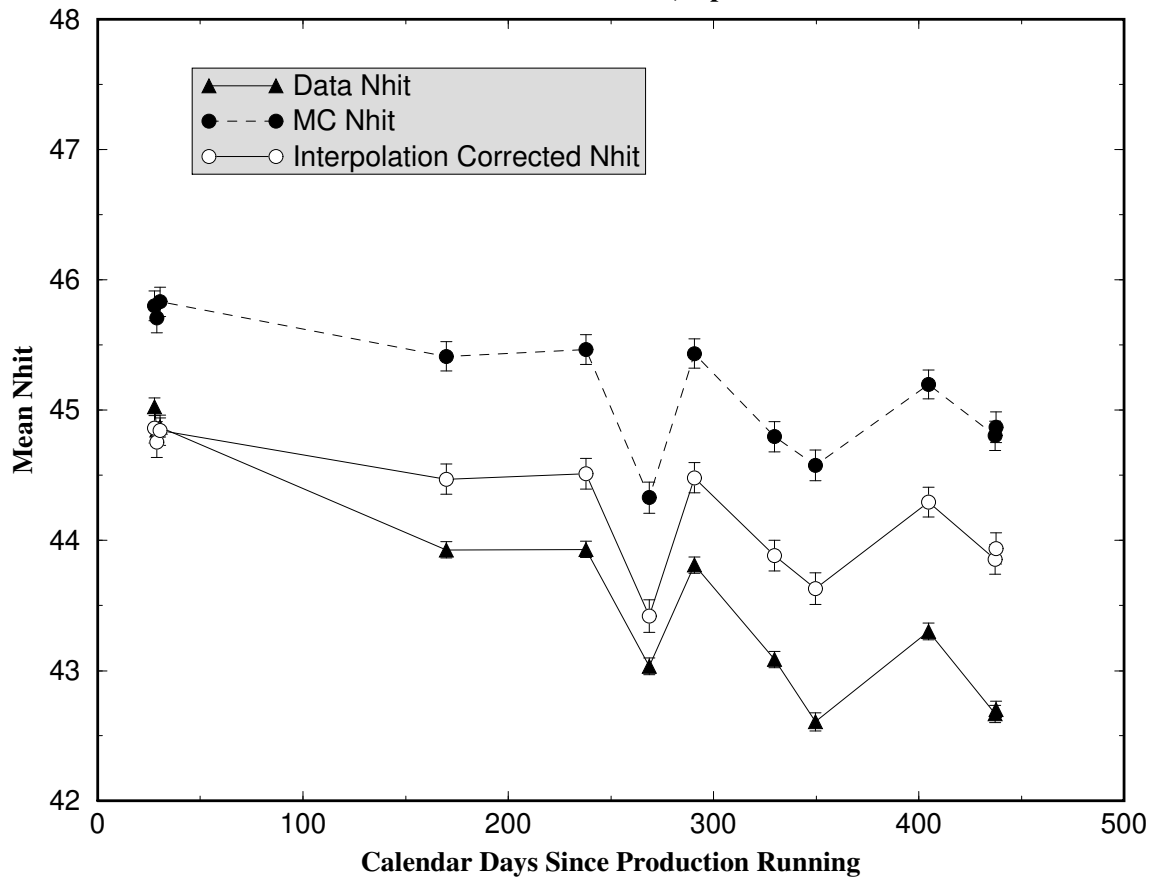


Figure 5.3: Comparison of energy scale between  $^{16}\text{N}$  calibration data and source MC as a function of days since production data taking.

## Energy Scale Stability

Nhit at Center of Detector; Optics 6b MC

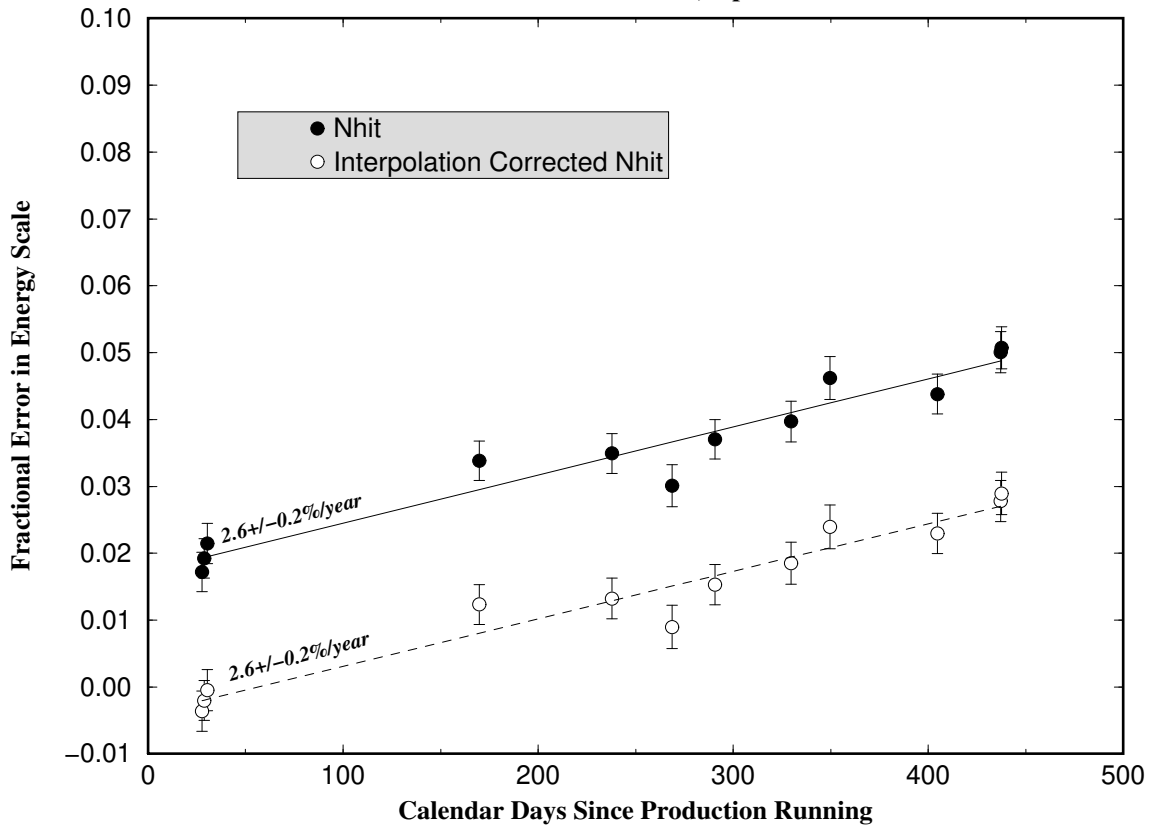


Figure 5.4: Fractional difference in energy scale between  $^{16}\text{N}$  calibration data and source MC as a function of days since production data taking.

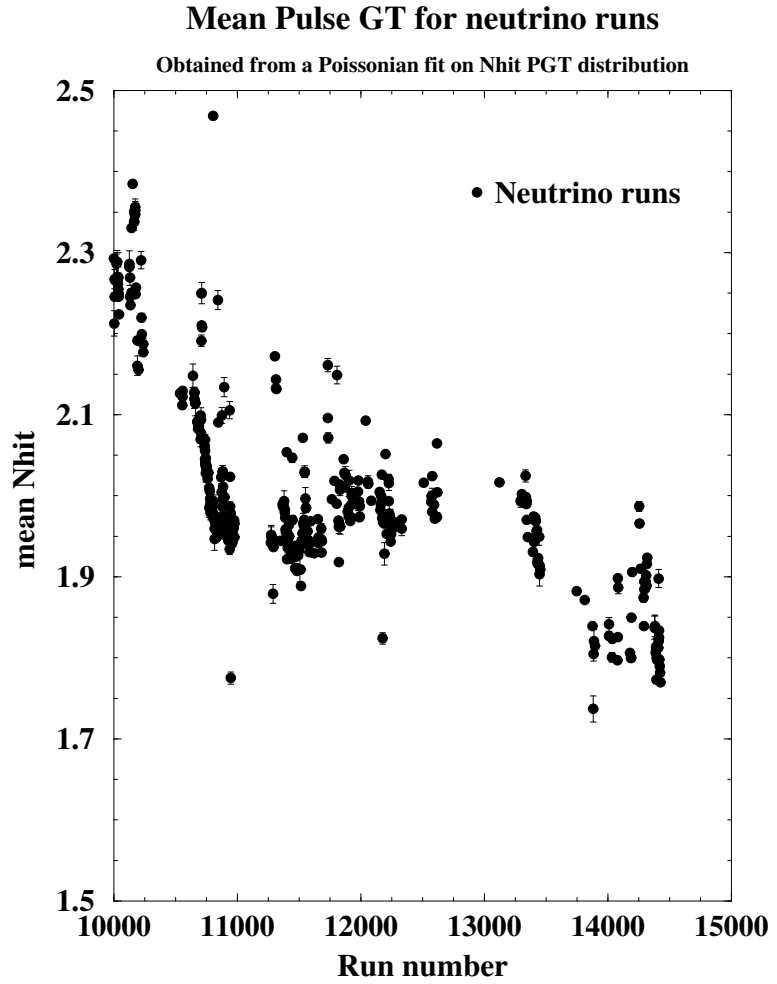


Figure 5.5: Poisson mean  $N_{\text{Hit}}$  versus run number from fits to PULSE-GT triggered data collected in tandem with neutrino data. The means have been corrected for number of channels online from DQXX information. The full data set extends up to run 14685 which corresponds to 432 calendar days since the beginning of production running (run 10000). Figure courtesy of V. Rusu.

variation in scale as a systematic uncertainty, the choice is made to apply the time slope correction implied by Figure 5.4 to all subsequent Monte Carlo generation. An important test of this drift correction as well as the overall energy scale uncertainty is comparison of drift corrected Monte Carlo to other types of source data taken other times. These tests using  $^{252}\text{Cf}$  and pT source are presented in Sections 5.4.2 and 5.4.2, respectively.

### Energy Scale Rate Stability

Given the rate dependence of PMT time measurement discussed in Section 5.1.2, one may wonder whether total  $N_{\text{Hit}}$  has a similar rate dependence. Figure 5.6 shows the  $N_{\text{Hit}}$  distributions for two  $^{16}\text{N}$  calibration source runs near the center of the detector with different trigger rates. The low rate (2 Hz) run (13520) more closely resembles the neutrino data rate than the 150 Hz high rate run. No rate dependence for total  $N_{\text{Hit}}$  is evident from these runs. This is an important check on our energy-like variable, because high rate  $^{16}\text{N}$  calibration data is used to set the Monte Carlo energy scale for this analysis.

### Energy Scale from $^{16}\text{N}$ Scans

In this section, comparisons between  $^{16}\text{N}$  6.13 MeV  $\gamma$ -ray source MC and calibration data are presented. These comparisons test how well the MC represents the energy scale of energetic electrons produced through Compton scattering by the source  $\gamma$ -ray.

The  $^{16}\text{N}$  is a triggered  $\gamma$ -ray source, with the primary branching ratio (66%) being a monoenergetic 6.13 MeV  $\gamma$ -ray. This decay is accompanied by a  $\beta$  (4.3 MeV endpoint) which provides a trigger signal through coupling to a plastic scintillator/PMT pair. The two other significant branches are a ground state transition (10.4 MeV endpoint

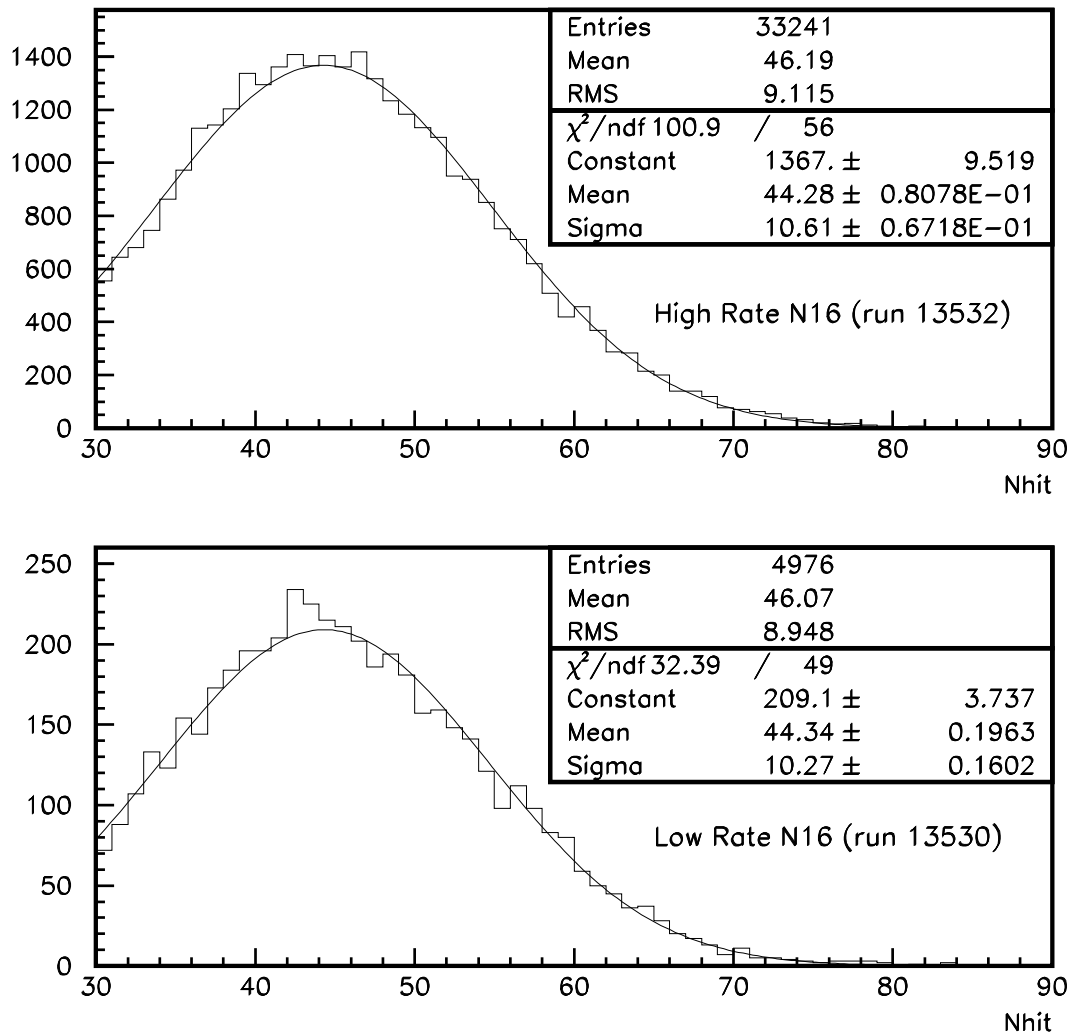


Figure 5.6:  $N_{\text{Hit}}$  distributions for two  $^{16}\text{N}$  calibration source runs near the center of the detector with different trigger rates. The low rate (2 Hz) run (13520) more closely resembles the neutrino data rate than the 150 Hz high rate run (13532).

$\beta$ , no  $\gamma$ ) occurring 28% of time and 4.8% contribution from a 7.1 MeV  $\gamma$  with 3.3 MeV endpoint  $\beta$ . The  $^{16}\text{N}$  is produced by bombarding  $^{16}\text{O}$  in  $\text{CO}_2$  gas with 14.2 MeV neutrons from a commercial deuterium-tritium (DT) generator fast neutron source. The  $\text{CO}_2$  gas is flowed through the DT generator and directly to the detector since the half-life of  $^{16}\text{N}$  is 7.13 secs. The stainless steel decay chamber is 0.5 cm thick to attenuate  $^{16}\text{N}$  decay  $\beta$ 's and is attached to a manipulator system for detector deployment. The  $^{16}\text{N}$  PMT is connected to a special front-end card channel which acts as an event tag and detector trigger<sup>9</sup> for the  $^{16}\text{N}$   $\gamma$ -rays. See [54] for a complete description of the  $^{16}\text{N}$  source.

Recall that  $^{16}\text{N}$  xz-plane scans taken in December 1999 were used to create energy scale interpolation grids for correcting the  $N_{\text{Hit}}$  of each Monte Carlo generated event. Part of the December 1999 scan was data taken off of the xz-plane and not used in generating the interpolation grid data. This yz-axis scan data was purposely reserved to check the Monte Carlo energy scaling both with and without the application of energy interpolation corrections. This comparison is shown in Figure 5.7. Although the number of positions sampled is rather limited, it is evident that the agreement is much better with the interpolation correction, consistent with the results from Appendix B. It also lends confidence that the energy scale interpolation scheme can be applied to data outside the plane of generation (xz-plane).

A second set of extensive detector scans with the  $^{16}\text{N}$  calibration source was performed in January 2001. In fact, this later scan was significantly more extensive than the December 1999 scan in both the xz-plane and yz-plane. This suggests that it might be fruitful to use the January 2001 scan to generate more well-determined

---

<sup>9</sup>except in special runs to study data cleaning performance, where it is important that the detector trigger timing is the same as in normal neutrino data taking. The role of data cleaning in data reduction is described in Chapter 6.

**Comparison of N16 MC and Actual Energy Response**

Dec99 D2O xscan (y=0 cm, z=0 cm), Optics 6b, Rfit < 550 cm

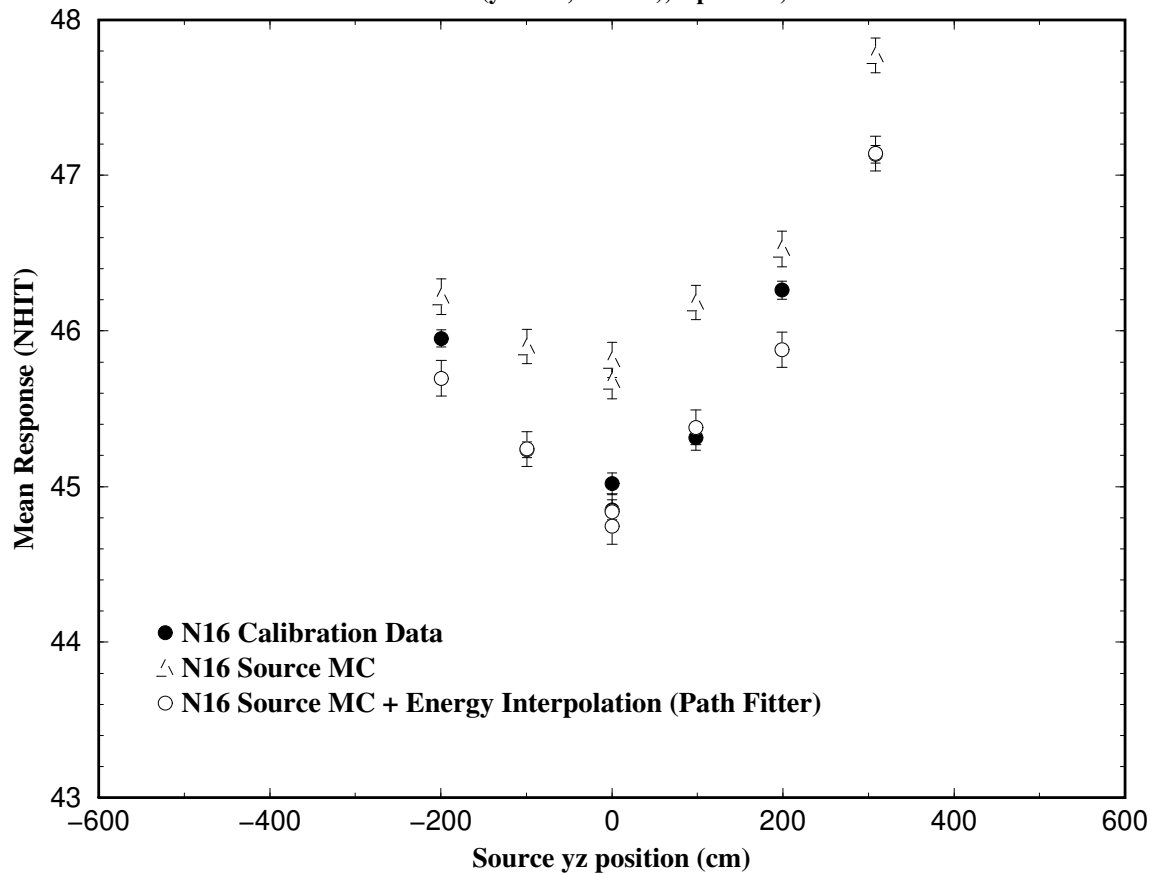


Figure 5.7: Energy scale with and without energy interpolation for the Dec99  $^{16}\text{N}$  yz-scan using the Path Fitter.

interpolation grids and then test the results with the December 1999 scan as opposed to the other way around that is done in this analysis. In any event, the energy scaling of source Monte Carlo (with time drift correction applied) and data was compared for the January 2001  $^{16}\text{N}$  scans and found to be in good agreement. A comparison between data and both  $N_{\text{Hit}}$  and interpolation corrected  $N_{\text{Hit}}$  is shown in Figure 5.8 for a scan along the x-axis as an example. Note that the energy interpolation corrected  $N_{\text{Hit}}$  is in much better agreement with the observed energy scale than uncorrected  $N_{\text{Hit}}$ , similar to the December 1999 scan results which were taken more than a year prior this  $^{16}\text{N}$  data.

In Figure 5.9, the fractional error in interpolation corrected  $N_{\text{Hit}}$  from source Monte Carlo when compared to the January 2001 x,y, and z-axis scan data is shown versus source radius. Note that the energy scale error increases as the source radius increases. If one assumes that the observed error at a given source radius is representative of the error at any position with that same radius (i.e. the error at a given source radius is spherically symmetric), then simple  $R^2$  weighting of the errors yields a estimate of the volume-weighted energy scale uncertainty equal to  $0.9 \pm 0.1\%$ . For comparison, the same uncertainty without energy interpolation is  $1.5 \pm 0.1\%$ .

### Energy Scale from Hot $^{252}\text{Cf}$ Neutron Source

The capture of neutrons on deuterium produces a 6.25 MeV  $\gamma$ -ray. This  $\gamma$ -ray is very close in energy to the  $\gamma$ -ray produced by the triggered  $^{16}\text{N}$  source, so a source of neutron captures on deuterium would provide a excellent cross-check on the energy scale uncertainty. Also, due to the long mean free path of neutrons in pure D<sub>2</sub>O ( $\sim 1.5$  m), a neutron source would provide an excellent probe of energy scale in regions of the detector inaccessible to the  $^{16}\text{N}$  source with the present manipulator system

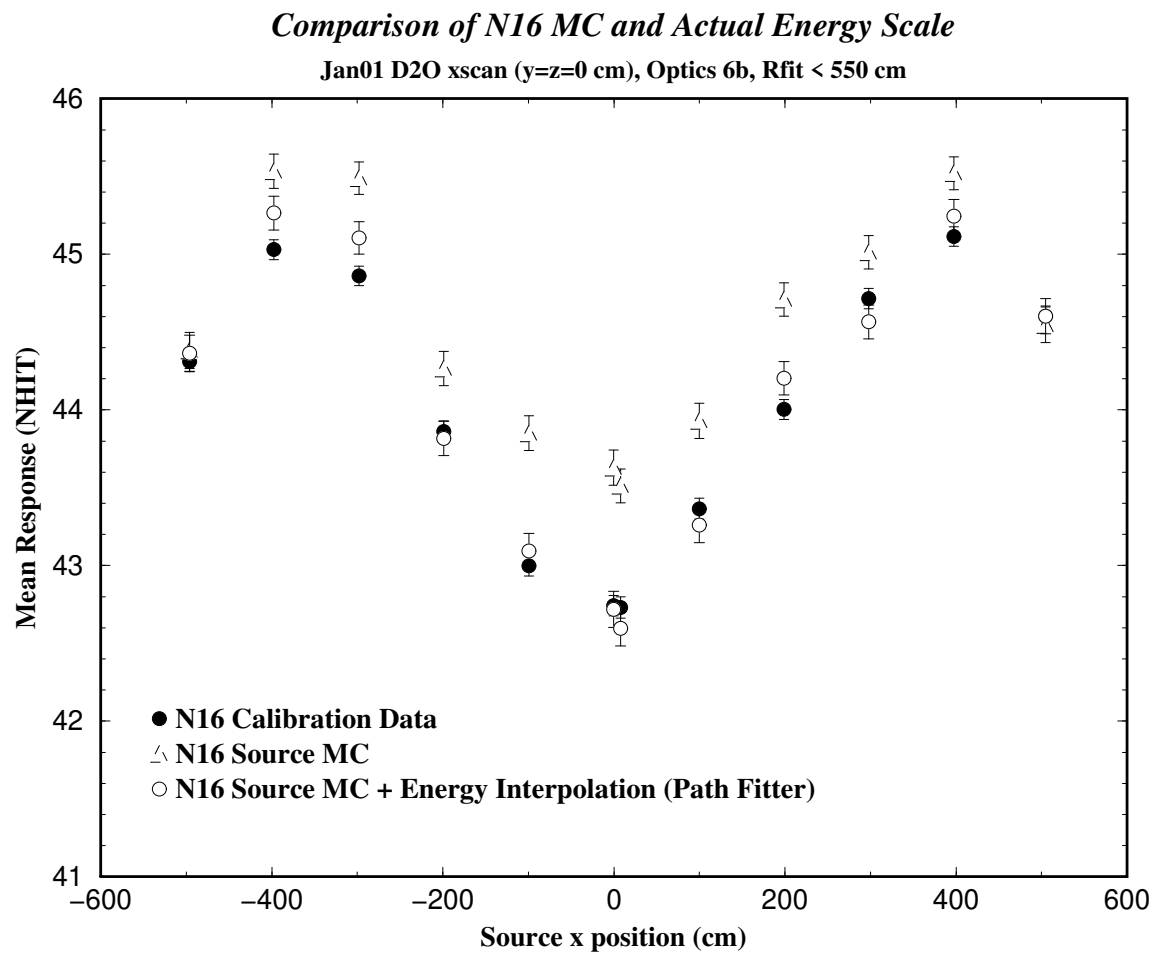


Figure 5.8: Energy scale with and without energy interpolation for the Jan01  $^{16}\text{N}$  x-axis scan using the Path Fitter.

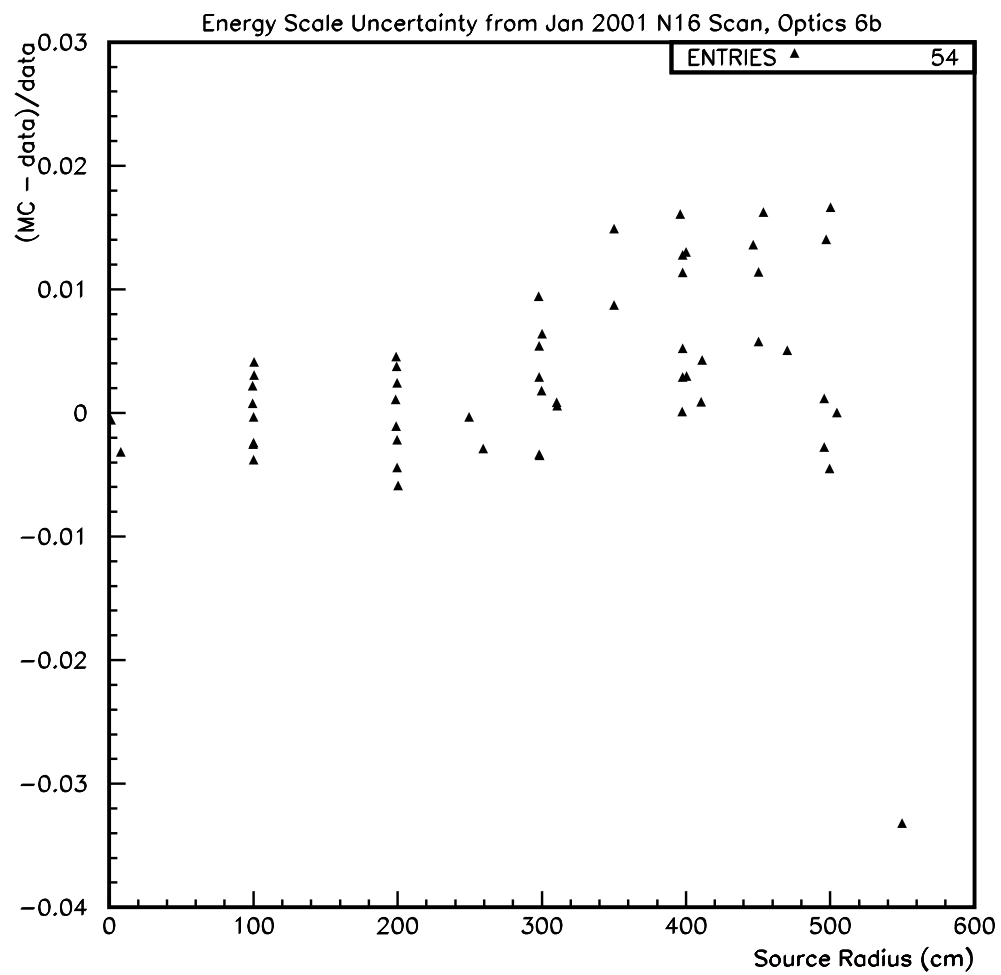


Figure 5.9: Fractional error in interpolation corrected  $N_{\text{Hit}}$  versus source radius from source Monte Carlo when compared to the January 2001 x,y, and z-axis scan data.

(planes other than xz and yz, and the very outer regions of the D<sub>2</sub>O in these planes).

The neutron source used in SNO is a <sup>252</sup>Cf source encapsulated in acrylic. Two different sources with different strength - 1 nCi and a “hot” 10 nCi source - were deployed. Neutrons which are produced in the fission process of <sup>252</sup>Cf leave the source and enter the detector where they are subsequently thermalized and captured (mostly on hydrogen and deuterium). The source is untriggered, so care must be taken to cull the neutron initiated events from the data. For a more general description of acrylic encapsulated sources developed for use in SNO, see [55].

The hot <sup>252</sup>Cf source was deployed in August 2000 and November 2000 at various positions within the detector. The data was fully reconstructed with the Path Fitter. Some higher-level cuts were applied to the data to remove non-Cerenkov events primarily from manipulator light - the Path Fitter figures-of-merit (recall Section 4.3.5) and two cuts described in Chapter 6 (Correlation  $\chi^2$  and In-time Ratio). In addition, only events reconstructing more than 150 cm from the source were accepted as neutron captures to remove events initiated by  $\beta$ s and  $\gamma$ s from fission fragments within the source. The filtered data was then separated into equal volume (reconstructed  $R^3$ ) bins and the  $N_{\text{Hit}}$  distribution within each bin fit to a Gaussian to get the energy scale and resolution. The exact same procedure was repeated for the <sup>252</sup>Cf source simulation and the energy scale within each equal volume bin compared to the data. Figure 5.10 shows the data  $N_{\text{Hit}}$  and energy interpolation corrected  $N_{\text{Hit}}$  from the source MC for the August 2000 and November 2000 hot <sup>252</sup>Cf runs.

Since the energy scale was determined for MC and data in equal volume bins, a simple average of the (absolute) fractional differences gives the volume-weighted scale uncertainty from the neutron source data. This gives  $0.8 \pm 0.2\%$  and  $0.4 \pm 0.2\%$  for the August 2000 and November 2000 volume-weighted error, respectively. The energy

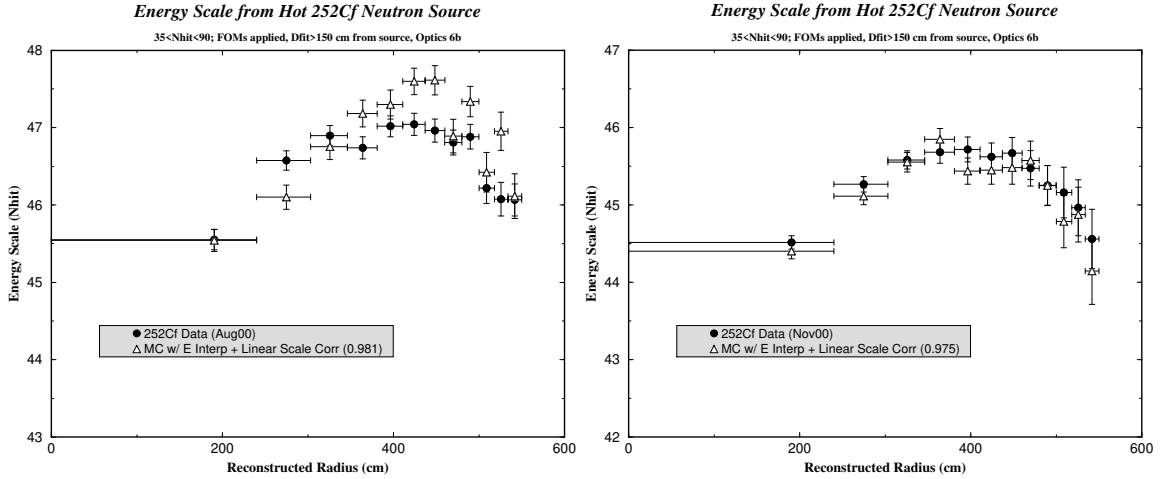


Figure 5.10: Comparison between  $^{252}\text{Cf}$  data and interpolation corrected source MC energy scale for (left) August 2000 and (right) November 2000 neutron source runs.

Run	Optics 1		Optics 2		Optics 3	
	$N_{\text{Hit}}$	$N_{\text{Corr}}$	$N_{\text{Hit}}$	$N_{\text{Corr}}$	$N_{\text{Hit}}$	$N_{\text{Corr}}$
Aug 2000	$0.9 \pm 0.3$	$0.7 \pm 0.1$	$1.7 \pm 0.1$	$1.0 \pm 0.1$	$1.1 \pm 0.4$	$0.9 \pm 0.1$
Nov 2000	$0.5 \pm 0.3$	$0.3 \pm 0.3$	$1.0 \pm 0.2$	$0.8 \pm 0.2$	$0.6 \pm 0.1$	$1.1 \pm 0.2$

Table 5.2: Energy scale uncertainties for the alternate optics sets from comparison of the neutron source data and MC ( $N_{\text{Corr}}$  is the interpolation corrected  $N_{\text{Hit}}$  ).

scale uncertainties for the alternate optics sets were also examined with the neutron source data, along with comparisons of uncorrected  $N_{\text{Hit}}$  and interpolation corrected  $N_{\text{Hit}}$ . Table 5.2 summarizes these results.

In the context of energy scale drift, it is interesting to note that much better agreement between neutron source data and MC is obtained when the drift correction is applied. This is true for both the August 2000 and November 2000 data. Without any scale drift correction, the volume weighted error is increased to 2.5% and 1.6% for the August 2000 and November 2000 data, respectively.

## Energy Scale from $pT$ Source

The  $pT$  source is a very important source for SNO because it provides an upper energy calibration point (19.8  $\gamma$ -rays) well beyond the  $^8B$  endpoint. Taken together with the  $^{16}N$  source, these two sources essentially bracket the entire energy range of interest for solar neutrino analyses.

The  $pT$  source works by accelerating protons onto a tritium target, producing 19.8 MeV  $\gamma$ -rays through  $^3H(p,\gamma)^4He$  reactions. Hydrogen ions are produced by accelerated electrons within a gas discharge region. Ionizing electrons are confined within a cold Penning trap, which also increases their path length through the gas to increase the probability of multiple ionization. This design also allows the source to be run in DC rather than pulsed mode, which could cause electrical interference in the detector. The target chamber is operated at negative high voltage which accelerates the discharged ions toward the tritium target. The entire source is only 50 cm in length so that it can be deployed at various locations inside the detector. The source is untriggered and produces a high rate of neutrons (largely from  $^3H(t,nn)^4He$ ), so the data must be cleaned of unwanted high  $N_{\text{Hit}}$  events (e.g. PMT flashers) to get at events initiated by electrons Compton scattered by the 19.8 MeV  $\gamma$ -rays. See [56] for more information about the  $pT$  source design.

The  $pT$  source data were passed through the standard data cleaning cuts (described in Chapter 6) to remove instrumental backgrounds and then fully reconstructed with the Path Fitter. In addition, the same high level cuts used to clean the  $^{252}\text{Cf}$  hot neutron source data were applied to the  $pT$  source data. Figure 5.11 shows the resulting  $N_{\text{Hit}}$  spectrum for  $pT$  source run 15172 at the center of the detector, where the 19.8 MeV  $\gamma$ -ray peak is clearly evident. An overlay of the  $pT$  source MC

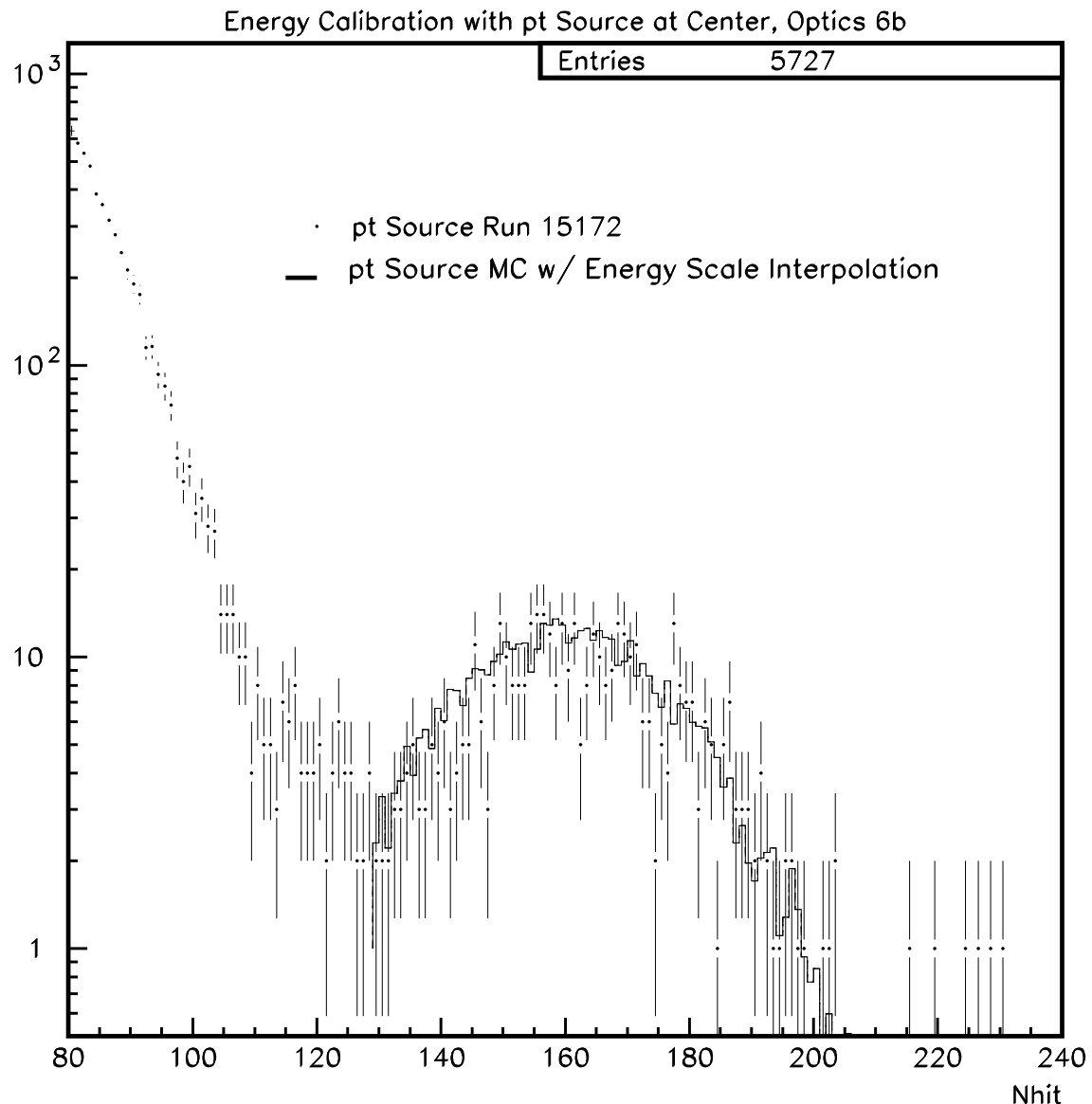


Figure 5.11:  $N_{\text{Hit}}$  distribution of pT source run 15172 at the center of the detector after data cleaning and high level cuts. Overlayed is the interpolation corrected MC of the pT source.

with energy interpolation applied is also shown in Figure, demonstrating the excellent level of agreement between the MC and data at the pT energy (at the center). The fractional error in the energy interpolation  $N_{\text{Hit}}$  for the sum of all pT source taken at the center (runs 15172-15177) is found to be  $0.3 \pm 0.5\%$ . As was the case for the neutron data, the pT source MC is in much better agreement with the data when the linear scale drift correction is applied - the error is 2.7% without this scale drift correction.

## Energy Resolution

In the previous section, energy scale uncertainty was studied by comparing the Gaussian mean of the  $N_{\text{Hit}}$  distributions for various calibration data and source Monte Carlo. In this section, the energy resolution uncertainty is investigated, which (for  $N_{\text{Hit}}$ -based analyses) is defined as the error in width of Monte Carlo  $N_{\text{Hit}}$  spectra when compared to source calibrations.

Figure 5.4.2 shows the energy resolution for x-axis and z-axis scans of the  $^{16}\text{N}$  calibration source compared to source Monte Carlo. Notice that the Monte Carlo energy resolution is systematically lower than the resolution extracted from  $^{16}\text{N}$  source data by about 3% on average. While this discrepancy is not completely understood, it does set the scale of our systematic error on energy resolution. As we will see in Chapter 8, this turns out to be small contribution to our overall systematic uncertainty on the CC and ES flux measurements.

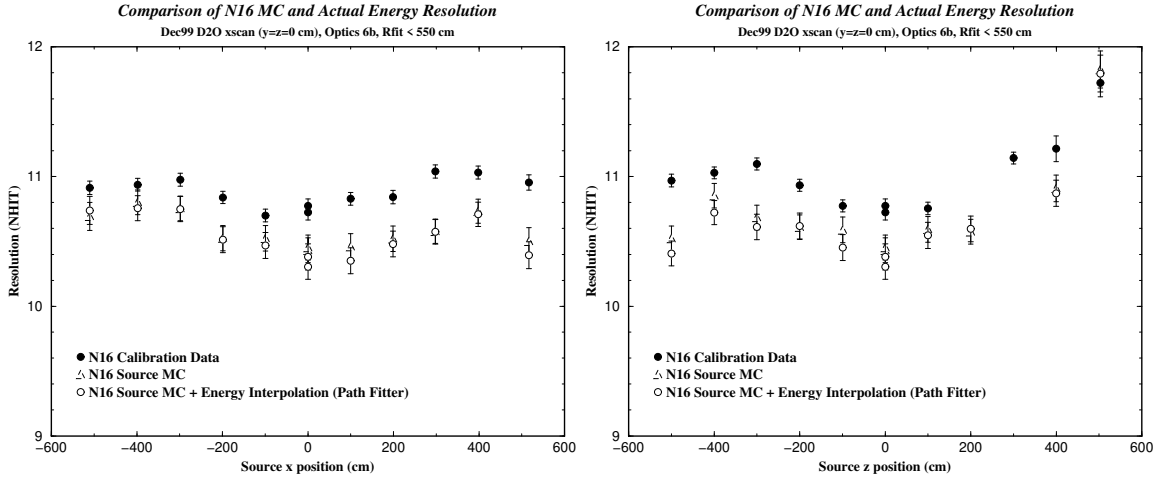


Figure 5.12: Energy resolution for (left) x-axis and (right) z-axis scans of the  $^{16}\text{N}$  calibration source compared to source Monte Carlo. For the Monte Carlo, resolution both with and without energy scale interpolation is shown.

## 5.5 Reconstruction Characteristics

Recall from discussions in Section 5.4 that uncertainties in the energy scale and resolution enter directly into uncertainties on solar neutrino results because of the need to place a cut on energy to avoid backgrounds. In a similar way, uncertainties in reconstruction characteristics translate into uncertainties in the results because of the need for a fiducial volume cut to avoid backgrounds that originate in the exterior regions of the detector. The fiducial volume cut is a cut on reconstructed position (typically reconstructed radius) not direction, so one might expect that uncertainties in the reconstruction of direction will enter into the systematic error to a lesser extent than position uncertainty. While this is generally true, systematic errors are not all in the acceptance errors from cuts on the data, but rather also involve errors in the extracted signal from *shapes* of the PDFs used in the extraction.

### 5.5.1 Vertex Resolution and Shift

In this section, the vertex resolution and mean shift in the fit vertex from the “true” electron position are determined. These studies use the  $^{16}\text{N}$  calibration source described in Section 5.4.2 and a  $^8\text{Li}$  triggered electron source. The energy spectrum of  $^8\text{Li}$  decay  $\beta$ ’s is very similar to the  $^8\text{B}$  neutrino spectrum. This is because both  $^8\text{Li}$  and  $^8\text{B}$  can decay to the same nuclear state ( $^8\text{Be}$ ) and are isospin mirrors of each other. The possibility of using this source to increase SNO’s sensitivity to measuring  $^8\text{B}$  spectral distortions is discussed in [57]. The  $^8\text{Li}$  is made through  $^{11}\text{B}(\text{n},\alpha)^8\text{Li}$  reactions by bombarding a  $^{11}\text{B}$  target with fast neutrons from the DT generator. Some fraction of the  $^8\text{Li}$  produced in the DT target chamber is swept to a decay region in the detector by an aerosol flow of He gas and NaCl. The short half-life of  $^8\text{Li}$  ( $T_{1/2} = 1.2$  secs) makes getting a substantial yield of decays in the detector a challenging task. The decay chamber is a stainless steel sphere 5” in diameter and thin-walled ( $\sim 0.02$ ” thickness) to minimize  $\beta$  energy losses ( $\sim 2$  MeV is lost traversing the source wall). The tag signal from the source is derived from scintillation light produced in the He gas by  $\alpha$  particles accompanying the  $^8\text{Li}$   $\beta$  decay. This scintillation light is detected by a PMT mounted inside the decay chamber. A detailed description of the  $^8\text{Li}$  source can be found in [58].

Both  $^{16}\text{N}$  and  $^8\text{Li}$  sources generate electrons with position distributions that are known, at least in principle. These electron source distributions, when convolved with an assumed shape for the underlying fit position distribution, can be fit to the data to estimate the resolution and mean vertex shift for reconstructed electron events in the detector. That is, a function  $\xi(x_{fit}; \sigma, \mu)$  is fit to the 1D reconstructed position

distribution (here shown in  $x$ ),

$$\xi(x_{fit}; \sigma, \mu) = \int_{-\infty}^{\infty} F(x_{fit}, \sigma, \mu; x_{src}) S(x_{src}) dx_{src} \quad (5.1)$$

where  $S$  is the electron source distribution and  $F$  is the reconstruction response function to electrons which depends on the vertex resolution ( $\sigma$ ) and shift ( $\mu$ ). The form chosen for  $F$  is a simple Gaussian,

$$F(x_{fit}, \sigma, \mu; x_{src}) = \frac{1}{\sqrt{2\pi}\sigma} e^{\frac{[(x_{fit}-x_{src})-\mu]^2}{2\sigma^2}} \quad (5.2)$$

motivated by Monte Carlo studies of reconstructed electron position distributions<sup>10</sup>.

For  $^{16}\text{N}$ , the form of  $S(x_{src})$  is the 1D projection of the 3D scattering distribution,  $S(r) \sim e^{-\frac{r}{\lambda}}/r^2$ , with  $\lambda = 37$  cm. The  $^8\text{Li}$  source is approximated as a source of electrons on a shell  $2a=10.7$  cm in diameter. Therefore,  $S(x_{src})$  is given by

$$S(x) = \begin{cases} \frac{2\pi\sqrt{a^2-x^2}}{4\pi a^2}, & x < a \\ 0, & \text{otherwise} \end{cases} \quad (5.3)$$

Figure 5.13 shows the electron source distributions used to extract  $\sigma$  and  $\mu$  from  $^{16}\text{N}$  and  $^8\text{Li}$  along with example fits to the calibration data.

## Vertex Resolution

Figures 5.14 and 5.15 show comparisons of the vertex resolution as a function of source z-position ( $x \sim y \sim 0$ ) obtained from the  $^{16}\text{N}$  and  $^8\text{Li}$  source, respectively. Comparisons

---

<sup>10</sup>A better fit to MC distributions is obtained using the sum of a Gaussian and exponential, as these distributions suggest exponential rather than Gaussian tails. The added complexity of extra fit parameters was deemed unnecessary as we are only use these fits to estimate the *uncertainties* in MC reconstruction characteristics rather than constructing reconstruction response functions.

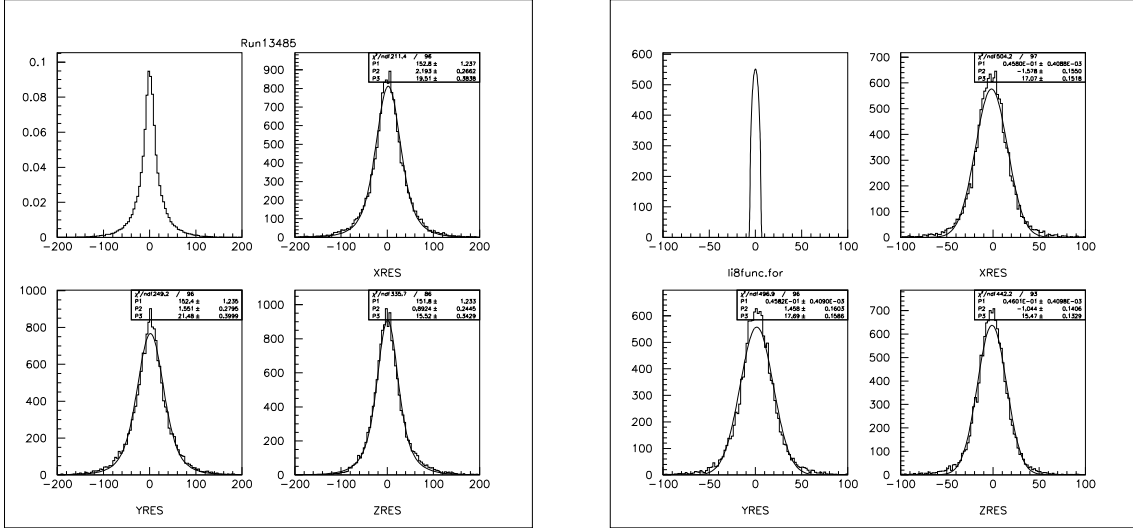


Figure 5.13: The electron source distributions used to extract  $\sigma$  and  $\mu$  from (left)  $^{16}\text{N}$  and (right)  $^8\text{Li}$  along with example fits to the calibration data.

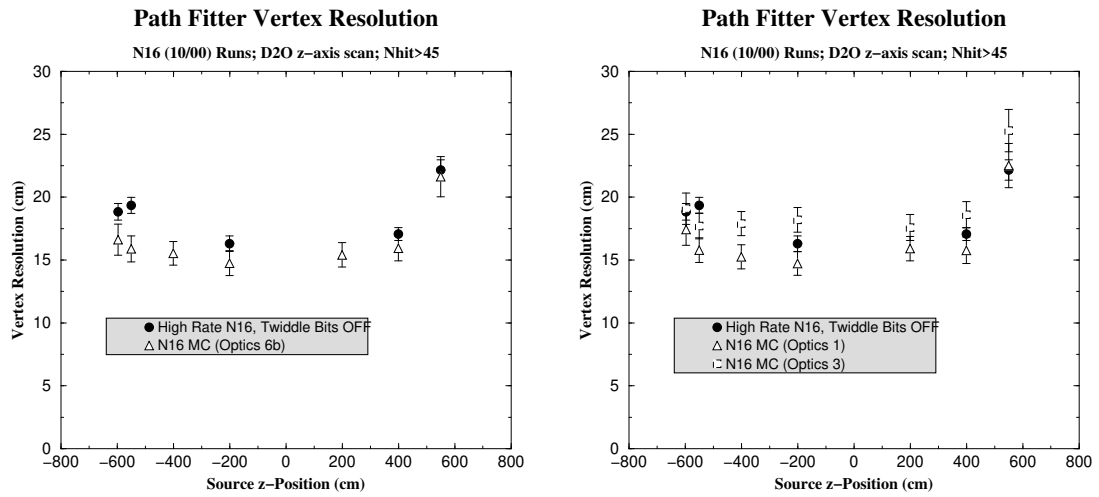


Figure 5.14: Comparison of vertex resolution from  $^{16}\text{N}$  source MC and data as a function of source z-position - (left) Optics6b and (right) extreme optics.

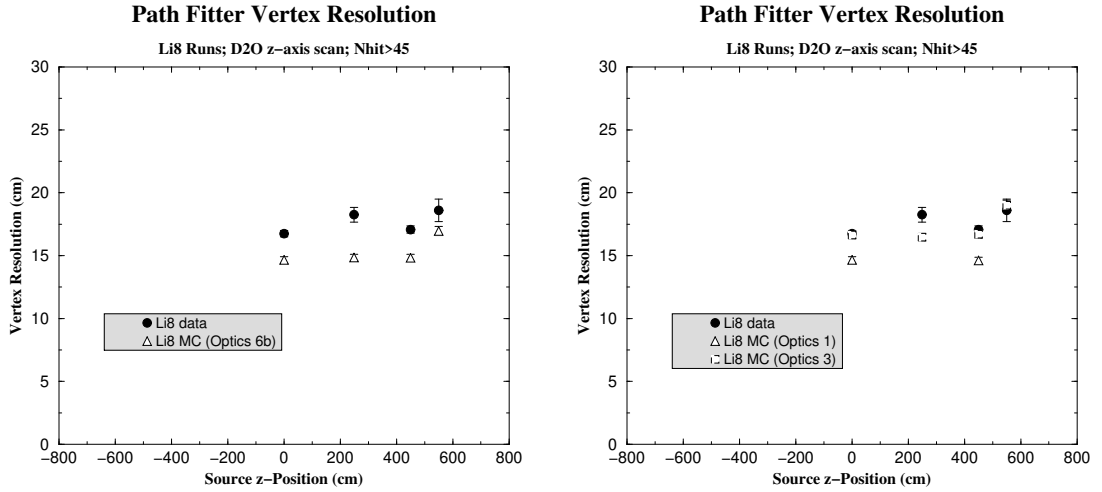


Figure 5.15: Comparison of vertex resolution from  ${}^8\text{Li}$  source MC and data as a function of source z-position - (left) Optics6b and (right) extreme optics.

are made between calibration data and source MC for the central optics (Optics 6b) and extreme optics for reconstruction (Optics 1 and 3). The  ${}^{16}\text{N}$  MC resolution is in good agreement with the data, although the MC appears to be systematically low by about 2 cm. The agreement is slightly worse for the  ${}^8\text{Li}$  source, with discrepancies of up to 3 cm in the resolution. For both sources, the range in resolution for the extreme optics sets essentially brackets the calibration data. The resolution difference between the extreme optics is about 2.5 cm, which sets the likely scale for effects of optical uncertainties on vertex resolution. In Figure 5.16, the vertex resolution results from  ${}^{16}\text{N}$  and  ${}^8\text{Li}$  sources are directly compared and shown to be in reasonable agreement with one another.

In addition to the source position dependence, it is interesting to investigate how well the MC models the energy ( $N_{\text{Hit}}$ ) dependence of the vertex resolution. This is particularly relevant for consideration of systematic uncertainties in an  $N_{\text{Hit}}$  bin-by- $N_{\text{Hit}}$  bin CC flux extraction to produce a spectrum (discussed in Section 8.2.3).

## Path Fitter Vertex Resolution

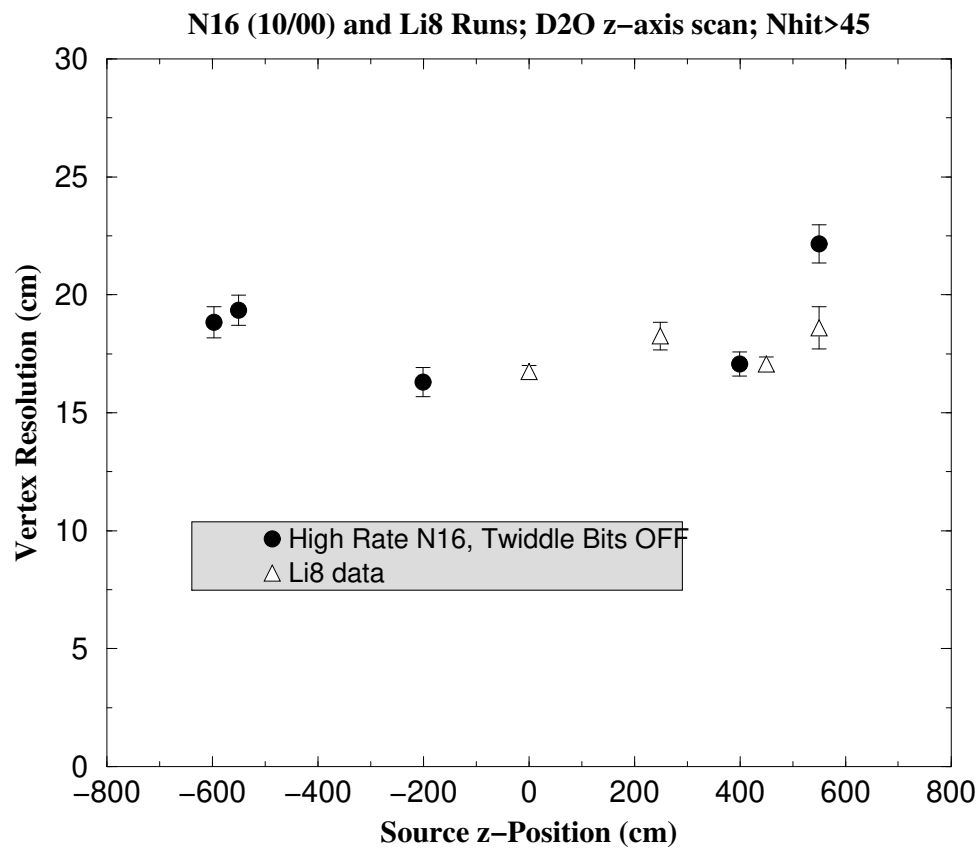


Figure 5.16: Comparison of vertex resolution from  $^{16}\text{N}$  and  $^8\text{Li}$  calibration data as a function of source z-position.

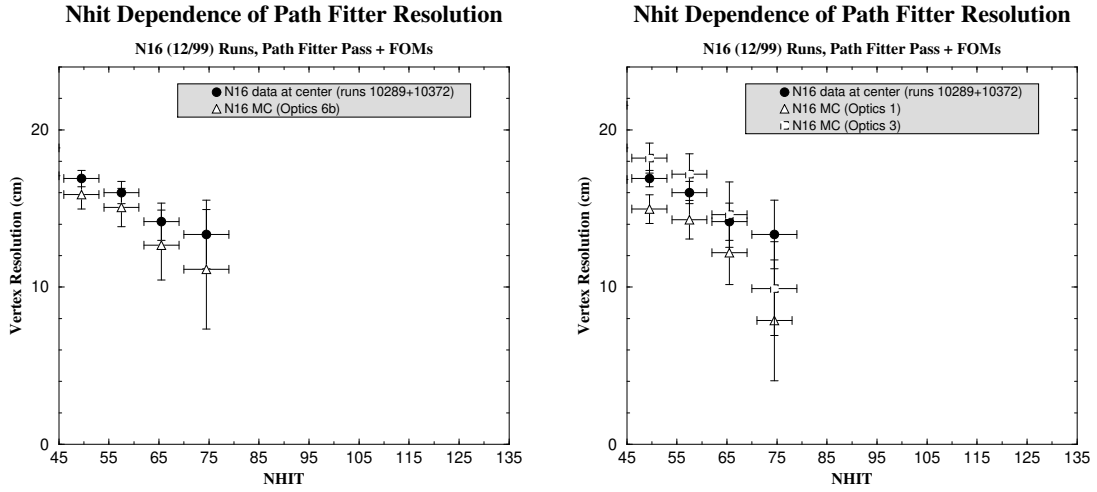


Figure 5.17: Comparison of vertex resolution from  $^{16}\text{N}$  source MC and data as a function of  $N_{\text{Hit}}$  - (left) Optics6b and (right) extreme optics.

Figures 5.17 and 5.18 show comparisons of the vertex resolution as a function of  $N_{\text{Hit}}$  obtained from the  $^{16}\text{N}$  and  $^{8}\text{Li}$  source at the center of the detector, respectively. Comparisons are made between calibration data and source MC for the various optical parameter sets. For  $^{16}\text{N}$ , agreement in the shape of the resolution as a function of  $N_{\text{Hit}}$  is quite good and largely unaltered by the extreme optical sets.

The agreement is not quite as good for the  $^{8}\text{Li}$  source, particularly at low  $N_{\text{Hit}}$  where disagreement in resolution is  $\sim 3$  cm at  $45 N_{\text{Hit}}$ . There are several possible reasons for the apparent worse agreement between source data and MC at low  $N_{\text{Hit}}$ . It could be that poor modeling of the source geometry is such that, for example, less light is shadowed by the source in the MC which leads to better reconstruction accuracy. Another possible explanation is that residual  $^{16}\text{N}$  contamination in the tagged  $^{8}\text{Li}$  events are present. This contamination would decrease as a function of increasing  $N_{\text{Hit}}$  in much the same way as shown in Figure 5.19 because of the shape of the  $^{16}\text{N}$   $N_{\text{Hit}}$  spectrum (see Figure 5.20). A large fraction of  $^{16}\text{N}$  events can be removed with a

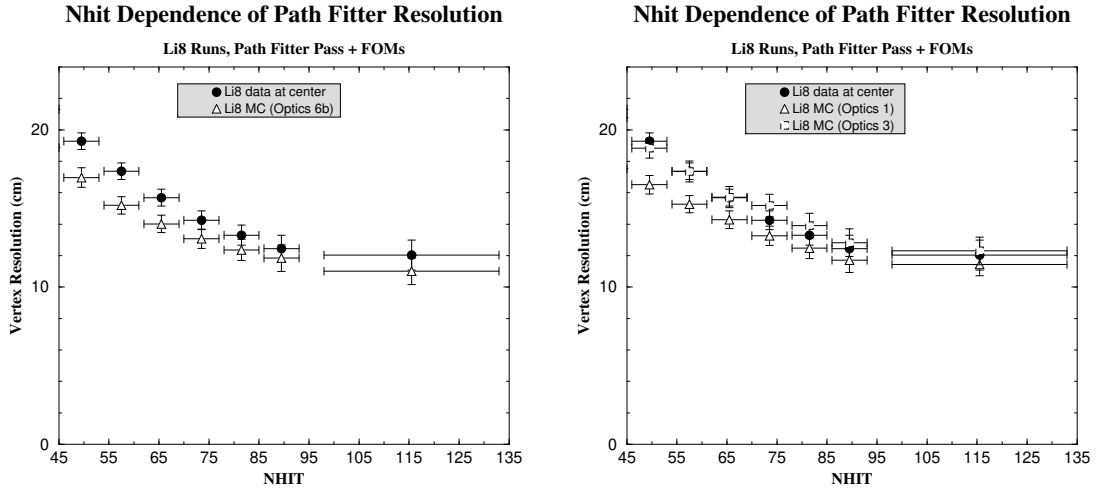


Figure 5.18: Comparison of vertex resolution from  ${}^8\text{Li}$  source MC and data as a function of NHIT - (left) Optics6b and (right) extreme optics.

simple cut on time and charge of the  ${}^8\text{Li}$  PMT signal, where the cut contour [59] can be determined by running pure  ${}^{16}\text{N}$  through the  ${}^8\text{Li}$  gas line. If residual  ${}^{16}\text{N}$  events are in the tagged  ${}^8\text{Li}$  data, then it will broaden the extracted resolution because one is fitting the position distribution under the hypothesis it is comprised of electrons rather than  $\gamma$ -rays<sup>11</sup>.

### Vertex Shift

The mean displacement of the fit vertex relative to the true electron position is vertex shift. If the Monte Carlo does not accurately reproduce the vertex shift effects at work in reconstruction of real events in the detector, the MC calculated acceptance within some applied fiducial volume will be incorrect. This reconstruction uncertainty is completely analogous to the effect of energy scale uncertainty on the CC and ES flux measurements.

---

<sup>11</sup>which produce an extended source of electrons through Compton scattering in the water.

## Nhit Dependence of Path Fitter Resolution

N16 (12/99) and Li8 Runs, Path Fitter Pass + FOMs

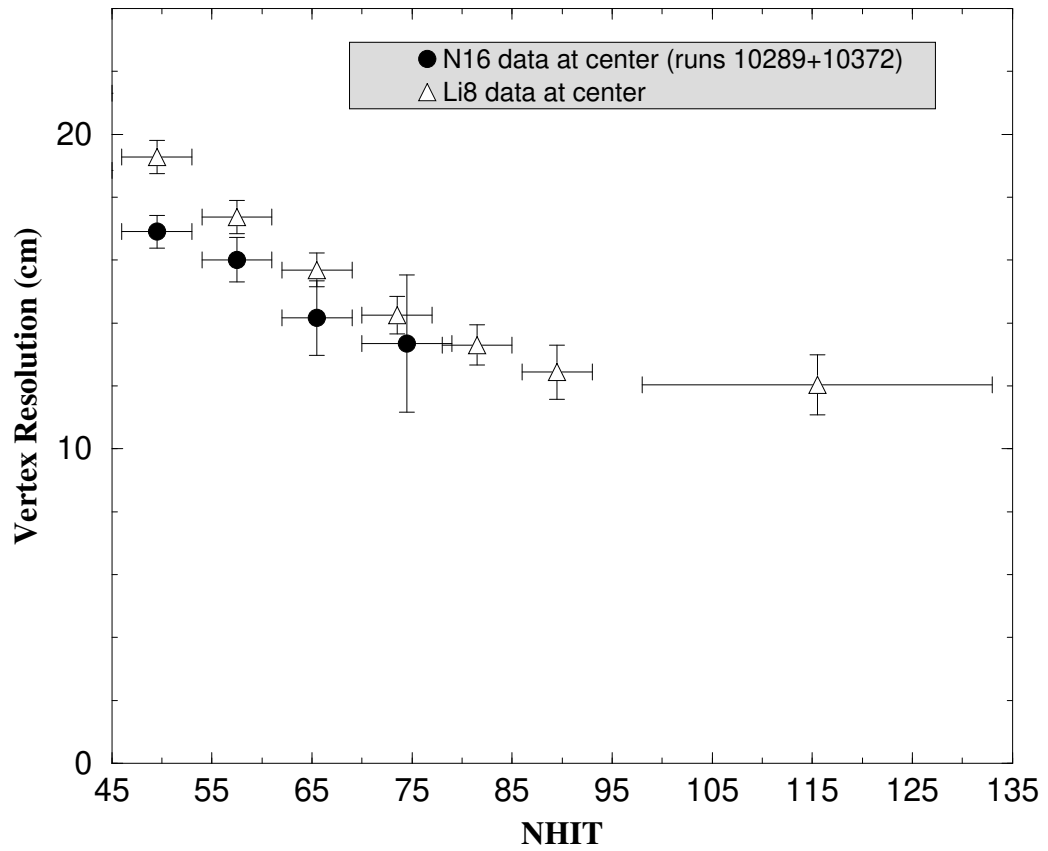


Figure 5.19: Comparison of vertex resolution from  $^{16}\text{N}$  and  $^8\text{Li}$  calibration data as a function of NHIT.

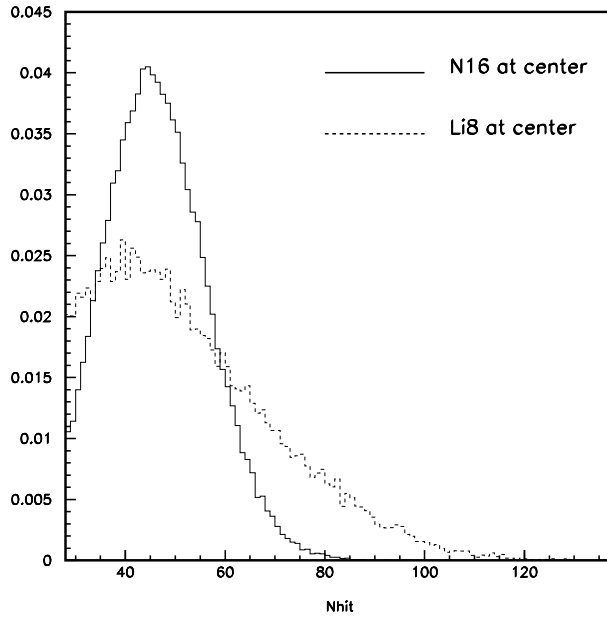


Figure 5.20: Comparison of  $^{16}\text{N}$  and  $^8\text{Li}$   $N_{\text{Hit}}$  distribution for source at the center of the detector.

The vertex shift results are derived from exactly the same fits to calibration data and source MC presented in the context of vertex resolution, except that the Gaussian fit  $\mu$ 's rather than  $\sigma$ 's are compared. An illustrative example of vertex shift is shown in Figure 5.21, which shows a scatter plot of reconstructed vertex for four different  $^8\text{Li}$  source positions. The source is represented by a circle approximately to scale. Note that the centroid of the cloud of fit positions is steadily displaced in z-position from the source position as the source is moved in the  $+z$  direction. If this inward shift was not also modeled in the Monte Carlo, then the Monte Carlo over-predict the actual number of neutrino events accepted within the fiducial volume<sup>12</sup>. It will become evident in the discussion that follows that the MC *does* indeed track vertex shift effects to a certain degree.

<sup>12</sup>This is only true, of course, if events from  $^8\text{Li}$  electrons are a good approximation to neutrino-induced electron events

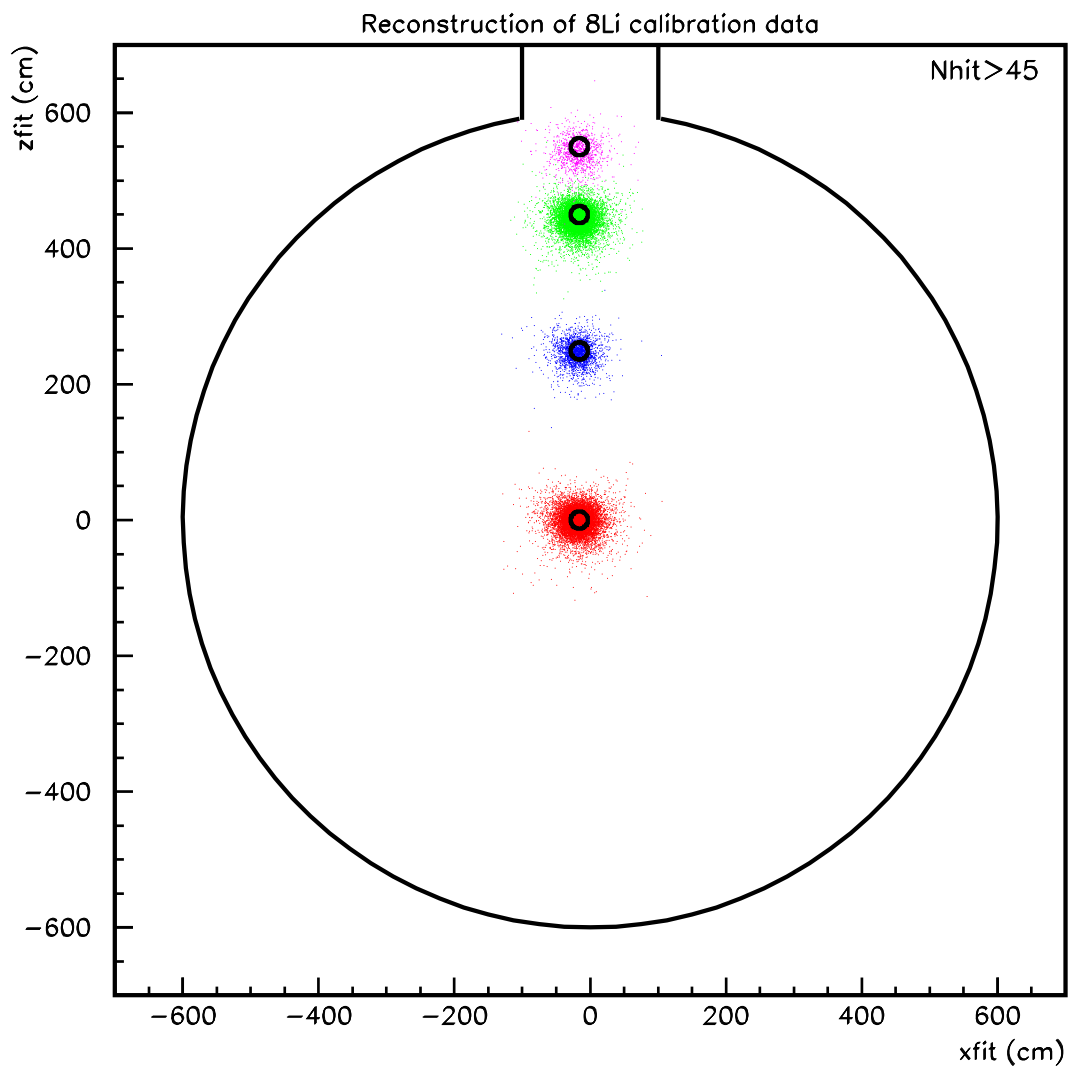


Figure 5.21: Scatter plot of reconstructed vertex for four different  ${}^8\text{Li}$  source positions. The source is represented by a circle approximately to scale relative to the size of the acrylic vessel.

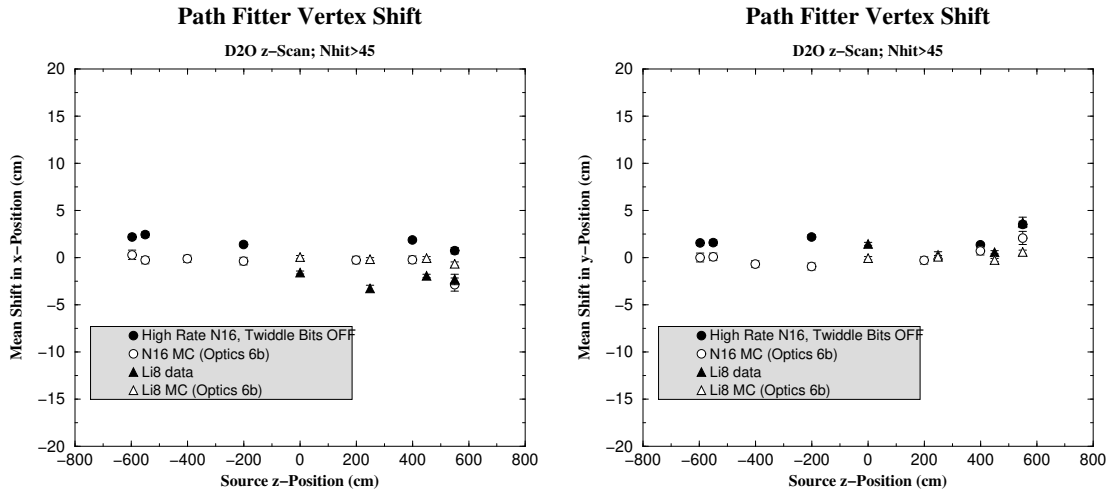


Figure 5.22: Comparison of (left) x and (right) y vertex shift from  $^{8}\text{Li}$  and  $^{16}\text{N}$  source MC and data as a function of source z-position.

Figure 5.22 shows a comparison of x and y vertex shift from  $^{8}\text{Li}$  and  $^{16}\text{N}$  source MC and data as a function of source z-position. There is no evidence for any shift in the fit vertex beyond fluctuations on the order of the source positioning uncertainty ( $\sim 2$  cm). The vertex shift in z-position does show a dependence on the source position along the z-axis, which is consistent for both of the sources (see Figure 5.23). The sign of the effect is to push events inward as the source is moved outward along the z-axis, with a slope of about 1 cm shift per 1 m source displacement. Notice that the MC shows a similar trend that is in reasonable agreement with the source data except possibly when the source is nearest to the AV neck (largest z-position). The extreme optics MC sets also show a similar, but slightly larger slope with the same sign of the effect.

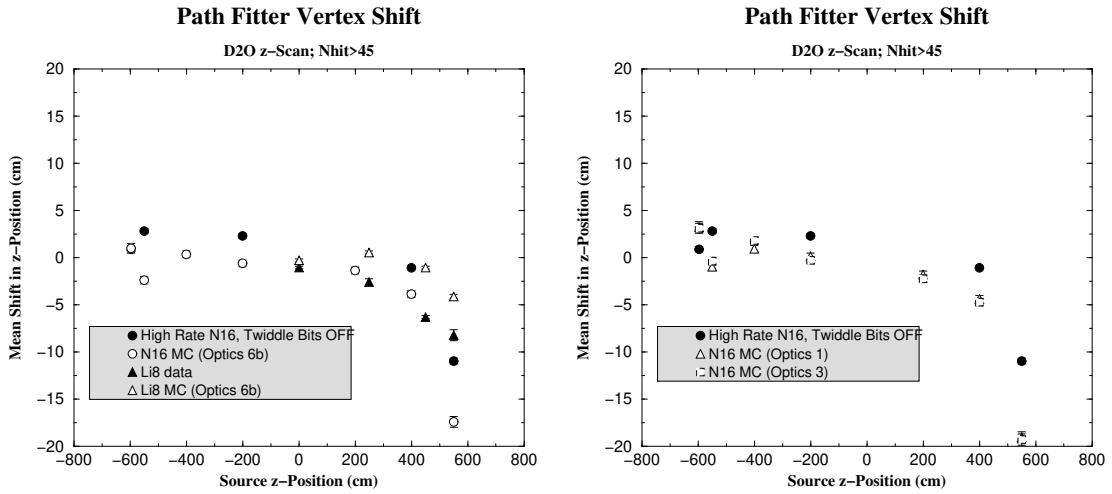


Figure 5.23: Comparison of z vertex shift from  ${}^8\text{Li}$  and  ${}^{16}\text{N}$  source MC and data as a function of source z-position - (left) Optics6b and (right) extreme optics.

### 5.5.2 Angular Resolution

In the previous section, uncertainties in vertex reconstruction were presented. These uncertainties were determined by comparing  $\gamma$  and electron calibration source data to Monte Carlo predictions for vertex shift and resolution. In this section, similar comparisons are made to determine the angular resolution uncertainty.

The ideal calibration source for measurement of angular resolution would be a directed source of single electrons with tunable energies. The angular resolution function for a given electron position, direction, energy in the detector would then be the fraction of events reconstructing within an interval  $[\theta, \theta + \delta\theta]$ , where  $\theta$  is the angle between the reconstructed and known initial electron direction. As previously mentioned, we do have a tagged source of single electrons - the  ${}^8\text{Li}$  source. The initial direction of electrons from this source is not known on an event by event basis, however, so the  ${}^8\text{Li}$  source is not very useful from the standpoint of angular resolution uncertainty.

The  $^{16}\text{N}$  calibration source data can be used as a surrogate for determining angular resolution uncertainty [60]. A Compton scattered electron from a 6.13 MeV  $\gamma$ -ray is preferentially scattered in the forward direction relative to the incident  $\gamma$ -ray direction. This is because the  $\gamma$ -ray energy is considerably larger than rest mass of the electron. But the  $^{16}\text{N}$  source is essentially an isotropic source of  $\gamma$ -rays, so how do we know the incident  $\gamma$ -ray direction on an event-by-event basis? If the scattering vertex,  $\vec{r}_e$ , is known, then  $\gamma$ -ray direction is related to the  $^{16}\text{N}$  source position,  $\vec{r}_s$ , by the simple vector relation (See Figure 5.24)

$$\hat{d}_\gamma = \frac{\vec{r}_e - \vec{r}_s}{|\vec{r}_e - \vec{r}_s|} \quad (5.4)$$

The dot product of this  $\gamma$ -ray direction unit vector with the reconstructed direction gives the cosine of the angle between these two vectors,

$$\cos \theta_{\gamma e} = \hat{d}_\gamma \cdot \hat{d}_{fit} \quad (5.5)$$

The fit vertex,  $r_{fit}$ , is used as an estimator of the true Compton scattering vertex ( $r_{fit} = \hat{r}_e$ ) so that Equation 5.5 simply becomes

$$\cos \theta = \frac{\vec{r}_{fit} - \vec{r}_s}{|\vec{r}_{fit} - \vec{r}_s|} \cdot \hat{d}_{fit} \quad (5.6)$$

Note that this manner of determining the angular resolution couples in vertex reconstruction uncertainties, since the vertex is required to calculate the reconstructed direction of the Compton scattered electron relative to the incident  $\gamma$ -ray direction for a given event. In order to minimize the effect of finite vertex resolution on the angular resolution measurement, only events reconstructing at distance from the  $^{16}\text{N}$

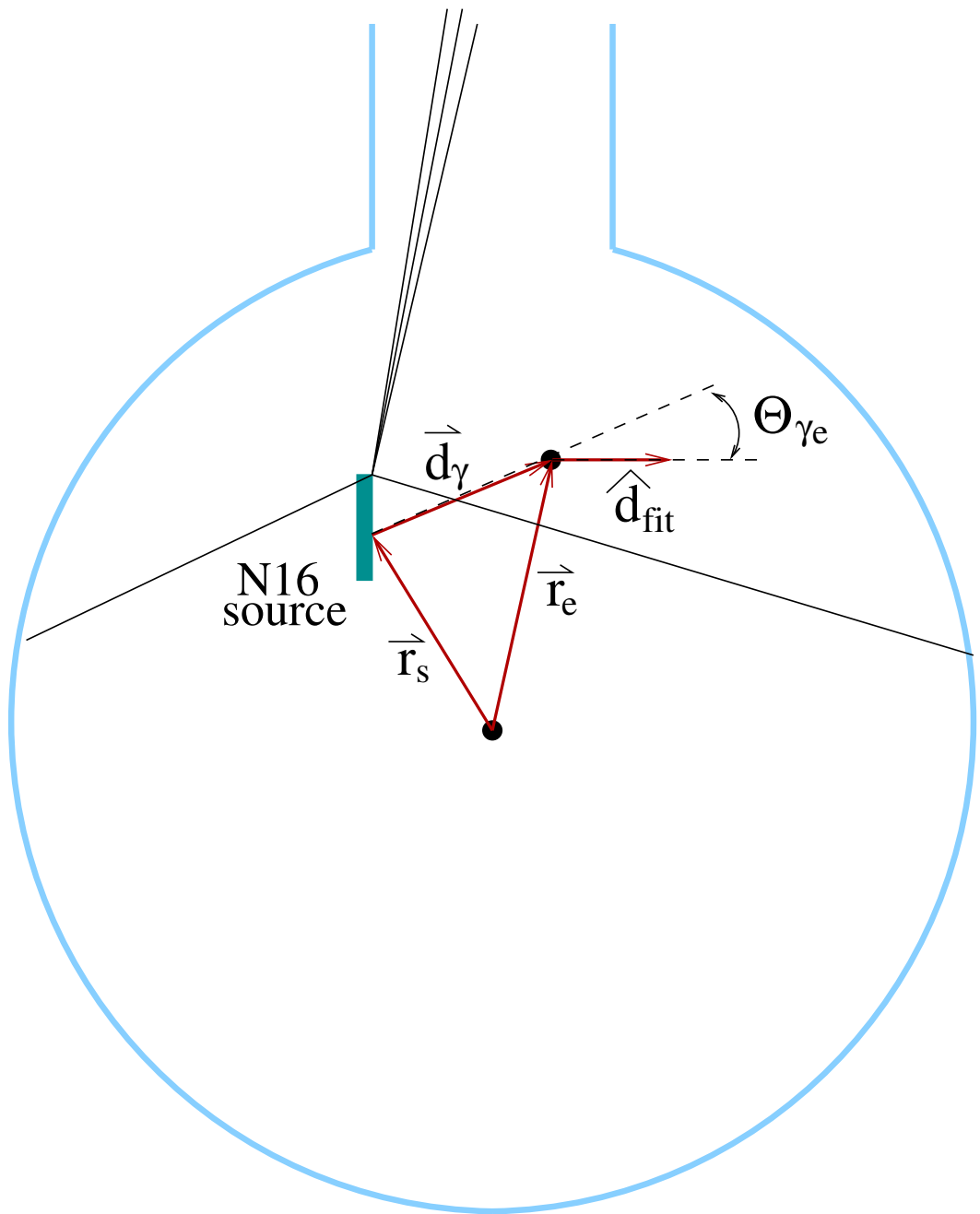


Figure 5.24: Diagram showing vectors involved in measurement of angular resolution using the  $^{16}\text{N}$   $\gamma$ -ray calibration source.

source that is large compared to the vertex resolution are considered.

Figure 5.25 shows a comparison of the  $\cos \theta$  distributions between  $^{16}\text{N}$  calibration data at the center of the detector and source Monte Carlo for events reconstructing more than 1.5 m from the source. From both Figure 5.25 and the log-scale version of this figure (Figure 5.26), it is apparent that the Monte Carlo is in good agreement with  $^{16}\text{N}$  source calibrations for angular resolution in this particular location.

## 5.6 Trigger Efficiency

This section contains a general discussion of the SNO  $N_{\text{Hit}}$  trigger efficiency. See [61] for a more complete description. The author was primarily responsible for developing the methods of measurement as well as data collection and analysis.

### 5.6.1 Introduction

In order to calculate the flux of neutrinos incident on SNO, one needs to connect the observed rates of various types of interactions to the probability of actually triggering the detector on the products of these interactions (e.g.  $e^-$ ,  $n$ ) as well as know the number of targets and the differential cross sections. These trigger probabilities are the acceptances for various types of particles produced by neutrino interactions and depend on the position, direction and energy of the particles as well as host of detector properties such as PMT efficiency/coverage, optical properties of the different media, etc. One particularly important detector property that acceptance depends upon is the trigger efficiency, which is how often the trigger hardware issues a global trigger (i.e. initiates an event) in response to a set of PMTs hit at given times. Therefore, understanding the efficiency of the trigger system is a crucial part of determining the

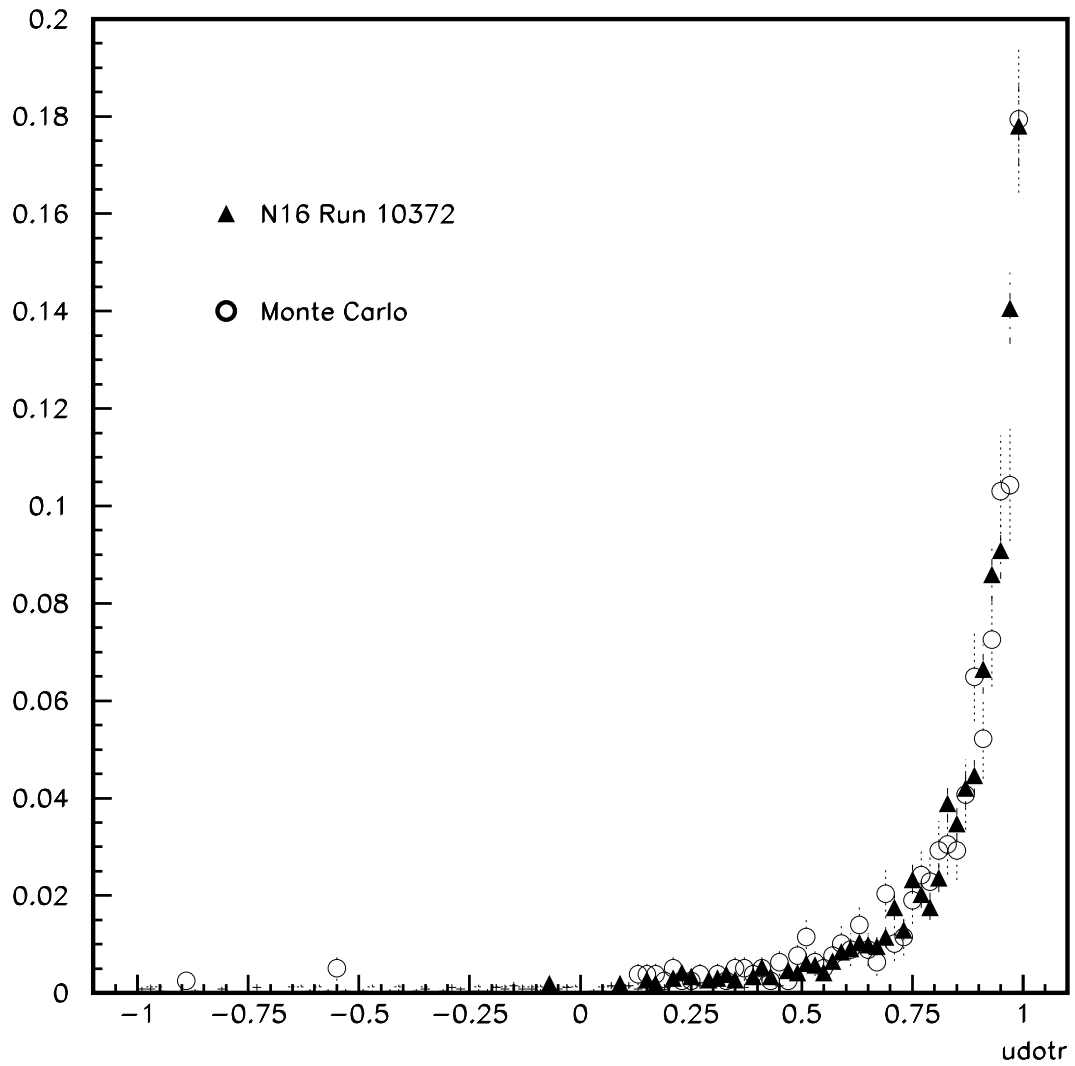


Figure 5.25: Comparison of the  $\cos \theta$  distributions between  $^{16}\text{N}$  calibration data at the center of the detector and source Monte Carlo for events reconstructing more than 1.5 m from the source.

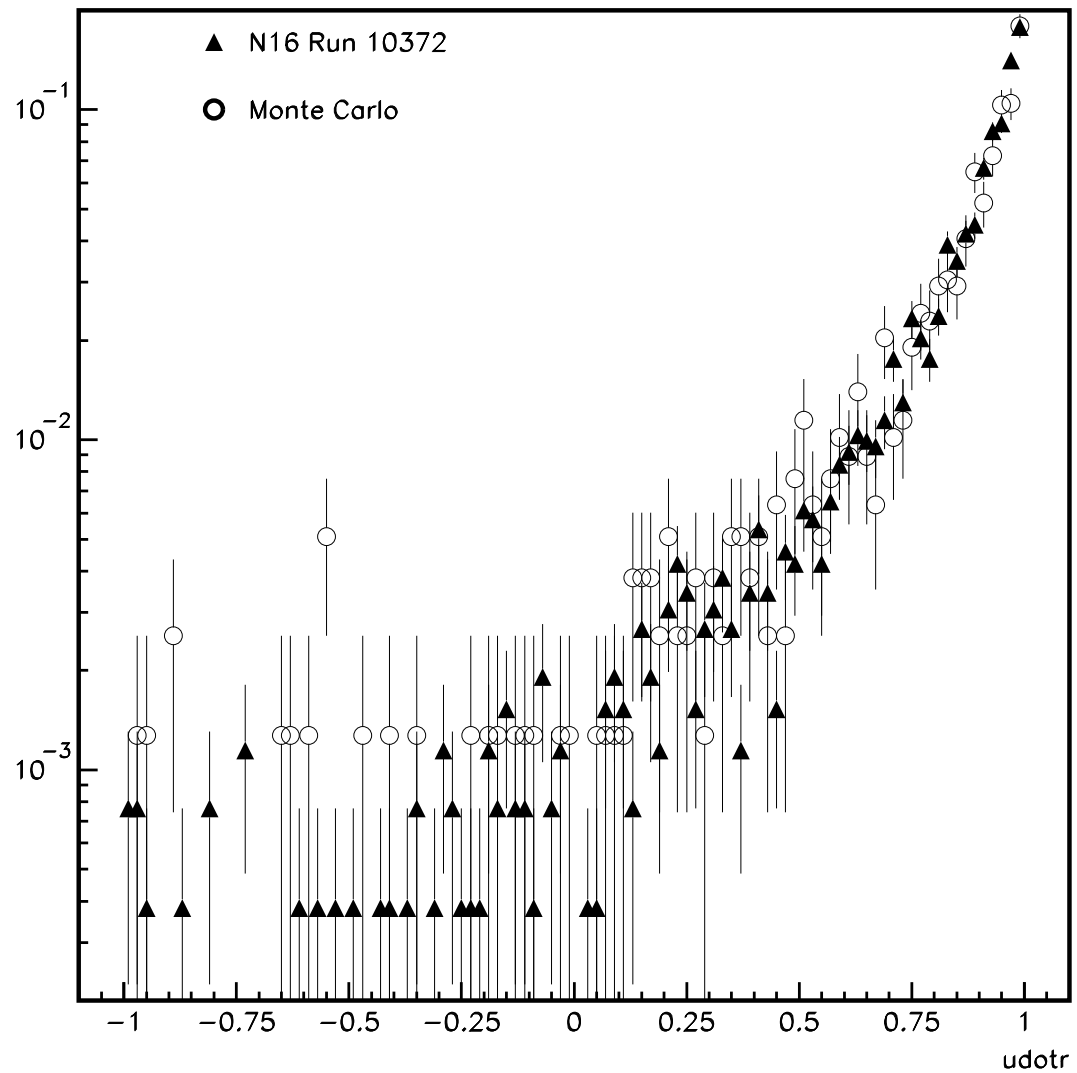


Figure 5.26: Log-scale version of Figure 5.25 showing that the angular resolution tail from  $^{16}\text{N}$  is also in good agreement with Monte Carlo.

acceptance for particles produced by neutrino interactions in the detector.

Although the trigger efficiency is an important part of any physics analysis in SNO, a knowledge of the exact shape of the efficiency curve is not necessary for all analyses. For higher energy neutrino analyses, it may be sufficient to simply know that the trigger efficiency is very close to unity over this energy range so one does not need to worry about trigger contributions to the efficiency. However, as one attempts to push the solar neutrino analysis lower in threshold, the details of the trigger efficiency shape become increasingly important.

In addition to being crucial for data analysis, the trigger efficiency also has a profound impact on how the data is collected. In order to collect as much physics data as possible in the low end of the solar ( ${}^8\text{B}$ ) neutrino spectrum (e.g. where MSW-induced spectral distortions are potentially important), we would like to set our hardware trigger threshold as low as possible<sup>13</sup>. However, there is a large exponential wall of radioactive background events at low energy as well as significant contributions from random coincidences of PMT and electronics noise which ultimately limits how much we can lower our trigger threshold and still stably acquire data. While acute attention to cleanliness is what makes the level of radioactive backgrounds acceptable for analysis, the sharpness of the trigger efficiency curve is a main reason why we are able to stably trigger the detector at a very low threshold in energy (currently 5-10 Hz at 16  $N_{\text{Hit}}$  which is  $< 2$  MeV). This is because a very sharp efficiency curve allows one to be very *efficient* at triggering on events *above* threshold while being very *inefficient* at triggering on events *below* threshold where the rate gets exponentially large.

---

<sup>13</sup>Looking for spectral distortions near SNO's low hardware threshold ( $\sim 2$  MeV) is very difficult at best, however, due to the poor energy resolution and the steeply falling radioactive background wall at these energies.

## 5.6.2 Trigger Efficiency and Acceptance

Measurement of the  $N_{\text{Hit}}$  trigger efficiency involves answering the following question:

For a given trigger hardware threshold, with what probability does the detector trigger as a function of the number of channels hit in coincidence?

In this context, two channels are considered “in coincidence” if they fire within the  $N_{\text{Hit}}$  coincidence time of each other determined by the average width of the analog primitives summed together - 93 ns for the NHIT100 trigger and 20 ns for the NHIT20 trigger. The answer to this question is a curve for each hardware trigger threshold setting, which gives the trigger probability as a function of  $\tilde{N}$ , the number of coincident, or “in-time”, hits. If the shape of the trigger efficiency curve is the same over all relevant threshold settings, then it may be sufficient to simply translate one measured curve rather than apply a different curve for each threshold, but this needs to be investigated with calibration data. It is certainly important to measure the efficiency curve at the current trigger thresholds set in the production data taking. In addition, for higher energy analyses it may be sufficient to know at what  $N_{\text{Hit}}$  (actually  $\tilde{N}$ ) we are 100% efficient rather than the detailed shape of the trigger efficiency curve, as previously mentioned.

It is important to distinguish between trigger efficiency and detector acceptance. Detector acceptance is the probability for the detector to trigger on a particular type of physics signal (e.g. a 5 MeV electron at (0,0,0) in the +z-direction). While the trigger efficiency depends solely on the performance of the detector hardware (and DAQ), the acceptance is much more difficult to determine and depends on many things, some of which are listed below:

- Trigger efficiency for the triggering conditions (trigger thresholds, masks)

- Optical properties (attenuation/scattering in  $H_2O/D_2O$ /AV, AV/PMT reflectivity)
- Detector gain (PMT gain/Q.E., channel efficiencies)
- Geometry (event position/direction, PMT geometry, etc.)
- Physics (Particle energy, Cerenkov light production, electron scattering, etc.)

Therefore, the trigger efficiency is an important piece of information for understanding our detector acceptance, but it is only one piece. Other calibration data and physics/detector simulation is needed to fully estimate the acceptance in the absence of absolute calibration sources.

### 5.6.3 Sources of inefficiency

Although no results of the trigger efficiency measurement have been presented at this point, it is anticipated that, despite our best intentions, SNO does not have a perfectly efficient trigger. As such, this section describes a few sources of inefficiency which can lead to deviations from a perfect step-function trigger (see Figure 5.27).

As discussed in Section 3.5, the trigger system is largely an analog system. This has numerous advantages over a digital system, including speed (fast trigger determination leading to small trigger and channel dead time) and simplicity (trigger information contained in single analog sum). However, maintaining the analog integrity of an approximately  $10^4$  channel sum from 19 separate crates (each of which are bustling with digital activity) to a central rack over 100 ft of cable provides its own set challenges. Below are some analog characteristics which can lead to inefficiencies in the system:

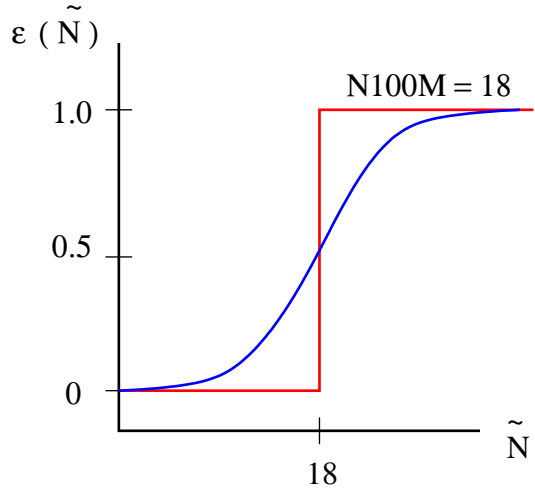


Figure 5.27: Dramatization of how the various sources of trigger inefficiencies can alter the trigger efficiency curve in an ideal system (shown as a step function,  $\tilde{N}$  is the number of in-time hits). The true trigger efficiency curve (shown as a smooth curve) may also be translated along the  $\tilde{N}$ -axis by some types of inefficiencies so that the 50% efficiency point is no longer where  $\tilde{N}$  equals the hardware trigger threshold.

- **Finite rise/fall of analog trigger primitives:** Much of the analog trigger design effort went into generating sharp analog trigger primitives and maintaining short rise/fall times throughout the entire  $N_{\text{Hit}}$  sum. However, some degradation of the trigger pulses is inevitable (e.g. some integration by cable capacitances, etc.) and this results in a loss of efficiency (see Figure 5.28). This effect gets larger as the trigger pulses get more out of time, so one expects this type of inefficiency to be worse for events originating away from the center of the detector where geometric effects will spread out the PMT hit times.
- **Variations in width/amplitude:** Ideally, all analog trigger primitives are exactly the same - 30 mV in amplitude and either 20 ns or 93 ns in duration depending which trigger type one is talking about (NHIT20 or NHIT100) - regardless of which channel fires to give the pulse. In reality, there is a nonzero

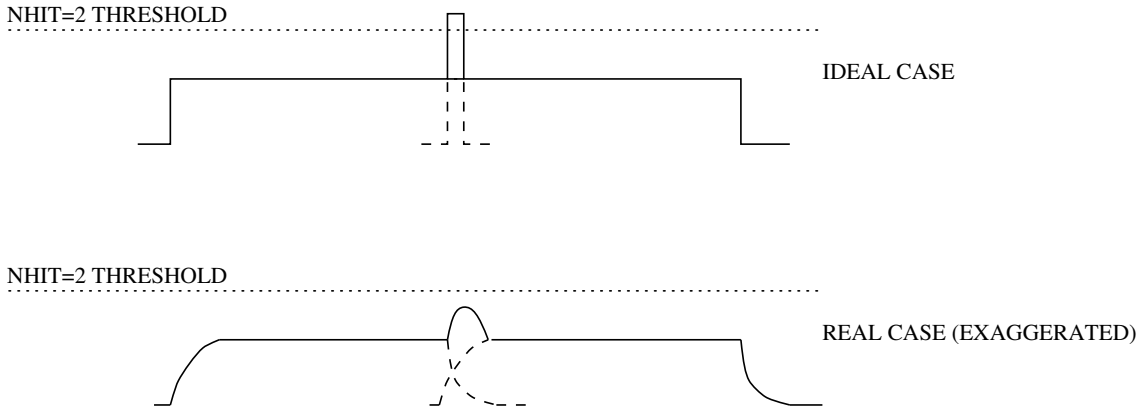


Figure 5.28: Exaggerated diagram of the effects of analog pulse shape on trigger efficiency. In the Figure, a threshold set at  $N_{\text{Hit}} = 2$  triggers for ideal pulses, but not for those with finite rise and fall times.

spread in the distribution of both width and amplitude of the analog primitives which leads to a smearing of the trigger efficiency curve.

- **Electronics noise/pickup:** Any type of electronic noise that is picked up on the trigger lines can lead to inefficiencies in the trigger by altering the shape of the analog sum. This can lead to spurious misses or extra global triggers, depending on the shape and sign of the pickup as well as where in the analog sum it occurs.
- **Baseline/threshold variations:** Any changes in the DC offset of the analog sum or the hardware threshold will change the effective  $N_{\text{Hit}}$  threshold (unless, of course, both change by same amount and in the same direction) and lead to a smearing of the trigger efficiency. These changes could be due to some low frequency pickup, temperature variations,  $1/f$  noise in the current mirror elements, etc.

Aside from these “features” of an analog system, there are some other important

sources of trigger inefficiencies worth mentioning:

- **CMOS (a.k.a “ $N_{\text{Hit}}$ ”) dropout:** This is actually a special type of baseline variation. In this case, the baseline shift is by one unit of  $N_{\text{Hit}}$  and can last for milliseconds or longer, depending on the average rate of the offending channel causing the dropout. What happens is that occasionally a channel-level discriminator will fire in response to a very short threshold crossing in time (i.e. noise or the tip of a PMT signal) and signal the CMOS chip to fire with a runt signal rather than full pulse. These runt pulses can turn on the current source within a CMOS chip that is the  $N_{\text{Hit}} = 1$  analog primitive but fail to turn it off. This current is then summed into the analog network (as is the current from all other channels) and results in a DC-like shift in the analog sum baseline for as long as the channel is “stuck”. Fortunately, this current source seems to get “un-stuck” by the next normal firing of that channel, so the baseline shift from a single channel lasts on average only a few milliseconds ( $\sim 600$  Hz channel rates). However, the dropout is frequent enough so that with  $\sim 10^4$  channels contributing, random dropout coincidences lead to a continually fluctuating baseline of  $\sim 1 - 2 N_{\text{Hit}}$  in magnitude. Since the baseline shift due to a given channel always has the same sign - it always *lowers* the effective trigger threshold for a period of time - this causes the system to trigger at a lower number of in-time hits than it would otherwise and leads to a shifting of this efficiency curve toward lower  $\tilde{N}$ .
- **Orphans:** Since the number of in-time channels,  $\tilde{N}$ , is determined by counting hits in the event, any channels that fire and contribute to the  $N_{\text{Hit}}$  sum but are dropped from the event data stream appear as a trigger inefficiency. These

“orphan” PMT bundles are either associated into the wrong event (i.e. they have a GTID matching a trigger GTID still in the event builder’s circular buffer) or are collected with other orphan PMT bundles into an “orphanage”. These orphan PMT bundles can either be due to a corrupted GTID in a PMT data bundle (hardware orphans) or inefficiencies in the readout/building of events (software or readout-related orphans).

- **Digital inefficiencies:** It is also possible that digital inefficiencies can contribute to the shape of the trigger efficiency curve. For example, how often does a raw trigger pulse from a masked in trigger not generate a global trigger? For healthy raw trigger pulses (20 ns in duration with normal ECL logic levels), production testing of the digital boards with calibration pulses indicates that this contribution is negligible. However, similar to the case of CMOS dropout, discrimination of the final analog sum can lead to runt raw triggers from the MTC/A one-shot to be input on the MTC/D. In this case the MTC/D will still issue a global trigger, however the trigger word latch arrives after the end of the masked in runt raw trigger pulse initiating the event. Since the detector *does* trigger on this threshold crossing its not a loss of efficiency but rather a loss of information about which masked in raw trigger fired.
- **Dead trigger channels:** Channels which are active in acquiring data but do not contribute to the  $N_{\text{Hit}}$  trigger sum are an obvious source of inefficiency. In some sense, these channels are exactly opposite to orphans which contribute to the  $N_{\text{Hit}}$  analog sum but do not give any data to the event. These channels could be inactive because of a hardware problem (e.g. CMOS problem) or their signal path is broken in some way. Alternatively, these channels may have their

triggers deliberately disabled due to some other trigger problem (e.g. excessive CMOS dropout), however there is trigger status information put in the data stream by the DAQ which allows one to know how many disabled channels contributed to a particular event.

#### 5.6.4 Method of Measurement

In order to measure the  $N_{\text{Hit}}$  trigger efficiency, one needs a source of correlated hits to determine the trigger system response to a variety of situations encountered in normal data taking. In the early days of system development, pedestals were used as such a source since one could fire any desired number of channels using the MTC/D on-board pulser. The problem with using pedestals, however, is that they have a fixed time correlation and do not provide a stringent enough test of the analog trigger system to feel comfortable about the system performance under the battle conditions of asynchronous data.

The laserball calibration source provides a triggered source of correlated light in the detector, leading to correlated PMT hits needed for the  $N_{\text{Hit}}$  trigger efficiency measurement. The light from the source is approximately isotropic light with sharp timing ( $\sim 2$  ns) and the source can be moved around the detector to test the position dependence of the efficiency. Another important feature of the laserball system for trigger efficiency is the ability to vary the intensity of the light so that one can test the occupancy dependence and map out as much of the efficiency curve as possible.

It is also possible to use normal  $N_{\text{Hit}}$  triggered data as a source of correlated hits to estimate the trigger efficiency. In this case, one uses the fact that in normal data taking there are multiple thresholds on the same  $N_{\text{Hit}}$  sum, so one can use the lower

threshold as a triggered “source” of correlated hits to study the response of the higher  $N_{\text{Hit}}$  threshold.

Eventually, it would be useful to check the trigger efficiency results with some combination of the  $^{16}\text{N}$  and the  $pT$  calibration sources, which would allow a measurement using Compton scattered electrons rather than diffused laser light. There is no advantage in using this data over the laserball source data except as a check and possibly the psychological advantage of using data more closely resembling the data upon which the trigger efficiency results will be applied (i.e. events due to Cerenkov light). The problem with only using  $^{16}\text{N}$  calibration data is that it does not have sufficient coverage in  $N_{\text{Hit}}$  to sample the interesting parts of the trigger efficiency curve (i.e. near threshold).

In early methods of trigger efficiency measurement, the MTC/D trigger word bits were used to determine how often the various trigger thresholds fire in response to laser light, after careful timing in of the laser trigger signal. This method proved too restrictive due to the narrow latching window for coincident raw triggers, however it is still used as an approximate check on the results. To overcome the shortcomings of methods using the MTC/D trigger word as a latch of the  $N_{\text{Hit}}$  triggers that fire in each event, a new method was devised which greatly increases the width of the latching window from 20 ns to  $\sim 85$  ns. This allows for a more realistic determination of which  $N_{\text{Hit}}$  triggers fire along with the laser trigger (EXT\_ASYNC) in a given event since one is much less sensitive to phantom inefficiencies resulting from narrow raw trigger timing (e.g. reflection triggers). In addition, the more robust trigger latching provides a natural way to measure the trigger efficiency for sources away from the center of the detector without having to change the laser trigger delay timing at each position.

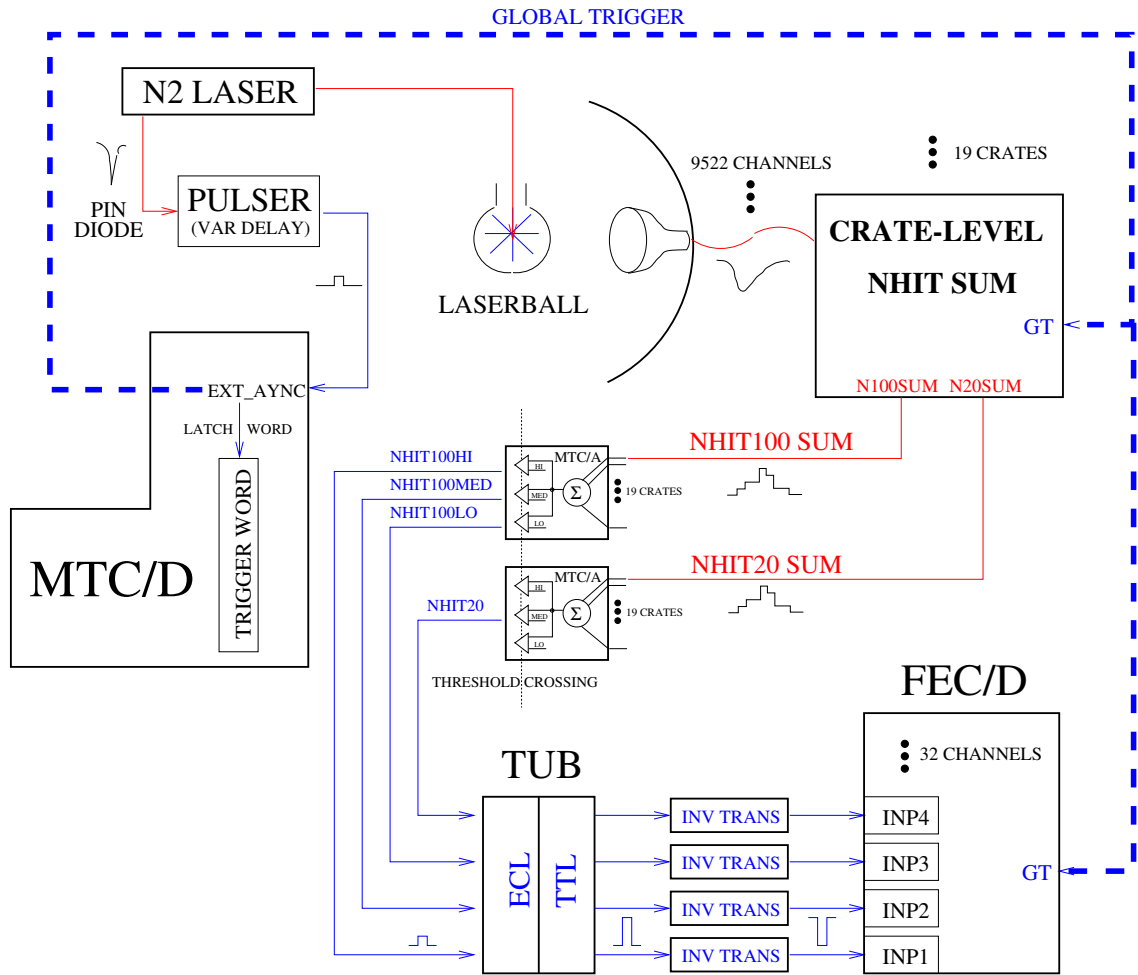


Figure 5.29: Block diagram of trigger efficiency measurement method using the laser-ball with the FEC/D as the trigger latch. The hit status of the FEC/D channels is used to determine which  $N_{\text{Hit}}$  triggers fire during a particular laser event.

The main idea of the method is to use the FEC/D channels - spare calibration channels in slot 15 of crate 17 - as the trigger word instead of the MTC/D. A block diagram of the system configuration during this method of measurement is shown in Figure 5.29. In the FEC/D laserball method, one or more of the  $N_{\text{Hit}}$  raw trigger cables (i.e. the digital ECL lines after the discrimination of analog sum, see Section 3.5) feeding the MTC/D are disconnected. These lines are terminated and converted from ECL to TTL logic levels using one of the many useful features of the Trigger Utility Board (TUB). These TTL lines are then connected to inverting transformers (i.e. transformers with their output lines switched - essentially an analog inverter) and each are plugged into one of the FEC/D channel inputs. So each of the FEC/D channels connected in this way receives a negative going TTL pulse when the corresponding  $N_{\text{Hit}}$  trigger fires in an event.

The laserball calibration source is used for this measurement in the following way. Each laser pulse is coupled through a set of fiber optic cables to a diffusing ball (the laserball) in the detector to produce an approximately isotropic source of light with adjustable intensity. There is also a PIN diode monitoring the light from the laser which supplies a trigger for the diffused light in the detector. This PIN diode signal is discriminated by a pulser which provides an adjustable delay between the PIN diode pulse and a 20 ns ECL pulse that is sent to an external (asynchronous) trigger input on the MTC/D. A global trigger (GT) is then issued by the MTC/D since one masks in the EXT\_ASYNC trigger type.

In this method, the laser trigger is delayed as much as possible without losing prompt tubes off the early side (the “curl”) of the TAC window<sup>14</sup>. This moves the

---

<sup>14</sup>Note that *delaying* the laser trigger moves the tubes hit by light as well the FEC/D channels *earlier*.

FEC/D channel times as early as possible to get the largest dynamic range on the  $N_{\text{Hit}}$  trigger firing time. This dynamic range is constrained by the cable length to the FEC/D as well as how much the global trigger (initiated by the laser trigger) can be delayed without losing the earliest prompt light PMTs. With the laser trigger delays used for the measurements in this report, the dynamic range turns out to be  $\sim 85$  ns on the late end of the time the  $N_{\text{Hit}}$  raw triggers fire the FEC/D channels on the prompt laser light.

The data is analyzed by sliding a 93 ns window throughout the spectrum of hit PMT times to determine the maximum number of in-time channels,  $\tilde{N}$ , in each event. To determine whether or not a particular  $N_{\text{Hit}}$  trigger fired in a given laser triggered event, one simply looks to see if the corresponding FEC/D channel is in the event. In practice, there is an additional check on the low gain integrated charge (QLX) for any FEC/D channel in the event to ensure that the channel fired on a TTL pulse from the corresponding raw trigger rather some sort of noise or pickup. Therefore, for a given value of  $\tilde{N}$  representing the maximum number of hits in any 93 ns time window, the trigger efficiency is the ratio of the number times the  $N_{\text{Hit}}$  trigger is observed to fire based on the FEC/D channels to the total number  $\tilde{N}$  occurrences over all events.

### 5.6.5 Results

In this section, trigger efficiency results using the FEC/D latch method are presented. Details about the analysis used to arrive at these results can be found in [61].

The results of the trigger efficiency analysis using the laserball with FECD/latch method are shown in Figures 5.30 and 5.31 for the laserball at the center of the detector and at  $z = -5$  m, respectively. The results at the center indicate  $\sim 3.5$

## Trigger Efficiency Using FEC/D Latch Method

Laserball Runs 5743–7, 5749–51 with  $x = y = z = 0$

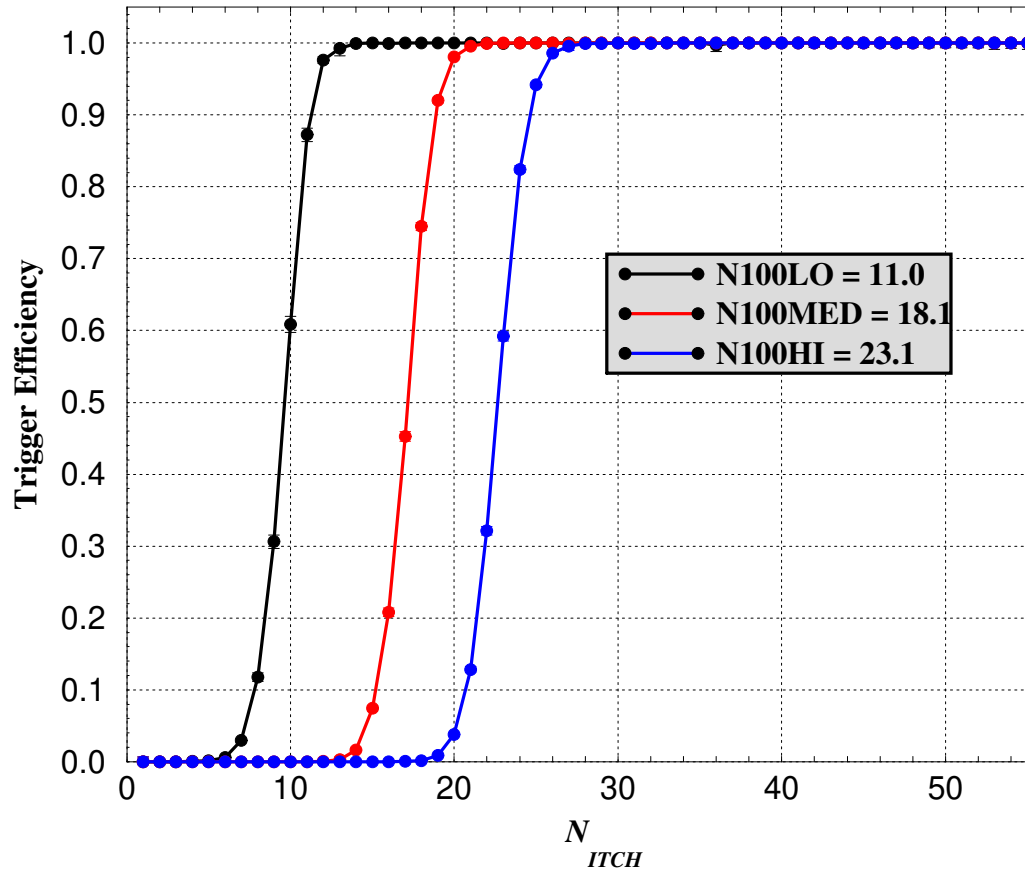


Figure 5.30: Measured trigger efficiency using the laserball with the FEC/D as the trigger latch. The laserball position is  $x = y = z = 0$ .

## Trigger Efficiency Using FEC/D Latch Method

Laserball Runs 5769–71, 5773–5 with  $x = y = 0, z = -5$  m

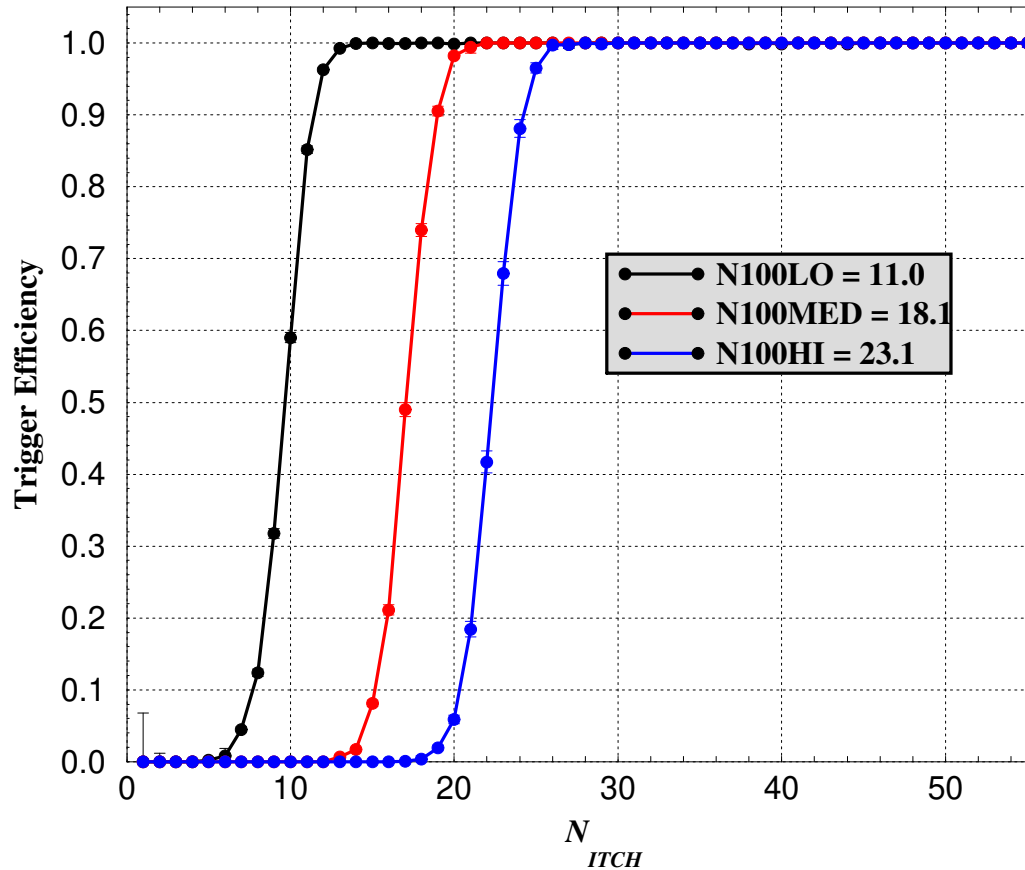


Figure 5.31: Measured trigger efficiency using the laserball with the FEC/D as the trigger latch. The laserball position is  $x = y = 0, z = -5$  m.

$N_{\text{Hit}}$  turn-on for the N100L threshold and  $\sim 3.8 N_{\text{Hit}}$  turn-on for the N100MED and N100HI threshold triggers. The trigger efficiency for the laserball at  $z = -5$  m is almost identical to the results at the center, except near threshold where the efficiency is rapidly changing and the maximum difference is between 2% and 25% for the low and high  $N_{\text{Hit}}$  thresholds, respectively. While most prompt hits are close in-time for the laserball at the center of the detector, at  $z = -5$  m the hits from an isotropic source are more spread out in time due to geometric effects, so this is a good test of the analog integrity of the  $N_{\text{Hit}}$  primitives summed together in the trigger system. The sharper and more uniform the analog N100 primitives throughout the  $N_{\text{Hit}}$  sum, the less position variation there will be in the  $N_{\text{Hit}}$  trigger efficiency. Another interesting feature of the measured efficiency curves is that deviation between the  $N_{\text{Hit}}$  hardware threshold and the 50% efficiency  $N_{\text{Hit}} (\tilde{N})$  decreases approximately linearly with  $\tilde{N}$ . This is most likely due in part to the changing fractional contribution of CMOS dropout to the effective threshold. Recall from the discussion of trigger inefficiencies in Section 5.6.3 that CMOS dropout leads to a *reduction* in the effective  $N_{\text{Hit}}$  threshold which shifts the efficiency curve toward lower  $\tilde{N}$  for the period of time that an offending channel is dropped out.

It was previously mentioned that most early neutrino analyses in SNO will be at energies well above our hardware threshold of 16  $N_{\text{Hit}}$ <sup>15</sup>. Based on the trigger efficiency results presented in report, one might expect the detector to be fully efficient at triggering on the higher energy neutrinos, but this is ultimately an acceptance question which depends only in part on the trigger efficiency. Therefore, it is important to know under what conditions the trigger system is very near 100% efficient so

---

<sup>15</sup>Trigger efficiency measurements were performed for an 18  $N_{\text{Hit}}$  threshold on the N100MED trigger, which was the threshold at start of production neutrino data taking.

$\tilde{N}$	Laserball z (m)	$\epsilon(\tilde{N})$	
		N100MED = 18.1	N100HI = 23.1
21	0	$0.996^{+0.003}_{-0.005}$	$0.125^{+0.005}_{-0.005}$
22	0	$0.9992^{+0.0003}_{-0.001}$	$0.335^{+0.007}_{-0.007}$
23	0	$1.000^{+0}_{-0.0004}$	$0.599^{+0.008}_{-0.008}$
21	-5	$0.997^{+0.001}_{-0.006}$	$0.19^{+0.01}_{-0.01}$
22	-5	$1.000^{+0}_{-0.002}$	$0.42^{+0.02}_{-0.02}$
23	-5	$1.000^{+0}_{-0.003}$	$0.69^{+0.02}_{-0.02}$

Table 5.3: Trigger efficiency results near full efficiency for the N100MED threshold using FEC/D latch method.

that contributions to the acceptance from the trigger efficiency are negligible.

Table 5.3 contains the numerical trigger efficiency results for the N100MED and N100HI thresholds around the number of in-time hits where the N100MED efficiency approaches unity. If one considers  $\epsilon > 99.9\%$  as representing negligible inefficiency in the trigger, then it is apparent from Table 5.3 that the system is fully efficient (within one standard deviation) at  $\tilde{N} = 22$ . To add a margin of safety in the results, one can consider the main physics trigger for the detector - the N100MED - fully efficient at  $\tilde{N} = 23$  for sources within 5 m of the center.

There is an additional safety margin in the validity of the full efficiency result due to contributions from other masked in triggers. Recall from Section 3.5.3 that a global trigger is issued on the logical **OR** of all masked in trigger types, so to properly answer the relevant question - “how often does the trigger system issue a global trigger on  $\tilde{N}$  channels firing in coincidence?” - one needs to consider contributions from all masked in trigger types. For example, the N100HI threshold is  $\sim 60 - 70\%$  efficient at  $\tilde{N} = 23$  so one might expect that a large fraction of the medium threshold “misses” will still fire the high threshold and trigger the detector. This is a bit naive because

of the strong correlation between the two thresholds - they discriminate the same analog sum so a miss of one may be correlated to a miss in the other - but the effect of the other masked in triggers can only *increase* the efficiency at a given  $\tilde{N}$ .

Additional checks and systematics on the trigger efficiency can be found in Appendix C, as well as a discussion of how to scale the trigger efficiency for disabled trigger channels.

## 5.7 Summary

In this chapter, calibrations of the SNO detector that are relevant for this analysis were discussed. In addition to the low-level calibrations (ECA, PCA, HCA, optical) which are a pre-requisite for interpreting the data stream, several higher level calibrations (energy, reconstruction, trigger efficiency) which enter into the systematic uncertainties on solar neutrino results were presented. The energy and reconstruction studies of calibration source data compared to source Monte Carlo results set the scale of systematic uncertainty in the use Monte Carlo to characterize signal and background distributions in reconstructed radius, direction, and energy ( $N_{\text{Hit}}$ ). In the next chapter, we begin analysis of the neutrino data by presenting reduction of the calibrated but otherwise raw data stream into a data set that is useful for neutrino signal extraction.

# Chapter 6

## Data Reduction

Everything about the SNO detector - from design, to construction, to its previous and current mode of operation - is ultimately motivated by the primary goal of recording as much data on the neutrino signals of interest (based on the physics goals for the experiment) with highest signal-to-background ratio as possible. The purpose of data reduction is to achieve the second part of this goal - that is, to maximize the signal-to-background ratio of the data using known properties of neutrino interactions in the detector and information that the detector provides. The largest cut on detector information by far has already been discussed in great detail in Sections 3.5 and 5.6 - the trigger system. This system instructs the front end electronics to save accumulated PMT information only when there is a sufficient number of in-time PMT hits, using the fact that neutrinos interact in localized regions of the detector and generate light over short time scales compared to the time resolution of the system (dominated by PMT transit time jitter). As emphasized in Section 5.6 on trigger efficiency, the main design goal of the trigger electronics is to make this cut on PMT information as sharp as possible.

After the trigger system decides that an event is interesting enough to store - neutrino induced or not - the PMT and trigger information for that event become part of the data stream that is analyzed. It is now up to the analyzers to further reduce the data using this stored information and knowledge about how neutrinos interact with the detector. Many of the analysis tools used to perform this reduction of data have already been presented - reconstruction (Chapter 4) and energy (Section 5.4) cuts, higher-level Cerenkov signal cuts, etc. In this chapter, selection of the data set used for this thesis and the cuts applied to this data before signal extraction and residual background estimation (see Chapter 8) are presented in a systematic way.

## 6.1 Run Selection

For the purpose of neutrino data collection in SNO, a run is designed to represent a constant detector configuration with standard triggering configuration for neutrino detection (recall Table 3.1). In practice, a maximum run duration is also imposed (24 hours) which is merely for bookkeeping purposes as a new run with the same detector configuration is automatically initiated. After the runs are collected and archived, the set of runs used by the collaboration for solar neutrino analyses is generated by the Run Selection Committee. Run selection is based on information from a DAQ generated run header in the data file as well as investigation of shift reports to look for problems with the detector hardware, software, or other conditions that would compromise data integrity. One always has to be careful about subjective selection of data, as anomalous data collection could represent real physics (e.g. a supernovae) rather than problems with the detector. Therefore, the majority of run selection is based on pre-determined, objective criteria (e.g. electronics crates off-line, activity on

deck) applied to the data rather than reports from operators. However, operators are trained to spot purely hardware and software related problems, so this information is considered. See [2] for a more detailed discussion of run selection criteria.

The data upon which this thesis is based consists of 410 selected runs taken from November 2, 1999 (run 10000) to January, 4, 2001 (run 14685) . These runs comprise 245.6 days of neutrino livetime, however, a fraction of this data is kept blind (i.e. unexamined) within the collaboration<sup>1</sup> at the time of writing this thesis. In particular, only 10% of the data after July 1, 2001 (end of run 12168) is allowed to be analyzed. Therefore, the actual livetime for this analysis is 169.3 days.

## 6.2 Removal of Instrumental Backgrounds

In addition to Cerenkov light, there are many things going on both inside and outside of the detector that satisfy the trigger criteria and will consequently generate data. The vast majority of these events originate from the instrumentation itself (e.g. PMTs) and are therefore referred to as “instrumental backgrounds”. As we will see, these range from the trivially identified to the down-right frightening.

An enormous amount of collaboration analysis effort - arguably more than any other analysis topic - has gone into the study of instrumental backgrounds [62–64]. This effort includes identifying these backgrounds, studying properties such as event topology and time dependence, developing a suite of cuts which remove the vast majority of all known instrumental backgrounds, and determining the unavoidable sacrifice of neutrino data involved in cutting these backgrounds from the data set. The scale of this analysis effort is not without good reason - the rate of instrumen-

---

<sup>1</sup>This is intended to limit *statistical* bias in analysis of the neutrino data.

tal backgrounds dominates the expected number neutrino events by more than two orders of magnitude under steady-state conditions. When bursts of instrumental backgrounds occur (which are not at all uncommon), this dominance over neutrino events is far larger.

This section begins with a brief stroll through the SNO instrumental background zoo and ends with a description of the cuts used to remove these backgrounds from the data stream. A zoo is maybe not all that bad an analogy, not only because these backgrounds consist of many strange animals from all corners of the world (detector), but also because we believe we have enough handles on these backgrounds to view them as locked up in cages for harmless viewing.

### 6.2.1 Zoology of the SNO Instrumental Backgrounds

This section on the zoology of SNO instrumental backgrounds is not meant to be a comprehensive discussion by any means. Rather, it is included to give the reader a sense of the types of instrumental effects that can complicate analysis of the data from a complex solar neutrino experiment such as SNO.

#### PMT Flashers

The spontaneous emission of light by PMTs under high voltage was one of the first phenomena observed<sup>2</sup> in operating the detector. While the exact mechanism is not completely understood, it is likely that light is emitted as a result of a partial high voltage discharge deep inside the tubes, probably within the dynode structure.

---

<sup>2</sup>One of the first people to observe flashers in SNO was Peter Wittich who noticed intermittent, anomalous PMT pulses on the ESUM trigger signal. Consequently, these are referred to as “Wittich Pulses” in the literature. Initially ignored by others, these pulses were later understood to represent the voltage incarnation of SNO’s largest solar neutrino background.

The total rate of flasher events is on the order of 1 event per minute or about 1 flasher/week/PMT (see Figure 6.1). At  $N_{\text{Hit}}$  thresholds above the background wall of Cerenkov light ( $\sim 45 - 50 N_{\text{Hit}}$ ) from U/Th radioactivity, PMT flashers represent by far the largest solar neutrino background. As a result, flashers have been studied by many people and much has been learned about them. A few of their characteristics are listed below:

- Flasher events are not the result of a few tubes generating light. Rather, it appears that *all* PMTs flash at some level implying that the effect is a generic feature inherent to SNO PMTs under HV. Some PMTs flash more than others within a given time period; however, the same worst offenders do not appear in every time interval.
- There is evidence for a charging and subsequent discharging effect in the time structure of the events occurring over long periods of time. Specifically, many PMTs are observed to flash with an accelerating time structure and then stop for periods of time that are long compared to the normal time between flashes.
- The light from flashers completely covers the energy ( $N_{\text{Hit}}$ ) range relevant for solar neutrinos. The flasher  $N_{\text{Hit}}$  spectrum extends from tens of hit PMTs up to 300 - 400  $N_{\text{Hit}}$ .
- Several flasher characteristics are found to be HV-dependent. For example, using the fact that PMTs in SNO are operated over a range of HV in an attempt to match PMT gains ( $\sim 1600 - 2300$  V) one observes that both the average flasher rate and  $N_{\text{Hit}}$  increase with higher HV setting. There also seems to be some conditioning effects at work after changes in HV setting (see Figure 6.1)

00/01/05 15.24

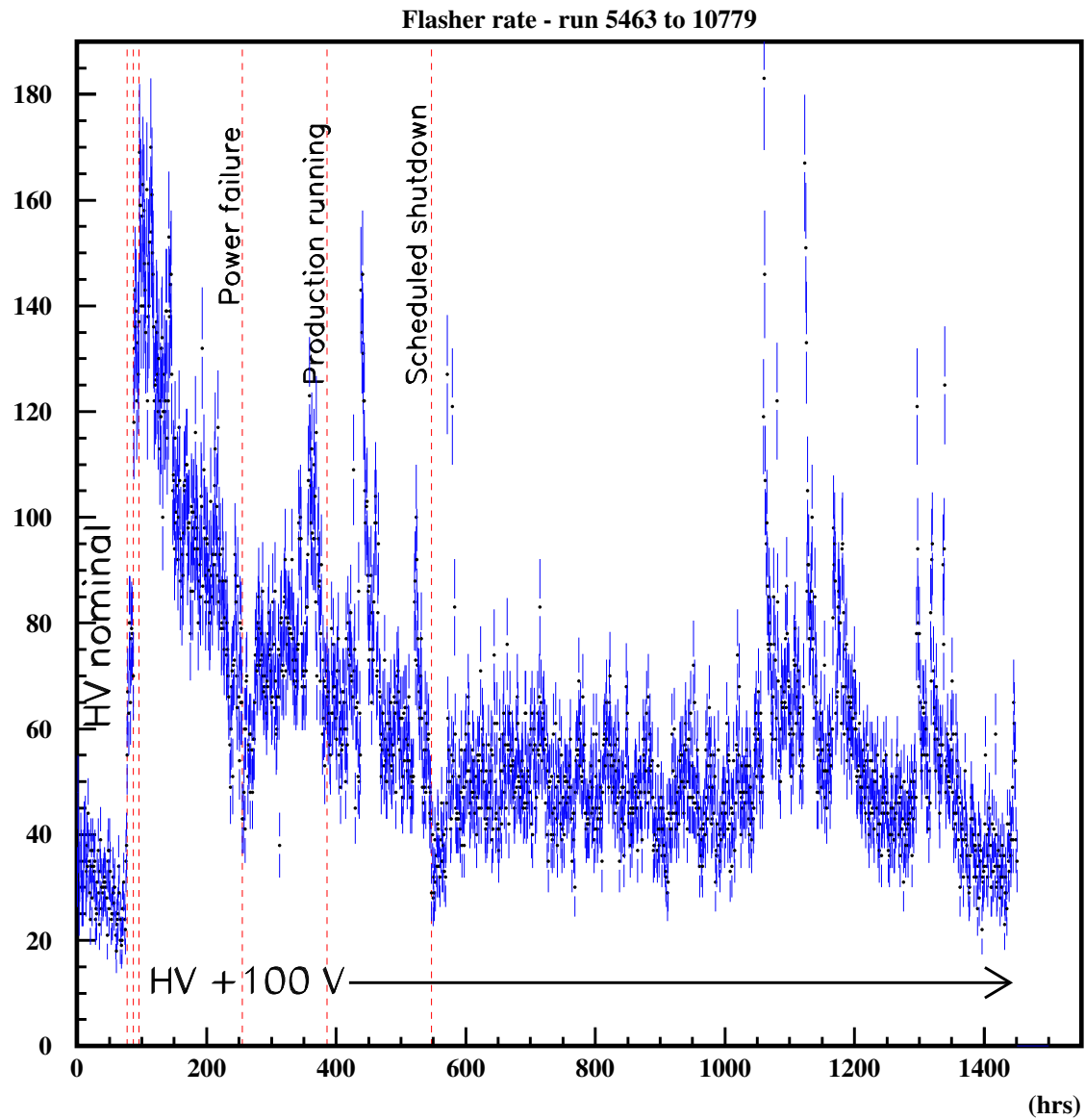


Figure 6.1: Flasher rate over 160 hrs of neutrino livetime around the beginning of production running (run 10000). The plot in this figure is a histogram of number of flashers events per 1 hr bin.

for rate dependence and conditioning).

- Bursts of flasher events are evident in the data. Many of these occur directly following seismic events in the mine (e.g. blasting, rock bursts). A hydrophone has been installed in the light water (outside the PSUP) which generates tagged triggers on any significant acoustic signal in the water. Flasher bursts are observed to correlate with these so-called “HIB” triggers and also geophone data from INCO.
- The voltage signals from flashers are very large (several tens of volts) compared to typical single photoelectron signals ( $\sim 30$  mV). This results in a large integrated charge on the flasher channel<sup>3</sup> and a cluster of pickup hits in the surrounding electronics channels and channels connected to nearby PMT cables.
- A long (several microseconds) after-pulse follows most flasher events. The hypothesis is that flasher light generated inside the tube generates a very large number of photoelectrons when it passes through the photocathode on its way out into the detector and these electrons ionize residual gas inside the PMT enclosure.
- The pattern of light imaged on the opposite side of the detector is elongated with respect to one axis (i.e. elliptical). If one integrates the pattern of hits from a single flashing PMT, one can clearly see this elongated pattern along with other regions of PMT hits that are different for different PMTs. These isolated pockets of hits and elongated patterns are suggestive of some shadowing effects inside the PMTs from where the light is generated.

---

<sup>3</sup>Actually, the Q integrals (QHS, QHS, QLX) wind up being *below* pedestal due to some saturation effect on the front-end electronics.

- Within a given flasher event, the time spread of PMTs hit by light from the flashing PMT is larger than that of Cerenkov light. This important observation is the basis for a data cleaning cut developed by the author and is discussed in Section 6.2.7.

Although the rate of PMT flashers relative to the expected solar neutrino rate is alarming, it should be clear from the previous (partial) list of characteristics that the vast majority of these events are quite distinct from neutrino induced events. A particularly nasty type of flasher (a “blind” flasher) does not “see” its own light. For example, a tube could be very low gain or have a broken signal path such that no appreciable signal is observed on the flashing PMT. In the very low gain PMT case, the distinctive pickup cluster surrounding the flashing PMT channel may be completely absent. The main weapon against blind flashers is the careful identification of low gain PMTs and broken signal-path channels during periods of maintenance and laserball calibration. Data collected between these periods may still contain blind flasher events, however, so other means of removing these events are required. The large time spread of hits from flasher light, briefly described in Section 6.2.7, is one valuable handle. Reconstruction and high-level Cerenkov signal-box cuts also cut blind flashers because of the time spread and elongated pattern of hits, and also because they originate far from the fiducial volume imposed in the analysis.

## High Voltage Breakdown

High voltage breakdown triggers the detector because of the large signals involved - up to the full 2 kV HV discharge. High voltage breakdown in the wet end connector of the signal/HV cable has already been discussed in Section 3.2.2. HV breakdown can

also occur above the deck in the cables or the HV electronics (paddle card, PMTIC). These events are very distinct from neutrino events and can easily be removed with charge, electronics cluster, and burst-based cuts. HV breakdown events are usually a mere annoyance to stable data taking (except when their rate is high!), but can sometimes stop a run by tripping the current limit on a given crate supply.

### **Flat-TAC events**

It is observed that bursts of DC-like light in the detector can occur which appear as events with flat or nearly flat TAC spectra. These events are often associated with the loss of a PMT's ability to function. Many of the OWL tubes fire in these events and have large charge. The interpretation is that these events are caused by sparking in the PMT base from a compromised water seal that ultimately leads to the demise of that PMT.

### **Neck Light**

Light originating from the acrylic vessel neck region is observed in the data. The hypothesis is that this light originates from some static discharge of the acrylic neck or piping that exists in this region, as the rate of neck events drastically increases when large water circulation changes are made. Other sources of static charge are likely contributing to light from the neck region. To help identify these events, additional PMTs were placed in the neck region and instrumented to the electronics. These events also have a broad time distribution and are consequently tagged by time spread cuts.

## Manipulator and Umbilical light

Large amounts of light are found to accompany source deployment. The light generation is particularly high when sources are being moved around the detector by the manipulator system. This so-called “manipulight” - presumably due to charge-discharge on manipulator-related hardware - is not an issue during neutrino data taking as no sources are deployed during this time, but its existence does increase the time required to perform calibrations. It is also found that light is generated by the source umbilical during deployment.

## Electronics pickup

Events can be generated by pickup in the electronics. This includes both external noise sources and internal sources such as digital noise from readout and other bus accesses. Hits from electronic noise can coincide with Cerenkov light hits to increase the probability that these light hits satisfy the trigger criteria and generate an event. Since there is higher probability for certain channels to fire from pickup, these events usually have distinct crate-space topologies. In particular, the outer channels (0 and 31) and FECs (0 and 15) have in general worse problems with pickup than other channels so that electronics pickup events often appear ring-like in a crate-space view. Isolated electronics pickup events can be identified by charge and cluster based cuts as well as cuts on the isotropy of hits within a crate. Coincidence of electronics pickup with hits from Cerenkov light is more difficult to identify.

## 6.2.2 Approach to Instrumental Background Removal

In Section 6.2.1, several types of instrumental backgrounds found in the data were presented. The approach taken to removing instrumental backgrounds is to carefully study the way the detector responds to Cerenkov light and develop cuts that remove events which are very unlikely to be a result of Cerenkov light in the detector rather than produce algorithms that are designed to cut specific types of instrumental backgrounds. The identified instrumental backgrounds samples are used as a guide for determining which quantities are likely to remove the vast majority of these types of events. They also serve as an approximate way of determining the efficiency with which the developed cuts remove these particular background types.

As the data cleaning cuts represent the very front end of the analysis, an attempt was made to make the cuts robust to detector changes and to keep them as simple as possible. For these reasons, reconstruction algorithms (which were in flux at the time of data cleaning cut development) are not a part of data cleaning. Higher level cuts based on reconstruction are a part of the data reduction process but are applied after the majority of instrumental backgrounds have been removed. These post-reconstruction cuts are described in Section 6.4.

## 6.2.3 Junk Cut

By the name of this cut, one might think that this cut is all one needs to remove unwanted events. In actuality, this cut removes the following event types with hardware and DAQ pathologies:

- Orphan events. See Section 5.6.3 for the description of an orphan event.

- Events with multiple channel entries (very infrequent).

#### 6.2.4 Burst Cuts

Many of the instrumental types have a burst-like time structure. For example, we saw from Section 6.2.1 that bursts of flashers often accompany seismic events in the mine. Bursts of several solar neutrinos on the time scale of seconds is extremely unlikely. The following burst-type cuts on the time structure of events were used:

- **Retrigger:** Cuts events which follow another event by less than  $5 \mu\text{sec}$ .
- **Burst:** Cuts all events in any set of three events or more which occur in a total time of 1 msec or less.
- $N_{hit}$  **Burst:** Cuts all events in any set six or more  $N_{hit} > 40$  events which occur in a total time of 4 sec or less.

#### 6.2.5 Charge Cuts

The fact that most PMT hits from neutrino events are single photoelectron, coupled with knowledge of the PMT + channel charge response provides constraints on the total amount of integrated charge one expects for neutrino events. The charge information can also be combined with time and  $N_{Hit}$  information to make charged-based cuts more powerful and robust. The following charge-based cuts were used:

- **QCluster:** Cuts events which have four or more channels hit in a five channel-wide sliding window, and at least one channel has a QH (QL) charge 2000 (300) counts above pedestal.

- **QvT**: Cuts events which have a maximum QH (QL) charge of more than 1000 (180) counts away from the average charge and were hit at a time more than 60 ns earlier than the median time.
- **$Q/N_{hit}$** : Cuts events which have an average charge less than 0.25 photoelectrons after the highest 10% of the charges are removed.
- **Analog Measurement Board (AMB)**: Cuts events which have the normalized Analog Measurement Board's *integral* or *peak* measurement of the ESUMHI signal more than  $3.7\sigma$  away from the average for events with the same  $N_{hit}$ .
- **ESUM Trigger**: Cuts events in which only the ESUMHI trigger was recorded to have fired.
- **OWLEHI Trigger**: Cuts events in which the OWLEHI trigger was recorded to have fired.

### 6.2.6 Hit Geometry Cuts

It is very unlikely for neutrino events to produce certain hit PMT and channel patterns that instrumental backgrounds exhibit in the detector. With this in mind, the following cuts on hit PMT and channel patterns were used:

- **Flasher Geometry (FGC)**: Cuts events which have a channel or PMT position cluster that is accompanied by PMT hits whose average distance from the cluster is more than 1200 cm.
- **Crate Isotropy**: Cuts events with more than 70% of the hits in one crate, and more than 80% of those hits are two or fewer FECs.

- **Neck:** Cuts events which have either two of the neck PMTs hit or one neck PMT hit at an early time relative to the other hits in the event.
- **OWL:** Cuts events which have five or more outward-looking (OWL) PMTs hit.

### 6.2.7 Time Spread Cuts

It was noted in Section 6.2.1 that some instrumental background events (e.g. flashers, flat-TAC) have broad TAC spectra. The TAC spectra for neutrino events are comparatively narrow due to the sharp nature of Cerenkov light generation relative to the transit time jitter of SNO PMTs. Since the data cleaning cuts as designed do not to rely upon fit information, one needs to worry a bit about how geometric effects from event location broaden the Cerenkov light TAC spectra. However, limits on the width of the time distribution can be deduced and used as a cut on certain types of instrumental background events.

Two event time spread cuts used by the collaboration for data cleaning were developed by the author. These cuts are briefly described below:

#### Fitterless Time Spread (FTS) Cut

In section 6.2.1, a particularly worrisome type of flasher event was described where the PMT initiating an event through spontaneous emission of light and the characteristic surrounding channels of cross-talk are not included in the event. One handle on these so-called “blind” flasher events is that the hits on opposite side of the detector from the flashing PMT have broad TAC spectra compared to hits from Cerenkov light. The FTS cut was designed to exploit this property of flasher events. The idea is to use the median absolute time difference ( $\delta t \equiv |t_i - t_j|$ ) of all “close” hit PMT

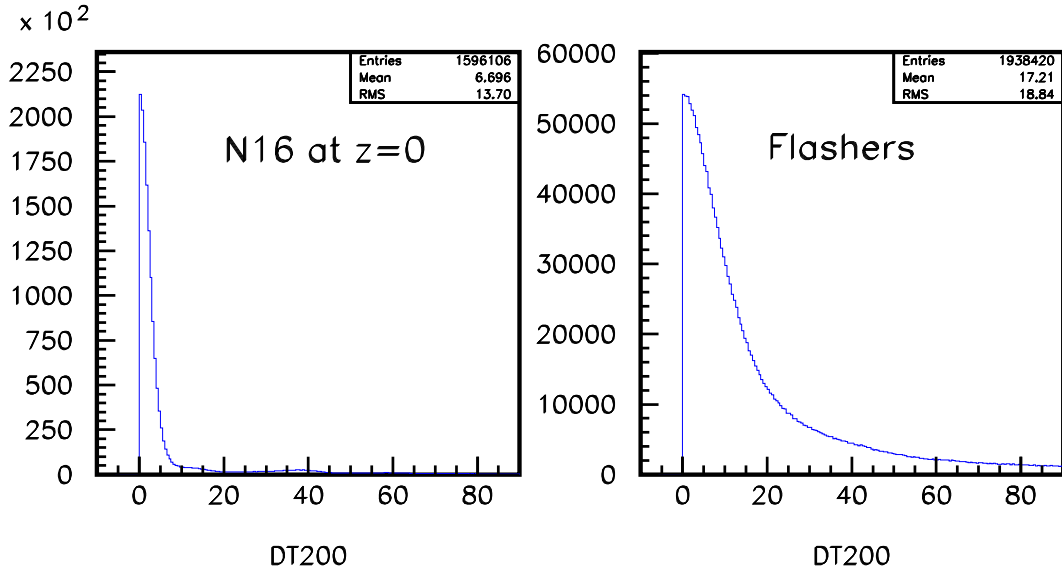


Figure 6.2: Distribution of  $\delta t$  for hit PMT pairs with  $|\vec{r}_i - \vec{r}_j| < 2$  m in  $^{16}\text{N}$  calibration data at the center and flasher events where cluster tubes are ignored.

pairs in an event as a cut statistic. We expect  $\delta t$  for hit PMTs in the same region of the detector to be small for Cerenkov sources located inside the  $\text{D}_2\text{O}$  volume and one meter or so beyond.

Figure 6.2 shows the  $\delta t$  distributions for PMT hits from  $^{16}\text{N}$  and flasher events. The median  $\delta t$  distribution for these events is shown in Figure 6.3, where it can be seen that reasonably good separation between  $^{16}\text{N}$  and flasher events is obtained.

Events are tagged for removal by the Fitterless Time Spread (FTS) cut if the median  $\delta t$  of PMT pairs within 3 m of each other is greater than 6.8 ns. Pairs with very large absolute time differences ( $> 25$  ns) are ignored and at least 15 pairs satisfying the distance and time difference are required before the event can be tagged. More details regarding the FTS cut can be found in [65, 66].

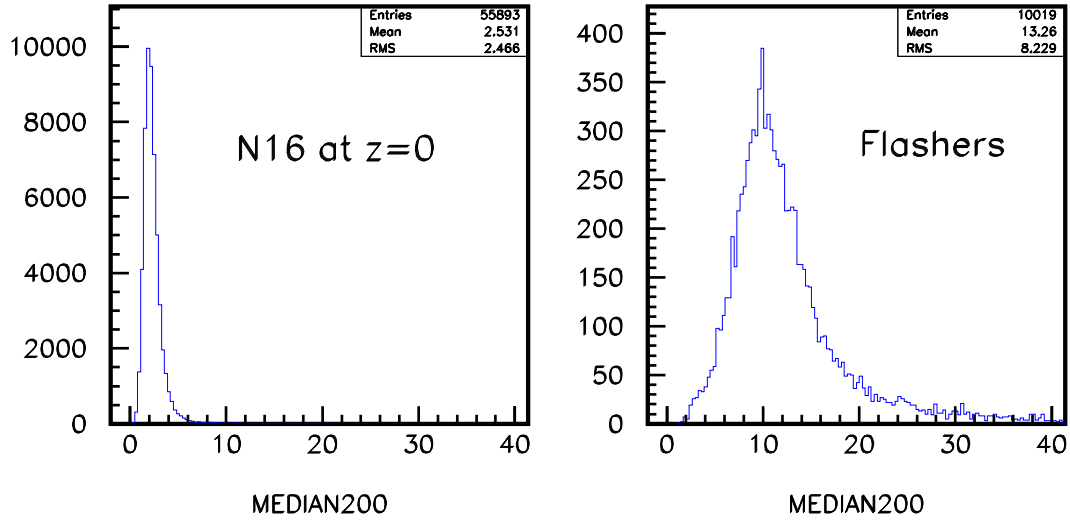


Figure 6.3: Distribution of median  $\delta t$  calculated from hit PMT pairs with  $|\vec{r}_i - \vec{r}_j| < 2$  m in  $^{16}\text{N}$  calibration data at the center and flasher events where cluster tubes are ignored. Only events having at least five pairs to calculate the median are included in the plots.

### In-time Channel (ITC) Cut

It was mentioned in Section 6.2.1 that events with flat or nearly flat TAC spectra often accompany a PMT's demise. To combat these and other types of events with very broad TAC spectra the In-time Channel (ITC) cut was developed. This cut is designed to be much simpler and more robust than the FTS cut, which relies on both PMT time *and* angular information to tag events. The cut statistic is the maximum number of hits within a sliding 93 ns window applied to the time spectrum - the number of “in-time” hits - in a given event.

As an example, a flat-TAC burst occurred in run 10700, after which a PMT which had been working was found to no longer function properly. The distribution of in-time hits both before and during the flat-TAC burst of run 10700 are shown in Figure 6.4 along with the distribution for  $^{16}\text{N}$  data. Notice that the  $^{16}\text{N}$  distribution

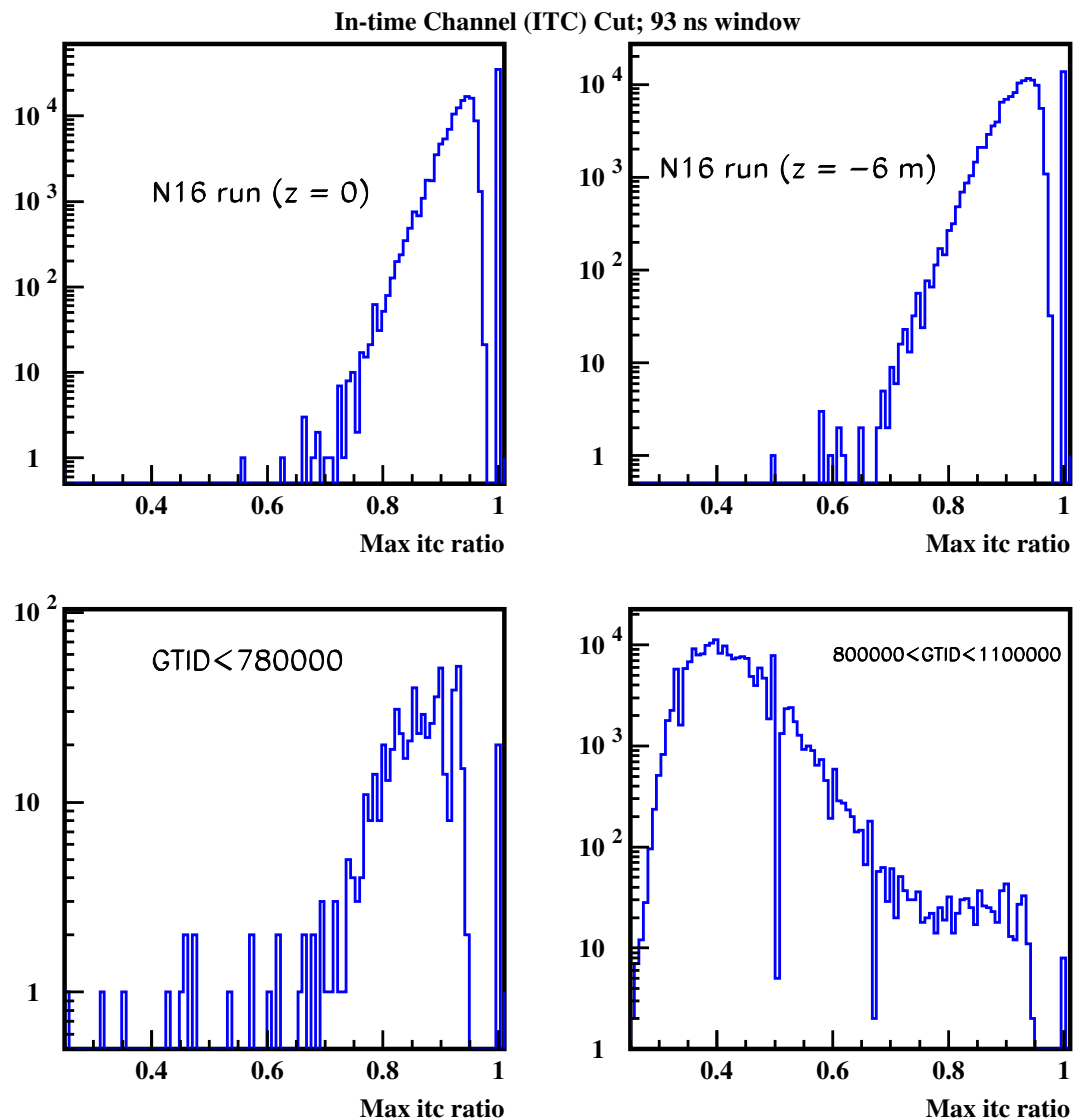


Figure 6.4: Distribution of ITC ratio for  $^{16}\text{N}$  calibration data (top) and events in run 10700 before (bottom left) and during (bottom right) the flat-TAC burst.

resembles that of the events preceding the burst and has the majority of hits in-time. This is contrasted with the events comprising the flat-TAC burst which have a much smaller number of in-time channels.

Events are tagged by the ITC cut if they have fewer than 60% of their PMT hits in-time. More details regarding the ITC cut can be found in [67].

### 6.3 Vertex and Direction Goodness-of-Fit Cuts

The goodness-of-fit (GOF) criteria calculated for each event fit by the Path Fitter was discussed in detail in Section 4.3.5. The purpose of this section is not to describe these algorithms again, but rather to present how Path Fitter reconstructed data is cut by these GOFs.

Recall from the discussions in Section 4.3 that the Path Fitter reconstructs events under the hypothesis that they are initiated by Cerenkov light from a single electron. If the global likelihood maximum is found, the fitter will return the most likely electron position, direction and time for this hypothesis. An event which is inconsistent with this hypothesis should not be included in the data set because the vertex, direction, and time can not be trusted even if they are the most likely parameters for an electron. Application of GOF criteria is not only important to remove bad fits of good Cerenkov events (e.g. from poor maximization of likelihood), but is also critical for rejection of residual instrumental backgrounds. For example, when flashers are fit under the single electron hypothesis using both PMT time and angular information, the majority of the fits are inside the D<sub>2</sub>O even though the light originates on the PSUP. Application of Path Fitter GOF criteria greatly reduces the number of successful fits inside the D<sub>2</sub>O for this background.

### 6.3.1 Azimuthal Angular Symmetry Cut

Recall that this test returns the KS probability for the azimuthal angular distribution of PMT hits at the fit position/direction to have been drawn from a uniform distribution. Due to their elongated hit PMT patterns, reconstructed flasher events often have a very poor azimuthal symmetry probability because the Path Fitter will typically adjust the direction fit so that all the hit PMTs are in one part of Cerenkov cone. The cut value used to reject bad fits based on their azimuthal symmetry KS probability is  $10^{-4}$ ; fits with a KS probability lower than this are rejected.

### 6.3.2 2-D Angular $(\cos \alpha, \psi)$ Distribution Cut

This test returns the 2-D KS probability,  $P_{ang2d}$ , for the polar and azimuthal distribution of PMT hits at the fit position/direction to have been drawn from the  $\cos \alpha, \psi$  distribution used to fit the event (see Section 4.3.5). In a sense, the azimuthal symmetry test is a subset of this test (i.e. one dimension of probability), although more simple because it ignores solid angle effects of the PMTs. This latter point is the reason why the azimuthal symmetry probability exhibits a slight radial bias toward cutting more good events at larger radius.

The 2-D angular KS test does not exhibit any significant radial bias but does sacrifice more good events as the event energy ( $N_{\text{Hit}}$ ) increases. Consequently, the cut value is relaxed at higher  $N_{\text{Hit}}$  to flatten the sacrifice dependence on  $N_{\text{Hit}}$  but still remain fairly aggressive on the cut. The following cut function is used to reject Path Fitter reconstructed events:

$$P_{ang2d} < \frac{4 \times 10^6}{N_{\text{hit}}^6} \quad (6.1)$$

The suspected reason for this bias (cutting more events at high  $N_{\text{Hit}}$ ) is the fact

that a 5 MeV electron angular distribution is used to test the fit, but higher energy events have a sharper angular distribution in  $\cos\alpha$ . Simply replacing the 5 MeV electron angular distribution with an energy dependent angular distribution or at least averaging over the neutrino spectrum would likely improve this GOF criteria.

## 6.4 Post-reconstruction Cerenkov Signal Cuts

The Path Fitter GOF cuts mentioned in Section 6.3 test the consistency of the fit vertex and direction with the hypothesis used to fit the event. For all practical purposes, these cuts can be regarded as a part of the Path Fitter, just as a cut on  $\chi^2$  is used to determine whether the Time Fitter passes or fails an event. In this section, two additional post-reconstruction cuts used in this analysis are presented. These cuts apply generic criteria for well reconstructed Cerenkov light events that can be used for any fitter, although these cuts may be more powerful for some fitters than others because of the manner in which they fit events. These two cuts - the Correlation Chisquare ( $\chi^2_{corr}$ ) and In-time Ratio (ITR) - combine to test the consistency of an event with the known angular correlation between hit PMT pairs and narrow distance-corrected timing distribution of Cerenkov light. Aside from the energy of the event, these two characteristics of Cerenkov light can, in a loose sense, be thought of as a *definition* of Cerenkov light events in the detector because any other type of event with these characteristics cannot be distinguished from a Cerenkov light event with the SNO detector.

### 6.4.1 Angular Correlation Cut: The Correlation $\chi^2$

The correlation  $\chi^2$  cut was developed at Penn by Bill Heintzelman. The correlation  $\chi^2$ ,  $\chi^2_{corr}$ , is a measure of the difference between the distribution of hit PMT pair angles observed in an event (the angular correlation distribution) and the distribution expected from Cerenkov light. The fitted vertex is used as the origin for PMT pair angle calculations. Therefore, the  $\chi^2_{corr}$  statistic is a measure of the consistency of observed hit PMT angular correlations with Cerenkov light from the fitted vertex. Monte Carlo generated angular correlation distributions were calculated in several different  $N_{\text{Hit}}$  bins. The appropriate one is used as the standard function for comparison to the event distribution at a given  $N_{\text{Hit}}$ . The calculation of  $\chi^2_{corr}$  includes PMT solid angle directly and also takes into account the fact that the bins of the angular correlation function are not statistically independent. See [68] for a complete description of  $\chi^2_{corr}$  and its application to removing instrumental backgrounds.

For this analysis, reconstructed events are cut from the data set if  $\chi^2_{corr} > 100$ . From the studies shown in [68], this appears to be an appropriate cut value for maximal acceptance of Cerenkov events with reasonable power to cut instrumental backgrounds like flashers.

### 6.4.2 In-time Ratio (ITR) Cut

The In-time Ratio (ITR) cut [48] is a post-reconstruction time test developed by Vadim Rusu at Penn. The ITR variable,  $R_{it}$  is a simple yet powerful statistic for rejecting instrumental backgrounds and poorly reconstructed Cerenkov events.  $R_{it}$  is defined as the ratio of the number PMT hits,  $N_{it}$ , within an asymmetric window around the prompt time to the number of PMT hits passing the full timing calibration.

Specifically,  $N_{it}$  is the number of PMT hits satisfying the following condition:

$$-2.5ns < t_p - (t_c + \frac{d_p}{c}) < 5.0ns$$

where  $t_p$  is the recorded PMT time,  $t_c$  is the fit time,  $d_p$  is the distance between the fit vertex and the PMT, and  $c$  is the mean speed of light in water. The motivation for an asymmetric window is the fact that scattering produces a late tail on the time distribution. For this analysis, reconstructed events are cut from data set if  $R_{it} < 0.5$ .

## 6.5 Muon Follower Cut

Although muon events themselves do not represent a worrisome background to solar neutrinos due to their very high energy, their products do provide backgrounds. Muons which traverse the heavy water region can produce neutrons which are indistinguishable from NC events (free neutron in both cases). Muons can also produce spallation products which are high energy (<13 MeV) beta emitters with long (10 msec to several seconds) lifetimes. The low rate ( $\sim 70$  per day) of muons reaching the depth of the detector affords SNO the luxury of simply cutting out any events following an identified muon event with minimal sacrifice of neutrino livetime. Therefore, events that are within 20 seconds after an identified muon event are cut from the data set.

## 6.6 Signal Acceptance of Combined Cuts

The data cleaning and post-reconstruction cuts used to reduce the data into a set usable for signal extraction have been presented. In addition to having some idea

of their efficiency for cutting instrumental backgrounds, it is important to know the signal acceptance ( $\alpha_s$ ) for these cuts. The signal *sacrifice* is defined as  $1 - \alpha_s$ .

The total sacrifice from data cleaning cuts is measured [59, 64] to be  $0.4 \pm 0.2\%$  for  $45 < N_{\text{Hit}} < 150$  and  $R_{fit} < 600$  m. This was determined through study of the number of triggered  $^{16}\text{N}$  and  $^8\text{Li}$  events that are tagged by the data cleaning cuts.

In a similar way, the total sacrifice from Path Fitter failures and post-reconstruction cuts is derived from analysis of  $^{16}\text{N}$  and  $^8\text{Li}$  calibration data. Figure 6.5 shows the sacrifice versus source radius obtained from x and z-axis scans of the  $^{16}\text{N}$  source and z-axis scan of the  $^8\text{Li}$  source. The volume-weighted sacrifice from fitter failures and post-reconstruction cuts is found to be  $1.0 \pm 0.2\%$ . The fitter-related cut sacrifice stability over time is probed by comparing the sacrifice from  $^{16}\text{N}$  data taken nearly a year apart. This is shown in Figure 6.6, where there is good agreement in sacrifice between the two runs. Other checks on the time stability of data cleaning cuts can be found in [69–71], where it is determined that sacrifice time dependence represents a small overall contribution ( $< 0.3\%$ ) to our systematic uncertainty.

From these studies, the combined total signal (CC and ES) sacrifice from data cleaning, fitter, and post-reconstruction cuts is estimated to be  $1.4 \pm 0.3\%$ .

## 6.7 Fiducial Volume and $N_{hit}$ cuts

The data cleaning and fitter-related cuts are designed to remove events from non-Cerenkov light sources (e.g. instrumental backgrounds) and also poorly reconstructed events initiated by Cerenkov light. It is anticipated that application of these cuts to the neutrino data set will leave us with a reduced data set largely free of non-Cerenkov backgrounds. However, there are other backgrounds which need to be removed from

## Sacrifice from Fitter FOMs and High-level Cuts

Nhit>65

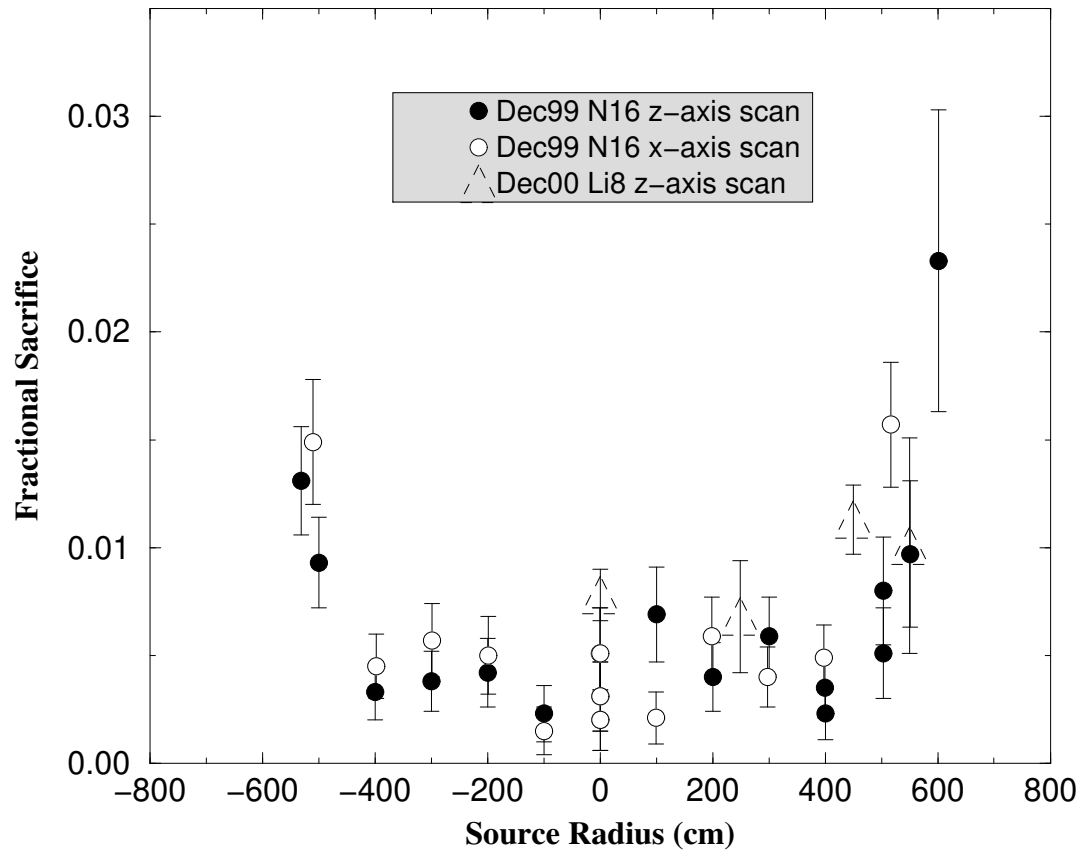


Figure 6.5: Sacrifice versus source radius obtained from x and z-axis scans of the  $^{16}\text{N}$  source and z-axis scan of the  $^8\text{Li}$  source.

## Sacrifice from Fitter FOMs and High-level Cuts

**Nhit>65**

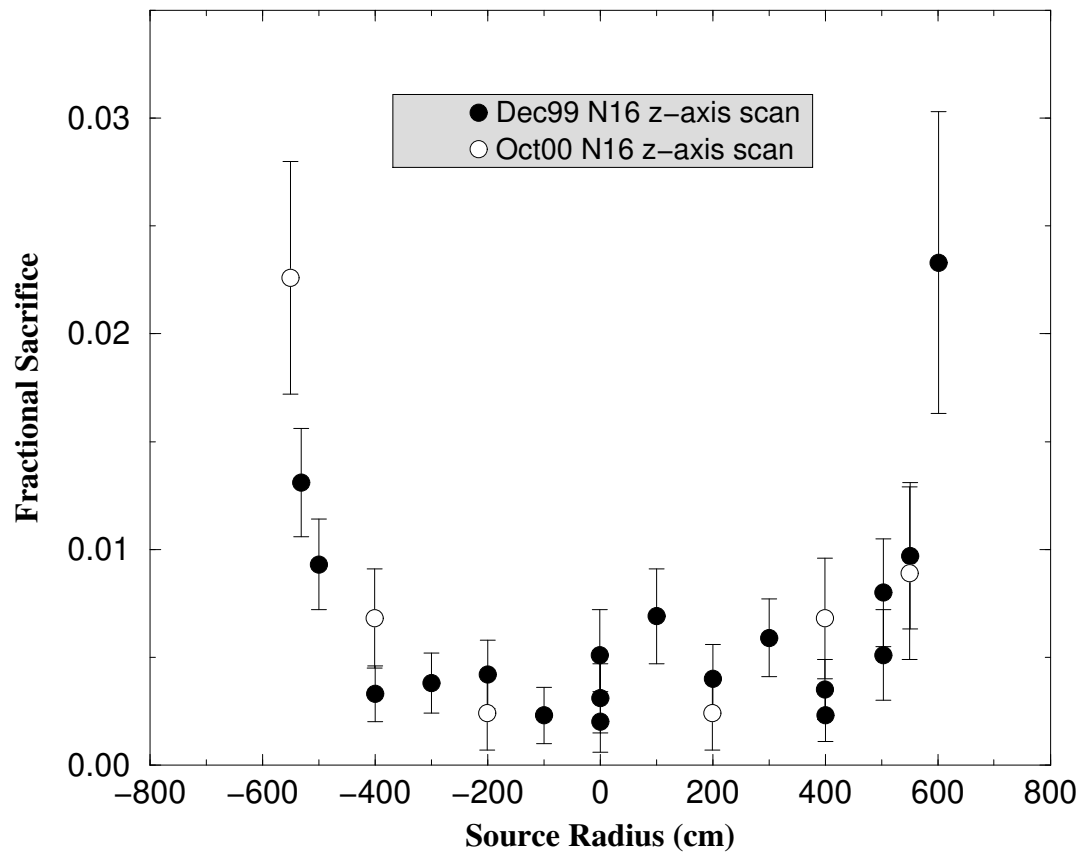


Figure 6.6: Fitter-related cut sacrifice stability over time, probed by comparing the sacrifice from  $^{16}\text{N}$  calibration data taken nearly a year apart.

the reduced data set before neutrino signals can be extracted.

Non-neutrino induced backgrounds dominate the reduced data set unless cuts on energy ( $N_{\text{Hit}}$ ) and reconstructed position (fiducial volume) are performed. Radioactive backgrounds from U/Th chain  $\beta - \gamma$  decays represent a low energy background wall of Cerenkov light events. These backgrounds can be effectively removed from the data set with a cut on  $N_{\text{Hit}}$ . The fiducial volume cut takes advantage of the fact that the detector was designed so that radioactive backgrounds at high energy (which cannot be removed with an energy cut) originate in the exterior regions of the detector. The background one worries about in this regard is from external high energy  $\gamma$ -rays, where “high energy” refers to  $\gamma$  energies greater than 2.6 MeV, which is the highest energy  $\gamma$  one expects from U or Th chain radioactivity. The  $\gamma$ -rays originate primarily from thermal neutron captures on high density materials such as PSUP steel and cavity rock, where the free neutrons are produced in  $(\alpha, n)$  from U and Th decay chain  $\alpha$  emissions. The  $R_{fit}^3$  distribution of events for several  $N_{\text{Hit}}$  thresholds is shown in Figure 6.7.

In this analysis, we apply fiducial volume ( $R_{fit} < 550$  cm) and energy ( $N_{\text{Hit}} > 65$ ) cuts to the data. With this high  $N_{\text{Hit}}$  cut, we expect the data set to be essentially free of low energy radioactive backgrounds. For events inside 550 cm, external  $\gamma$ -ray backgrounds are expected to represent a small contribution to the data set. A limit on high energy  $\gamma$ -ray backgrounds inside the fiducial volume is presented in Section 7.2. The specific fiducial volume cut radius was chosen not only from background considerations but also because it was deemed the largest usable radius from the standpoint of energy uncertainty. Because of the limited position sampling available for the  $^{16}\text{N}$  calibration source, energy interpolation corrections are not reliable for events reconstructing further than 550 cm from the center of the detector.

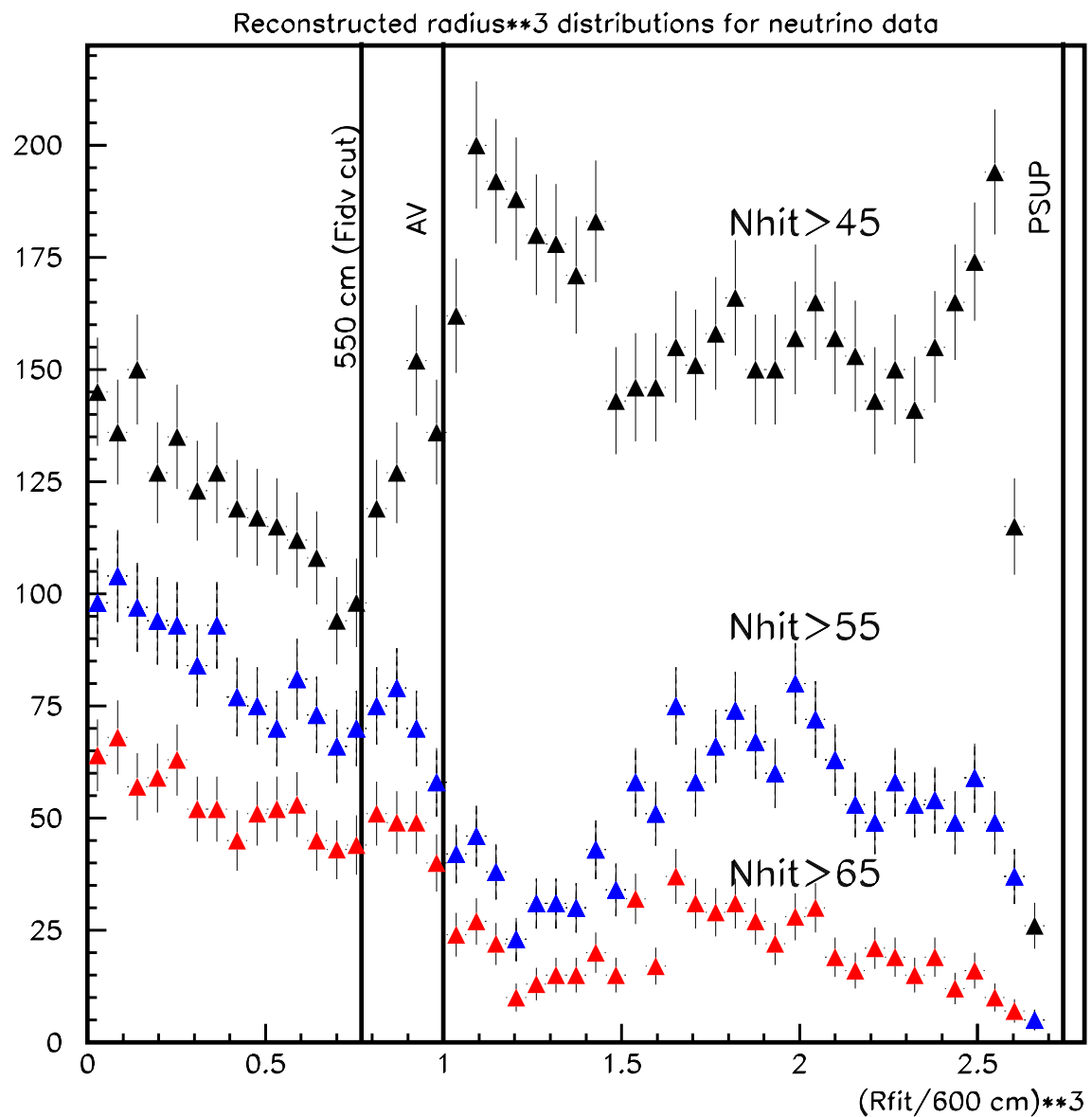


Figure 6.7:  $R_{fit}^3$  distribution of events after data cleaning for 45, 55, and 65  $N_{\text{Hit}}$  thresholds.

Cuts Applied	Events Remaining
Raw Data above 30 $N_{\text{Hit}}$	4065334
Data Cleaning	1443876
Path Fitter Pass	905340
Path Fitter FOMs	866105
Fiducial Volume ( $R < 550$ cm)	25078
ITR + $\chi^2_{corr}$	18071
Muon Following Short	17339
Energy ( $N_{\text{Hit}} > 65$ ) <sup>*</sup>	747

Table 6.1: Progression of data reduction cuts. <sup>\*</sup>In practice, the discreteness of  $N_{\text{Hit}}$  is removed by uniformly jittering *both* data and Monte Carlo  $N_{\text{Hit}}$  within each bin for purposes of signal extraction. Therefore, the energy cut is not technically a cut on  $N_{\text{Hit}}$ , but rather a cut on the uniformly jittered  $N_{\text{Hit}}$ .

## 6.8 Application of Cuts to Selected Data Set

The cuts described in the chapter were applied to the neutrino data set consisting of 169.3 days of livetime. Table 6.1 shows the number of events in the raw data set surviving the data reduction cuts. The effect of reduction cuts on the neutrino data  $N_{\text{Hit}}$  distribution is shown in Figure 6.8.

## 6.9 Summary

In this chapter, the cuts used to reduce the raw neutrino data set were presented. These cuts were designed to remove instrumental and radioactive backgrounds, as well as poorly reconstructed events. Application of these cuts to the neutrino data was shown to reduce the data set by nearly four orders of magnitude. In the next chapter, the level of residual background events from low energy radioactivity, external high-energy  $\gamma$ -ray backgrounds, and instrumental backgrounds are estimated.

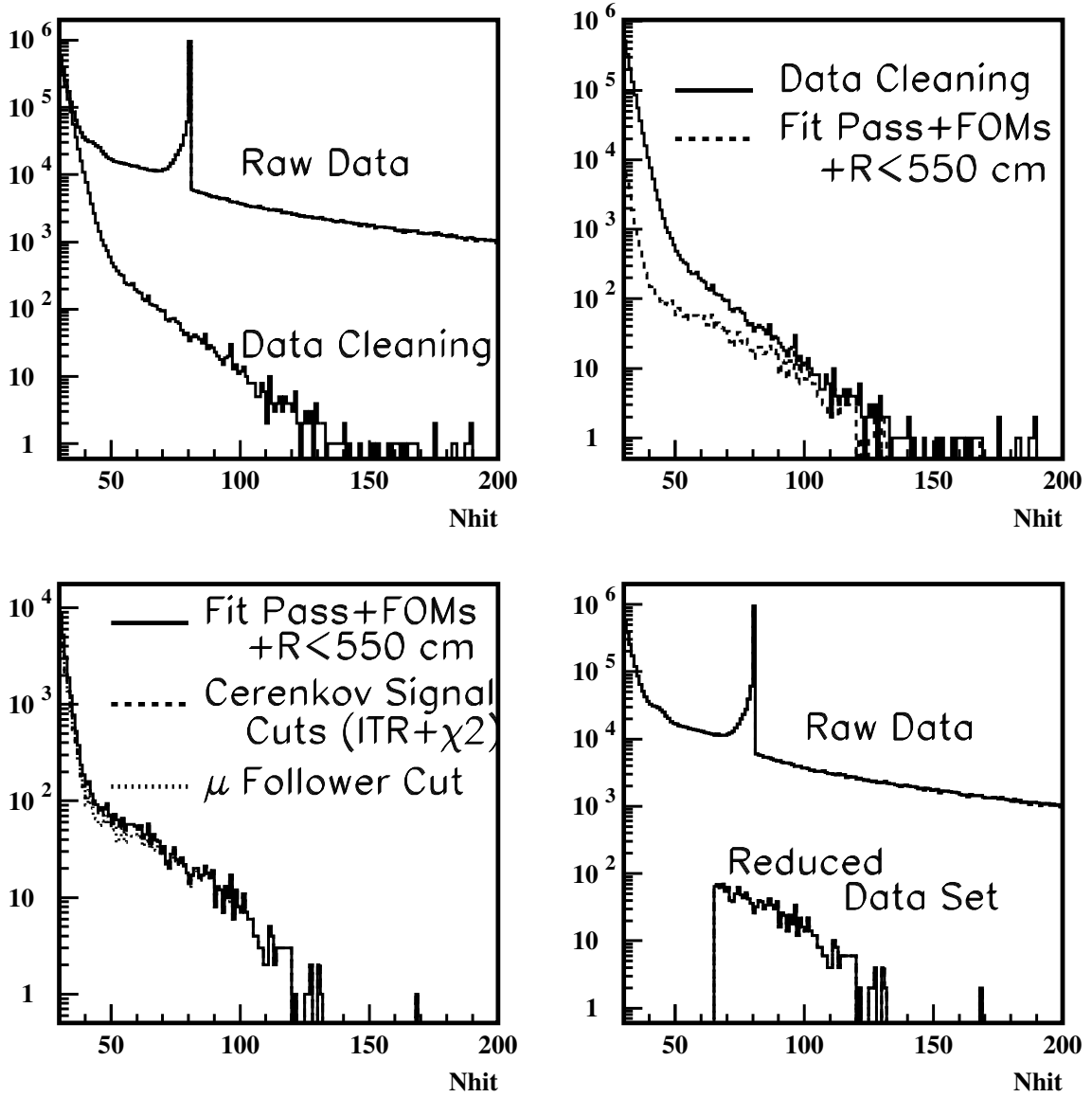


Figure 6.8: Effect of reduction cuts on the neutrino data  $N_{\text{Hit}}$  distribution above 30  $N_{\text{Hit}}$ . The labels refer to the  $N_{\text{Hit}}$  distribution after the indicated cut(s), except for “raw data” which represents all data between 30 and 200  $N_{\text{Hit}}$ . The spike of PMT hits near 80  $N_{\text{Hit}}$  in the raw data represents an “orphanage” of PMT data bundles which the event builder could not associate with any trigger.

# Chapter 7

## Background Estimation

In this chapter, the treatment of remaining solar neutrino backgrounds is discussed. If residual backgrounds exist in the reduced data set input to the signal extraction algorithms, then each background event will end up being classified as one of the signals depending on where it falls in the  $N_{\text{Hit}}$ ,  $R^3$ , and  $\cos \theta_{\odot}$  distributions. The backgrounds of primary concern to the high threshold, restricted fiducial volume analysis presented in this thesis are backgrounds from U/Th radioactivity, high energy  $\gamma$ -rays, and instrumental backgrounds. The methods used to limit these backgrounds in the analysis are presented in the following sections along with the results of these analyses.

### 7.1 Low Energy Backgrounds

Backgrounds from U and Th chain  $\beta - \gamma$  decays ultimately limit the energy threshold for solar neutrino analyses. These backgrounds produce an exponentially falling “wall” of Cerenkov light events in an  $N_{\text{Hit}}$  distribution which dominate solar neutrino

events below  $\sim 4.5$  MeV in electron energy. For analyses involving neutral current solar neutrino signals, knowledge of these backgrounds is critically important. This is because any  $\gamma$ -ray with energy above 2.2 MeV can produce a free neutron through deuteron photodisintegration. A neutron capture event resulting from this background process is indistinguishable from the neutral current reaction.

For the analyses presented in this thesis, exact knowledge of low energy background levels is not necessary. These backgrounds can be effectively removed by imposing a high energy or  $N_{\text{Hit}}$  threshold. In particular, the 65  $N_{\text{Hit}}$  threshold ( $\sim 7$  MeV) used in this analysis is  $\sim 2$  MeV (on average) above where the exponential part of the low energy background wall is extrapolated to zero (See Figure 7.1). Therefore, it is anticipated that low energy backgrounds will represent a negligible source of neutrino background in this analysis.

In actuality, low energy backgrounds do not simply fall exponentially to zero because of the finite energy resolution of the detector and also coincidence of decay events. Therefore, one still needs some way of limiting low energy background events in the region of interest. Estimation of low energy backgrounds is approached through use of Monte Carlo, which contains an accurate model of the detector energy and reconstruction characteristics.

The largest contribution to the high energy tail of low energy radioactive backgrounds comes from  $^{208}\text{Tl}$  ( $^{232}\text{Th}$  chain) and  $^{214}\text{Bi}$  ( $^{238}\text{U}$  chain) decays because these nuclei have the largest  $\beta$ -decay Q-values (5.0 MeV for  $^{208}\text{Tl}$  and 3.3 MeV for  $^{214}\text{Bi}$ ). Simplified decay schemes for  $^{208}\text{Tl}$  and  $^{214}\text{Bi}$  can be found in [72]. If we assume that the  $^{238}\text{U}$  ( $T_{1/2} = 4.47 \times 10^9 \text{ y} = 1.41 \times 10^{17} \text{ s}$ ) and  $^{232}\text{Th}$  ( $T_{1/2} = 1.41 \times 10^{10} \text{ y} = 4.45 \times 10^{17} \text{ s}$ ) chains are in secular equilibrium (i.e. the number of daughter decays per second equals the number of parent decays per second), we can calculate the number of expected

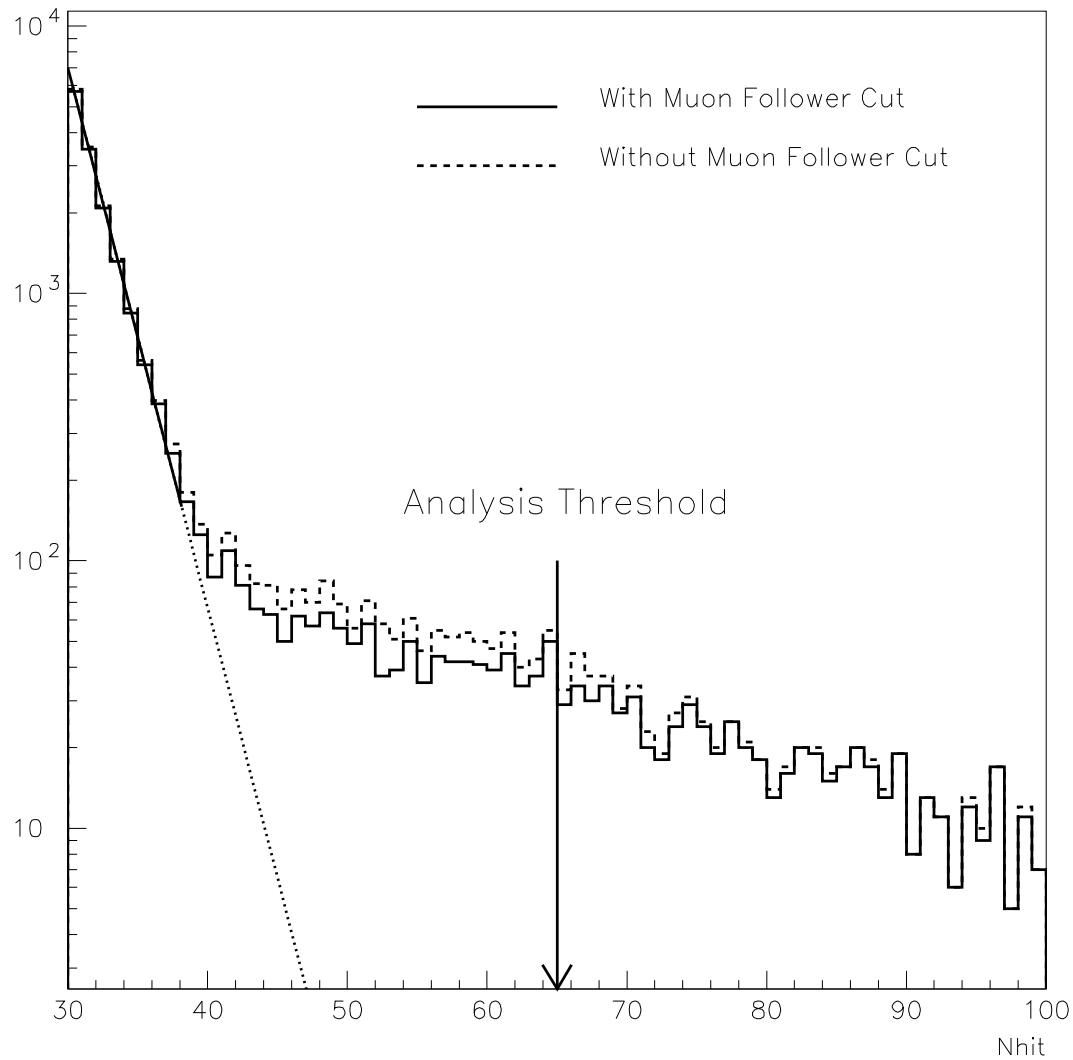


Figure 7.1:  $N_{\text{Hit}}$  distribution for cleaned data showing the analysis threshold relative to the exponential wall from low energy radioactive backgrounds. Also shown is the effect of removing the muon follower short cut. Notice that this cut predominately removes events from the neutron capture ( $\text{D}_2\text{O}$ )  $N_{\text{Hit}}$  region, as expected.

	D <sub>2</sub> O		H <sub>2</sub> O		AV	
	<sup>232</sup> Th	<sup>238</sup> U	<sup>232</sup> Th	<sup>238</sup> U	<sup>232</sup> Th	<sup>238</sup> U
Design Goal (pg/g)	0.0037	0.045	0.037	0.45	1.1	1.1
Assay Derived Limits (pg/g)	0.0017	0.013	0.18	0.45	1.1	1.1
Total Region Mass (tonnes)	1000		1667		13.7	
Total U/Th Mass ( $\mu$ g)	1.7	13	300	750	15	15
Decays During Livetime ( $\times 10^6$ )	0.105	2.37	17.7	136.4	0.887	2.73

Table 7.1: Summary of U/Th contamination in D<sub>2</sub>O, H<sub>2</sub>O, and AV regions. The second row entries are conservative 3 $\sigma$  limits from water assay measurement shown in [3] and acrylic panel radioactivity measurements found to be below design goals [24]. The last row entries are the calculated limits on the number of <sup>208</sup>Tl (<sup>232</sup>Th chain) and <sup>214</sup>Bi (<sup>238</sup>U chain) decays in each region over the 169.3 day neutrino livetime.

number of <sup>208</sup>Tl and <sup>214</sup>Bi decays over our 169.3 day neutrino livetime from measured U/Th contamination in the various regions of the detector. For example, if the <sup>238</sup>U chain is in equilibrium we have

$$N_{238\text{U}} R_{238\text{U}} = N_{214\text{Bi}} R_{214\text{Bi}} \quad (7.1)$$

where N is the number of nuclei and R is the decay rate, related to the half-life,  $T_{1/2}$ , by  $R = (\ln 2)/T_{1/2}$ . Therefore, the number of <sup>214</sup>Bi decays per second per gram of <sup>238</sup>U is

$$\frac{6.023 \times 10^{23}}{238} \times \frac{\ln 2}{1.41 \times 10^{17}} = 12,441 \text{ } ^{214}\text{Bi decays/s/g } ^{238}\text{U}$$

Similar calculation yields 4044 <sup>208</sup>Tl decays/s/g <sup>232</sup>Th. Table 7.1 summarizes U/Th contamination limits derived from measurements which have been performed for the D<sub>2</sub>O, H<sub>2</sub>O, and AV regions. Also shown are the calculated numbers of <sup>214</sup>Bi and <sup>208</sup>Tl decays in each region from these limits during our neutrino livetime.

The total number of <sup>214</sup>Bi and <sup>208</sup>Tl decays shown in Table 7.1 for the D<sub>2</sub>O and

AV regions were simulated using the Monte Carlo. The largest  $N_{\text{Hit}}$  observed in any of the simulations was 55  $N_{\text{Hit}}$  for several different random number seeds. Therefore we conclude that low energy background events from U/Th in the  $\text{D}_2\text{O}$  and AV regions are likely to represent negligible contributions to our overall systematic uncertainty. Low energy radioactivity from regions outside the AV region ( $\text{H}_2\text{O}$  and PMTs) represent negligible backgrounds for the fiducial volume ( $<550$  cm) and  $N_{\text{Hit}} (>65)$  thresholds used in this analysis. To contribute to our reduced data set, these background events would have to surpass our high  $N_{\text{Hit}}$  threshold *and* get badly mis-reconstructed into our fiducial volume in a way that passes the fitter FOMs and Cerenkov signal box cuts.

## 7.2 High Energy $\gamma$ -ray Backgrounds

Given a cleaned and reconstructed neutrino data set above some  $N_{\text{Hit}}$  (or energy) threshold, how many of the events reconstructing inside the fiducial volume are due to high energy external  $\gamma$ -ray interactions? In this context, “external” corresponds to sources from the PSUP/PMT region and beyond, and “high energy” refers to  $\gamma$  energies greater than 2.6 MeV, which is the highest energy  $\gamma$  one expects from U or Th chain radioactivity. One source of these  $\gamma$ -rays is thermal neutron capture on high density materials such as PSUP steel and cavity rock, where the free neutrons are produced in  $(\alpha, n)$  from U and Th decay chain  $\alpha$  emissions. Another principle source is direct  $\gamma$  production through  $(\alpha, p\gamma)$  on light nuclei such as Al in the reflectors and PMT glass [73].

While internal  $\beta-\gamma$  backgrounds to the solar neutrino signal can be largely limited by a simple  $N_{\text{Hit}}$  cut owing to the comparatively low energies involved ( $E_\gamma < 2.615$

MeV and  $\beta$  endpoint  $< 5.5$  MeV), such an  $N_{\text{Hit}}$  cut is ineffective against external  $\gamma$  backgrounds which can extend up to 10 MeV in energy [73]. One approach is to carefully model the PSUP and cavity regions using the appropriate geometry and radioactivity from assays of construction materials or *in situ* measurements as were performed on the cavity  $\gamma$ 's using a large volume NaI detector [74]. Monte Carlo simulations using these models will then yield an expected rate of high energy  $\gamma$ 's and a prediction for the number of  $\gamma$ 's reconstructing in the fiducial volume over some period of time. While this approach provides a very important check to see if one expects a significant problem based on assay measurements, it really represents a rough lower limit on the rate which is only as good as the models and cannot take into account inhomogeneous effects like hot-spots in the PSUP/PMT region. While one might expect the models to predict an energy *spectrum* which is reasonably close to reality, getting the correct absolute rate of such a background using assays and models alone is a much more difficult task.

Although it was mentioned that one cannot reject external  $\gamma$ -ray backgrounds on the basis of  $N_{\text{Hit}}$  alone, one can use the fact that sources of such  $\gamma$ 's are reasonably far from the  $D_2O$  and external to the light collection region so that the majority of events are radially inward. This is particularly true for cavity  $\gamma$ 's which must travel many scattering lengths to enter the PSUP region. Therefore, one can examine the correlations between position and direction of reconstructed events to look for a radially inward, high  $N_{\text{Hit}}$  component to the data near the PSUP region indicative of external high energy  $\gamma$  backgrounds.<sup>1</sup> The rate of such a component, coupled with the reconstruction characteristics of inward  $\gamma$ -rays near the PSUP based on calibrations,

---

<sup>1</sup>One needs to be careful about the acceptance issues of  $N_{\text{Hit}}$  threshold, concentrator shadowing, etc., when one makes statements based on reconstructed direction at large R.

can then be used to limit the rate of external high energy  $\gamma$ -rays reconstructing inside the fiducial volume of the detector and producing a background to the solar neutrino signal.

### 7.2.1 Description of the Method

The method currently used by the SNO collaboration to limit high energy backgrounds was developed by the author and is described in this section. For a more complete presentation of high energy background analysis is SNO, see [75].

$^{16}\text{N}$  calibration data is collected with the source near the PSUP and the reconstruction characteristics of the tagged  $\gamma$  events are used to estimate the way that external  $\gamma$ -rays enter into the neutrino data as a background. In a crude sense, the  $^{16}\text{N}$  source can be considered a triggered “hot PSUP” source in the approximation where the net effect of the PSUP radioactivity is to yield 6.13 MeV  $\gamma$ ’s at the source position and all the external  $\gamma$ -rays come from the PSUP. Of course there is no real basis for this assumption, particularly when one considers models of PSUP and cavity wall radioactivity which predict a spectrum of  $\gamma$ ’s extending up to  $\sim 10$  MeV, so this method should only be regarded as providing information at one  $\gamma$  energy. Spectral considerations can then be studied using the  $^{16}\text{N}$  source Monte Carlo in SNOMAN to extrapolate in energy.

The method of estimating backgrounds due to high energy external  $\gamma$ -rays reconstructing into the fiducial volume is a two stage process shown in Figure 7.2. First, calibration data is reconstructed to produce an estimate for the position and direction of the Compton scattered electron (or some fitter-dependent average vertex for multiple Comptons) in each event. The fraction of radially inward events reconstructing at

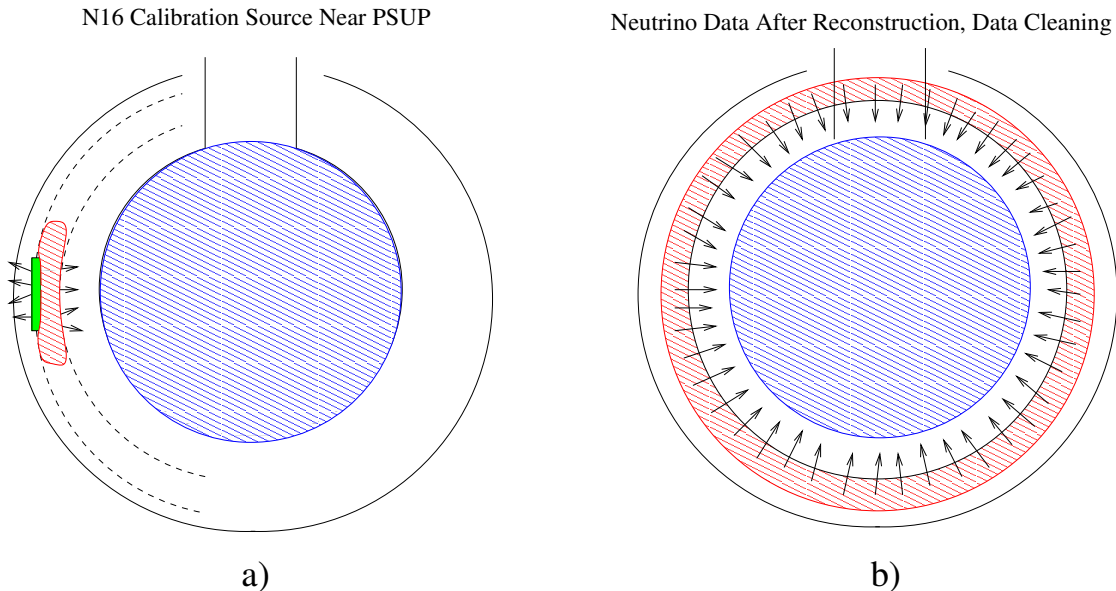


Figure 7.2: Pictorial description of the method used to estimate the amount of high energy  $\gamma$  background reconstructing into the fiducial volume. (a)  $^{16}\text{N}$  source near the PSUP is used to characterize the reconstruction properties of  $\gamma$ 's at large radius. The ratio,  $\mathcal{R}$ , of events reconstructing inward and near the source to the number of events reconstructing inside the  $D_2\text{O}$  is computed. (b) The neutrino data sample is cleaned and reconstructed, and the number of events reconstructing inward at large radius is recorded. Under the assumption that events in this region are dominated by high energy  $\gamma$  interactions, one can use this number of events and  $\mathcal{R}$  computed from the calibration data to estimate the amount of this background reconstructing inside the  $D_2\text{O}$ .

large radius is compared to the fraction of events that reconstruct inside the fiducial volume (in any direction), and the ratio,  $\mathcal{R}$ , of these two fractions is computed. The motivation for constructing this ratio is that we can apply it to the cleaned neutrino data to estimate the number of external  $\gamma$ 's reconstructing inside the fiducial volume if we assume that *radially inward events at large radius (i.e. near the PSUP) are dominated by external  $\gamma$  interactions*. The validity of this assumption needs to be demonstrated from analysis of the data to lend credibility to the estimate, of course, but even if other types of background (e.g.  $H_2O \beta - \gamma$ 's) are present in this region this does not invalidate the method. First of all, it may be possible to estimate the relative contributions of high-energy  $\gamma$ 's and other backgrounds using  $N_{\text{Hit}}$  and  $R^3$  distributions, since one expects the external  $\gamma$ 's to have larger  $N_{\text{Hit}}$  and an exponential fall-off in radius. Also, this method provides an *upper limit* to the contamination if one simply considers all the radially inward events at a suitably large radius to be external  $\gamma$ 's. It is then possible that such a limit would suggest the contamination of reconstructed  $\gamma$  events into the fiducial volume is at an acceptably low level relative to the expected neutrino signal.

### 7.2.2 Application of Method to Neutrino Data Set

To determine the reconstruction characteristics of external high energy  $\gamma$ -rays, we use the tagged events from  $^{16}\text{N}$  run 13980 where the source radius was 853.7 cm (-586, 208, 585 cm). The ratio  $R$  was determined, where

$$\mathcal{R} = \frac{\# \text{ of events with } r < 550}{\# \text{ of events with } \hat{u} \cdot \hat{r} < -0.5 \text{ and } 700 < r < 800} \quad (7.2)$$

From this ratio, a limit is placed on the number of high energy  $\gamma$ -rays in the neutrino data sample that reconstruct inside the fiducial volume by observing the number of radially inward events at large radius.

Figure 7.3 shows  $\hat{u} \cdot \hat{r}$  versus  $R^3$  for run 13890 above 50  $N_{\text{Hit}}$ , where  $\hat{u}$  and  $\hat{r}$  are reconstructed unit direction and position vectors, respectively. There are 3073 events inside the “box” of  $\hat{u} \cdot \hat{r} < -0.5$  and  $700 < r < 800$  and 7 events reconstructing inside the fiducial volume. The upper limit on  $R$  is therefore  $3.4 \times 10^{-3}$ , at the 68% confidence level.

The  $\hat{u} \cdot \hat{r}$  versus  $R^3$  distribution for the cleaned, reconstructed 169.3 day neutrino data set above 50  $N_{\text{Hit}}$  is shown in Figure 7.4. Note the similarity between Figure 7.3 and the spray in inward events at large radius. There are several checks one can perform to convince oneself that these are indeed due to high energy  $\gamma$ -rays. For example, these inward-directed events are significantly higher in  $N_{\text{Hit}}$  than events at large radius in other directions beyond what one expects from acceptance effects alone, and have approximately the expected spectrum (see [76] and [77]). The number of events observed inside the box for the neutrino data set is 1150. If one assumes that these are all high energy  $\gamma$ -rays, then the  $1\sigma$  limit on the number of background events inside the fiducial volume is 3.9 events. This corresponds to a background of fewer than 0.023 events per day or 0.6% of the extracted CC rate at the 68% confidence level.

Several systematic uncertainties on these results were investigated. This included sensitivity to the “box” size used in the analysis, the dependence on  $\gamma$ -ray energy, and  $^{16}\text{N}$  source position dependence. To test spectral dependence, the  $^{16}\text{N}$  source Monte Carlo was used. The Monte Carlo was first shown to be in good agreement with the  $^{16}\text{N}$  calibration data and then different  $\gamma$ -ray energies were used in the simulation.

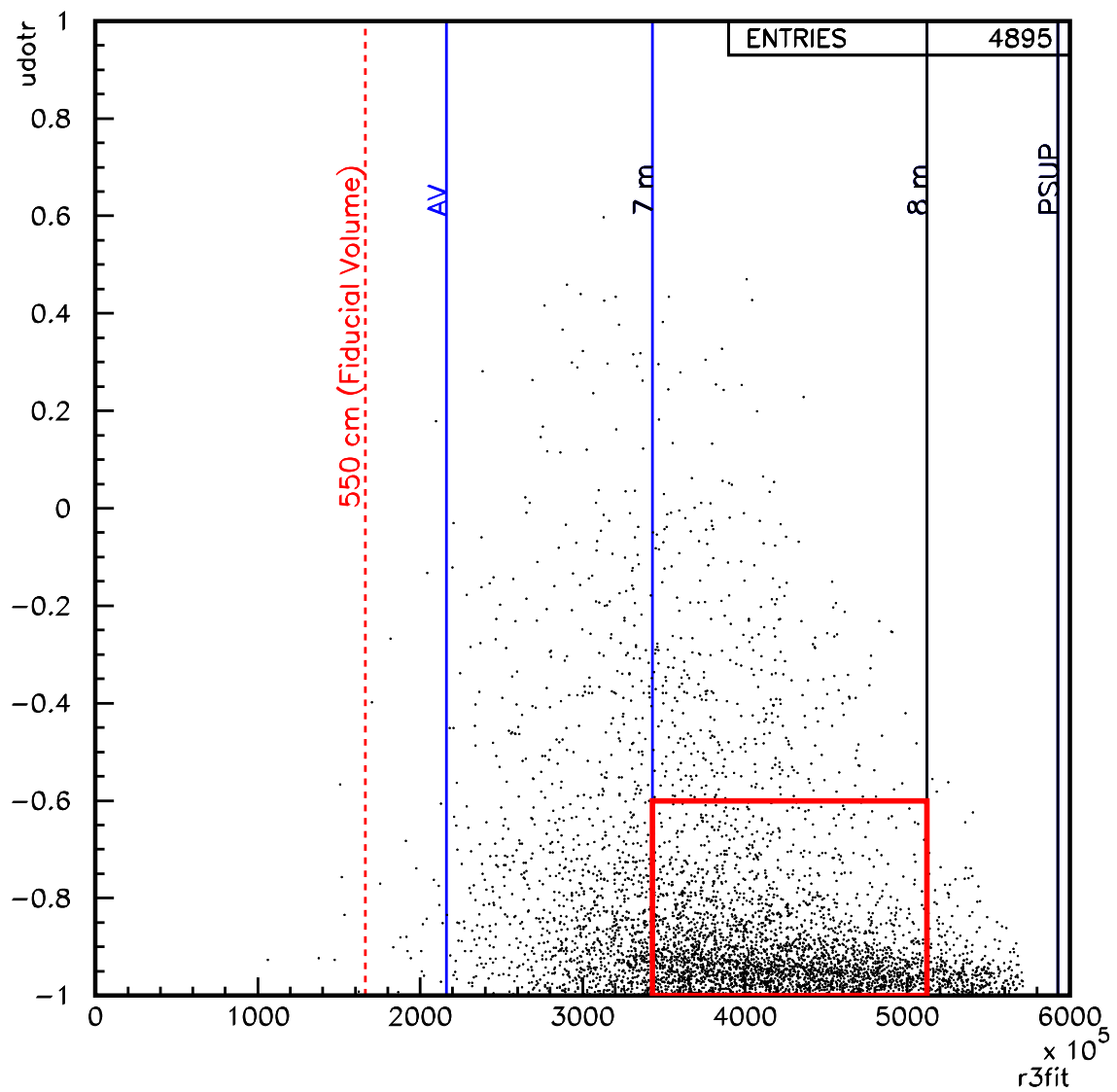


Figure 7.3:  $\hat{u} \cdot \hat{r}$  versus  $R^3$  distribution for tagged events from  $^{16}\text{N}$  run 13980 where the source was 853.7 cm (-586, 208, 585 cm).

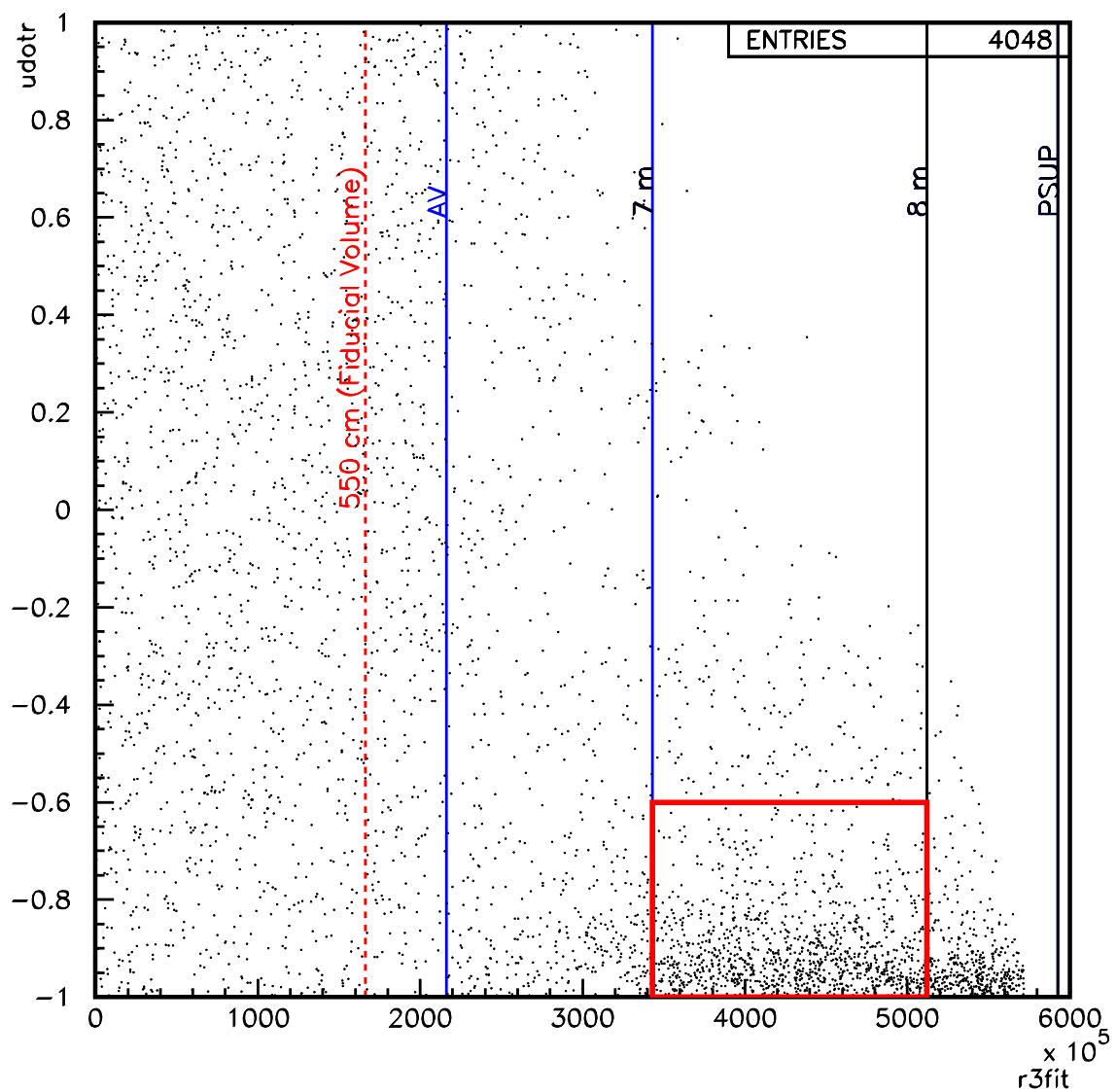


Figure 7.4:  $\hat{u} \cdot \hat{r}$  versus  $R^3$  distribution for the cleaned, reconstructed 169.3 day neutrino data set above 50  $N_{\text{Hit}}$ .

The  $^{16}\text{N}$  calibration source position dependence was probed by performing the analysis with a different source run near the PSUP - run 10573 (-586, 208, -500 cm). It was found that with a 550 cm fiducial volume and  $N_{\text{Hit}} > 50$ , the systematic uncertainties arising from these effects is below the statistical uncertainty. It was also found that the fractional number of high-energy  $\gamma$  rays inside the fiducial volume decreases slightly for increasing  $N_{\text{Hit}}$  threshold, lending confidence that the results can be applied to our higher  $N_{\text{Hit}}$  threshold where the  $^{16}\text{N}$  statistics are limited.

### 7.3 Non-Cerenkov Backgrounds

Determining the level of residual non-Cerenkov contamination is a much more difficult task, in principle, than either low or high energy backgrounds. The reason is simple - we do not have a set of calibration sources for these backgrounds which span all background types nor do we have a way to reliably simulate non-Cerenkov background sources.

The approach taken to estimating residual non-Cerenkov backgrounds is to use the post-reconstruction Cerenkov signal cuts described in Section 6.4 to extrapolate the instrumental background distributions (in the cut statistics) into the Cerenkov signal box defined by these cuts. This analysis was devised and performed by Vadim Rusu at Penn. The method is very similar to that used to limit high energy  $\gamma$ -ray backgrounds and represents a “bifurcated analysis” of the suite of data cleaning cuts and the Cerenkov signal box cuts (ITR and  $\chi^2_{\text{corr}}$ ) . The following assumptions are made in this method:

- Instrumental backgrounds tagged by the data cleaning cuts are representative (in terms of ITR and  $\chi^2_{\text{corr}}$ ) of the residual non-Cerenkov backgrounds in the

data set.

- In the cleaned data set, events outside the Cerenkov signal box are dominated by instrumental backgrounds.

The first assumption is analogous to the assumption in the high energy background analysis that  $^{16}\text{N}$  near the PSUP is a source of external  $\gamma$ -rays. The second assumption is analogous to assuming all radially inward, large R events are due to high energy  $\gamma$ -ray interactions. One determines from the events tagged by data cleaning and reconstructing inside the fiducial volume the ratio of events inside the Cerenkov signal box to outside the box. The estimated number of non-Cerenkov background events inside the fiducial volume for the cleaned data set is then this ratio multiplied by the number of events observed outside the Cerenkov signal box in this cleaned data set. The contamination determined by this method is shown in Figure 7.5 to be negligible for the  $N_{\text{Hit}}$  threshold used in this thesis.

## 7.4 Summary

In this chapter, limits on residual backgrounds in the reduced data set were presented. The levels of background events from low energy radioactivity, external high-energy  $\gamma$ -ray backgrounds, and instrumental backgrounds were found to be acceptably small for neutrino signal extractions. These extractions are presented in the next chapter, along with comparisons to SSM predictions.

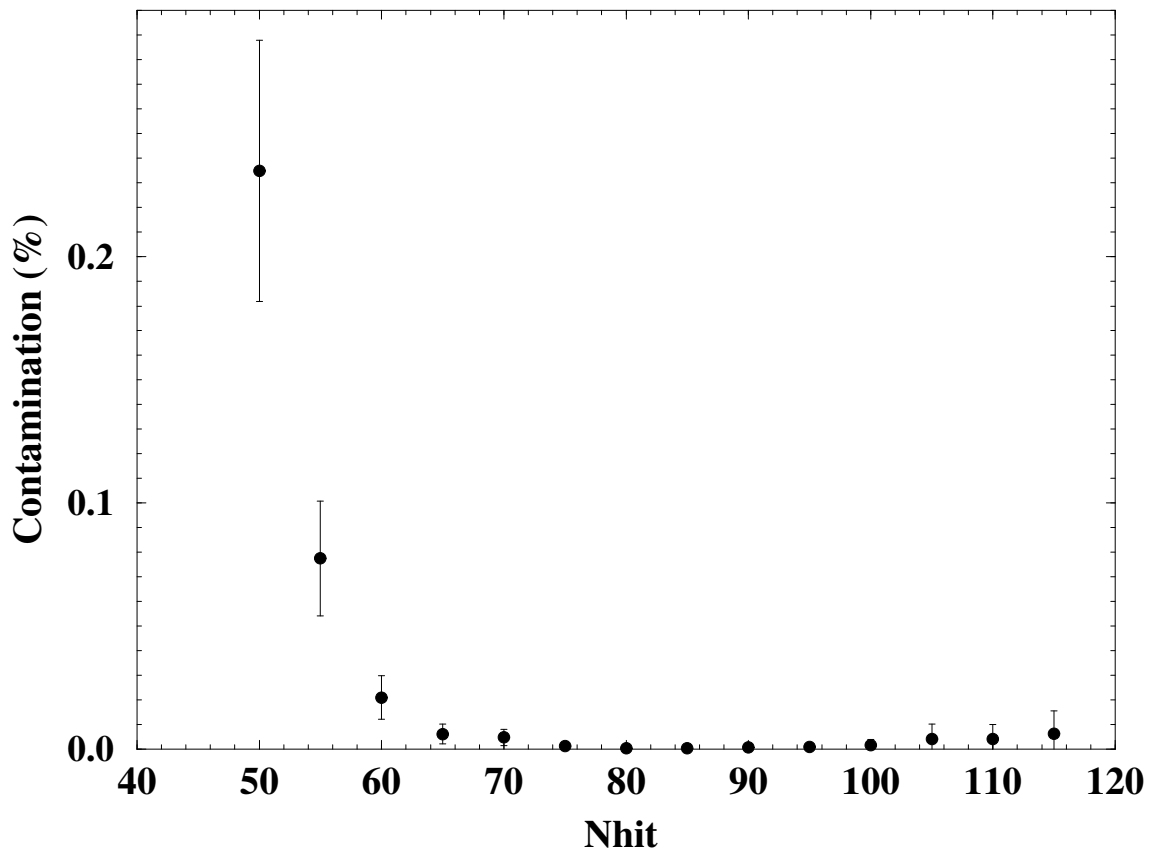


Figure 7.5: Non-Cerenkov contamination inside a 6 m fiducial volume as a function of  $N_{\text{Hit}}$  threshold. Figure courtesy of Vadim Rusu.

# Chapter 8

## Results

In this chapter, physics results extracted from the selected neutrino data set are presented. These results include measurement of the CC and ES rates relative to Standard Solar Model (SSM) predictions, the extracted CC  $N_{\text{Hit}}$  spectrum, and limits on the solar *hep* neutrino flux.

### 8.1 General Analysis Approach

In this section, the general approach to extracting CC and ES flux ratios (ratio of data to SSM predictions) is presented. The assumptions and approaches involved in the CC spectrum and *hep* flux limit analyses are completely analogous to that which is discussed in this section.

The general approach is to extract the number of CC, ES, and neutron events in the data sample using generalized maximum likelihood techniques. This fit then gives the most likely set of signal event numbers under the hypothesis that the data set is solely comprised of these signals. The validity of this hypothesis is critically dependent

upon the removal of backgrounds from instrumental (+ non-Cerenkov) events and non-neutrino sources of Cerenkov light. The suite of cuts used to remove the former background type was presented in Sections 6.2- 6.4. As discussed in Section 6.7, the fiducial volume and  $N_{\text{Hit}}$  cuts were largely chosen to minimize contributions from low energy radioactive and high energy  $\gamma$ -ray backgrounds. Limits on radioactive and instrumental backgrounds in the reduced data set were shown in Chapter 7 to be at acceptable levels to extract neutrino signals.

The signal PDFs used in signal extraction are derived from Monte Carlo. These PDFs are normalized distributions in cubed reconstructed radius ( $R^3$ ), interpolation corrected  $N_{\text{Hit}}$ ,<sup>1</sup> and cosine of the angle between reconstructed direction and direction from the Sun ( $\cos\theta_{\odot}$ ) for each signal type. The degree to which the Monte Carlo accurately represents the signal distributions depends on the accuracy of the differential cross-sections used by the Monte Carlo in addition to how well the Cerenkov light production and detector response are modeled. The latter is tested as thoroughly as possible by comparing calibration source data with Monte Carlo predictions for reconstruction and energy characteristics. These comparisons using a variety of calibration sources placed around the detector were presented in Chapter 5. The discrepancies between source data and Monte Carlo are then used to estimate the systematic error on energy and reconstruction characteristics upon which the flux measurements depend. This type of systematic error estimation relies on the assumption that discrepancies between the source data and MC responses are representative of the errors in using the MC to model the response to neutrino interactions in the detector. Propagation

---

<sup>1</sup>All Monte Carlo  $N_{\text{Hit}}$  values are adjusted using the energy scale interpolation scheme described in Section 5.4.2 and Appendix B. In all future reference to Monte Carlo  $N_{\text{Hit}}$ , the interpolation correction is implied. Also, some figures refer to “ $N_{\text{Corr}}$ ” which is equivalent to interpolation corrected  $N_{\text{Hit}}$ .

of these uncertainties through CC and ES flux analyses gives the total systematic error on these measurements.

For comparison to SSM predictions, the Monte Carlo is used to calculate the expected neutrino rates in the detector as well as the acceptance of the events in the analysis. The total  ${}^8\text{B}$  and *hep* neutrino flux values used in the Monte Carlo are from the Bahcall-Pinsonault 2000 standard solar model (BP2000). There is some unfortunate confusion which arises when one talks about the BP2000 total  ${}^8\text{B}$  neutrino flux. This flux has changed slightly from  $5.15 \times 10^6 \text{cm}^{-2}\text{s}^{-1}$  to  $5.05 \times 10^6 \text{cm}^{-2}\text{s}^{-1}$ , but both are often referred to as “BP2000”. In this thesis, the former (5.15) is referred to as “unmodified” and the latter (5.05) as “modified”.<sup>2</sup> The Monte Carlo used for this thesis is based on the unmodified BP2000. Therefore, all quoted results in this thesis reference the unmodified BP2000  ${}^8\text{B}$  total flux of  $5.15 \times 10^6 \text{cm}^{-2}\text{s}^{-1}$ , unless otherwise noted.

The CC, ES, and NC signal reaction rates for the BP2000 flux over our neutrino livetime are calculated by code within SNOMAN. These calculations use the number of neutrino targets ( $d$ ,  $e^-$ ), the differential neutrino cross sections for each reaction, and the flux of each neutrino type incident on the detector. The cross sections used for neutrino interactions on deuterium (CC and NC) are the NSGK potential model [78] with the effective field theory calculations described in [79] used to interpolate between tabulated energy points (after some tuning of model parameters). The solar neutrino survival probabilities are calculated using MSW code written by Naoya Hata and incorporated into SNOMAN by Doug McDonald. The detector response to neutrino interaction products ( $e^-$ ,  $n$ ) produced within the detector is then simulated by the

---

<sup>2</sup>The total *hep* flux is immune to this confusion because it is the same for both modified and unmodified BP2000 models.

Monte Carlo. The number of events passing the fiducial volume and  $N_{\text{Hit}}$  cuts after corrections are made for *measured* cut acceptance gives the number of expected events for each signal type which can be compared to signals extracted from the data.

## 8.2 Signal Extraction Techniques

The number of CC, ES, and “NC” events are extracted using Extended Maximum Likelihood (EMLH) methods (see [80], for example). The NC rate is in quotations because NC implies neutrino-induced free neutrons, however, only the total number of neutrons<sup>3</sup> which includes those from photodisintegration backgrounds are extracted. Application of these methods in extracting neutrino signals in SNO follows [81–83] and more recently [84].

The Monte Carlo is used to simulate CC, ES, and NC events in the detector. These simulations are performed over the livetime of the neutrino data set being analyzed. There are several reasons for taking care to simulate the neutrino signals in this way. First, one needs to account for the instantaneous solar direction in each simulated event because we are extracting events (in part) based on correlations to the incident neutrino direction. Also, to properly model the detector response in terms of energy and reconstruction, one needs to disable channels in the MC which were disabled during each of the neutrino runs. To ensure that the uncertainties in the PDF shapes are not limited by Monte Carlo statistics, one generates a large number of events compared to size of the data sample. In this analysis, 10 times the number of CC events and 50 times the number of ES and NC compared to BP2000 SSM prediction were generated. Probability density functions (PDFs) are then constructed from the

---

<sup>3</sup>with a uniform distribution inside the D<sub>2</sub>O

resulting  $N_{\text{Hit}}$ ,  $R^3$ , and  $\cos \theta_{\odot}$  distributions for each signal. These distributions are fit to parameterized functions (to be described in Section 8.2.2) which are used as the signal PDFs in extraction.

### 8.2.1 CC and ES Extraction - NHIT Constrained

We are interested in extracting the fractional number of events,  $\theta_i$ , from a presumed mixture of  $i$  signal types ( $i = \text{CC, ES, and NC}$ ). We write the PDF,  $\mathcal{P}(\vec{x}, \vec{\theta})$ , as a sum of the individual normalized signal PDFs,  $f_i(\vec{x})$ ,

$$\mathcal{P}(\vec{x}, \vec{\theta}) = \sum_{i=1}^3 \theta_i f_i(\vec{x}) \quad (8.1)$$

where  $\vec{x} \equiv (N_{\text{Hit}}, R^3, \cos \theta_{\odot})$  and  $\vec{\theta} \equiv (\theta_1, \theta_2, \theta_3)$ . Note that the individual  $\theta_i$  are not independent, since we must have  $\sum_{i=1}^3 \theta_i = 1$ . This constraint is removed in the extended maximum likelihood function,

$$\mathcal{L}(\nu, \vec{\theta}) = \frac{\nu^n}{n!} e^{-\nu} \prod_{i=1}^n \mathcal{P}(\vec{x}, \vec{\theta}) \quad (8.2)$$

where  $n$  is the number of events in the data sample and  $\nu$  is the Poisson mean total number of events which is now part of the fit. Equation 8.2 is really a traditional likelihood function expect that now the number of sample events,  $n$ , is considered part of the experimental results. Substitution of 8.1 into Equation 8.2 with some straightforward algebra leads to an equation for the log extended likelihood function

$$\log \mathcal{L}(\vec{w}) = - \sum_{j=1}^m w_j + \sum_{i=1}^n \log \left( \sum_{j=1}^m w_j f_j(\vec{x}_i) \right) \quad (8.3)$$

where  $w_j \equiv \nu\theta_j$  is the mean number of events for the  $j^{th}$  signal type to be fit to the data and  $\vec{w} \equiv (w_1, w_2, w_3)$ . Note that the  $w_j$ 's are *unconstrained* which allows their fit errors to reflect not only statistical error in the extracted number of events, but also error from covariances between the signal types. The set of  $w_j$  which maximizes Equation 8.3 is the most likely set of signal numbers for the data sample.

### 8.2.2 Parameterized PDFs

In this section, the PDFs used in signal extraction are presented. An approach to PDF generation is to use a single three-dimensional PDF in  $N_{\text{Hit}}$ ,  $R^3$ ,  $\cos\theta_\odot$  for each signal type. This set of three PDFs - one for each signal type - then contain all the information about correlations between the variables. The issues raised with such a prescription in the context of reconstruction and energy calibrations were discussed in Section 5.4.1. It is also observed that for the fiducial volume and  $N_{\text{Hit}}$  used in this analysis, correlations between the variables are actually reasonably small, with the one exception to this being the correlation between ES  $N_{\text{Hit}}$  and  $\cos\theta_\odot$ . So to a good approximation, we can write

$$f_i(\vec{x}) = \alpha_i(N_{\text{Hit}}) \beta_i(R^3) \gamma_i(\cos\theta_\odot) \quad (8.4)$$

This factorization effectively averages over the correlations between the variables. The aforementioned ES correlation is put in as several different  $\cos\theta_\odot$  distributions, one for each of four bins in  $N_{\text{Hit}}$ .

The  $\alpha$ ,  $\beta$ , and  $\gamma$  distributions for each signal are fit to smooth analytical functions. This parameterization of the PDFs is inherently a smoothing process, but the goodness of each fit demonstrated whether or not these functions are good represen-

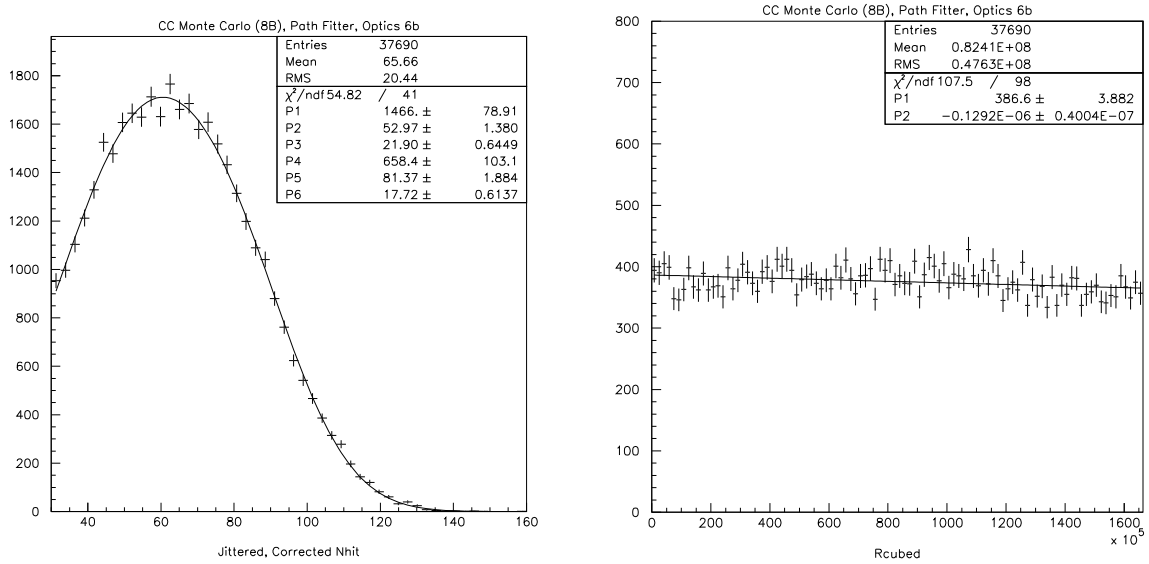


Figure 8.1: Monte Carlo CC distribution in (left)  $N_{\text{Hit}}$  and (right)  $R^3$  for 10xSSM (BP00) over the neutrino data livetime. The  $N_{\text{Hit}}$  distribution is fit to the sum of two Gaussian functions and the  $R^3$  distribution is fit to a linear function.

tations of the underlying distributions. A different approach would be to simply bin the distributions and use the bin values as the values of the PDF in the given variable one is considering. However, binning throws away information and it is not clear how to take into account the statistical errors within each bin for the uncertainty in the PDF shape. In the limit of large MC statistics, these two methods can be made equivalent and the parameterized approach is chosen in this analysis for simplicity. Figures 8.1- 8.5 show the parameterized PDFs used for each of the CC, ES, and NC neutrino signal reactions, where the chosen functional forms are indicated in the figure captions. A normalized uniform distribution is used for the NC  $\cos \theta_{\odot}$  PDF, as there is no direction information retained in the thermal neutron capture process.

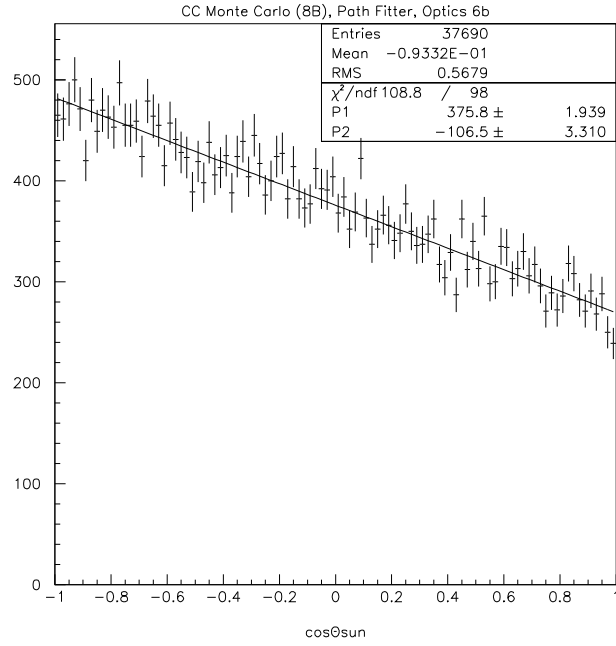


Figure 8.2: Monte Carlo CC distribution in  $\cos \theta_{\odot}$  for 10xSSM (BP00) over the neutrino data livetime. The  $\cos \theta_{\odot}$  distribution is fit to a linear function.

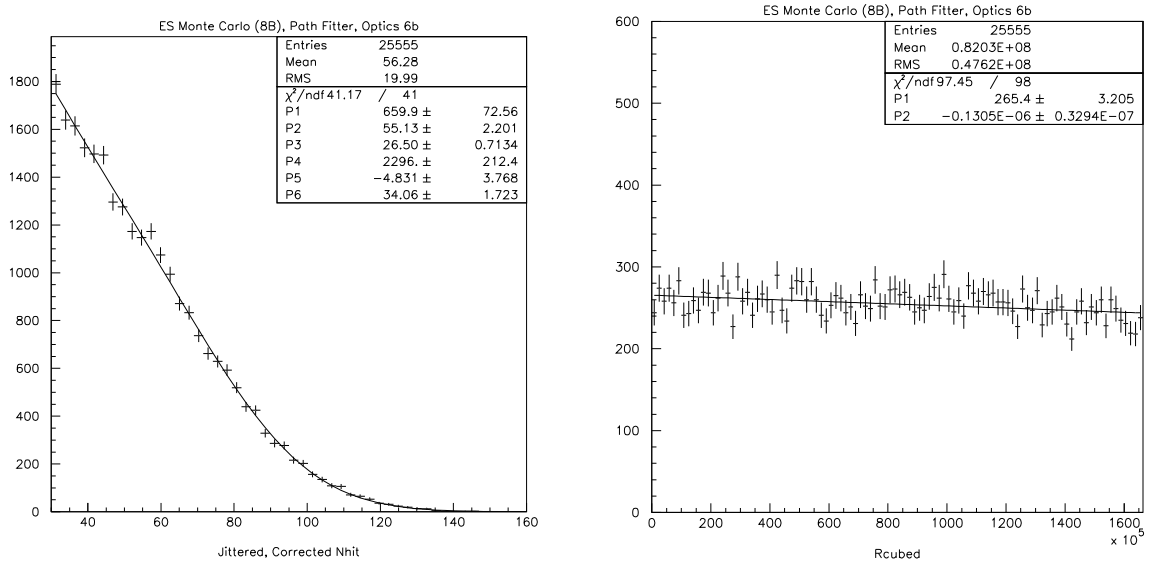


Figure 8.3: Monte Carlo ES distribution in (left)  $N_{\text{Hit}}$  and (right)  $R^3$  for 50xSSM (BP00) over the neutrino data livetime. The  $N_{\text{Hit}}$  distribution is fit to the sum of two Gaussian functions and the  $R^3$  distribution is fit to a linear function.

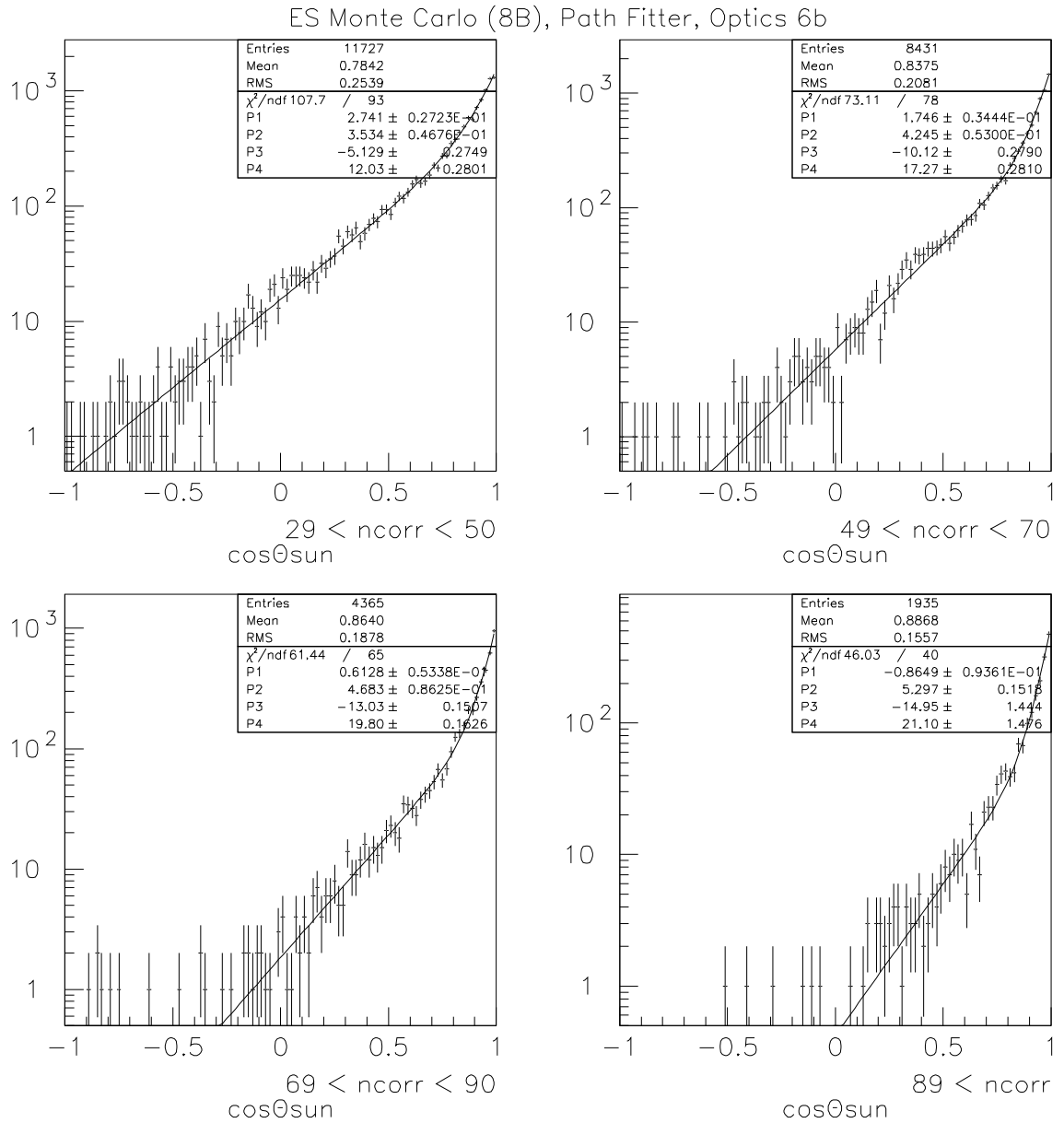


Figure 8.4: Monte Carlo ES distribution in  $\cos\theta_{\odot}$  for 50xSSM (BP00) over the neutrino data livetime. The  $\cos\theta_{\odot}$  distribution is fit to the sum of two exponential for each of the indicated  $N_{\text{hit}}$  (ncorr) bins.

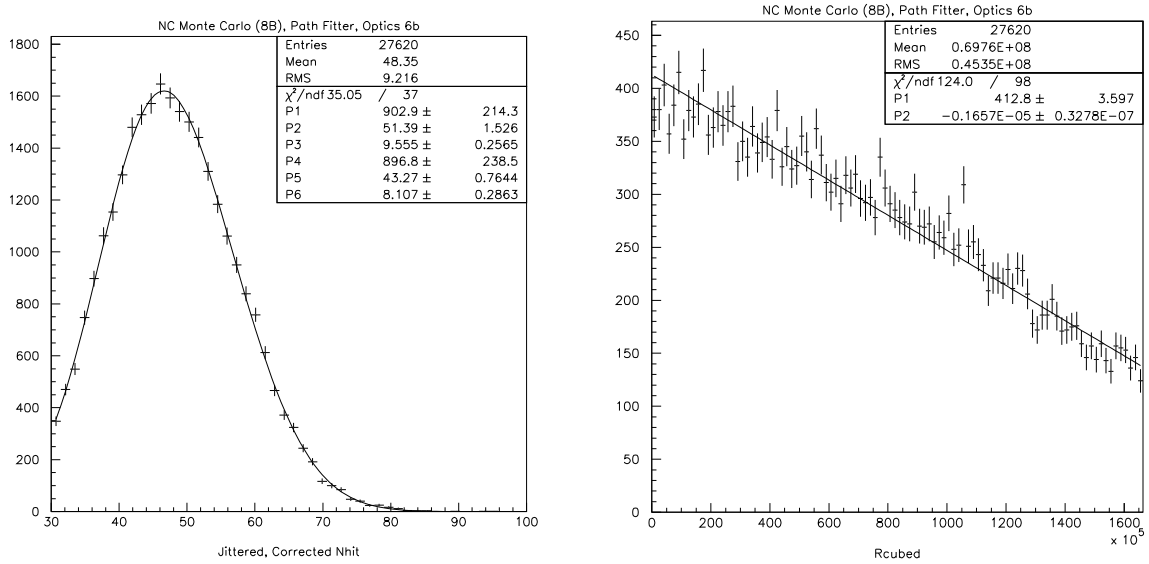


Figure 8.5: Monte Carlo NC distribution in (left)  $N_{\text{Hit}}$  and (right)  $R^3$  for 50xSSM (BP00) over the neutrino data livetime. The  $N_{\text{Hit}}$  distribution is fit to the sum of two Gaussian functions and the  $R^3$  distribution is fit to a linear function.

### Energy Scale Drift Correction

It was shown in Section 5.4.2 that the Monte Carlo over-predicts total  $^{16}\text{N}$  interpolation corrected (and uncorrected)  $N_{\text{Hit}}$  in an approximately linear fashion of 2.6% per year. If the  $^{16}\text{N}$  stability runs are representative of the total  $N_{\text{Hit}}$  of neutrino events during normal data taking, then the Monte Carlo should be corrected for this trend.

The trend shown in Figure 5.4 corresponds to the drift in *mean*  $N_{\text{Hit}}$  at the  $^{16}\text{N}$   $\gamma$ -ray energy. The resolution shows no obvious trend beyond that predicted by Monte Carlo, so we want a transformation for each Monte Carlo signal event which preserves the resolution but shifts each  $N_{\text{Hit}}$  in a way consistent with a mean response drift. If one considers  $N_{\text{Hit}}$  to be a Gaussian distribution with an electron energy dependent mean,  $\mu(E)$ , then the following  $N_{\text{Hit}}$  transformation produces the proper shift in the mean due to the scale drift but leaves the resolution unchanged from that predicted

by the Monte Carlo

$$N_{\text{Hit}} \rightarrow N_{\text{Hit}} + \Delta\mu(E, t) \quad (8.5)$$

where the shift in mean  $N_{\text{Hit}}$ ,  $\Delta\mu(E, t)$ , is given by

$$\Delta\mu(E, t) = s(t)\mu(E) - \mu(E) = (s(t) - 1)\mu(E) \quad (8.6)$$

where  $s(t)$  is the scaling required for the observed time drift. Specifically, Figure 5.4 shows that the fractional difference,  $f(t)$ , between Monte Carlo energy scale and that observed from the  $^{16}\text{N}$  stability runs is determined to be

$$f(t) = \frac{\mu_{MC} - \mu_{data}}{\mu_{data}} = (0.026 \pm 0.002)t - (0.0020 \pm 0.0002) \quad (8.7)$$

where  $t$  is the number of days since the start of production running divided by 365. This implies that we want to scale the Monte Carlo mean  $N_{\text{Hit}}$  by a factor  $s(t)$  given by

$$s(t) = \frac{1}{1 + f(t)} \quad (8.8)$$

so that  $s(t)\mu_{MC} = \mu_{data}$ . The form of  $\mu(E)$  is derived from Monte Carlo CC electrons generated uniform/isotropic in the  $\text{D}_2\text{O}$  and is shown in Figure 8.6 to be quite linear over the solar neutrino energy range of interest.

### 8.2.3 CC $N_{\text{Hit}}$ Spectrum Extraction

Extraction of the CC  $N_{\text{Hit}}$  spectrum is very similar to the total CC rate extraction method described in Section 8.2.1 except that the CC spectrum shape is fit rather than constrained. This type of extraction is similar to and motivated by the methods

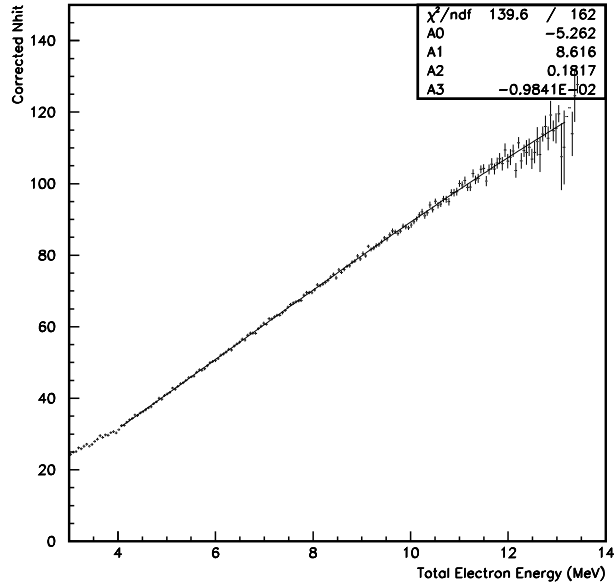


Figure 8.6: Mean  $N_{\text{Hit}}$  versus electron energy for Monte Carlo CC electrons generated uniform and isotropic inside the  $\text{D}_2\text{O}$  volume.

described in [85]. The neutrino data is binned in  $N_{\text{Hit}}$  and the number of CC events in each bin,  $\eta_j^{CC}, j = 1..k$ , is extracted using the  $R^3$  and  $\cos \theta_\odot$  distributions for CC, ES, NC, in addition to the *constrained*  $N_{\text{Hit}}$  shape for NC and ES. The shape of the ES  $N_{\text{Hit}}$  distribution is that which results from an undistorted  ${}^8\text{B}$ . This is motivated by the lack of substantial distortion in the recoil electron energy distribution from ES observed by the SuperKamiokande experiment, which currently has far more statistics than the SNO elastic scattering. As the SNO neutrino data set grows in statistics, one would be able to remove this constraint and fit out the ES  $N_{\text{Hit}}$  spectrum as well. In this analysis of limited statistics, an undistorted ES  $N_{\text{Hit}}$  shape is imposed to reduce the total number of free parameters in the fit. Inclusion of this hypothesis is not expected to compromise the CC spectral sensitivity to a significant degree because of the comparatively lower expected rate of ES events in the detector.

The extended log-likelihood function maximized to extract the CC  $N_{\text{Hit}}$  spectrum and the total number of ES ( $w_{ES}$ ) and NC ( $w_{NC}$ ) events is analogous to Equation 8.3 and is given by

$$\begin{aligned} \log \mathcal{L}(w_{NC}, w_{ES}, \vec{\eta}) = & -(w_{NC} + w_{ES} + \sum_{j=1}^k \eta_j^{CC}) \\ & + \sum_{i=1}^n \log \left[ w_{NC} \rho_{NC}(b_i) f_{NC}(\vec{x}_i) + w_{ES} \rho_{ES}(b_i) f_{ES}(\vec{x}_i) + \eta_{b_i}^{CC} f_{CC}(\vec{x}_i) \right] \end{aligned} \quad (8.9)$$

where  $\vec{x} \equiv (R^3, \cos \theta_{\odot})$ ,  $\vec{\eta} \equiv (\eta_j^{CC}, j = 1..k)$ ,  $b_i$  is the  $N_{\text{Hit}}$  bin of the  $i^{\text{th}}$  event, and  $\rho_{NC}$ ,  $\rho_{ES}$  are the binned  $N_{\text{Hit}}$  shapes for the NC and ES reactions, respectively.

## 8.3 Extracted Solar Neutrino Signals

In this section, the extracted signals from 169.3 days of livetime are presented. This includes the total number of CC, ES and “NC” events assuming an undistorted  ${}^8\text{B}$  neutrino energy spectrum and also the extracted CC  $N_{\text{Hit}}$  spectrum.

### 8.3.1 CC and ES - Nhit Constrained Fit

The total number of CC, ES, and “NC” events in the 169.3 day data set were extracted using the signal extraction technique described in Section 8.2.1 and the signal PDFs presented in Section 8.2.2. The negative of Equation 8.3 was minimized using CERNLIB’s MINUIT package to get the most likely numbers of signal events in the data set consistent with fitting hypothesis. The results are shown in Table 8.1.

How consistent is the data with the number of extracted events shown in Table 8.1 and our fitting hypothesis? The data distributions in  $N_{\text{Hit}}$ ,  $R^3$ , and  $\cos \theta_{\odot}$  with the signal PDFs scaled to the number of extracted events of each signal type are shown in Figures 8.7 and 8.8.

Signal Type	Extracted Events
CC	$630.60^{+31.82}_{-30.94}$
ES	$73.19^{+13.06}_{-12.21}$
“NC”	$43.21^{+19.10}_{-18.32}$

Table 8.1: Number of extracted signal events from the 169.3 day data set. The indicated errors are statistical only.

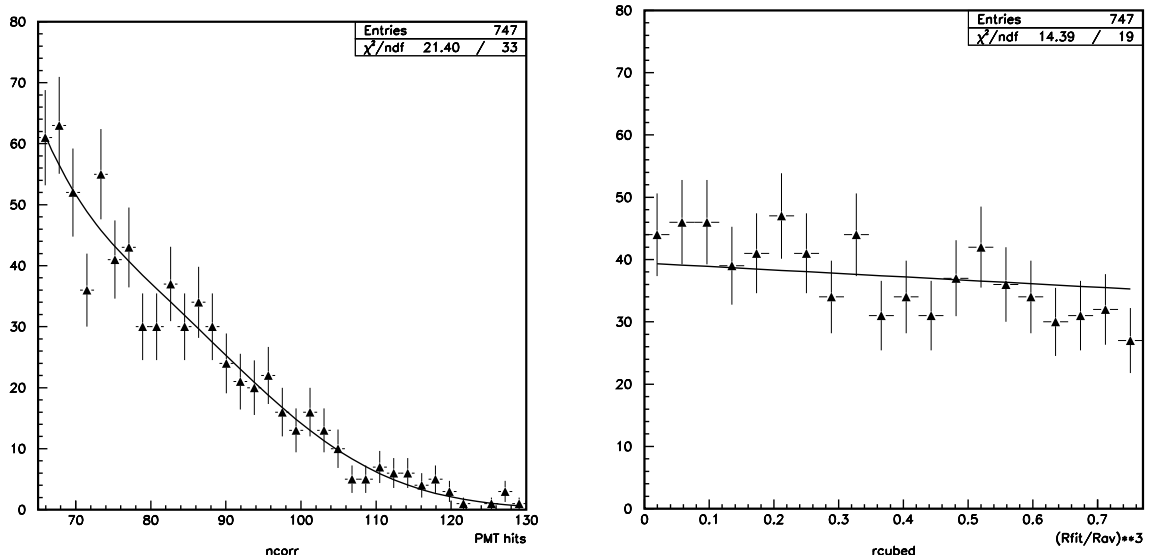


Figure 8.7: (left)  $N_{\text{Hit}}$  and (right)  $R^3$  distributions for the 169.3 day neutrino data set with the signal PDFs scaled to the number of extracted CC, ES, and “NC” signal events superimposed.

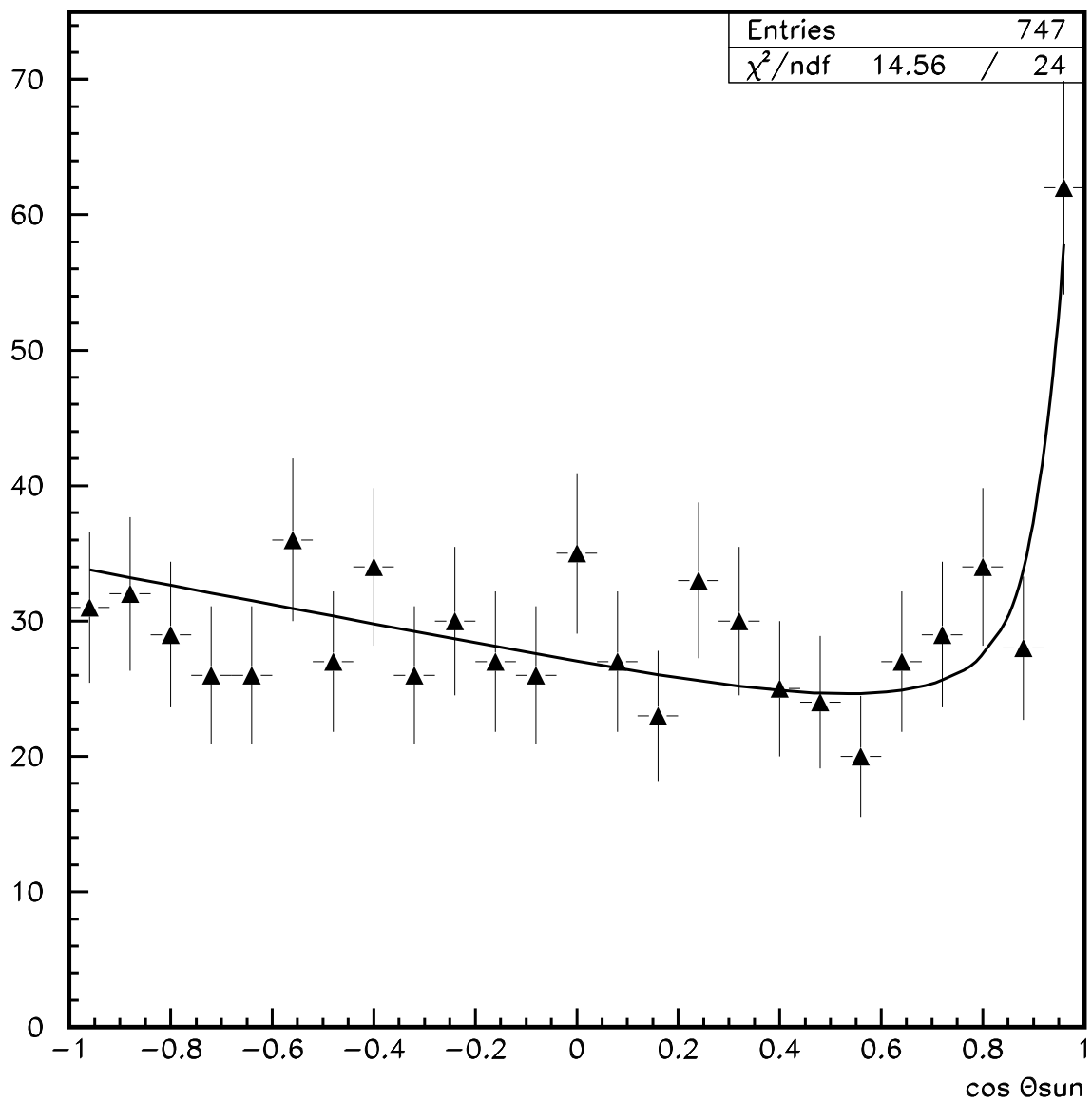


Figure 8.8:  $\cos \theta_{\odot}$  distribution for the 169.3 day neutrino data set with the  $\cos \theta_{\odot}$  signal PDFs scaled to the number of extracted CC, ES, and “NC” signal events superimposed.

The  $\chi^2/dof$  for each distribution is very good, suggesting that the data can be consistently fit to our signal distributions resulting from an undistorted  ${}^8\text{B}$  neutrino energy spectrum of solar neutrinos. The quality of the fits also give us some confidence that we are indeed analyzing in a relatively background free region, although they do not *prove* that this is indeed the case. In the  $N_{\text{Hit}}$  distribution, for example, one could always find a conspiratorial background which exactly “fills in” a true spectral distortion to give the observed results. This is the independent background estimates presented in Chapter 7 are so important.

### 8.3.2 CC $N_{\text{Hit}}$ Spectrum

The CC  $N_{\text{Hit}}$  spectrum is extracted from the data using the methods described in Section 8.2.3. Specifically, the data was binned into 23 bins with  $55 \geq N_{\text{Hit}} \geq 200$  - the first 22 bins are of equal three  $N_{\text{Hit}}$  width and the last bin representing  $121 \geq N_{\text{Hit}} \geq 200$ . The number of CC events extracted in each of the 23 bins is shown in Figure 8.9. The indicated errors are statistical only. The three  $N_{\text{Hit}}$  bins below 65  $N_{\text{Hit}}$  are included to show the extracted shape below our analysis threshold but are not used in our subsequent analysis. This is because systematics have not been studied below our analysis threshold of 65  $N_{\text{Hit}}$ .

## 8.4 CC and ES Fluxes Compared to SSM Predictions

In this section, the extracted CC and ES event numbers presented in Section 8.3.1 are compared to Monte Carlo predictions for the (unmodified) BP2000 SSM  ${}^8\text{B}$  neutrino

## CC NHIT Spectrum

Using Constrained NC and ES Nhit Spectra

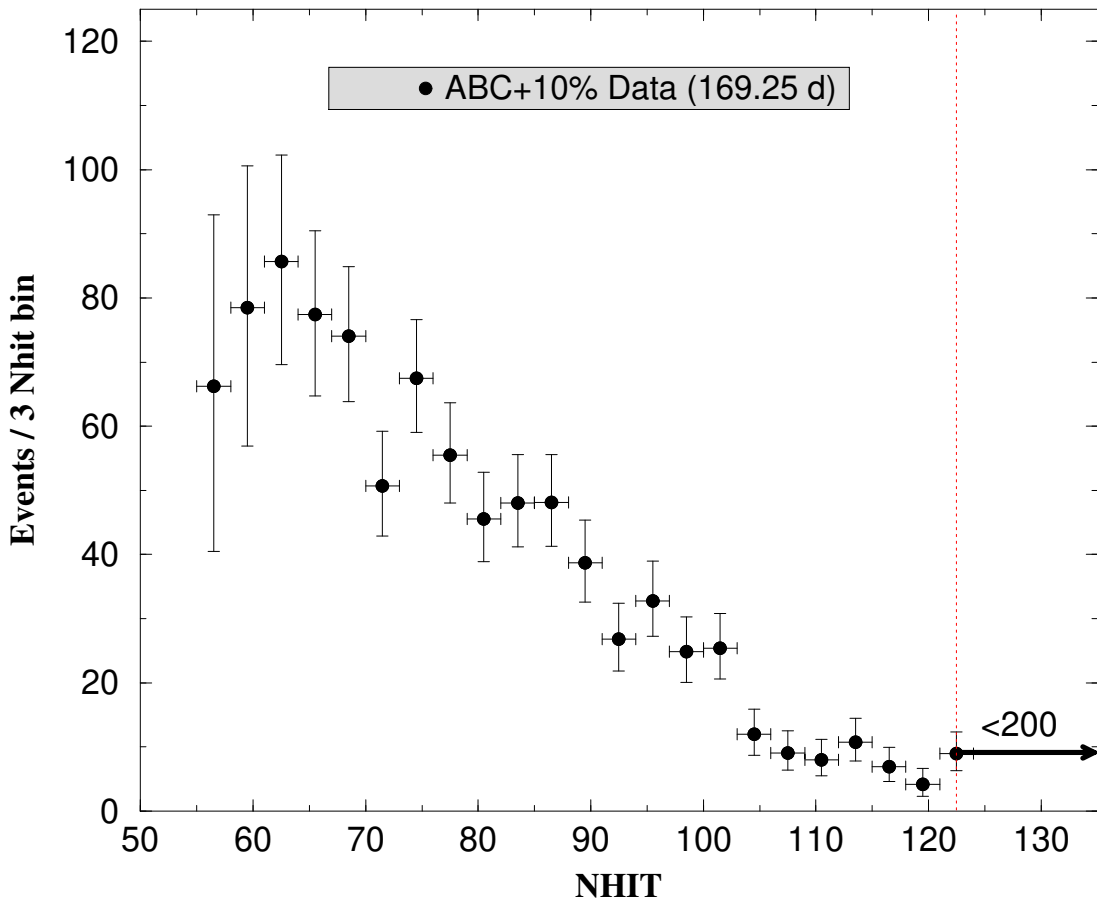


Figure 8.9: Extracted CC  $N_{\text{Hit}}$  spectrum for the 169.3 day neutrino data set. The last data point represents the number of events extracted in a bin extending up to 200  $N_{\text{Hit}}$ . Errors shown are statistical only.

Signal Type	Expected # of Events
CC	$1848.5 \pm 13.6$
ES	$150.5 \pm 1.7$
NC	$24.9 \pm 0.7$

Table 8.2: Number of expected signal events over the 169.3 day data set from  ${}^8\text{B}$  assuming BP2000 SSM. Corrections described in this section have not been applied.

flux ( $5.15 \times 10^6 \text{ cm}^2 \text{ s}^{-1}$ ) and spectrum inferred from measurements described in [86]. The same Monte Carlo used for generating signal PDFs is used to determine the expected number of signal events (see Section 8.2).

The expected number of events for our 169.3 day livetime satisfying the fiducial volume and  $N_{\text{Hit}}$  cuts used in this analysis ( $R_{fit} < 550 \text{ cm}$  and  $N_{\text{Hit}} > 65$ ) is shown in Table 8.2.

Before useful comparisons can be made between the extracted signal rates and the MC predictions shown in Table 8.2, several corrections must be included.

- *${}^{17}\text{O}$  and  ${}^{18}\text{O}$  isotopic abundance:*  ${}^8\text{B}$  neutrinos can interact via charged-current on the loosely bound neutrons in  ${}^{17}\text{O}$  and  ${}^{18}\text{O}$  nuclei present in the heavy water. These interactions give signals which are very similar to CC reactions on deuterons, so a correction for their isotopic abundances must be included in the expected number of events based on Monte Carlo (which did not include these additional interactions). According to [87], the rate of CC events must be scaled up by  $0.793 \pm 0.012\%$  to account for the measured isotopic abundances.
- *Fitter and cut acceptance:* Corrections must be made for acceptance of the reconstruction algorithm as well as any other cuts placed on the data (data cleaning, fitter FOMs, high-level) for Cerenkov light events above our  $N_{\text{Hit}}$  threshold and originating within our fiducial volume. From Figure 6.5, the volume-

weighted sacrifice (i.e. 1 - acceptance) for events inside 550 cm and  $N_{\text{Hit}} > 65$  is estimated to be  $1.0 \pm 0.2\%$ . Combining this with the current best estimate for total sacrifice from data cleaning of  $0.4 \pm 0.3\%$ , we get the an total sacrifice from data cleaning, fitter-related, and high-level cuts of  $1.4 \pm 0.3\%$ .

- *Livetime correction for burst cuts:* The muon follower short cut and other burst-based cuts (see Section 6.2.4) introduce a dead time for neutrino analysis in the selected data set. The overall correction to the livetime for these cuts is estimated [88] to be  $1.9 \pm 0.1\%$ .
- *Earth’s orbital eccentricity:* A correction to the expected flux must be made for the 1.7% eccentricity of the earth’s orbit. The required correction on a month-to-month basis for the run list approved by the Run Selection Committee is calculated in [89]. For the 169.3 day livetime used in this analysis, the eccentricity correction is to scale the flux ratio (data / MC) by a factor of  $1/(1.0103 \pm 0.0015)$  [90].

The combination of these corrections amounts to multiplying the total number of expected events by  $0.985 \pm 0.003$  for CC and  $0.977 \pm 0.003$  for ES reactions.

Using these corrections, we expect 1820.8 CC and 147.0 ES events over our livetime with the cuts imposed in the analysis. The observed number of CC events is  $630.60^{+31.82}_{-30.94}$  and the number of ES events is  $73.19^{+13.06}_{-12.21}$ . This gives the following ratios of observed CC and ES signals to (unmodified) BP2000 SSM predictions:

$$R_{CC} \equiv \frac{CC_{\text{data}}}{CC_{\text{SSM}}} = 0.346^{+0.017}_{-0.017} \text{ (stat)} \quad R_{ES} \equiv \frac{ES_{\text{data}}}{ES_{\text{SSM}}} = 0.498^{+0.089}_{-0.083} \text{ (stat)}$$

## 8.5 Systematic Errors

In this section, the systematic errors on the CC and ES flux measurements are determined. Uncertainties which affect the flux measurements fall into two categories in terms of the way they are considered in the analysis. Errors in the Monte Carlo distributions of signal observables -  $N_{\text{Hit}}$ ,  $R^3$ , and  $\cos \theta_{\odot}$  - affect both the number of events extracted from the neutrino data set by altering the PDF shapes as well as the signal acceptances that determine the expected number of events. Comparison of calibration data with source Monte Carlo is used to estimate the systematic error on using the Monte Carlo for signal distributions. These comparisons were presented in Chapter 5 in the context of energy calibration and reconstruction characteristics. To propagate these uncertainties through the CC and ES flux analyses, the Monte Carlo signal distributions are shifted or smeared by amounts determined by the uncertainties demonstrated in the calibration source comparisons. For example, the Monte Carlo does not exactly reproduce the angular resolution observed in reconstruction of  $^{16}\text{N}$  calibration data. To estimate the effect of this uncertainty on the ES flux measurements, the reconstructed angle relative to the solar direction is smeared by the appropriate amount. Other systematics errors enter into the flux analyses as an error in the expected number of events for a particular neutrino flux without significantly affecting the PDF shapes themselves. Neutrino livetime is an example of this type of uncertainty.

### 8.5.1 Sources of Systematic Uncertainty

Systematic errors on the CC and ES flux measurements are considered in turn in the following sections.

## Energy Scale

It was shown in Section 5.4.1 that the energy scale using total interpolation-corrected  $N_{\text{Hit}}$  agrees with  $^{16}\text{N}$ ,  $^{252}\text{Cf}$ , and pT calibration source data at the 1% level after a time drift correction of 2.6% per year was applied. These sources bracket the energy spectrum of electrons expected from solar neutrinos above our analysis threshold. Although the time drift correction is sizable compared to the uncertainty suggested by calibration data, it is worth noting that the majority of data set used in this analysis (100% from Nov99 - June00, 10% thereafter until Jan01) only extends 240 days into production running which gets drift corrected up to 1.7%. Considering the additional uncertainties involved in the energy scale time dependence, we estimate an energy scale uncertainty of 1.3%.

The effect of a 1.3% energy scale uncertainty on the CC and ES flux measurements was determined by shifting the  $N_{\text{Hit}}$  of each Monte Carlo event by 1.3% and re-doing the signal extraction. Through this procedure, it was found that the uncertainty on the CC and ES flux measurements is  $^{+4.6\%}_{-4.5\%}$  and  $^{+4.6\%}_{-3.7\%}$ , respectively.

## Energy Resolution

Based on comparisons between  $^{16}\text{N}$  calibration and source Monte Carlo, the energy resolution is under-predicted by the Monte Carlo by 3% (volume-weighted uncertainty). Specifically, at the  $^{16}\text{N}$   $\gamma$ -ray energy, the source data and Monte Carlo resolutions are 11 and 10.6  $N_{\text{Hit}}$  on average. To estimate the effect of this uncertainty on the flux measurements, the Monte Carlo  $N_{\text{Hit}}$  is smeared by a Gaussian with a variance of  $11^2 - 10.6^2 = 8.6$  for electron energies near the mean energy ( $\sim 5.5$  MeV) of electrons produced through Compton scattering by 6.13 MeV  $\gamma$ s. At other ener-

gies, the Gaussian sigma is scaled by  $\sqrt{E/5.5\text{MeV}}$ . Smearing the energy resolution of Monte Carlo events in this way is found to decrease the CC flux ratio by 0.2% and increase the ES flux ratio by 0.1%.

## Vertex Shift

In Section 5.5.1, the shift in mean vertex relative to the  $^{16}\text{N}$  and  $^8\text{Li}$  source positions was determined. Considering the vertex shift discrepancies between data and Monte Carlo, we estimate the vertex shift uncertainty to be a purely radial shift of  $\frac{\Delta r}{R} = \frac{8\text{cm}}{1200\text{cm}} = 0.7\%$ . The sign of residual shift is that data is shifted more *inward* (i.e. to smaller radius) than that predicted by the Monte Carlo. The net effect after a fiducial volume cut is that the Monte Carlo predicts too few events reconstructing inside the fiducial volume of the detector. To estimate the effect of vertex shift on the results, each Monte Carlo event was shifted inward along its radial position vector by 0.7% \*  $r_{fit}$ . This resulted in the CC and ES flux ratios being decreased by 1.5% and 2.0%, respectively.

## Vertex Resolution

Vertex resolution was also studied using  $^{16}\text{N}$  and  $^8\text{Li}$  calibration data. Considering the vertex shift discrepancies between data and Monte Carlo as well as observed differences between the sources, we estimate that the Monte Carlo vertex resolution is  $\sim 2$  cm smaller than that observed in the data. To estimate the effect of this uncertainty on the flux measurements, the fit x, y, and z positions of Monte Carlo events were smeared by Gaussian functions with sigma equal to  $\sqrt{17^2 - 15^2} = 8$  cm. The effect of this smearing was to lower the CC flux and ES flux by 0.1%.

## Angular Resolution

Although we do not cut events based on their reconstructed direction, the  $\cos \theta_\odot$  PDF shapes are affected by angular resolution. Therefore, we expect the relative number of signal events extracted from neutrino data to be dependent on angular resolution at some level. In Section 5.5.2, it was shown that the angular resolution based on  $^{16}\text{N}$  calibration source data at the center of the detector was in good agreement with that derived from source Monte Carlo.

To estimate the level at which angular resolution enters into the uncertainties in the flux results,  $\cos \theta_\odot$  for CC and ES Monte Carlo events was adjusted to mimic the effects of better or worse angular reconstruction. For Monte Carlo CC events,  $\cos \theta_\odot$  was reassigned a uniform value for 5% of the events which flattened the  $\cos \theta_\odot$  slope by 6%. To increase the CC  $\cos \theta_\odot$  slope, 5% of the events were reassigned a uniform value in way that was proportional to  $\cos \theta_\odot$ . This increased the CC  $\cos \theta_\odot$  slope by 6%. For ES events, the Monte Carlo  $\cos \theta_\odot$  values were shifted toward larger  $\cos \theta_\odot$  by 0.008 (imposing the limit of  $\cos \theta_\odot = 1$ ) to mimic a sharpening of the angular resolution. To broaden the ES peak and add a tail on the  $\cos \theta_\odot$  distribution, 8% of the events were reassigned a uniform  $\cos \theta_\odot$  value. Comparison of the smeared Monte Carlo  $\cos \theta_\odot$  distributions to the angular resolution uncertainty determined from  $^{16}\text{N}$  (see Section 5.5.2) suggest that this smearing represents a conservative estimate of the systematic uncertainty due to angular resolution. The net effect of these smearing procedures is to change the CC flux ratio by  $\pm 0.2\%$  and the ES flux ratio by  $^{+2.6\%}_{-1.8\%}$ . We take  $^{+2.6\%}_{-1.8\%}$  as our ES uncertainty and  $\pm 0.4\%$  as a conservative estimate of our CC systematic uncertainty.

## Backgrounds

Limits on low energy, high energy  $\gamma$ -ray, and instrumental backgrounds in the reduced data set were presented in Chapter 7. Since these are backgrounds *limits* and not background *measurements*, these are included as systematics rather subtracted from the extracted numbers of signal events. From the analysis presented in Section 7.1, low energy radioactive backgrounds are considered to represent a negligible source of systematic uncertainty in the CC and ES flux measurements. Instrumental contamination was also shown in Section 7.3 to be at very low levels. Given that this method only limits the tail of instrumental backgrounds that leak through data cleaning rather than limiting all non-Cerenkov backgrounds, we estimate the systematic uncertainty due to non-Cerenkov backgrounds to be 0.2% for CC flux and 0.5% for ES flux. The analysis presented in Section 7.2 showed that the number of high energy  $\gamma$ -rays reconstructing inside the fiducial volume over our neutrino livetime can be limited to 3.9 events. If present in the data set, these events will distribute themselves among the signal types depending on their  $N_{\text{Hit}}$ ,  $R^3$ , and  $\cos \theta_{\odot}$  values. Unless these events happen to fall into the  $\cos \theta_{\odot} \sim 1$  bins, they will be more likely to add into CC or NC rather than the ES signal. We estimate a CC systematic error of 3.9 events (0.6%) and an ES systematic error of 1.3 events (1.8%) due to high energy  $\gamma$ -ray backgrounds.

## Trigger Efficiency

In Section 5.6 and [61], it was shown that the  $N_{\text{Hit}}$  trigger is  $>99.9\%$  with more than 22 hits in 100 ns coincidence. For the analysis threshold used in this thesis, trigger efficiency represents a negligible source of systematic uncertainty.

## Signal Acceptance

Based on comparisons of  $^{16}\text{N}$  and  $^8\text{Li}$  data (see Section 6.6), the uncertainty on the total sacrifice from the data cleaning, reconstruction, and high-level cuts is estimated to be 0.3%.

## Livetime

The uncertainty on the livetime for the approved neutrino run list used in this analysis is estimated by the Livetime Committee to be 0.1%.

## Oxygen Isotope Correction

The quoted uncertainty [87] on the CC rate correction for measured  $^{17}\text{O}$  and  $^{18}\text{O}$  isotopic abundances is 0.012%.

## Orbital Eccentricity Correction

The uncertainty on correction for eccentricity of the Earth’s orbit is estimated in [89] to be 0.15%.

## D<sub>2</sub>O Targets

The uncertainty on the number of deuteron and electron targets is assumed to be very small compared to other uncertainties. The isotopic purity of the D<sub>2</sub>O (99.918%) is measured to 0.1% accuracy.

## Cross Sections

The cross sections used for neutrino interactions on deuterium (CC and NC) are the effective field theory calculations described in [79]. With a choice of  $L_{1,a} = 5.6\text{fm}^3$  for the axial two body current coupling constant suggested by the authors, cross section calculations agree to better than 1% with NSGK potential model calculations [78] at tabulated energies. The authors quote a theoretical uncertainty of 3% on the CC total cross section, therefore, this is the uncertainty used in this thesis. We take the uncertainty on the total neutrino-electron elastic scattering cross section to be  $\pm 1.5\%$ .

## Solar Model

The uncertainty on the  ${}^8\text{B}$  flux quoted in [5] is +20% and -16%. Uncertainties from the  ${}^8\text{B}$  energy spectrum (Ortiz) are estimated from [86] to be 1.5%.

### 8.5.2 Systematic Error Summary

Table 8.3 shows a summary of the systematic errors. associated with the CC and ES flux measurements. Note that the cross section and solar model errors are reported separately from the total quoted systematic error. To summarize the flux results, we get for the flux ratio measured by the CC reaction

$$R_{CC} \equiv \frac{CC_{data}}{CC_{SSM}} = 0.346 \pm 0.017 \text{ (stat)} \quad {}^{+0.016}_{-0.017} \text{ (syst)} \quad \pm 0.010 \text{ (xsec)}$$

or a total  ${}^8\text{B}$  neutrino flux of (using  $5.15 \times 10^6 \text{cm}^{-2}\text{s}^{-1}$  for BP2000)

$$\phi_{{}^8\text{B}}^{CC} = 1.78 \pm 0.09 \text{ (stat)} \quad {}^{+0.08}_{-0.09} \text{ (syst)} \quad \pm 0.05 \text{ (xsec)} \quad (\times 10^6 \text{cm}^{-2}\text{s}^{-1})$$

The flux ratio from the ES reaction is measured to be

Source of Error	CC Flux	ES Flux
Energy Scale	+4.6 -4.5	+4.6 -3.7
Energy Resolution	-0.2	+0.1
Vertex Shift	-1.5	-2.0
Vertex Resolution	-0.1	-0.1
Angular Resolution	+0.4 -0.4	-1.8 +2.6
Backgrounds		
High energy $\gamma$ -ray	-0.6	-1.8
Low energy radioactivity	0.0	0.0
Instrumental	-0.2	-0.5
Trigger Efficiency	0.0	0.0
Livetime	$\pm$ 0.1	$\pm$ 0.1
Data Reduction	$\pm$ 0.3	$\pm$ 0.3
Orbital Eccentricity Correction	$\pm$ 0.15	$\pm$ 0.15
Oxygen Isotope Correction	$\pm$ 0.012	—
D <sub>2</sub> O Targets	$\pm$ 0.1	$\pm$ 0.1
Total Systematic Error	+4.6 -4.8	+5.3 -5.0
Cross section	3.0	1.5
Solar Model	+20 -16	+20 -16

Table 8.3: Summary of systematic errors (in percent).

$$R_{ES} \equiv \frac{ES_{data}}{ES_{SSM}} = 0.498^{+0.089}_{-0.083} \text{ (stat)} \pm 0.026 \text{ (syst)}$$

or a total  ${}^8\text{B}$  neutrino flux of

$$\phi_{{}^8\text{B}}^{ES} = 2.56^{+0.46}_{-0.43} \text{ (stat)} \pm 0.13 \text{ (syst)} (\times 10^6 \text{ cm}^{-2}\text{s}^{-1})$$

## 8.6 Sanity Checks

In this section, several sanity checks on the results are performed. Many useful quality checks on a large subset of the data used in this thesis have already been presented in the first SNO thesis on solar neutrino data [2]. Examples include reconstructed radial distributions showing AV boundary and demonstration that the ES peak is washed out by large changes in the assumed detector location. In terms of signal extraction, it has been demonstrated with an identical extraction technique (for all practical purposes) that the proper number of events (and errors) are extracted from series of Monte Carlo data sets [91]. The important sanity checks performed for this analysis, aside from all Monte Carlo comparisons with calibration source data presented in Chapter 5, are the degree to which the CC and ES flux measurements are robust to changes in the fiducial volume and energy threshold.

### 8.6.1 Dependence on Fiducial Volume

Figure 8.10 shows the CC and ES flux measurements relative BP2000 SSM predictions as a function of fiducial volume cut. It can be seen from Figure 8.10 that there is very little dependence of these measurements on fiducial volume cut from slightly more than half the  $\text{D}_2\text{O}$  volume out the AV boundary.

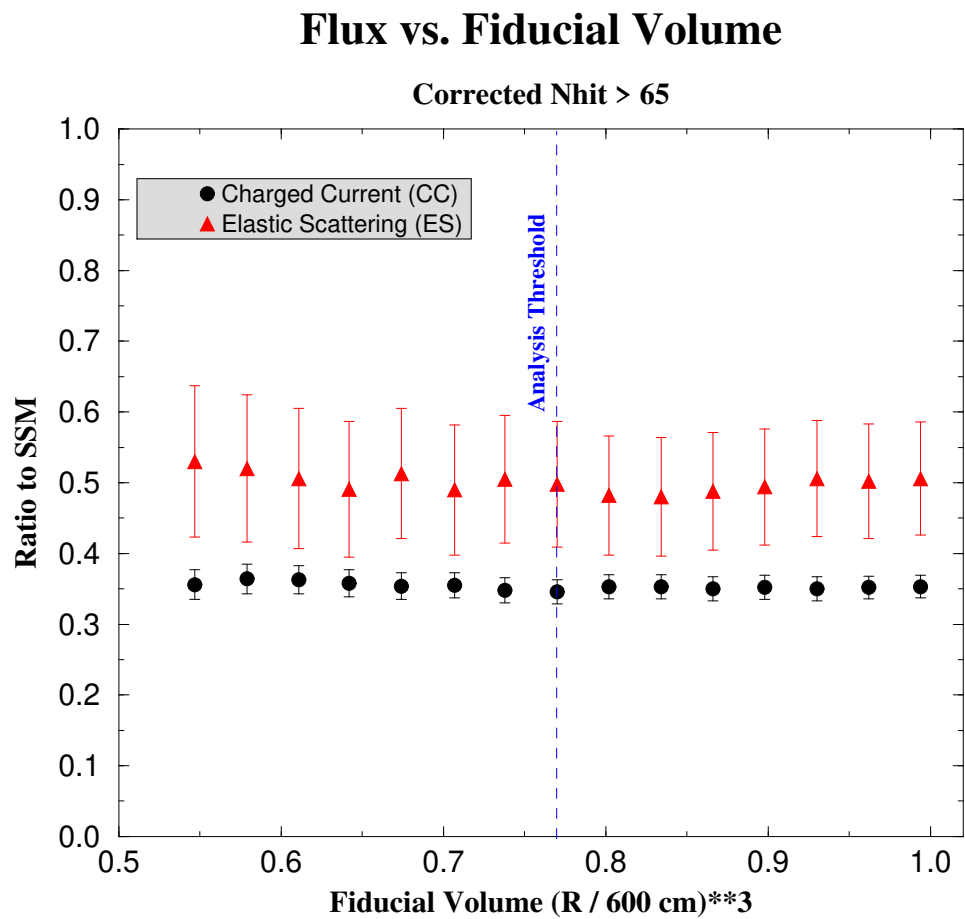


Figure 8.10: CC and ES flux measurements relative BP2000 SSM predictions as a function of fiducial volume cut. Errors shown are statistical only.

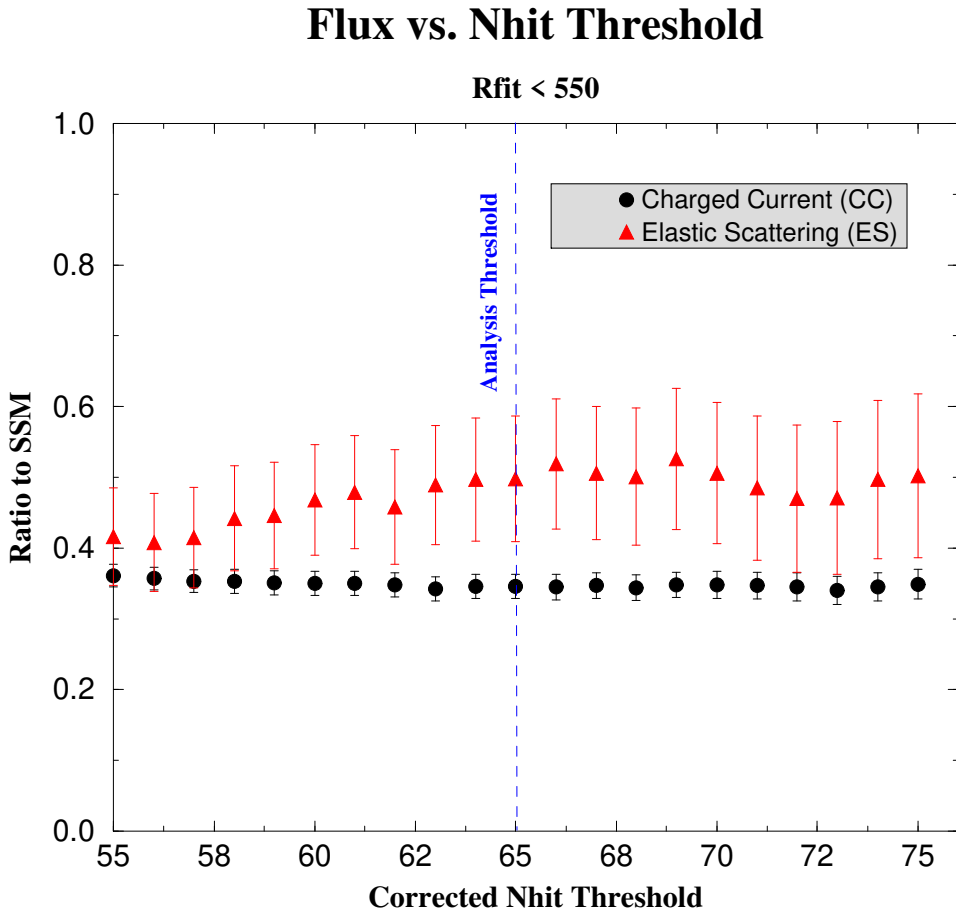


Figure 8.11: CC and ES flux measurements relative SSM predictions as a function of  $N_{\text{Hit}}$  threshold. Errors shown are statistical only.

### 8.6.2 Dependence on Energy Threshold

Figure 8.10 shows the CC and ES flux measurements relative SSM predictions as a function of  $N_{\text{Hit}}$  threshold. The CC and ES flux dependences on  $N_{\text{Hit}}$  are very small near the analysis threshold, which gives us confidence that these measurements are relatively robust to this threshold. At low  $N_{\text{Hit}}$  thresholds, there is a downward trend for ES and slightly upward trend for CC which is likely related to the increased

neutron component and/or backgrounds at low  $N_{\text{Hit}}$ . Also, the larger change in ES flux could be due to the fact the the ES statistics are quite poor above the analysis threshold of 65  $N_{\text{Hit}}$ , and therefore the lower threshold data represents a substantially different data set in a statistical sense.

### 8.6.3 Removal of Muon Follower Cut

Muons which traverse the D<sub>2</sub>O region can dissociate deuterons to produce free neutrons. As described in Section 6.5, the muon follower (short) cut is designed to cut capture events from these neutrons as well as decays of muon spallation nuclei. By removing the muon follower cut, some fraction of these events are introduced into the data set. However, not all of the muon associated events will be included, because the  $N_{\text{Hit}}$  burst cut described in Section 6.2.4 will remove a large fraction of the spallation events as well as high multiplicity ( $> 4$ ) muon follower neutron events. In addition, radioactive background events can pile-up with the muon event and are therefore re-introduced as well. The pile-up probability is only substantial at low  $N_{\text{Hit}}$  where the radioactive background rates are high. Above 65  $N_{\text{Hit}}$ , events introduced into the data set by removal of the muon follower cut represent a “spike” low multiplicity neutron capture events in the D<sub>2</sub>O, to a fairly good approximation.

Above our analysis threshold of 65  $N_{\text{Hit}}$ , 43 additional events were introduced by removing the muon follower cut. After signal extraction, the number of “NC” events increased by 28.2 events (65%) and the number of CC events increased by 16.9 events (2.7%). If we lower the threshold extraction threshold to 55  $N_{\text{Hit}}$  for increased neutron sensitivity, the additional number of events from removal of muon follower is 143. In this case, signal extraction results in 108.4 additional “NC” events (58%) and 33.0

additional CC events (3.7%). In both  $N_{\text{Hit}}$  threshold cases, the number of ES events changed by less than 2 events.

## 8.7 CC $N_{\text{Hit}}$ Spectrum Compared to SSM

In Section 8.3.2, the extracted CC  $N_{\text{Hit}}$  spectrum was presented. Comparison of this spectrum to the SSM predictions shows that the extracted CC  $N_{\text{Hit}}$  spectrum is well fit by an undistorted  ${}^8\text{B}$  neutrino energy spectrum. Therefore, with the energy threshold chosen for this analysis ( $N_{\text{Hit}} > 65$ ) the data implies a flux suppression of 0.35 without “significant” high energy distortions (see Figure 8.12). The disadvantage of producing an  $N_{\text{Hit}}$  rather than energy spectrum is that it is difficult to deduce from a plot like that shown Figure 8.12 the sensitivity one has to spectral distortions without detailed knowledge of the detector response.

Figure 8.13 represents the spectrum as the ratio to BP2000 SSM predictions, both with and with inclusion of the expected SSM *hep* flux. The  $\chi^2$  for a energy-independent 0.35 SSM  ${}^8\text{B}$  suppression is 14.96 (14.13) for 20 degrees of freedom without (with) including SSM *hep*. The corresponding probabilities are 77.9% without SSM *hep* and 82.4% with *hep* included. We therefore conclude that the CC  $N_{\text{Hit}}$  spectrum is consistent with a flat suppression of 35%. The error bars are statistical only and the three data points below our analysis threshold of 65  $N_{\text{Hit}}$  were ignored in the  $\chi^2$  calculations.

## CC NHIT Spectrum

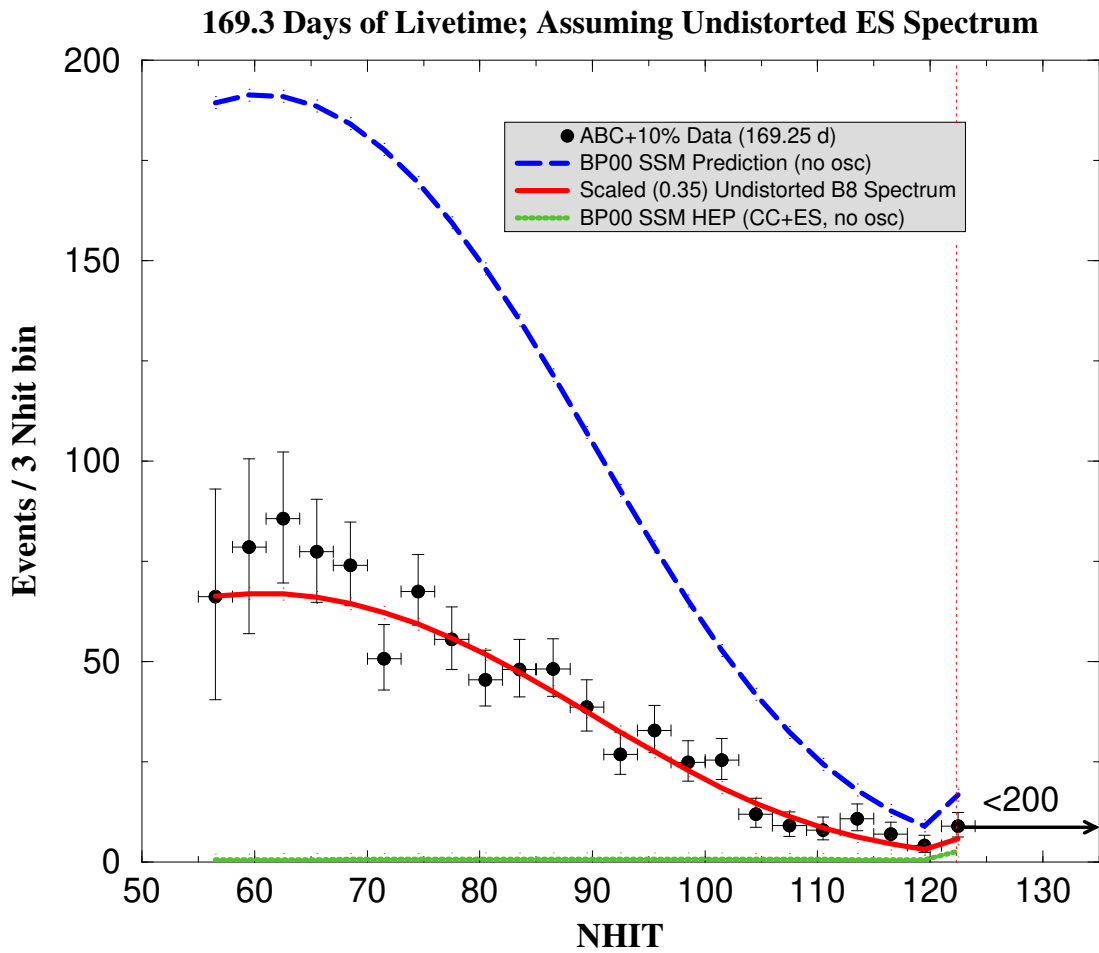


Figure 8.12: Comparison of the extracted CC  $N_{\text{Hit}}$  spectrum (169.3 days) with BP2000 SSM predictions. Errors shown are statistical only.

## CC NHIT Spectrum

169.3 Days of Livetime; Assuming Undistorted ES Spectrum

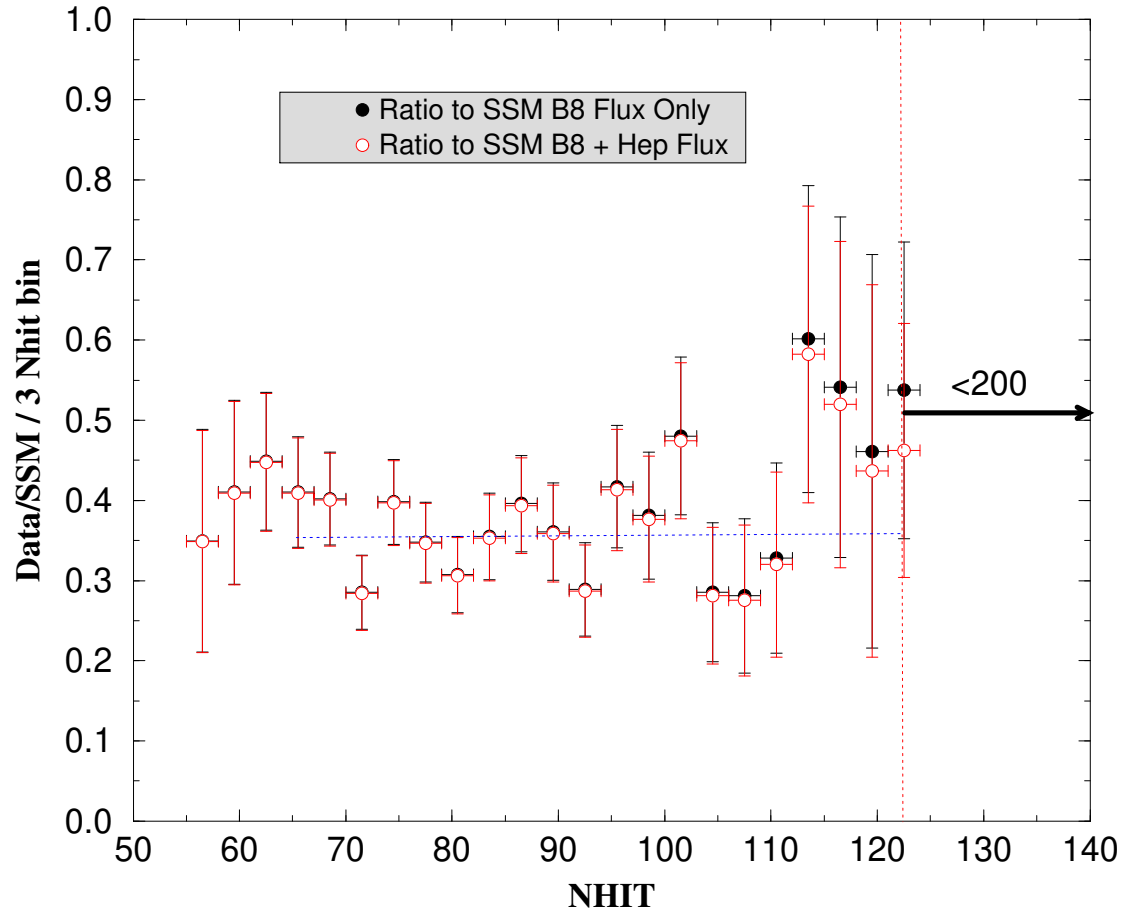


Figure 8.13: Ratio of extracted CC  $N_{\text{Hit}}$  spectrum (169.3 days) to BP2000 SSM predictions. The line represents the best energy-independent fit to the spectrum data ( $0.356 \pm 0.015$  for  ${}^8\text{B}$  and  $0.353 \pm 0.015$  for  ${}^8\text{B} + \text{hep}$ ). Errors shown are statistical only.

## 8.8 *hep* Neutrino Flux

The Standard Solar Model predicts neutrinos from a very rare part of the pp chain where  $^3\text{He}$  and a proton fuse giving the following reaction



The predicted flux is  $9.3 \times 10^3 \text{ cm}^2 \text{s}^{-1}$ , although no credible theoretical uncertainties have been assigned. While the predicted *hep* flux is less 0.2% of the  $^8\text{B}$  neutrino flux, the neutrino energy distribution does extend past the  $^8\text{B}$  endpoint (15 MeV) up to 18.77 MeV. This fact allows for a direct *hep* neutrino search by looking for CC and ES events past the  $^8\text{B}$  endpoint, properly taking into account energy scale and resolution uncertainties. The good energy response afforded by the CC reaction allows SNO to make a sensitive search for *hep* neutrinos in comparison to searches with the ES reaction.

Two approaches to measurement of the *hep* flux are performed. In one method, the number of events above some suitably chosen  $N_{\text{Hit}}$  threshold are counted. Comparison to the expected background from  $^8\text{B}$  neutrinos (BP200 SSM) gives a signal confidence level for *hep* neutrino induced events. The second method involves fitting for the number of CC and ES events produced by *hep* neutrino interactions using Monte Carlo derived distributions as PDFs. The *hep* signal then becomes an additional signal extracted from the neutrino data set in addition to the “NC” and  $^8\text{B}$  CC and ES signals.

### 8.8.1 Observations Near ${}^8\text{B}$ Endpoint

In this section, the number of events near the  ${}^8\text{B}$  endpoint are determined to search for an excess above that expected from  ${}^8\text{B}$  neutrinos themselves. In the absence of other backgrounds, these events (if they exist) are interpreted as the result of *hep* neutrino interactions in the detector.

The Monte Carlo derived  $N_{\text{Hit}}$  distributions for  ${}^8\text{B}$  and *hep* neutrinos reconstructing inside the fiducial volume are used to arrive at a threshold for optimal sensitivity. Note that this optimal threshold is determined by study of expected signal distributions *without reference to the neutrino data itself*. Figure 8.14 shows the combined CC+ES  $N_{\text{Hit}}$  distributions obtained from Monte Carlo of 100 and 4000 times the BP2000 SSM over our livetime for  ${}^8\text{B}$  and *hep* neutrinos, respectively. Note that the *hep*  $N_{\text{Hit}}$  distribution extends further in energy than the  ${}^8\text{B}$  distribution, as expected. Figure 8.15 shows total number of events expected in the 169.3 day data set as a function of  $N_{\text{Hit}}$  threshold for  ${}^8\text{B}$  and *hep* neutrinos.

To estimate the  $N_{\text{Hit}}$  threshold which maximizes our *hep* search sensitivity, the following procedure was used. For a given  $N_{\text{Hit}}$  threshold, the number of expected events from  ${}^8\text{B}$  and *hep* neutrinos based on SSM predictions were obtained (see Figure 8.15). It was assumed that the mean background to our *hep* search is the number of expected events from  ${}^8\text{B}$  neutrinos above the  $N_{\text{Hit}}$  threshold. If the *hep* neutrino flux is actually what the SSM predicts, then the number observed events is expected to be the summed Poisson fluctuation of the signal (*hep*) and background ( ${}^8\text{B}$ ). The Feldman and Cousins 90% confidence level upper limit [92] is then calculated (using computer code extracted from [93]) for the Poisson fluctuated number of “observed” events in the presence of known mean background from  ${}^8\text{B}$  for the given  $N_{\text{Hit}}$  threshold. This

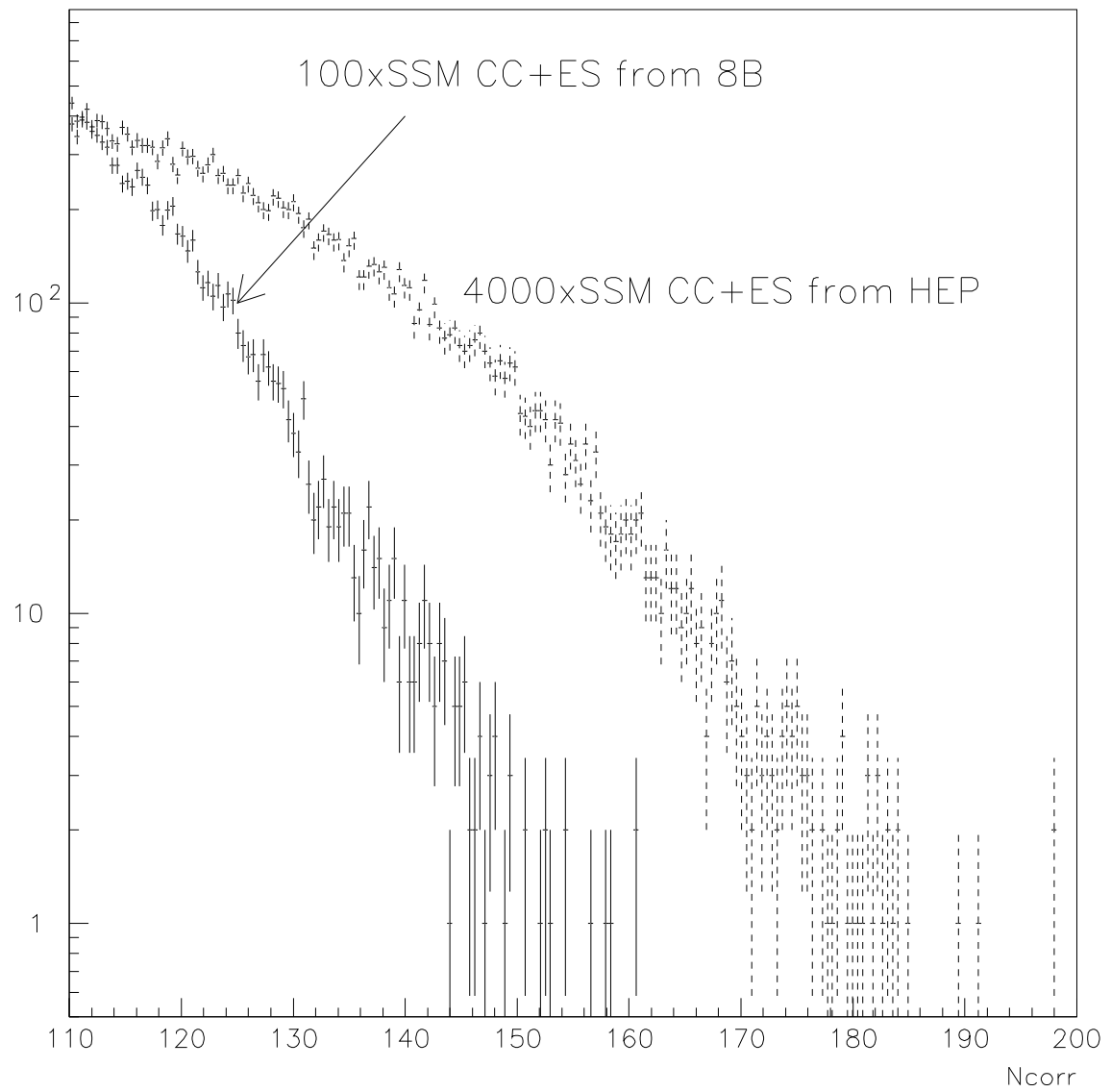


Figure 8.14: Combined CC+ES  $N_{\text{hit}}$  distributions obtained from Monte Carlo of 100 and 4000 times the BP2000 SSM over our livetime for  ${}^8\text{B}$  and *hep* neutrinos, respectively.

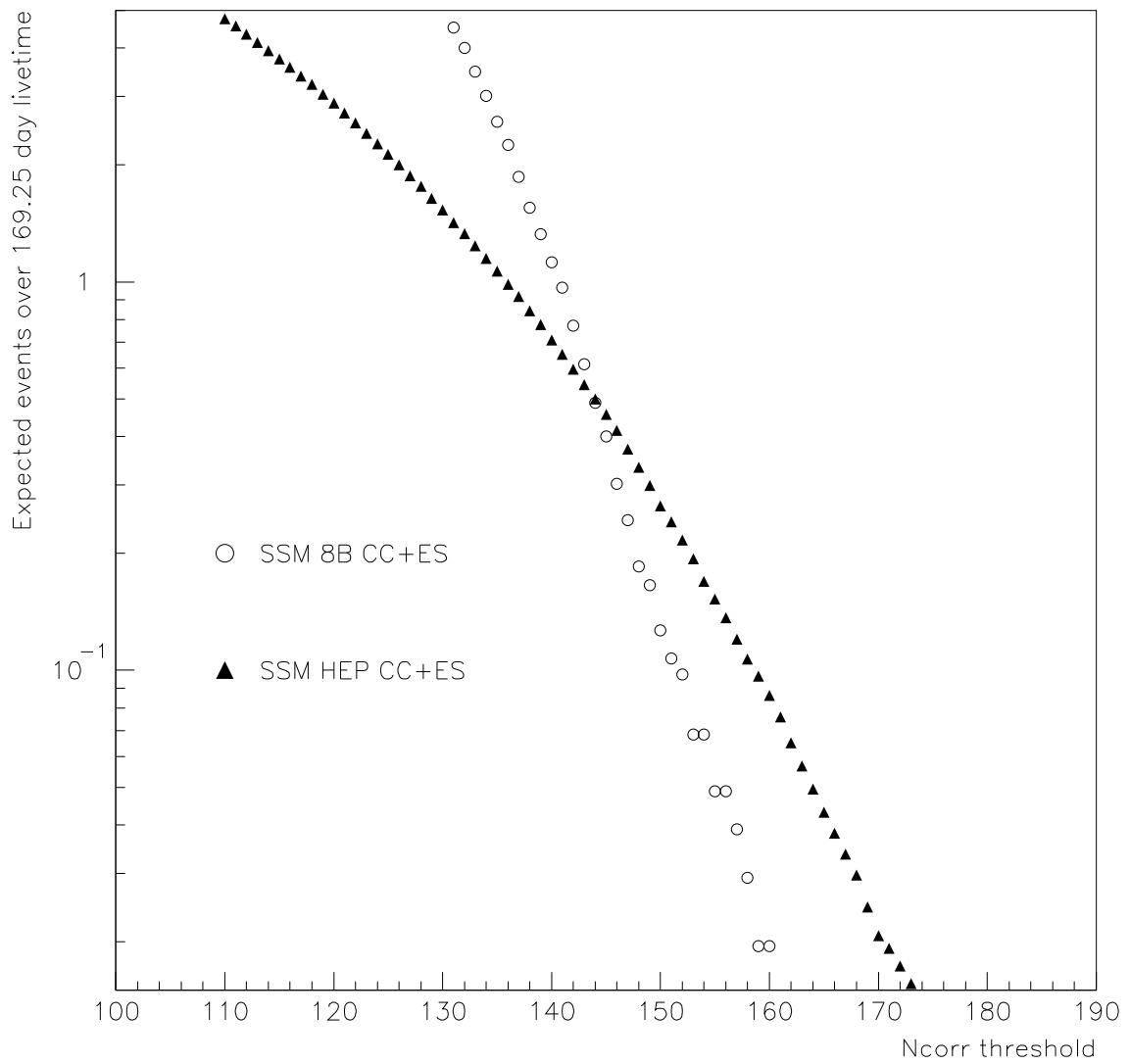


Figure 8.15: Total number of events expected in the 169.3 day data set as a function of  $N_{\text{Hit}}$  threshold for  ${}^8\text{B}$  and *hep* neutrinos.

procedure is followed for all thresholds above  $110 N_{\text{Hit}}$  to find the threshold with the lowest 90% upper bound on the number of signal events. This entire procedure is repeated many times to sample a sufficient number of background and signal fluctuations. For SSM  ${}^8\text{B}$  and *hep* signals, the distribution of  $N_{\text{Hit}}$  thresholds following this procedure is shown in Figure 8.16. Also shown is the distribution of  $N_{\text{Hit}}$  thresholds using the measured flux suppression of 0.35 times the SSM  ${}^8\text{B}$ . Based on the results found in this thesis, this is a more proper estimate of the expected *hep* flux background.

Motivated by the distributions shown in Figure 8.16, we chose an  $N_{\text{Hit}}$  threshold of 141 when considering the full SSM  ${}^8\text{B}$  flux as the expected background and an  $N_{\text{Hit}}$  threshold of 136 for a background of 0.35 x SSM. For the full SSM above a threshold of 141  $N_{\text{Hit}}$ , we expect a mean background of 0.965 events. For the 0.35 x SSM  ${}^8\text{B}$  flux background, we expect a mean background of 0.788 events.

One event at 168  $N_{\text{Hit}}$  is observed in the neutrino data set above both thresholds and inside our fiducial volume after standard reduction is applied. This event is shown in Figure 8.17. For the full SSM  ${}^8\text{B}$  flux background, the 90% and 99% confidence intervals are [0, 3.4] and [0, 5.9] events, respectively. The number of expected *hep* events above 141  $N_{\text{Hit}}$  is 0.65. Therefore, using this background, the 90% and 99% upper limits on the *hep* neutrino flux are 5.2 and 9.1 times the BP2000 SSM predictions, respectively. For the 0.35 x SSM  ${}^8\text{B}$  flux background, the 90% and 99% confidence intervals are [0,3.6] and [0, 6.1] events, respectively. The number of expected *hep* events above 136  $N_{\text{Hit}}$  is 0.98. Therefore, using the flux suppressed  ${}^8\text{B}$  background, the 90% and 99% upper limits on the *hep* neutrino flux are 3.7 and 6.2 times the BP2000 SSM predictions, respectively.

In the absence of backgrounds other than  ${}^8\text{B}$  neutrinos in this  $N_{\text{Hit}}$  regime, this

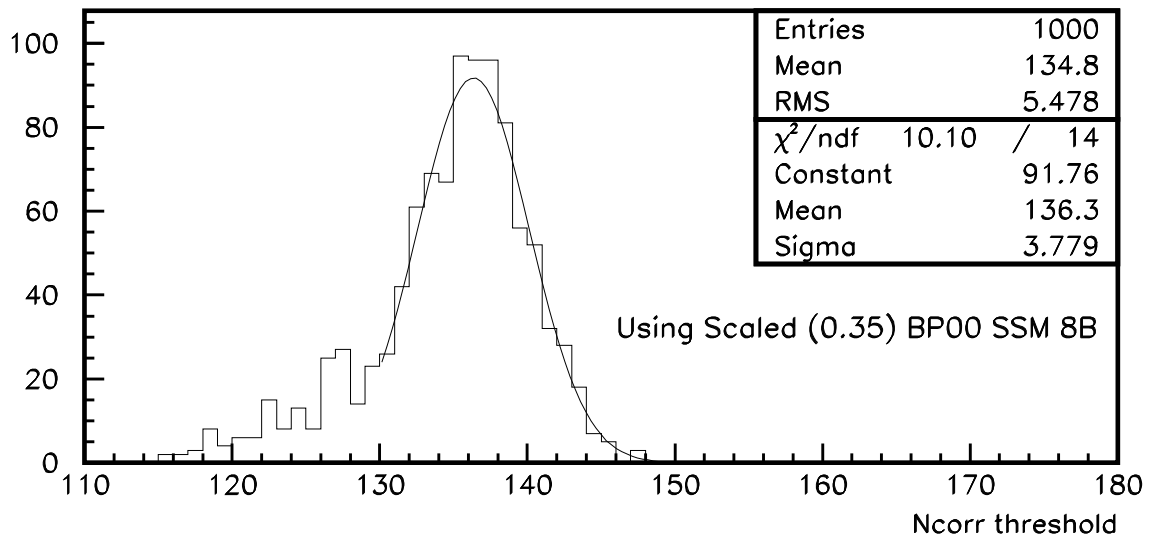
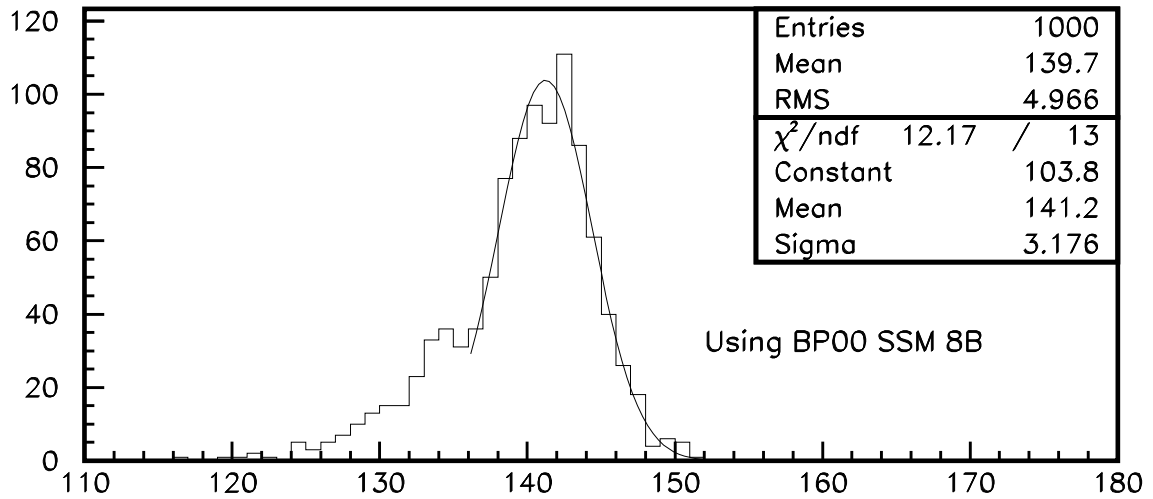


Figure 8.16: Distribution of  $N_{\text{Hit}}$  thresholds with the best expected sensitivity to a *hep* signal based on Monte Carlo signal (*hep* CC+ES) and background ( ${}^8\text{B}$  CC+ES) distributions. The top figure is for full SSM  ${}^8\text{B}$  and the bottom corresponds to the  ${}^8\text{B}$  background expected from the measurements in this thesis (0.35 SSM from CC).

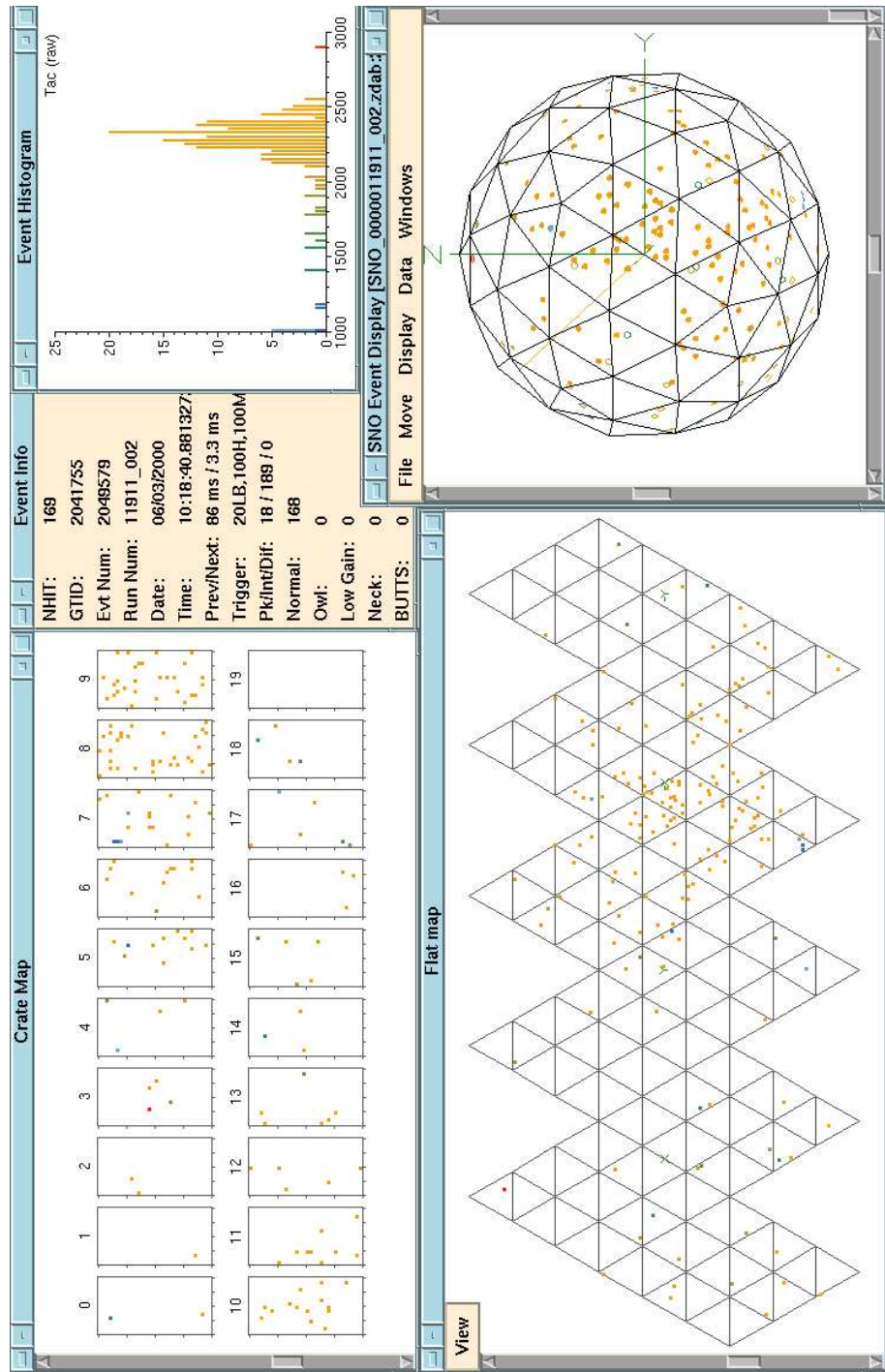


Figure 8.17: Event display of *hep* neutrino candidate event found at  $168 N_{\text{Hit}}$ .

	$N_{\text{Hit thr}}$	${}^8\text{B}$ Mean bg	Expect $hep$	# obs	90%,99% CI (SSM)
No syst smearing					
SSM ${}^8\text{B}$ bg	141	0.97	0.65	1	[0, 5.2], [0, 9.1]
0.35 SSM ${}^8\text{B}$ bg	136	0.79	0.98	1	[0, 3.7], [0, 6.2]
Smeared for energy resolution uncertainty					
SSM ${}^8\text{B}$ bg	141	1.14	0.69	1	[0, 4.7], [0, 8.4]
0.35 SSM ${}^8\text{B}$ bg	136	0.82	1.04	1	[0, 3.4], [0, 5.9]
Energy scale shifted for $+1\sigma$ scale uncertainty					
SSM ${}^8\text{B}$ bg	141	1.48	0.80	1	[0, 3.7], [0, 6.8]
0.35 SSM ${}^8\text{B}$ bg	136	1.22	1.18	1	[0, 2.7], [0, 4.8]
Energy scale shifted for $-1\sigma$ scale uncertainty					
SSM ${}^8\text{B}$ bg	141	0.97	0.59	1	[0, 5.7], [0, 10.1]
0.35 SSM ${}^8\text{B}$ bg	136	0.68	0.90	1	[0, 4.1], [0, 6.9]

Table 8.4: Summary of  $hep$  results using observations near the  ${}^8\text{B}$  endpoint.

one event can be interpreted as either a  $hep$  neutrino-induced event or fluctuation of the mean  ${}^8\text{B}$  background of 0.788 events. While neither of these hypotheses can be disproven, a look at the placement of this event within the Cerenkov signal box raises some suspicion about this event being neutrino-induced at all. Figure 8.18 shows ITR versus  $\chi^2_{corr}$  for the selected events comprising the reduced data set, where it can be seen that the  $hep$  candidate event is near the corner of the Cerenkov signal box. From Figure 8.18, it is likely that this event is instrumental in origin rather than from a neutrino interaction. One cannot definitively conclude from this plot that this is indeed the case, however, because Cerenkov light has a non-zero (albeit small) probability of having these parameters values.

Table 8.4 shows a summary of the  $hep$  neutrino results using observations near the  ${}^8\text{B}$  endpoint. Also included are the results when energy scale and resolution systematics are included. Note that the only energy systematic which worsens the  $hep$  limit obtained is a 1.3% downward shift in the energy scale. Including this systematic and using the measured  ${}^8\text{B}$  flux suppression obtained in this thesis, the

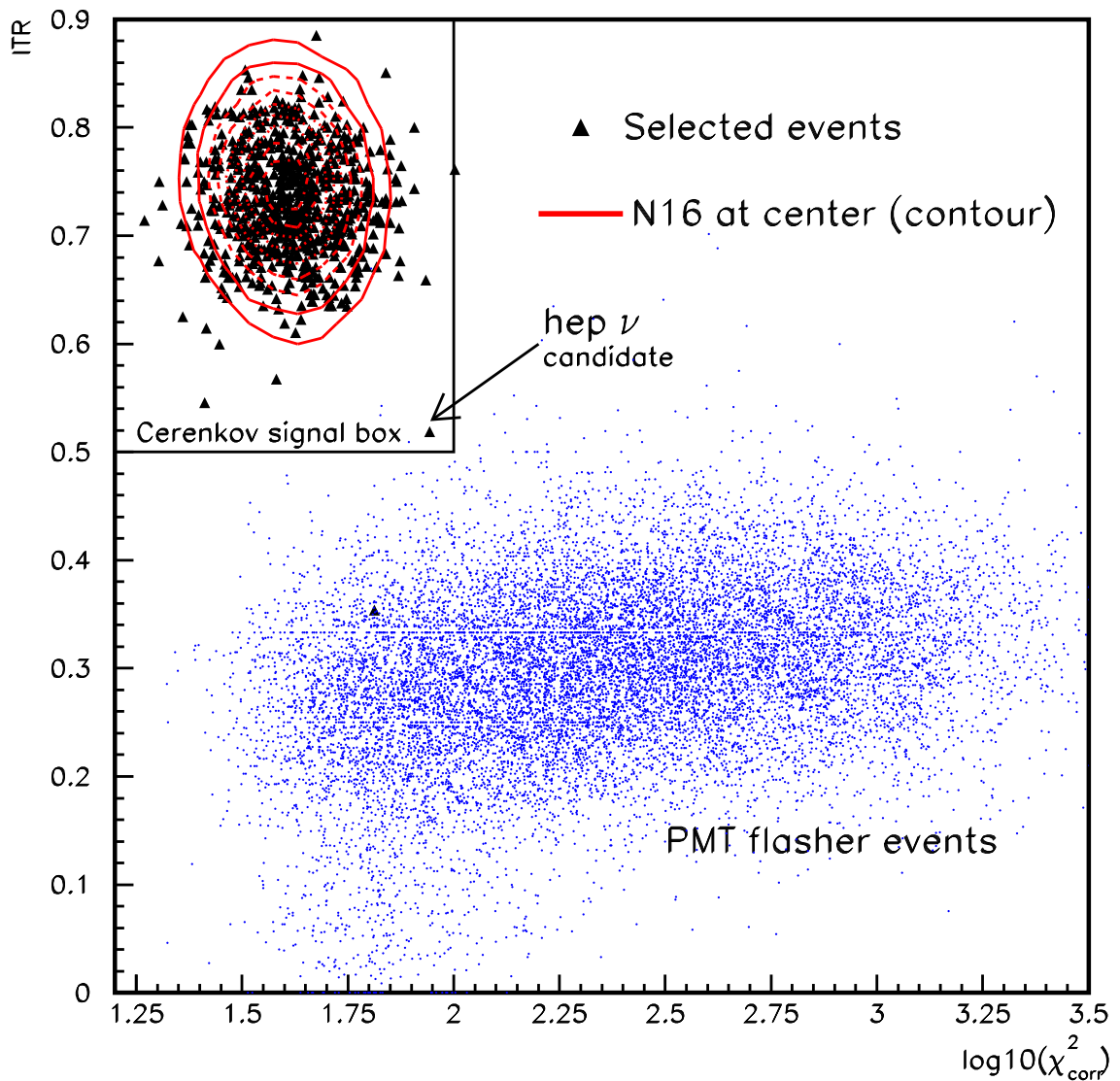


Figure 8.18: ITR versus  $\chi^2_{corr}$  for selected events comprising the reduced data set. This figure shows that the *hep* neutrino candidate event lies near the corner of the Cerenkov signal box. Also shown are  $^{16}\text{N}$  and flasher events, showing that the selected data closely resemble a Cerenkov light calibration source. Flasher events are simply shown for reference, rather than to imply that the the *hep* neutrino candidate event is the tail of the flasher distribution.

90% and 99% upper limits on the *hep* flux are 4.1 and 6.9 times the BP2000 SSM flux.

### 8.8.2 Fitting for the *hep* Signal

In addition to the  ${}^8\text{B}$  endpoint measurements presented in the previous sections, the number of *hep* neutrinos can be statistically determined from the complete data set using PDFs derived from *hep* Monte Carlo signal distributions. In this method, the *hep* neutrino signal is simply considered as another signal type to be extracted from the data using the signal extraction techniques described in Section 8.2.1.

The main observable which separates *hep* neutrinos from other signal types is that *hep* neutrinos have higher energies on average. Therefore, we anticipate that the *hep*  $N_{\text{Hit}}$  PDF will be the most important one for separating CC and ES *hep* events from the other signal types from  ${}^8\text{B}$ . The *hep* CC + ES signal  $N_{\text{Hit}}$  PDF is shown in Figure 8.19.

The number of *hep* events statistically extracted from the data set is  $15.14^{+11.61}_{-8.83}$ . Monte Carlo simulation of  $4000 \times \text{SSM}$  (BP2000) *hep* flux of  $9.3 \times 10^3 \text{cm}^{-2}\text{s}^{-1}$  yields 15.4 *hep* CC+ES events expected over our neutrino livetime. The  $3\sigma$  upper limit on the *hep* rate obtained by this method is 3.2 times the BP2000 SSM rate.

## 8.9 Summary

In this chapter, neutrino signals were extracted from the reduced data set corresponding to 169.3 days of livetime. The main focus of these extractions was the CC and ES total flux measurements, which were shown to be substantially lower than BP2000 SSM predictions - 35% of SSM flux for CC and 50% of SSM for ES. In addition, the

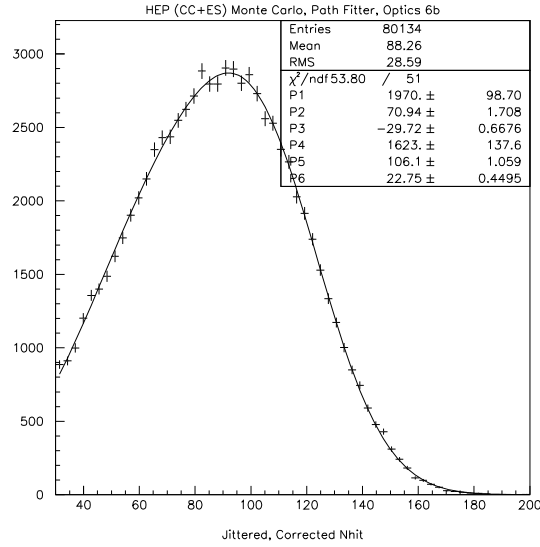


Figure 8.19: Monte Carlo *hep* CC+ES distribution in  $N_{\text{Hit}}$  for 40000xSSM (BP00) over the neutrino data livetime. The  $N_{\text{Hit}}$  distribution is fit to a sum of two Gaussian functions.

first CC  $N_{\text{Hit}}$  spectrum and *hep* neutrino flux analyses in SNO were presented. It was shown that the CC spectrum is consistent with that expected from an undistorted  $^8\text{B}$  neutrino spectrum. Two approaches to *hep* flux analysis were presented. Through observations near the  $^8\text{B}$  endpoint with consideration of energy systematics, *hep* flux limits of 4.1 (90% C.I.) and 6.9 (99% C.I.) times SSM expectations were obtained. A statistical fit for the *hep* flux signal yielded a  $3\sigma$  upper limit of 3.2 times the SSM expected flux.

# Chapter 9

## Conclusions and Discussion

In this chapter, we discuss what can be learned from the solar neutrino results presented in Chapter 8.

### 9.1 CC and ES Rates

It was mentioned in Chapter 2 that the CC and ES reactions have different sensitivities to neutrino flavor. In the context of solar neutrinos, the CC reaction only occurs for electron neutrinos while the ES reaction has mixed sensitivity to all neutrino flavors through the additional NC component to the scattering<sup>1</sup>. Therefore, comparison between observed rates of CC and ES events initiated by solar neutrinos can be used to probe the flavor content of  ${}^8\text{B}$  neutrinos reaching the Earth. If the solar neutrino problem is due to solar  $\nu_e$ 's oscillating into either muon or tau neutrinos, the flux derived from CC data will be smaller than the flux derived from ES data. Alternatively, if  $\nu_e \rightarrow \nu_s$  oscillations are the explanation of the solar neutrino problem,

---

<sup>1</sup>Recall that at solar neutrino energies, the cross section for  $\nu_e$  scattering on electrons is 6-7 times that of  $\nu_\mu$  and  $\nu_\tau$ .

the  ${}^8\text{B}$  flux determined from CC and ES rate measurements will be the same.

The measured  ${}^8\text{B}$  neutrino flux determined from the CC data is

$$\phi_{{}^8\text{B}}^{CC} = 1.78 \pm 0.09 \text{ (stat)} {}^{+0.08}_{-0.09} \text{ (syst)} (\times 10^6 \text{cm}^{-2} \text{s}^{-1})$$

and as measured by the ES reaction,

$$\phi_{{}^8\text{B}}^{ES} = 2.56 {}^{+0.46}_{-0.43} \text{ (stat)} \pm 0.13 \text{ (syst)} (\times 10^6 \text{cm}^{-2} \text{s}^{-1})$$

The ratio of these two flux measurements is

$$\left(\frac{CC}{ES}\right)_{SNO} = 0.695 {}^{+0.156}_{-0.120}$$

which is less than unity by  $2.0\sigma$ . Monte Carlo methods were used to estimate the error on the ratio assuming an asymmetric Gaussian distribution with appropriate variances for each of the CC and ES results<sup>2</sup>. The confidence level for a CC/ES ratio less than unity from Monte Carlo of these asymmetric Gaussian distributions is 95.5%. The fact that the SNO CC measured flux is  $2\sigma$  lower than that measured by the ES reaction is suggestive of active neutrino oscillations. However, the significance is poor due to the limited ES statistics in SNO for the 169.3 day livetime.

SuperKamiokande has collected a much larger sample of elastic scattering events which can be compared to the SNO CC measured neutrino flux. After 1258 days of solar neutrino data collection, SuperKamiokande measures a flux of  $2.32 {}^{+0.09}_{-0.08} \times 10^6 \text{cm}^{-2} \text{s}^{-1}$  above an electron energy threshold of 5 MeV [12]. The SNO CC to Superkamiokande ES flux ratio is

$$\frac{CC_{SNO}}{ES_{SK}} = 0.767 {}^{+0.067}_{-0.062}$$

---

<sup>2</sup>For simplicity, the CC and ES errors were assumed to be uncorrelated in the ratio error determination.

which is  $3.5\sigma$  from unity. The confidence level for a CC/ES ratio less than unity using the SuperKamiokande result and the same Monte Carlo method previously mentioned to estimate the ratio error is greater than 99.98%. We conclude that this result represents evidence for  $\nu_e \rightarrow \nu_{\mu,\tau}$  oscillations as an explanation of the solar neutrino problem. While a small admixture of  $\nu_e \rightarrow \nu_s$  oscillations cannot be ruled out, this result strongly disfavors exclusive oscillation into a sterile state for solar neutrinos. This result is also consistent with the first hint of active neutrino oscillations in SNO presented in [2].

It should be remarked that although the SNO ES statistics are rather limited, the ES results found in this thesis are consistent with the SuperKamiokande elastic scattering results. The SNO CC and ES signals are similar in many regards - same final state ( $e^-$ ), comparable energy distributions, etc - so we might expect that a serious problem with the CC analysis (e.g. mis-estimated signal sacrifice from reduction) would also manifest itself in ES results that are in disagreement with the high statistics SuperKamiokande result (assuming this to be correct). The consistency of our ES measurement with SuperKamiokande gives us some additional confidence in components of the CC analysis in common with the ES measurement of the  ${}^8\text{B}$  flux.

### 9.1.1 Neutrino Flavor Content of ${}^8\text{B}$ Flux

It has been demonstrated that the  $CC_{SNO}/ES_{SK}$  ratio is significantly less than one in this analysis. Since the relative sensitivity of neutrino elastic scattering from electrons for  $\nu_e$  and other active neutrinos ( $\nu_{\mu,\tau}$ ) is known, the flavor content of  ${}^8\text{B}$  neutrinos can be deduced by comparing CC and ES flux measurements. The SNO CC rate is used

to measure the total  ${}^8\text{B}$   $\nu_e$  flux,  $\phi_{\nu_e}$ ,

$$\phi_{CC} = \phi_{\nu_e} \quad (9.1)$$

The ES measured flux,  $\phi_{ES}$ , has sensitivity to both  $\nu_e$  and  $\nu_{\mu,\tau}$ , and may therefore consist of a mixture of these neutrino “types”<sup>3</sup>,

$$\phi_{ES} = \phi_{\nu_e} + \frac{1}{6.7} \phi_{\nu_{\mu,\tau}} \quad (9.2)$$

where the  $1/6.7$  factor is the ratio of total  $\nu_{\mu,\tau}$  to  $\nu_e$  ES cross sections over the relevant  ${}^8\text{B}$  solar neutrino energy range<sup>4</sup>.

Simple comparison of Equations 9.1 and 9.2 gives the following relations for the  $\nu_e$ ,  $\nu_{\mu,\tau}$ , and total active neutrino flux,  $\phi_{tot}$ ,

$$\phi_{\nu_e} = \phi_{CC} \quad \phi_{\nu_{\mu,\tau}} = 6.7(\phi_{ES} - \phi_{CC}) \quad \phi_{tot} = \phi_{\nu_e} + \phi_{\nu_{\mu,\tau}} = 6.7\phi_{ES} - 5.7\phi_{CC}$$

Inserting the SNO CC measurement obtained in this thesis of  $\phi_{{}^8\text{B}}^{CC} = 1.78_{-0.14}^{+0.13} \times 10^6 \text{cm}^{-2} \text{s}^{-1}$  and the SuperKamiokande ES measurement of  $2.32_{-0.08}^{+0.09} \times 10^6 \text{cm}^{-2} \text{s}^{-1}$  we get,

$$\phi_{\nu_{\mu,\tau}} = 3.62_{-1.08}^{+1.06} \times 10^6 \text{cm}^{-2} \text{s}^{-1} \quad \phi_{tot} = 5.39_{-1.09}^{+1.07} \times 10^6 \text{cm}^{-2} \text{s}^{-1}$$

Notice that the non-electron active neutrino component of the  ${}^8\text{B}$  flux is measured to be  $3.4\sigma$  from zero. Also, the total active flux of  ${}^8\text{B}$  neutrinos is consistent with the most recent BP2000 (modified) flux of  $5.05_{-0.81}^{+1.01} \times 10^6 \text{cm}^{-2} \text{s}^{-1}$ . These results are summarized in Figures 9.1 and 9.2.

---

<sup>3</sup>Muon and tau neutrinos cannot be distinguished in these CC and ES comparisons.

<sup>4</sup>This ratio is only weakly energy dependent over this neutrino energy range. For example, integration of the cross sections over electron energies from 5 MeV (SuperK threshold) to the kinematic limit yields 1/6.76 and 1/6.60 for the ratios at 7 MeV and 14 MeV neutrino energy, respectively. Radiative corrections have not been included.

## Neutrino Flavor Composition of B8 Flux

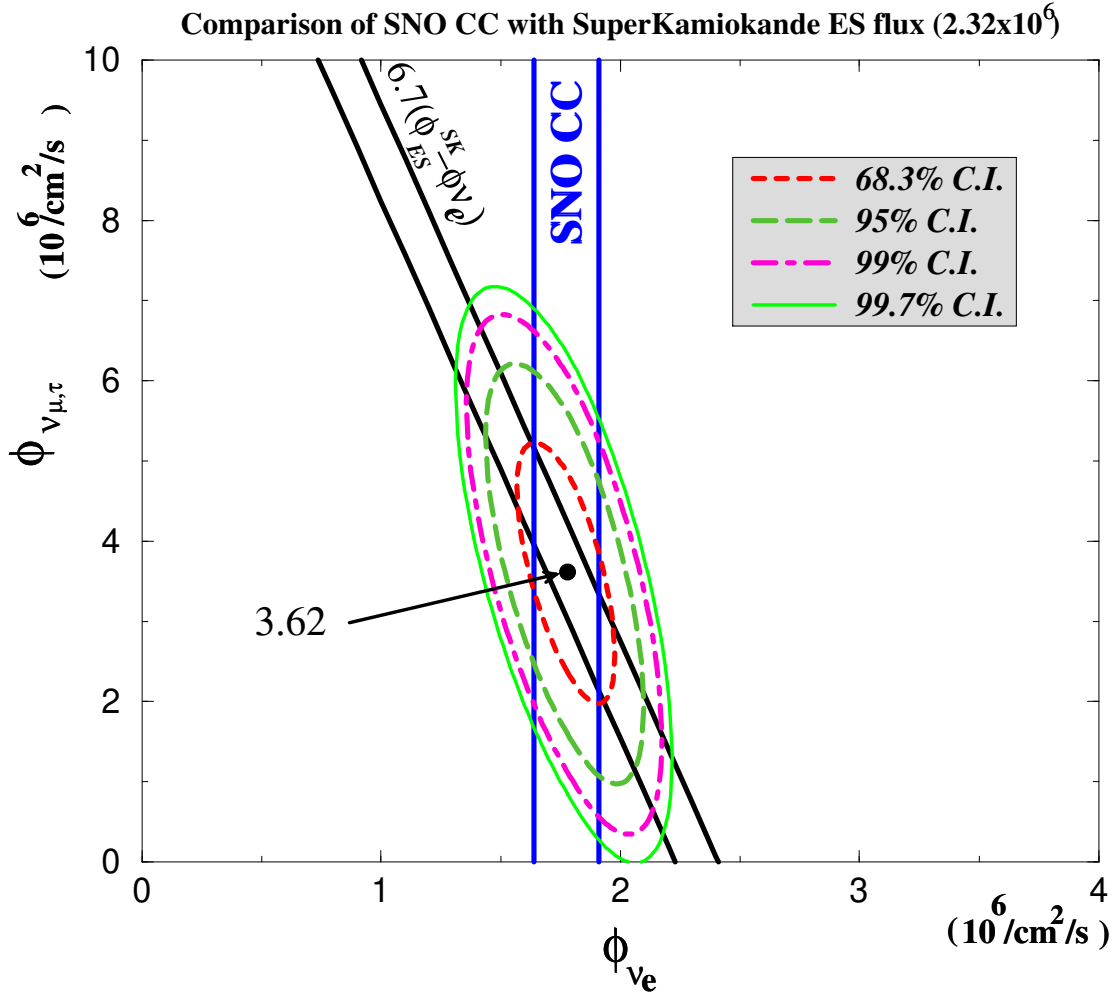


Figure 9.1: Measurement of the non-electron active neutrino component of the  $^8\text{B}$  flux through comparison of SNO CC and Superkamiokande ES flux results. The negatively sloping band represents the  $\pm 1\sigma$   $\nu_{\mu,\tau}$  flux versus the  $\nu_e$  flux. The measured  $\nu_e$  flux from the SNO CC rate is shown as a vertical band. The 68.3%, 95%, 99%, and 99.7% confidence intervals (ellipses) are shown in the figure along with the measured  $\nu_{\mu,\tau}$  flux of  $3.62^{+1.06}_{-1.08} \times 10^6 \text{ cm}^{-2} \text{s}^{-1}$ . Figure motivated from work by A. Hime.

## Neutrino Flavor Composition of B8 Flux

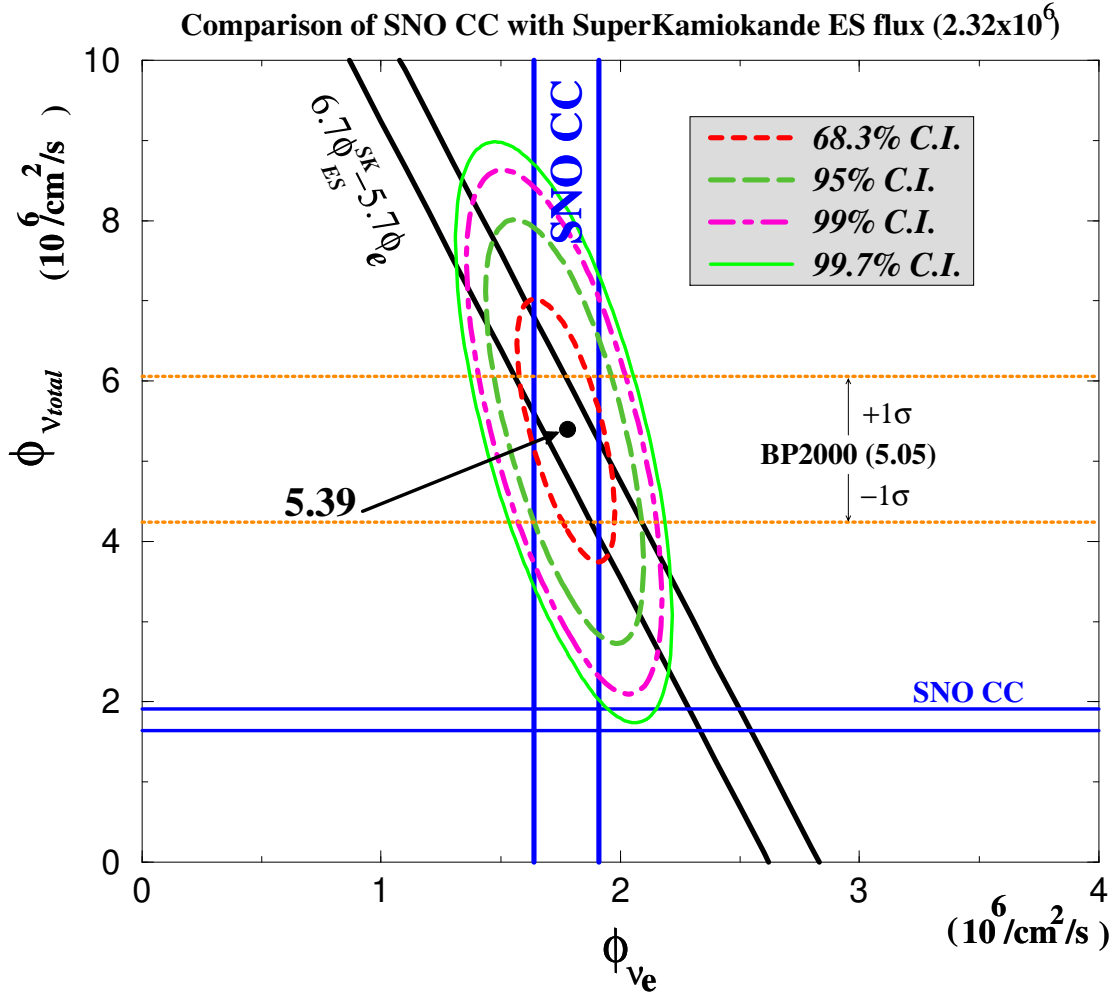


Figure 9.2: Measurement of the total active  $^8\text{B}$  neutrino flux though comparison of SNO CC and Superkamiokande ES flux results. The negatively sloping band represents the  $\pm 1\sigma$  total active neutrino flux versus the  $\nu_e$  flux. The measured  $\nu_e$  flux from the SNO CC rate is show as a vertical band. The 68.3%, 95%, 99%, and 99.7% confidence intervals (ellipses) are shown in the figure along with the measured total active neutrino flux of  $5.39^{+1.07}_{-1.09} \times 10^6 \text{ cm}^{-2} \text{ s}^{-1}$ . Also shown is the total neutrino flux predicted by the BP2000 SSM and the SNO CC result (simply the vertical band shown on the  $\nu_{total}$  axis). Figure motivated from work by A. Hime.

### 9.1.2 MSW Analysis of the CC Rate

It has been shown in this thesis that the measured CC rate is substantially lower than the rate from  ${}^8\text{B}$  neutrinos predicted by the BP2000 Standard Solar Model. This deficit of solar  $\nu_e$ 's measured through the CC reaction can be interpreted in the context of neutrino oscillations. In this section, we present the regions of the MSW plane (two-flavor oscillations) consistent with the CC measurement.

Allowed regions in the MSW plane ( $\Delta m^2$ ,  $\sin^2 2\theta$ ) are calculated by the following procedure. The Monte Carlo is used to generate CC events for  $10 \times$  SSM rate over our neutrino livetime assuming no oscillations. A  $33 \times 33$  grid of  $\log(\Delta m^2)$ - $\log(\sin^2 2\theta)$  points extending from  $\log(\Delta m^2) = [-3, -11]$  and  $\log(\sin^2(2\theta)) = [-4, 0]$  in the MSW plane is constructed. The MSW code within SNOMAN is used to calculate the  $\nu_e$  survival probability as a function of energy for each grid point. Events from the no-oscillation data set are randomly discarded according to the neutrino survival probability function at the MSW grid point. We have therefore constructed the number of expected events at each grid point in the MSW plane. This grid is fed into a bi-cubic spline interpolation routine which is used as a continuous function for interpolating the expected fraction of events at arbitrary points in the MSW plane.

The allowed regions in the MSW plane corresponding to a given CC flux ratio result,  $R^{meas}$ , are determined by calculating the  $\chi^2$ -function

$$\chi^2(\Delta m^2, \sin^2 2\theta) = \frac{[R^{meas} - R^{th}(\Delta m^2, \sin^2 2\theta)]^2}{\sigma^2} \quad (9.3)$$

where  $R^{th}$  is the expected flux ratio as a function of the MSW parameters (from the interpolation function) and  $\sigma$  is the total error combining statistical, systematic,

and uncertainty in the SSM total  ${}^8\text{B}$  flux. The allowed regions in the plane are determined from changes in the  $\chi^2$ -function,  $\Delta\chi^2$ , relative to the global minimum  $\chi^2_{min}$  in the plane. The allowed regions at some confidence level, CL, are those which satisfy  $\chi^2 \leq \chi^2_{min} + \Delta\chi^2(\text{CL})$ . For 2 degrees of freedom,  $\Delta\chi^2(95.4\%) = 6.17$  and  $\Delta\chi^2(99\%) = 9.21$ .

The 95.4% and 99% allowed regions for the CC flux measurement performed in this thesis,

$$R_{CC} \equiv \frac{CC_{data}}{CC_{SSM}} = 0.346 \pm 0.017 \text{ (stat)} {}^{+0.016}_{-0.017} \text{ (syst)} \pm 0.010 \text{ (xsec)}$$

including the solar model error of +20%, -16%, are shown in Figure 9.3.

## 9.2 CC Spectrum

The CC  $N_{\text{Hit}}$  spectrum extracted from the 169.3 day neutrino data set was presented in Section 8.3.2. It was discussed in Section 2.4 that neutrino oscillations can manifest themselves as an observed distortion in the energy spectrum of electrons produced by neutrino interactions in the detector because of the neutrino energy dependence of the survival probability. In this section, we compare the extracted CC  $N_{\text{Hit}}$  spectrum to the expected spectrum from various oscillation solutions.

Based on a recent global analysis [21] of current solar neutrino experimental results, several best fit oscillation parameters ( $\Delta m^2$ ,  $\tan^2 \theta$ ) are determined. The CC extracted  $N_{\text{Hit}}$  spectrum results overlaid with the predicted CC  $N_{\text{Hit}}$  spectra from  ${}^8\text{B}$  for several of these solutions are shown in Figure 9.4 for oscillation into active neutrinos and Figure 9.5 for oscillation into sterile neutrinos. These solutions all give different predictions for the  ${}^8\text{B}$  flux suppression (relative to SSM predictions), so they

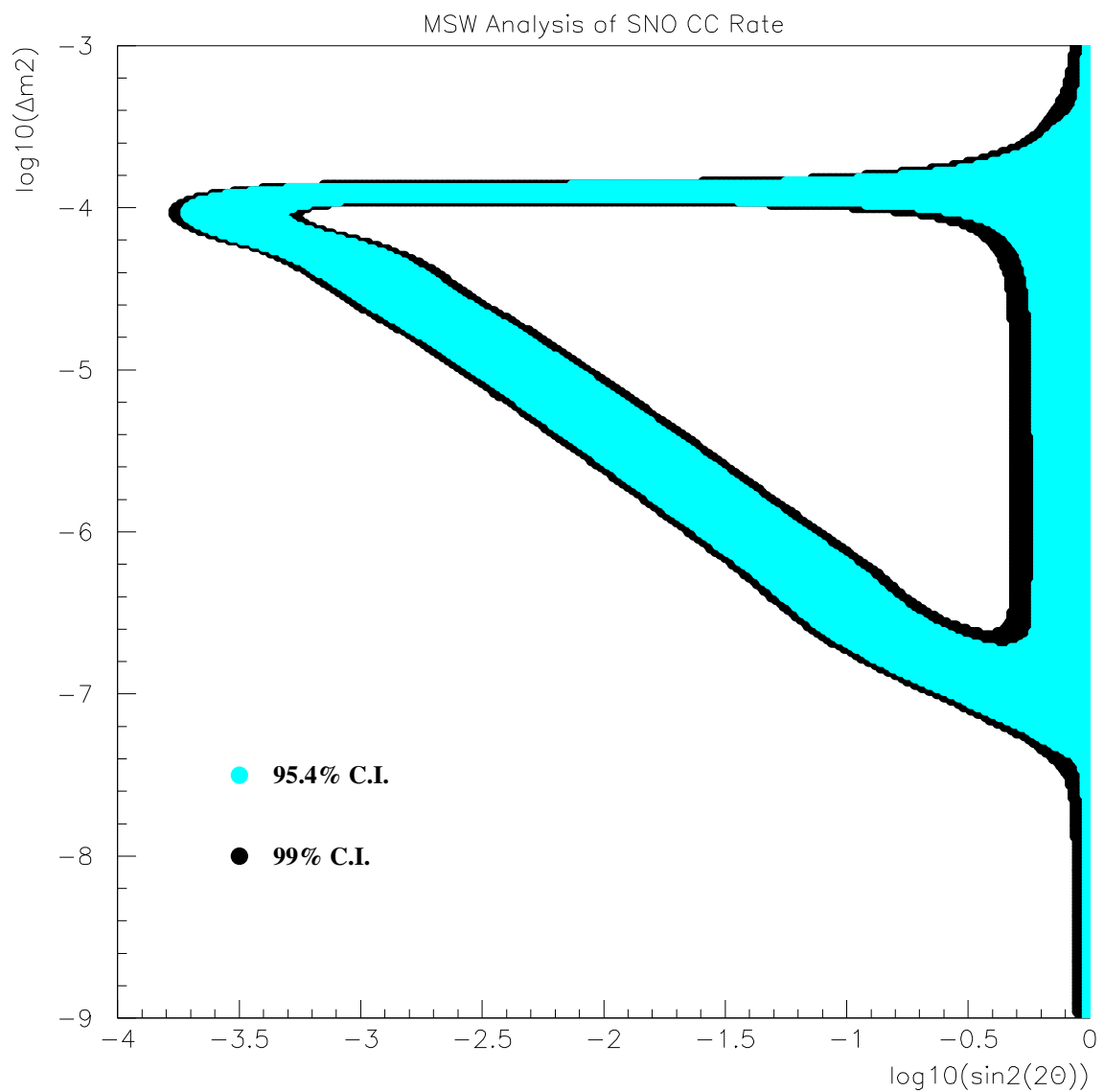


Figure 9.3: Allowed MSW regions at 95.4% and 99% confidence for the average CC flux (rate only) measurement presented in this thesis, relative to BP2000 SSM predictions.

## CC Spectrum Compared to Oscillation Solutions

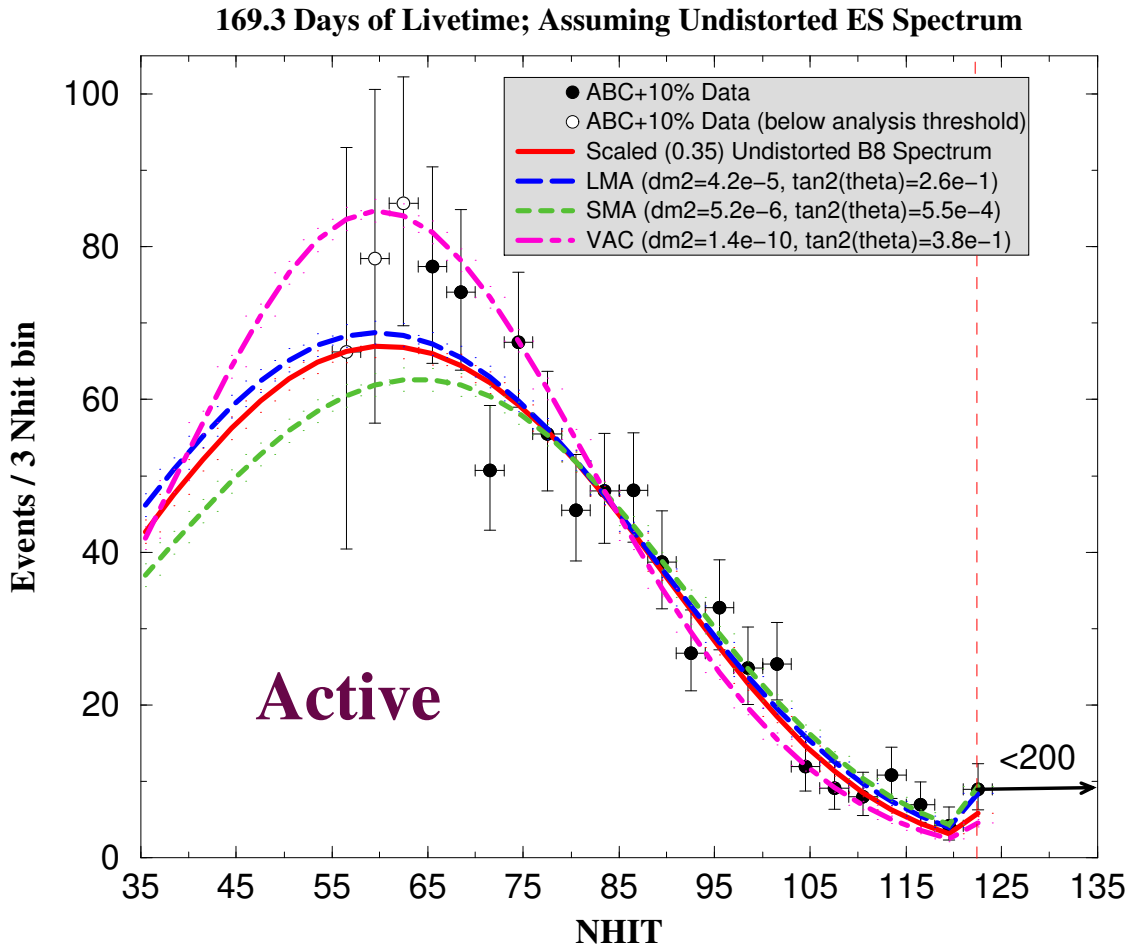


Figure 9.4: Comparison between the extracted CC  $N_{\text{Hit}}$  spectrum and global best fit solutions from [21] for active neutrino oscillations.

## CC Spectrum Compared to Oscillation Solutions

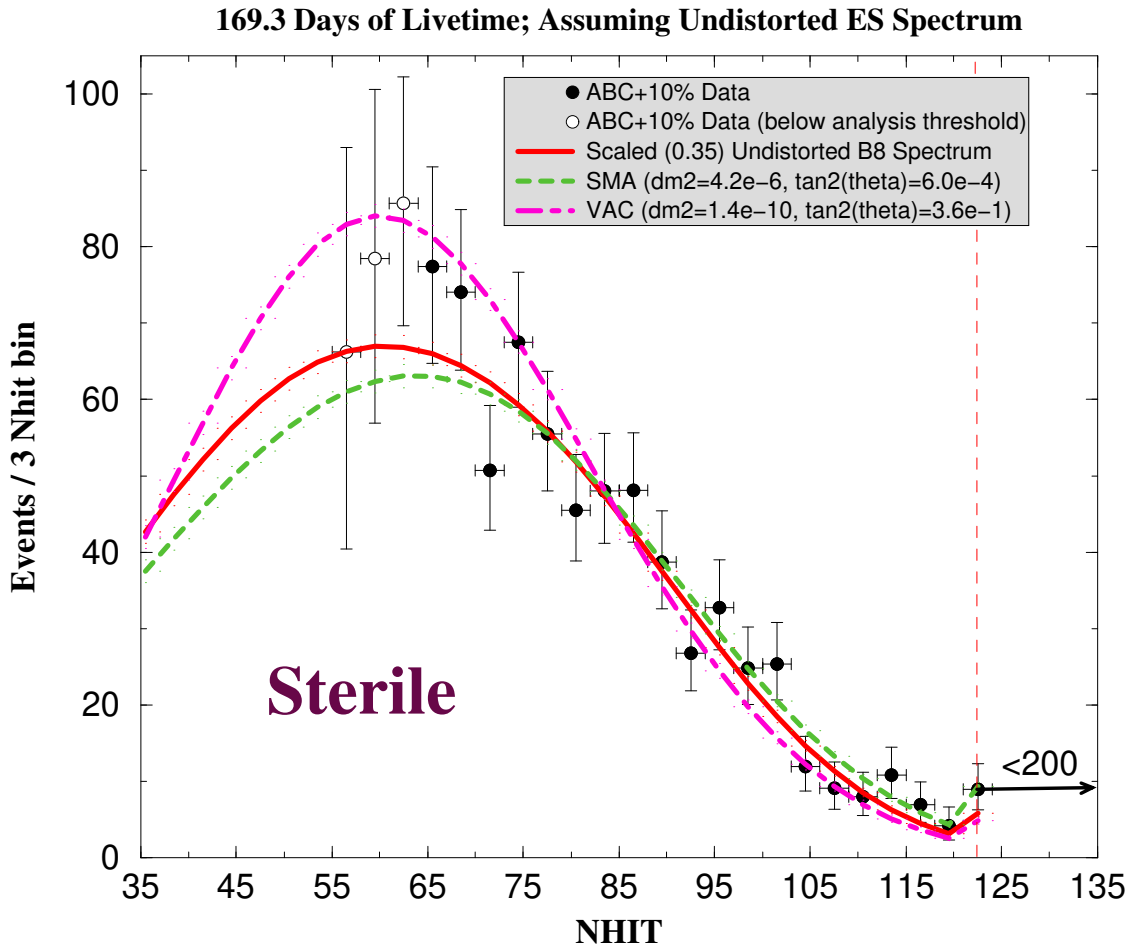


Figure 9.5: Comparison between the extracted CC  $N_{\text{Hit}}$  spectrum and global best fit solutions from [21] for sterile neutrino oscillations.

Solution	$\Delta m^2 (eV^2)$	$\tan^2 \theta$	$\chi^2$ (20 d.f.)	g.o.f.
LMA	$4.2 \times 10^{-5}$	$2.6 \times 10^{-1}$	13.21	86.8%
SMA	$5.2 \times 10^{-6}$	$5.5 \times 10^{-4}$	14.77	78.9%
LOW	$7.6 \times 10^{-8}$	$7.2 \times 10^{-1}$	13.91	83.5%
VAC	$1.4 \times 10^{-10}$	$3.8 \times 10^{-1}$	26.25	15.8%
Sterile SMA	$4.2 \times 10^{-6}$	$6.0 \times 10^{-4}$	14.66	79.6%
Sterile VAC	$1.4 \times 10^{-10}$	$3.6 \times 10^{-1}$	25.05	19.9%
Undistorted $^8\text{B}$	—	—	14.96	77.9%

Table 9.1: Global best fit solutions from [21] with the  $\chi^2$  and GOF obtained from CC spectrum measurement shown for each solution. A comparison of the CC spectrum results with an undistorted  $^8\text{B}$  spectrum are also shown.

have been scaled to the solar  $\nu_e$  suppression measured in this thesis through the CC reaction (35%). This is done to test the *shape* of their spectral predictions without reference to the total rate. Also shown is the scaled spectrum for undistorted  $^8\text{B}$ .

One can see from these figures that distinction between the various solutions becomes more significant at lower energy where distortions are more substantial. This is not all that surprising from the survival probabilities shown in Figure 2.6. Also, SuperKamiokande spectral data for which there is no substantial distortion above a 5 MeV threshold is included in the global analysis. Table 9.1 summarizes these solutions and also shows the  $\chi^2$  GOF for the measured CC  $N_{\text{Hit}}$  spectrum. It can be seen that discrimination between the MSW global best fit solutions is not possible in this analysis, as all give essentially the same good fit to the spectral data. The vacuum solutions, both for active and sterile neutrino oscillations, are slightly disfavored from the other solutions based on our CC spectrum results, however. More conclusive statements about the CC spectrum will be possible in future analyses of a larger data set which specifically address differential systematics.

### 9.3 *hep* Flux

Limits on the *hep* flux were obtained using both observations near the  ${}^8\text{B}$  endpoint and statistical extraction techniques. SuperKamiokande has reported [13] after 1258 days of neutrino livetime a 90% upper limit on the hep flux of 4.3 times the BP2000 SSM prediction using a technique analogous to  ${}^8\text{B}$  endpoint measurement presented in this thesis. We obtain a 90% upper limit of 4.1 times the BP2000 SSM *hep* flux. This limit is comparable to the SuperKamiokande limit after only 169.3 days of livetime due to the better energy response and larger cross section of the CC reaction compared to that from neutrino-electron elastic scattering.

It should be remarked that in this analysis,  ${}^8\text{B}$  neutrinos are assumed to represent the only *hep* neutrino background. A more complete treatment of other possible backgrounds at high energy should be included in future *hep* analyses. While limits on instrumental and high energy  $\gamma$ -ray backgrounds have been presented in this thesis, contributions from the low energy tail of atmospheric  $\nu$ 's have not been estimated.

### 9.4 Final Remarks

Evidence was presented in this thesis for  $\nu_e \rightarrow \nu_{\mu,\tau}$  oscillations through measurement of the  ${}^8\text{B}$  solar neutrino flavor content by comparison of the CC measured  ${}^8\text{B}$  flux with ES measurements from Superkamiokande. Pure  $\nu_e \rightarrow \nu_s$  oscillations are excluded at greater than the 99.7% C.I. As SNO continues to add statistics on its own ES signal, these results should be confirmed with a higher degree of certainty. It was recently brought to our attention that sizeable radiative corrections to the CC cross section

may be present. Calculations performed in [94, 95] suggest that these corrections<sup>5</sup> may increase the CC cross section over the solar neutrino energy range by up to 6%. An increase in the CC cross section only makes our evidence for  $\nu_e \rightarrow \nu_{\mu,\tau}$  oscillations stronger since it decreases the CC/ES ratio. However, we remark that our CC flux measurement would be reduced to  $\phi_{^8\text{B}}^{CC} = 1.67_{-0.13}^{+0.12} \times 10^6 \text{ cm}^{-2} \text{ s}^{-1}$  (33.1% of BP2000 modified) if the CC cross section is increased by 6% as the authors suggest.

While the evidence for a non-zero  $\nu_{\mu,\tau}$  component to solar  ${}^8\text{B}$  neutrino flux presented in this thesis has been interpreted in the context of neutrino oscillations, this may not be the only possible interpretation. As mentioned in Chapter 2, other neutrino flavor changing mechanisms have been proposed to explain the solar neutrino problem<sup>6</sup>. Many of these “exotic” mechanisms predict spectral distortions different from those consistent with the oscillation hypothesis, so future improvements in the CC spectrum measurement might play an important role in constraining these models. Also, a significant day-night asymmetry - if observed - would be very difficult to incorporate into many of these exotic solutions.

Measurement of the total neutrino flux by the neutral current reaction will provide a more direct test of the neutrino oscillation hypothesis when compared to the CC results. It will also test the total neutrino flux measurements obtained through the flavor analysis of CC/ES. We look forward to upcoming neutral current measurements in both the pure  $\text{D}_2\text{O}$  phase and future salt phase of the experiment. We also look forward to future searches in SNO for additional oscillation signatures (e.g. day-night asymmetry, spectral distortions) and other hints of new physics provided by Nature through neutrinos.

---

<sup>5</sup>and a correction for the value of  $g_A$  used in BCK and NSGK calculations.

<sup>6</sup>See Section 2.3.4 for examples and references.

# Appendix A

## The Path Fitter: Future Development

### A.1 Suggestions for Future Work

A few suggestions for future development of the Path Fitter reconstruction method are listed below.

- Path dependent speed of light.
- Double precision for both simulated annealing and MINUIT
- Use NHIT dependent angular distribution (need RSP-like object for position dependence?) for fitting and GOF calculation or at least one averaged over the electron spectrum from  $^8\text{B}$  neutrinos.
- Allow for alternate hypothesis/angular and time distributions like  $\gamma$ s and Cl captures?

- Fix up time GOF or develop new method.
- Re-investigate late light path calculations, particularly the effect of incorporating simple models of reflections and scattering.
- Turn on use of unhit tubes.
- Continue investigation PDF calculations that put each PMT at the Cerenkov angle and calculate the *scattering* probabilities. This was a considered as possible fix for the angular drive problem.
- Use PMT solid angle in  $\phi$ -symmetry GOF test.
- Figure out how to speed up calculation of 2d angular GOF test.

## A.2 The 'Paths' Approach

As described in Section 4.3.3, the original Path Fitter approach was to construct a PDF for each electron position, direction, and time that is a sum of all possible photon paths from the electron to a given PMT, weighted by the relative probability of each path (See Figure A.1). That is

$$\mathcal{P}_i(n_i, t_i; \vec{r}_e, \hat{d}_e, t_e) = \sum_{j \text{ paths}} P_{ij}(n_i, t_i; \vec{r}_e, \hat{d}_e, t_e) \quad (\text{A.1})$$

Grouping the overall PDF into the sum of direct light, scattering, and reflections, we get

$$\mathcal{P}_i(n_i, t_i; \vec{r}_e, \hat{d}_e, t_e) = f_{\text{direct}} P^{\text{direct}}(n_i, t_i; \vec{r}_e, \hat{d}_e, t_e)$$

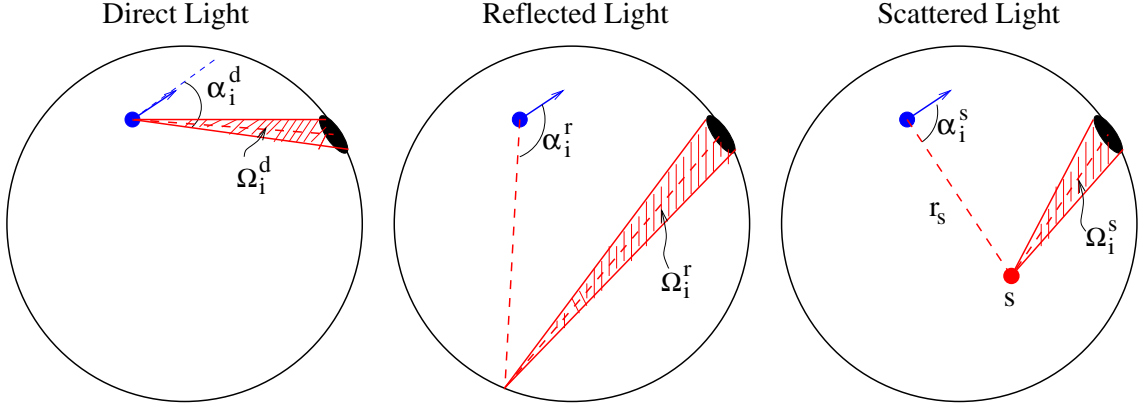


Figure A.1: Schematic pictures of the different photon path considered in the Path Fitter PDF calculations.

$$\begin{aligned}
 & + f_{refl} \sum_{j \in paths} P_j^{refl}(n_i, t_i; \vec{r}_e, \hat{d}_e, t_e) \\
 & + f_{scat} \int_{s \in V} P_s^{scat}(n_i, t_i; \vec{r}_e, \hat{d}_e, t_e) \quad (A.2)
 \end{aligned}$$

The point of this appendix is to document the calculations behind some of the attempts that were made to include, in a simple way, late light in the Path Fitter PDFs. The calculational toy model used was to assume spherical specular reflections off the PSUP and uniform, isotropic scattering in the water volume, with both assumed to be wavelength independent. Reflections and scattering are described in Section A.3 and A.4, respectively.

In Equation A.2, the direct light term represents a single path, which if one only considers PMTs hit once, we get

$$P^{direct}(t_i) = P^{TIM}(t_i) N_\gamma \rho_i e^{-N_\gamma \rho_i} \quad (A.3)$$

where

$$\rho_i = \frac{1}{2\pi} g(\cos \alpha_i^d) \Omega_i^d \quad (A.4)$$

Recall that  $g(\cos \alpha)$  is the angular distribution of Cerenkov photons and  $\omega_i^d$  is the solid angle subtended by the  $i^{th}$  PMT viewed from the hypothesized electron position.

The next two section outline how one could get PDFs for reflected and scattered light in this simplified calculational toy model.

### A.3 Spherical Specular Reflections

The dominant reflections in SNO events are reflection off of the PMT glass and concentrators. The actual reflection angles that result in the SNO geometry are complicated, particularly when one considers arbitrary source positions within the detector. However, one might expect there to be a near specular component to the reflections off the PMT glass, and so it is worthwhile considering how one would incorporate a simple specular reflection model into reconstruction.

The form of the PDF for reflections is same as Equation A.3, except now there are (as will be demonstrated in Section A.3.3) discrete specular reflection paths,  $j$ , that connect the hypothesized source position and  $i^{th}$  PMT,

$$P_j^{refl}(t_i) = P_j^{TIM}(t_i) N_\gamma \rho_{ij} e^{-N_\gamma \rho_{ij}} \quad (\text{A.5})$$

where

$$\rho_{ij} = \frac{1}{2\pi} g(\cos \alpha_{ij}^r) \Omega_{ij}^r \quad (\text{A.6})$$

In the case of reflections,  $\alpha_{ij}^r$  is the angle between the hypothesized electron direction and the vector from the electron position to the point on the PSUP where the  $j^{th}$  reflection takes place, and  $\Omega_{ij}^r$  is the solid angle subtended by the  $i^{th}$  PMT when viewed from the reflection point (see Figure A.1). Therefore, the entire problem is reduced to

solving the general spherical mirror problem for all possible specular reflection path connecting a point inside the sphere and a point on the sphere. This general solution derived in Section A.3.3 and code implementing this solution is installed as part of the Path Fitter in SNOMAN (see the routine **ftp\_refl\_solve.for**).

### A.3.1 Introduction

There are two distinct approaches to spherical reflections presented in this appendix, corresponding to two differently stated problems. In Section A.3.2, the problem of generating spherical reflections given a source point and the direction of the generated photon is discussed. In this case, a solution of the  $1^{st}$  order reflection problem involves finding the distance to the sphere, the reflection point on the sphere, and the direction of the reflected photon. This is more along the lines of a Monte Carlo approach where one can generate the  $n^{th}$  order reflection path of the photon through an iterative solution of the  $1^{st}$  order problem. The consideration of this formulation of the reflection problem is largely historical, as it was used in the “bomb” fitter briefly discussed in Section 4.3.3. Its inclusion in this appendix is mostly for completeness of the discussion on spherical reflections.

Incorporating reflections into the Path Fitter requires a different formulation of the reflection problem in terms of a source and sink point rather than a source point and direction. Section A.3.3 deals with the problem of generating all possible  $1^{st}$  order specular reflection paths between an arbitrary source point (e.g. a photon) within a sphere and a sink point on the sphere (e.g. a phototube). This involves finding the generated photon direction from the source point, the reflection point on the sphere, and the total path length for each reflection path solution. This approach is

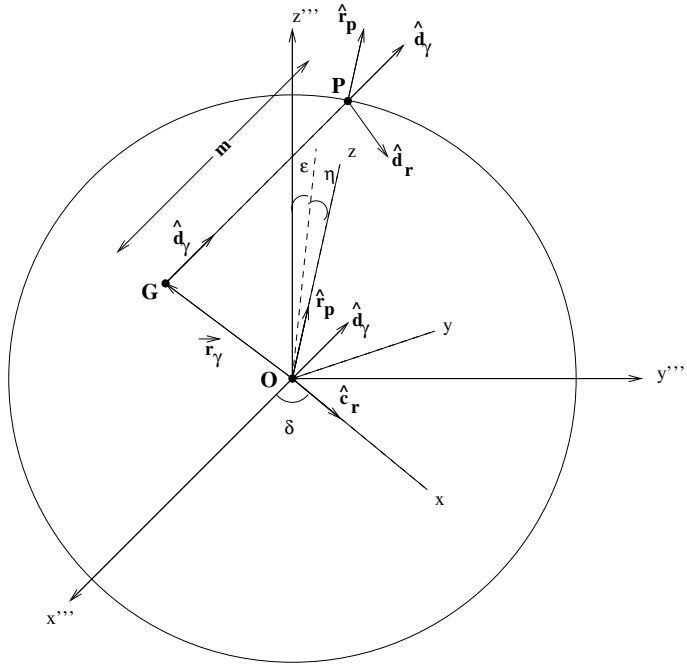


Figure A.2: Reflection problem defined by source point  $G$  and photon direction  $\hat{d}_\gamma$

potentially useful for a fitter which considers Cerenkov photon reflection paths from a relativistic electron to a hit phototube (e.g. the Path Fitter), however it lacks the ability to iteratively determine multiply reflected photon paths in a simple way like the previous approach.

### A.3.2 Reflection Paths Given Source Point and Direction

The problem of generating all possible reflection paths (up to  $n^{th}$  order) reduces to iterative calls to a routine which, given a photon generation point  $G$  and a directional unit vector  $\hat{d}_\gamma$ , can find (see Figure A.2):

- The distance,  $m$ , from the photon generation point to the sphere in the direction of  $\hat{d}_\gamma$ .

- The point on the sphere  $P$  where the reflection will take place.
- The directional unit vector  $\hat{d}_r$  of the reflected photon.

Let  $\vec{r}_\gamma \equiv \vec{OG}$  represent the generated photon position vector and  $\vec{r}_p \equiv \vec{OP}$  represent the reflected photon position vector on the sphere so that  $\vec{r}_p = R\hat{r}_p$ . Then we have the vector equation

$$m\hat{d}_\gamma + \vec{r}_\gamma = \vec{r}_p \quad (\text{A.7})$$

relating the photon direction to the generated and reflected points. Squaring both sides yields an equation quadratic in  $m$

$$m^2 + 2m\vec{r}_\gamma \cdot \hat{d}_\gamma + \vec{r}_\gamma^2 - R^2 = 0 \quad (\text{A.8})$$

which has solutions given by

$$m = -\vec{r}_\gamma \cdot \hat{d}_\gamma \pm \sqrt{(\vec{r}_\gamma \cdot \hat{d}_\gamma)^2 - (r_\gamma^2 - R^2)} \quad (\text{A.9})$$

Reflection solutions only exist for  $m$  nonnegative and real, so we require

$$m > 0 \quad \text{and} \quad (\vec{r}_\gamma \cdot \hat{d}_\gamma)^2 - (r_\gamma^2 - R^2) \geq 0 \quad (\text{A.10})$$

There are three specific cases to consider:

- *G inside sphere ( $r_\gamma < R$ ):* Positive root ensures there is one and only one solution:

$$m = -\vec{r}_\gamma \cdot \hat{d}_\gamma + \sqrt{(\vec{r}_\gamma \cdot \hat{d}_\gamma)^2 - (r_\gamma^2 - R^2)} \quad (\text{A.11})$$

- *G on sphere ( $r_\gamma = R$ ):* For  $m > 0$ , we get one solution:

$$m = -\vec{r}_\gamma \cdot \hat{d}_\gamma + \sqrt{(\vec{r}_\gamma \cdot \hat{d}_\gamma)^2} \quad (\text{A.12})$$

- *G outside sphere ( $r_\gamma > R$ ):* For  $m > 0$ , there are two cases:

- *Case 1:*  $(\vec{r}_\gamma \cdot \hat{d}_\gamma)^2 = r_\gamma^2 - R^2$

Photon tangent to sphere  $\Rightarrow$  one solution:

$$m = -\vec{r}_\gamma \cdot \hat{d}_\gamma \quad (\text{A.13})$$

- *Case 2:*  $(\vec{r}_\gamma \cdot \hat{d}_\gamma)^2 > r_\gamma^2 - R^2$

Photon within tangents to sphere  $\Rightarrow$  two solutions:

$$m = \begin{cases} -\vec{r}_\gamma \cdot \hat{d}_\gamma - \sqrt{(\vec{r}_\gamma \cdot \hat{d}_\gamma)^2 - (r_\gamma^2 - R^2)} & \text{(near point)} \\ -\vec{r}_\gamma \cdot \hat{d}_\gamma + \sqrt{(\vec{r}_\gamma \cdot \hat{d}_\gamma)^2 - (r_\gamma^2 - R^2)} & \text{(far point)} \end{cases} \quad (\text{A.14})$$

Once  $m$  is known, the vector to the reflection point on the sphere is simply given by

$$\vec{r}_p = m\hat{d}_\gamma + \vec{r}_\gamma \quad (\text{A.15})$$

Now that the reflection point has been determined, the reflected directional unit vector  $\hat{d}_r$  can be computed assuming specular reflection.  $\hat{d}_r$  is related to  $\hat{r}_p$  and  $\hat{d}_\gamma$  by the following three relations:

$$\begin{aligned} \hat{r}_p \cdot \hat{d}_\gamma &= -\hat{r}_p \cdot \hat{d}_r & (\theta_i = \theta_r) \\ (\hat{r}_p \times \hat{d}_\gamma) \cdot \hat{d}_r &= 0 & (\text{coplanar}) \\ \hat{d}_r \cdot \hat{d}_r &= 1 & (\text{unit vector}) \end{aligned}$$

Direct algebraic solution of this system of equations is intractable in the original (SNO) coordinate system for arbitrary  $\hat{r}_p$  and  $\hat{d}_\gamma$ . The strategy is then to rotate into a system in which the previous set of equations is easily solved for  $\hat{d}_r$  and then rotate back into the original system. The rotated system is chosen such that the z-axis lines up with  $\hat{r}_p$  and  $\hat{d}_\gamma$  lies in the xz-plane. So in the final rotated system (unprimed), the reflected directional unit vector is  $\hat{d}_r = d_{r_x} \hat{x} + d_{r_y} \hat{y} + d_{r_z} \hat{z}$  and

$$\begin{aligned}\hat{r}_p \cdot \hat{d}_\gamma &= -\hat{r}_p \cdot \hat{d}_r \Rightarrow d_{r_z} = -d_{\gamma_z} \\ (\hat{r}_p \times \hat{d}_\gamma) \cdot \hat{d}_r &= 0 \Rightarrow d_{r_y} = 0 \\ \hat{d}_r \cdot \hat{d}_r &= 1 \Rightarrow d_{r_x} = \pm \sqrt{1 - d_{\gamma_z}^2}\end{aligned}$$

Therefore, in the rotated system,

$$\hat{d}_r = \pm \sqrt{1 - d_{\gamma_z}^2} \hat{x} - d_{\gamma_z} \hat{z} \quad (\text{A.16})$$

where + is for  $d_{\gamma_x} > 0$  and - is for  $d_{\gamma_x} \leq 0$ .

So the problem is now reduced to computing the rotation matrix  $\mathcal{R}$  (and  $\mathcal{R}^{-1}$  through matrix inversion or inverse rotation) between the original (triple-primed) and final rotated (unprimed) coordinate systems. This is accomplished by a (ZXY) Euler rotation about three Euler angles  $\delta, \epsilon, \eta$ . In words, this is a rotation around the  $z'''$ -axis by angle  $\delta$ , then rotation around the  $x''$ -axis by angle  $\epsilon$ , and finally a rotation around the  $y'$ -axis by angle  $\eta$ . Suitably chosen  $\delta, \epsilon$ , and  $\eta$  then aligns the z-axis with  $\hat{r}_p$  and  $\hat{d}_\gamma$  will lie in the xz-plane, allowing use of the previously derived equation for  $\hat{d}_r$ .

The angle  $\delta$  is related to the  $x'''$ -component of a unit vector  $\hat{c}_r$  lying in the  $x'''y'''$ -plane which is coplanar to the vectors  $\hat{r}_p$  and  $\hat{d}_\gamma$ . Specifically,  $\delta = \cos^{-1}(c_{r_{x'''}})$ , and so

we now need to calculate  $\hat{c}_r$  in the triple-primed system. Leaving the tedious algebraic details out, the solution for  $\hat{c}_r = c_{r_{x''''}} \hat{x} + c_{r_{y''''}} \hat{y}$  of the equations

$$(\hat{r}_p \times \hat{d}_\gamma) \cdot \hat{c}_r = 0 \quad \hat{c}_r \cdot \hat{c}_r = 1 \quad (\text{A.17})$$

yields

$$c_{r_{x''''}} = \frac{r_{p_{x''''}} d_{\gamma_{z''''}} - r_{p_{z''''}} d_{\gamma_{x''''}}}{n_c} \quad \text{and} \quad c_{r_{y''''}} = \frac{r_{p_{y''''}} d_{\gamma_{z''''}} - r_{p_{z''''}} d_{\gamma_{y''''}}}{n_c} \quad (\text{A.18})$$

where

$$n_c = \sqrt{(r_{p_{x''''}} d_{\gamma_{z''''}} - r_{p_{z''''}} d_{\gamma_{x''''}})^2 + (r_{p_{y''''}} d_{\gamma_{z''''}} - r_{p_{z''''}} d_{\gamma_{y''''}})^2} \quad (\text{A.19})$$

So then,

$$\delta = \cos^{-1} \left( \frac{r_{p_{x''''}} d_{\gamma_{z''''}} - r_{p_{z''''}} d_{\gamma_{x''''}}}{\sqrt{(r_{p_{x''''}} d_{\gamma_{z''''}} - r_{p_{z''''}} d_{\gamma_{x''''}})^2 + (r_{p_{y''''}} d_{\gamma_{z''''}} - r_{p_{z''''}} d_{\gamma_{y''''}})^2}} \right) \quad (\text{A.20})$$

The angle  $\epsilon$  is related to the  $z''$ -component of the unit vector  $\hat{r}_p$  projected in the  $y''z''$ -plane. Therefore, we need to do the previous  $z''''$  rotation by angle  $\delta$  and transform  $\hat{r}_p$  into the double-primed system (the system after the  $\delta$  rotation). Then,

$$\epsilon = \cos^{-1} \left( \frac{r_{p_{z''}}}{\sqrt{r_{p_{y''}}^2 + r_{p_{z''}}^2}} \right) \quad (\text{A.21})$$

Now when we perform a rotation by angle  $\epsilon$  around the  $x''$ -axis, the  $\hat{z}'$ ,  $\hat{x}'$ ,  $\hat{r}_p$ , and  $\hat{d}_\gamma$  unit vectors are all coplanar. This leaves one more rotation around the  $y'$ -axis to generate the desired final rotated (unprimed) system (and the rotation matrix  $\mathcal{R}$ ) by

angle  $\eta$  given by

$$\eta = \cos^{-1}(r_{p_{z'}}) \quad (\text{A.22})$$

Now that we have  $\mathcal{R}$ , we can translate any vector  $\vec{V}'''$  in the triple-primed (original) system to the unprimed (rotated) system by

$$\vec{V} = \mathcal{R}\vec{V}''' \quad (\text{A.23})$$

In order to transform back, we need to compute  $\mathcal{R}^{-1}$  through either matrix inversion or by doing the inverse rotation (i.e. (YXZ) Euler rotation with Euler angles  $-\eta$ ,  $-\epsilon$ ,  $-\delta$ ) and then

$$\vec{V}''' = \mathcal{R}^{-1}\vec{V} \quad (\text{A.24})$$

Therefore, with  $\mathcal{R}$ ,  $\mathcal{R}^{-1}$ , and the previous relations, the reflected direction of the photon in the SNO frame is determined.

As mentioned earlier, one of the nice things about setting up and solving the spherical reflection problem in terms of a generation point and an initial photon direction is that multiple reflections are handled simply by iteration of the above algorithm. As an example, Figure A.3 shows a few 5<sup>th</sup>-order reflection paths off a two sphere system generated using a fortran routine which implements the algorithm in this section.

### A.3.3 Reflection Paths Given Source and Sink Points

In this case, we are given a photon source point E within a spherical region of radius R centered at point O and a photon detection point P on the surface of the sphere (see Figure A.4). For all possible specular reflection paths from E to P, we wish to

99/01/06 12.33

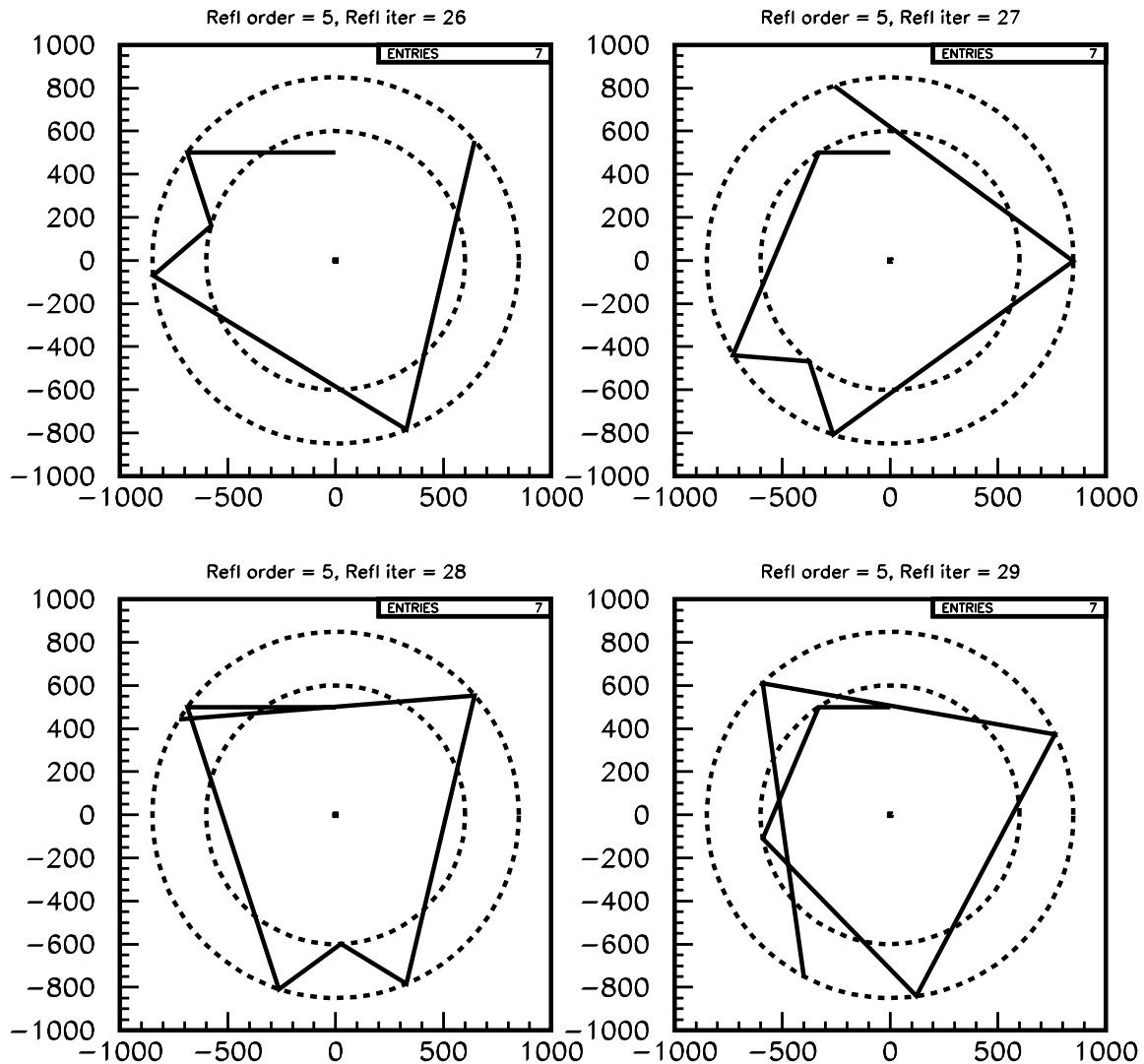


Figure A.3: Reflection paths off concentric spheres of radius 850 and 600cm for an initial photon at (0,500) in the (-1,0) direction

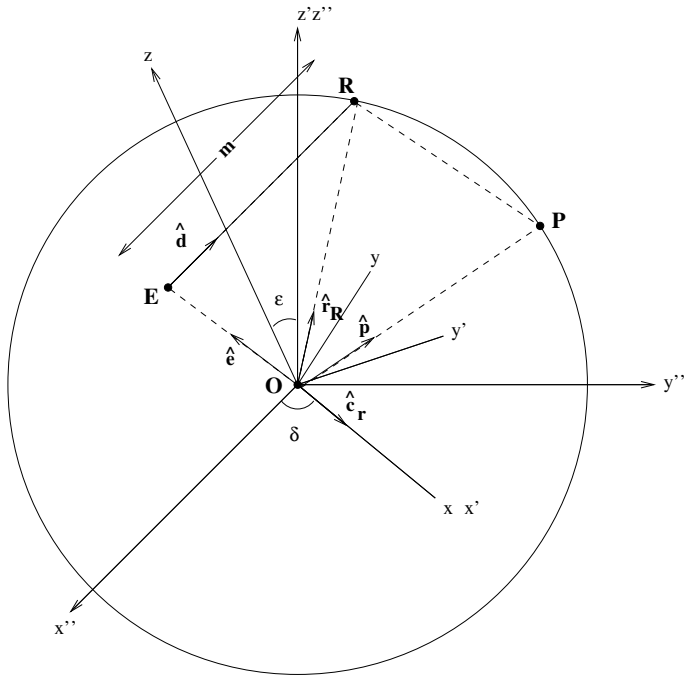


Figure A.4: Reflection problem defined by source point E and sink point P

find:

- The point on the sphere R where the reflection will take place.
- The directional unit vector  $\hat{d}$  of the generated photon from the source point E.
- The total path length from the photon generation point E to the sink point P (i.e.  $\vec{ER} + \vec{RP}$ ) in the direction of  $\hat{d}$ .

It should be noted that the labeling of source and sink points is merely for conceptual purposes - we are just trying to find a point R on the sphere connecting points E and P which is consistent with the constraints of specular reflection.

The intersection of a plane defined by the points E, P, and O and a sphere of radius R centered at O is a great circle of radius R. It is upon this great circle

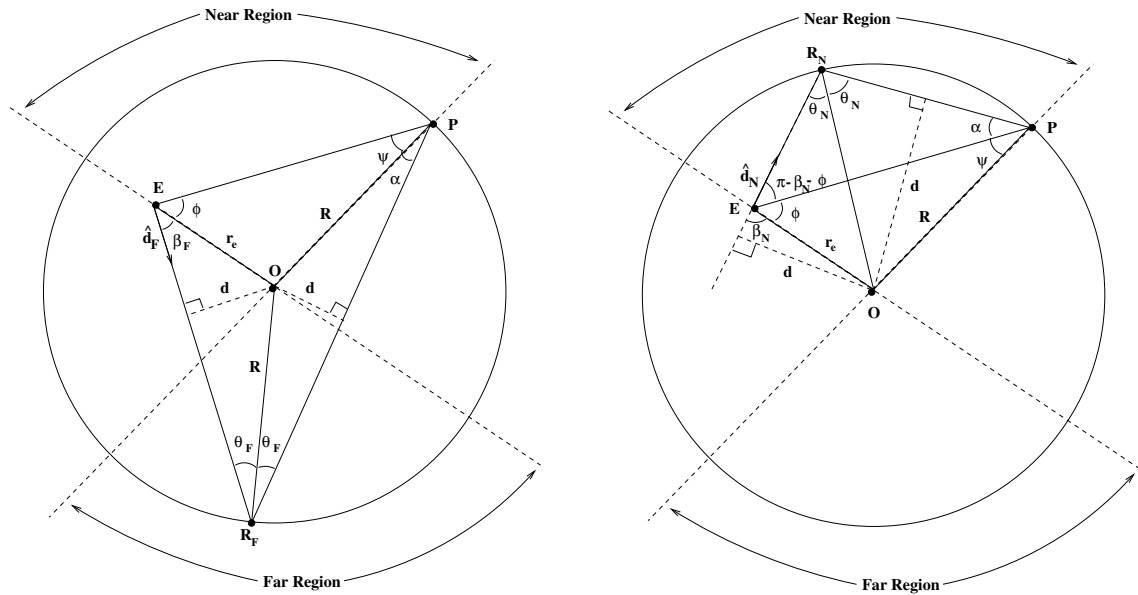


Figure A.5: Geometry involved in near and far reflection solutions.

that the reflection problem is solved in the analysis which follows. It may or may not be intuitive that for non-antipodal points  $E$  and  $P$  (i.e.  $E$ ,  $P$ , and  $O$  are *not* colinear) all solutions *must* lie on this great circle, so the degree to which other specular reflection solutions exist will be later investigated. For  $E$  and  $P$  antipodal, there is clear degeneracy in the choice of a plane though  $E$ ,  $P$ , and  $O$  cutting the sphere and these intersections define a set of great circles on which the reflection problem needs to be solved. However, this solution set is equivalent to the ring defined by the intersection of the plane passing through the two solution points, obtained on any one great circle in the set, that is perpendicular to line  $\vec{OE}$  (or equivalently  $\vec{OP}$  or  $\vec{PE}$ ).

The geometry involved in solving the problem on the great circle is shown in figure A.5 for reflections in the far and near regions of the circle. It should be obvious that any specular reflection point  $R$  must lie in one of these regions, otherwise a vector

from the origin cannot bisect the reflection angle. After lines of (necessarily equal) length  $d$  are drawn perpendicular to lines  $\vec{ER}$  and  $\vec{PR}$ , elementary trigonometry yields the following relations for the far and near reflection solutions:

$$\frac{d}{R} = \sin\theta_F \quad \frac{d}{r_e} = \sin\beta_F \quad \frac{d}{R} = \sin\alpha \quad 2\theta_F + \alpha + \beta + \phi + \psi = \pi \quad (\text{far region})$$

$$\frac{d}{R} = \sin\theta_N \quad \frac{d}{r_e} = \sin\beta_F \quad \frac{d}{R} = \sin\alpha + \psi \quad 2\theta_N + \alpha - \beta - \phi = 0 \quad (\text{near region})$$

Combining the four equations for the far reflection as well as for the near reflection and incorporating the dot product relation

$$\phi + \psi = \pi - \cos^{-1}(\hat{e} \cdot \hat{p}) \quad (\text{A.25})$$

we get a transcendental equation in  $\beta_F$  and  $\beta_N$  for the near and far regions, respectively:

$$\frac{R}{r_e} \sin\left\{\frac{1}{3}[\cos^{-1}(\hat{e} \cdot \hat{p}) - \beta_F]\right\} - \sin\beta_F = 0 \quad (\text{far region})$$

$$\frac{R}{r_e} \sin\left\{\frac{1}{3}[\pi - \cos^{-1}(\hat{e} \cdot \hat{p}) + \beta_F]\right\} - \sin\beta_F = 0 \quad (\text{near region})$$

These transcendental equations can be solved for  $\beta$  numerically using root finding algorithms such as bisection or Brent's Method.

We now want to generate the rotation matrix  $\mathcal{R}$  relating the original (double-primed) coordinate system to a system (unprimed) where  $\hat{e}$  and  $\hat{p}$  are in the xz-plane so that we can specify the reflection solution points. This is accomplished by a (ZX) Euler rotation about two Euler angles  $\delta$  and  $\epsilon$ . With appropriate replacement of variables, the angles  $\delta$  and  $\epsilon$  are the same as in Section A.2, namely,

$$\delta = \cos^{-1}\left(\frac{p_{x''}e_{z''} - p_{z''}e_{x''}}{\sqrt{(p_{x''}e_{z''} - p_{z''}e_{x''})^2 + (p_{y''}e_{z''} - p_{z''}e_{y''})^2}}\right) \quad \epsilon = \cos^{-1}\left(\frac{e_{z'}}{\sqrt{e_{y'}^2 + e_{z'}^2}}\right)$$

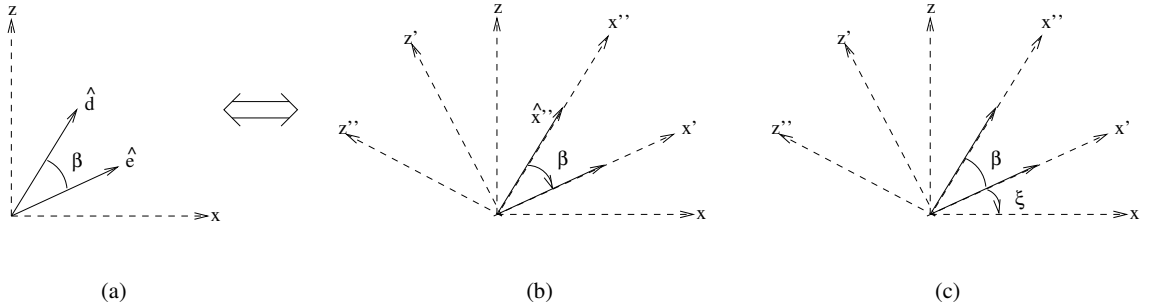


Figure A.6: (a)  $\hat{d}$  referenced by angle  $\beta$  off arbitrary vector  $\hat{e}$  (b) rotation of  $\hat{x}''$  by angle  $-\beta$  (c) then by angle  $-\xi$ .

This set of rotations yield the rotation matrix  $\mathcal{R}$ , and an (XZ) Euler rotation about angles  $-\delta$  and  $-\epsilon$  generates the inverse rotation matrix  $\mathcal{R}^{-1}$  so that we can transform any vector from one system to another by

$$\vec{V} = \mathcal{R} \vec{V}'' \quad \text{and} \quad \vec{V}'' = \mathcal{R}^{-1} \vec{V}$$

Now that we have the set of solutions for near and far reflection angles  $\beta_i$  and the rotation matrices  $\mathcal{R}$  and  $\mathcal{R}^{-1}$ , its just a matter of calculating the vectors  $\hat{d}$  and  $\vec{R} \equiv \vec{OR}$  in the unprimed system and rotating them into the original (double-primed) system. The unit vector  $\hat{d}$  specifying the photon direction relative to the source point vector  $\vec{OE}$  is easily calculated in the unprimed frame again using rotation of axes. Figure A.6 shows how the solution to this problem is equivalent to rotating a unit vector  $\hat{x}''$  by angles  $-\beta$  and  $-\xi$ . Note that  $\sin\xi = e_z$  and  $\cos\xi = \pm e_x$ , where  $+$  is for  $e_x > 0$  and  $-$  is for  $e_x < 0$ . Using the rotation matrix  $\mathcal{R}'$  (not to be confused with the previously defined matrix  $\mathcal{R}!$ ) for a rotation by angle  $\theta$  in the plane,

$$\mathcal{R}'(\theta) = \begin{pmatrix} \cos\theta & \sin\theta \\ -\sin\theta & \cos\theta \end{pmatrix} \quad (\text{A.26})$$

then for  $e_x > 0$ ,

$$\hat{d} = \mathcal{R}'(-\xi)\mathcal{R}'(-\beta) \hat{x}''$$

$$\begin{pmatrix} d_x \\ d_z \end{pmatrix} = \begin{pmatrix} e_x & -e_z \\ e_z & e_x \end{pmatrix} \begin{pmatrix} \cos(-\beta) & \sin(-\beta) \\ -\sin(-\beta) & \cos(-\beta) \end{pmatrix} \begin{pmatrix} 1 \\ 0 \end{pmatrix} = \begin{pmatrix} e_x \cos \beta - e_z \sin \beta \\ e_x \sin \beta + e_z \cos \beta \end{pmatrix}$$

and for  $e_x < 0$ ,

$$\hat{d} = \mathcal{R}'(-\xi)\mathcal{R}'(-\beta)(-\hat{y}'') \quad (\text{A.27})$$

$$\begin{pmatrix} d_x \\ d_z \end{pmatrix} = \begin{pmatrix} -e_x & -e_z \\ e_z & -e_x \end{pmatrix} \begin{pmatrix} \cos(-\beta) & \sin(-\beta) \\ -\sin(-\beta) & \cos(-\beta) \end{pmatrix} \begin{pmatrix} -1 \\ 0 \end{pmatrix} = \begin{pmatrix} e_x \cos \beta + e_z \sin \beta \\ e_x \sin \beta - e_z \cos \beta \end{pmatrix}$$

It should be clear from Figure A.5 that while these relations for  $\hat{d}$  are correct in the near region, for the far region the directional unit vector gets an extra minus sign. So in terms of  $\beta$  and  $\hat{e}$ , the photon directional unit vector in the far region is

$$\hat{d}_F = \begin{cases} (e_z \sin \beta_F - e_x \cos \beta_F) \hat{x} - (e_x \sin \beta_F + e_z \cos \beta_F) \hat{z}, & \text{for } e_x > 0 \\ -(e_x \cos \beta_F + e_z \sin \beta_F) \hat{x} + (e_z \cos \beta_F - e_x \sin \beta_F) \hat{z}, & \text{for } e_x < 0 \end{cases} \quad (\text{A.28})$$

and in the near region

$$\hat{d}_N = \begin{cases} (e_x \cos \beta_N - e_z \sin \beta_N) \hat{x} - (e_x \sin \beta_N + e_z \cos \beta_N) \hat{z}, & \text{for } e_x > 0 \\ (e_x \cos \beta_N + e_z \sin \beta_N) \hat{x} + (e_x \sin \beta_N - e_z \cos \beta_N) \hat{z}, & \text{for } e_x < 0 \end{cases} \quad (\text{A.29})$$

Now that we have  $\hat{d}$ , we can calculate the vector  $\vec{R}$  specifying the point in the sphere in which the reflection takes place and the total path length  $\vec{ER} + \vec{OR}$ . For both the near and far solutions, we have the vector relation

$$m\hat{d} + r_e\hat{e} = R\hat{r}_R \quad (\text{A.30})$$

Squaring both sides of this equation we get

$$m^2 + r_e^2 + 2mr_e(\hat{e} \cdot \hat{d}) = R^2 \quad (\text{A.31})$$

Substituting  $\hat{e} \cdot \hat{d} = -\cos\beta$  for the far reflection and  $\hat{e} \cdot \hat{d} = \cos\beta$  for the near solution, we get

$$\vec{R} = \begin{cases} m\hat{d}_F + r_e\hat{e}, & \text{in far region} \\ m\hat{d}_N + r_e\hat{e}, & \text{in near region} \end{cases} \quad (\text{A.32})$$

where  $m$  is the length of  $\vec{ER}$  given by

$$m = \begin{cases} r_e \cos\beta_F + \sqrt{R^2 - r_e^2 \sin^2\beta_F}, & \text{in far region} \\ -r_e \cos\beta_N + \sqrt{R^2 - r_e^2 \sin^2\beta_N}, & \text{in near region} \end{cases} \quad (\text{A.33})$$

Therefore, the total path length  $m_{tot} \equiv |\vec{ER} + \vec{RP}| = m + |\vec{R} - \vec{P}|$  or

$$m_{tot} = \begin{cases} r_e \cos\beta_F + \sqrt{R^2 - r_e^2 \sin^2\beta_F} + \sqrt{2R(R - \hat{p} \cdot \vec{R}_F)}, & \text{in far region} \\ -r_e \cos\beta_N + \sqrt{R^2 - r_e^2 \sin^2\beta_N} + \sqrt{2R(R - \hat{p} \cdot \vec{R}_N)}, & \text{in near region} \end{cases} \quad (\text{A.34})$$

where  $\vec{R}_F$  and  $\vec{R}_N$  are the vectors to the reflection points in the far and near region respectively which were previously determined.

Using the inverse rotation matrix  $\mathcal{R}^{-1}$ , we can rotate the derived vectors  $\hat{d}$  and  $\vec{R}$  into the original (double-primed) coordinate system. Therefore, the direction  $\hat{d}$  of the photon from source point E, the point R on the sphere where the reflection will

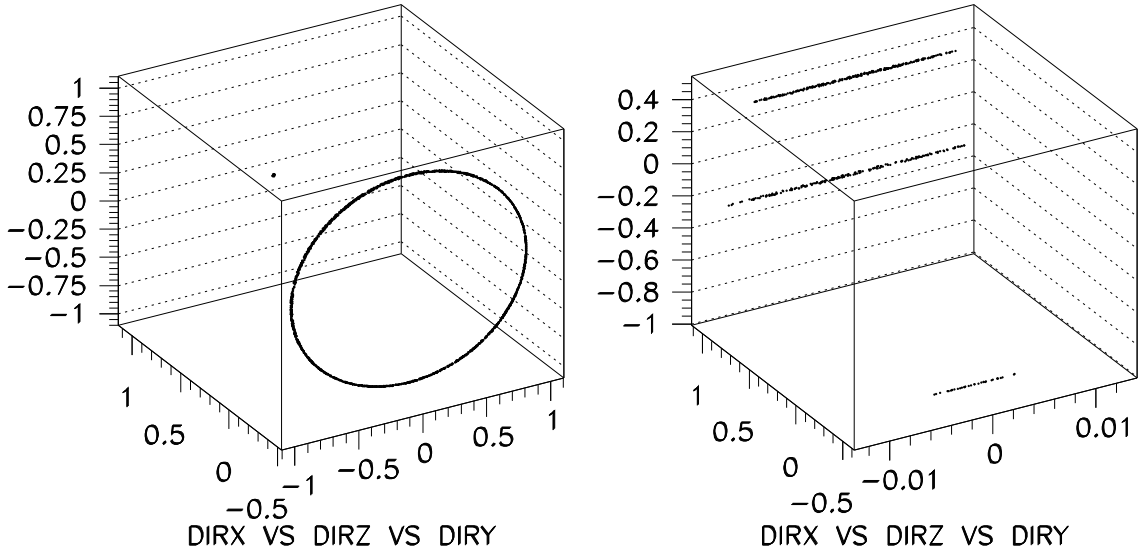


Figure A.7: Photon direction cosines for (a) antipodal and (b) non-antipodal source and sink points.

take place, and the total photon path length  $m_{tot}$  for all possible specular reflection paths between E and P have been determined.

Earlier in the section it was stated that all specular reflection points for non-antipodal points lie on the unique great circle defined by these points. The computer routine which implements the algorithm described in section A.3.2 can be used to test this conjecture. In fact, this routine can be used to find all 1<sup>st</sup> order reflection paths between two points by generating photons in all directions from the source point and recording the direction of any photons ending up within some small tolerance on the sink point. The mean of the distribution of those photon directions should be a good estimator of the true photon direction solution between the source and sink points. Figure A.7 shows the results of such an approach for one set of (a) antipodal and (b) non-antipodal source and sink points, which backs up the previous conjecture about the non-antipodal pair solution set. Figure A.7(a) corresponds to the source point at

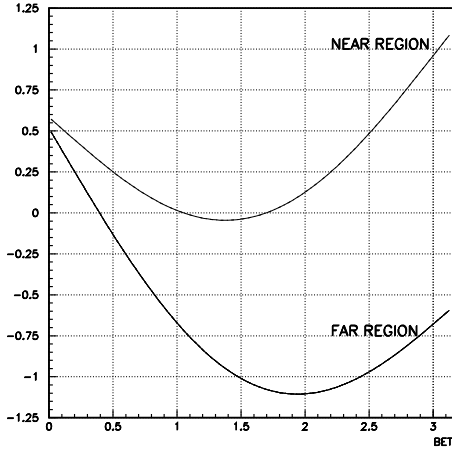


Figure A.8: Plots of the transcendental equations in the near and far regions for non-antipodal source and sink points.

$(0, 0, \frac{2}{3}R)$  and the sink point at  $(0, 0, -1)$ , in which the ring of direction solutions is evident. Figure A.7(b) corresponds to the source point at  $(0.905R, 0, 0.095R)$  and sink point at  $(0, 0, 1)$ , in which all three solutions lie in the  $xz$ -plane. What do we get from the computer routine implementing the algorithm described in this section for the non-antipodal pair example above? Figure A.8 shows the transcendental equations for this source/sink pair in which three solutions - one far reflection and two near reflections - are clearly evident. When these  $\beta$  solutions are properly transformed to give the allowed photon directions, they correspond precisely to the means of the  $dir_x$ ,  $dir_y$ , and  $dir_z$  distributions (see Figure A.7(b)) generated by the computer routine from section A.3.2. The results from analysis of the non-antipodal pair example are summarized in Table A.1:

Point to point algorithm				Point and dir algorithm		
$\beta(rad)$	$dir_x$	$dir_y$	$dir_z$	$dir_x$	$dir_y(10^{-3})$	$dir_z$
0.3944	-0.8781	0.0	-0.4785	$-0.8780 \pm 0.0001$	$-0.6 \pm 0.4$	$-0.4787 \pm 0.0002$
1.047	0.4073	0.0	0.9133	$0.4074 \pm 0.0002$	$0.5 \pm 0.3$	$0.9132 \pm 0.0001$
1.700	-0.2320	0.0	0.9727	$-0.2320 \pm 0.0002$	$0.4 \pm 0.4$	$0.9727 \pm 0.0001$

Table A.1: Results for the non-antipodal pair: source pt at  $(0.905R, 0, 0.095R)$  and sink pt at  $= (0, 0, 1)$  implementing the algorithms described in section A.3.2 and section A.3.3. A tolerance of 10 cm was used in the “point and dir” method of section A.3.2 and  $1\sigma$  errors are shown.

## A.4 Uniform Scattering

In this section, the problem of including a simple scattering model into the Path Fitter PDF is discussed. In this case, we outline how one would include uniform, isotropic scattering, with photons scattered exactly once on their way from the hypothesized electron position to a given PMT.

The form of the PDF for scattering is same as Equation A.3, except now there are a continuum of paths - one for each scatterer at S, that connect the hypothesized source position and  $i^{th}$  PMT,

$$P_s^{scat}(t_i) = P_s^{TIM}(t_i) N_\gamma \rho_{is} e^{-N_\gamma \rho_{is}} \quad (\text{A.35})$$

where  $\rho_{is}$  is the probability for a Cerenkov photon generated by the electron and scattered at S to be detected by the  $i^{th}$  PMT.

The scattered light PDF is constructed by considering the probability that a PMT at  $\vec{r}_i$  is hit at time  $t_i$  by an photon scattered isotropically within the volume constrained by the PSUP. Incorporating scattering into the PDF is complicated in general, so the following simplifying assumptions are made:

- A photon generated at E scatters exactly once along its path to P
- The angular distribution of scattered photons at any scatter point S is uniform (i.e. scattering is isotropic)
- The scattering volume within the PSUP is uniform with a scattering length  $\lambda_s$

The scattered light PDF is then constructed by calculating the probability  $P_s$  for a photon to hit a PMT at P with time  $t_i$  after scattering at an arbitrary point S within the PSUP volume V, and then integrating over all possible S in V (see Figure A.4),

$$P^{scat}(t_i) = \int_{S \in V} P_s^{scat}(t_i) dV \quad (\text{A.36})$$

The angular probability,  $\rho_{is}$ , in Equation A.35 can be thought of as the product of several probabilities,

$$\rho_{is} = P_1 P_2 P_3 P_4 \quad (\text{A.37})$$

where the probabilities  $P_i$  are shown below

- $P_1$  = probability that a relativistic electron moving in a direction  $\hat{d}_e$  will generate a Cerenkov photon in a direction  $\hat{d}_\gamma(\theta, \phi)$   
 $= g[\alpha_s(\theta, \phi)]$ , where  $\alpha_s(\theta, \phi) = \cos^{-1}[\hat{d}_e \cdot \hat{d}_\gamma(\theta, \phi)]$
- $P_2$  = probability of scattering after a distance r, which is the interaction probability times the photon survival probability over a distance r  
 $= \frac{1}{\lambda_s} e^{-\frac{r}{\lambda_s}}$
- $P_3$  = probability of scattering at S into the solid angle  $\Omega(r, \theta, \phi)$  subtended by a PMT at P times the probability of scattering in a direction  $\hat{SP} \equiv \hat{r}'(r, \theta, \phi)$

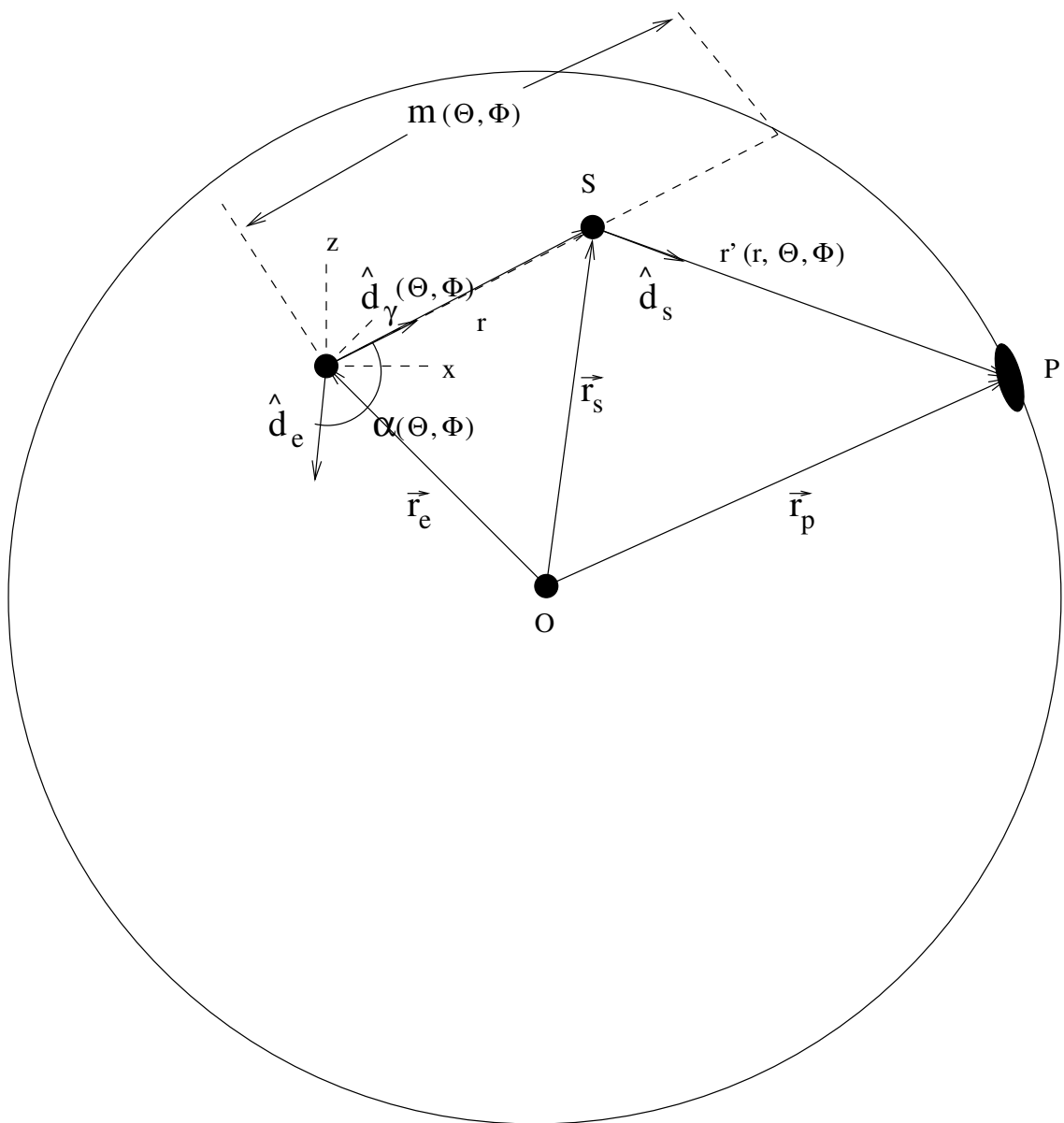


Figure A.9: Figure showing the vectors involved in the scattering problem.

$$= \Omega(r, \theta, \phi) \frac{1}{4\pi} = [\hat{r}'(r, \theta, \phi) \cdot \hat{r}_p)] \frac{\pi r_e^2}{[r'(r, \theta, \phi)]^2} \frac{1}{4\pi},$$

where  $\vec{r}'(r, \theta, \phi) = \vec{r}_p - \vec{r}_s$  is the distance from the scatterer at S to the PMT at P.

- $P_4$  = probability of traveling a distance  $r'(r, \theta, \phi)$  without scattering, which under our assumption of exactly one scatter,  
 $= 1$  (otherwise it would be  $e^{-\frac{r'(r, \theta, \phi)}{\lambda_s}}$ )

The total scattering probability is then calculated by integrating over all  $S\epsilon V$ , and is given by

$$P^{scat}(t_i) = \int_0^{2\pi} \int_0^\pi \int_0^{m(\theta, \phi)} P^{TIM}(t_i, r, \theta, \phi) N_\gamma \rho_i(r, \theta, \phi) e^{-N_\gamma \rho_i(r, \theta, \phi)} \sin\theta \ r^2 \ dr d\theta d\phi \quad (\text{A.38})$$

where

$$\rho_i(r, \theta, \phi) = \frac{1}{4\pi \lambda_s} g[\alpha_s(\theta, \phi)] \Omega(r, \theta, \phi) e^{-\frac{r}{\lambda_s}} \quad (\text{A.39})$$

and

$$m(\theta, \phi) = -\vec{r}_e \cdot \hat{d}_\gamma(\theta, \phi) + \sqrt{(\vec{r}_e \cdot \hat{d}_\gamma(\theta, \phi))^2 - (r_e^2 - R^2)} \quad (\text{A.40})$$

is the distance from the electron to the PSUP along in the direction intersecting the scattering point S (i.e.  $\hat{d}_\gamma(\theta, \phi)$ )

Recall that  $P^{TIM}(t_i, r, \theta, \phi)$  is the time function that represents the probability of recording a PMT time  $t_i$  given a photon TOF,  $\frac{r+r'(r, \theta, \phi)}{c}$ . One could imagine a using a Gaussian time jitter for the form of  $P_{TIM}(r, \theta, \phi)$ ,

$$P^{TIM}(r, \theta, \phi) = \frac{1}{\sigma \sqrt{2\pi}} e^{-\frac{1}{2\sigma^2} \{t_i - [\frac{r+r'(r, \theta, \phi)}{c} + t_e]\}^2}. \quad (\text{A.41})$$

Note that the scattering probability shown in Equation A.38 involves 3D integra-

tion at each hypothesized electron position, direction, and time. This is very computationally intensive. One could make the simplifying approximation of no PMT jitter, handwaving that the time smearing from the scattering dominates over PMT jitter, which reduces the dimensionality of the integration. This effectively replaces  $P^{TIM}(t_i, r, \theta, \phi)$  with a  $\delta$ -function at the scattered photon TOF, and is given by

$$P^{TIM}(r, \theta, \phi) = \delta(r - r_{TOF}(\theta, \phi)), \quad (\text{A.42})$$

where  $r_{TOF}(\theta, \phi)$  is the root (if one exists) of the equation

$$t_p - \left[ \frac{r + r'(r, \theta, \phi)}{c} + t_e \right] = 0 \quad (\text{A.43})$$

such that  $0 \leq r_{TOF}(\theta, \phi) \leq m(\theta, \phi)$

Inserting the  $\delta$ -function form of  $P^{TIM}(r, \theta, \phi)$  and performing the radial integration yields

$$P^{scat}(t_i) = \int_0^{2\pi} \int_0^\pi N_\gamma \rho_i(r_{TOF}, \theta, \phi) e^{-N_\gamma \rho_i(r_{TOF}, \theta, \phi)} \sin\theta \ r_{TOF}^2 \ d\theta d\phi \quad (\text{A.44})$$

This form of probability could then be used as the scattering PDF in fitting events, once the scattering length is known.

# Appendix B

## Energy Scale Interpolation

In this appendix, a method for energy scale interpolation is presented. The purpose is to correct the average Monte Carlo (MC) energy response function based on  $^{16}\text{N}$  calibrations to reduce the sensitivity of energy scale to optical model uncertainties.

### B.1 Preparing the Grid

This section describes construction of the grid used to interpolate the difference between calibration data and  $^{16}\text{N}$  source MC (see Figure B.1). The  $^{16}\text{N}$  xz-scan data was reconstructed using the standard SNOMAN time fitter. This reconstruction was similarly performed on MC using the Optics 6b optical constants for  $^{16}\text{N}$  source simulation with the source at the same positions as the xz-scan data. 100k events were generated in the MC. Each of the MC and calibration data events were separately placed in one of four bins according their reconstructed direction relative to a point

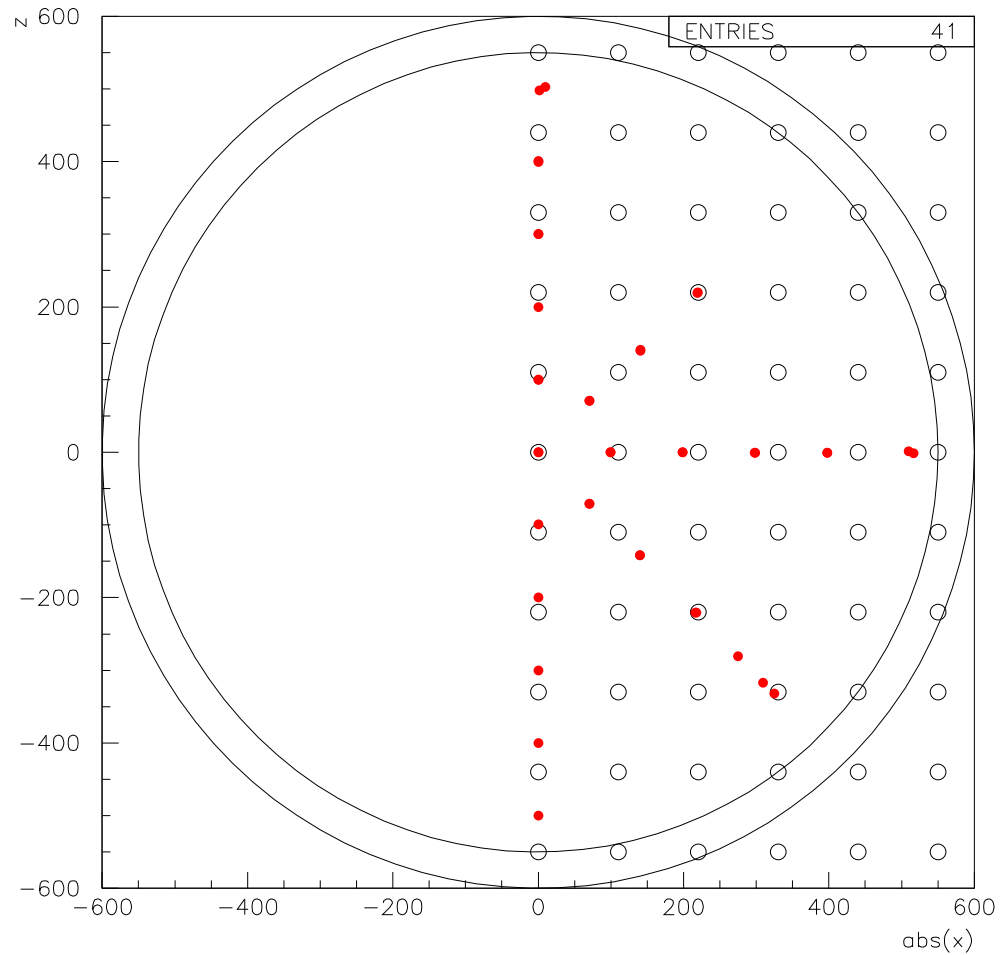


Figure B.1: Figure showing the grid used in energy scale interpolation (black circles). The red points are  $^{16}\text{N}$  source positions used in the grid generation. Sources with  $x < 0$  are mapped to positive- $x$  source positions to gain statistics, effectively averaging over azimuthal asymmetries near the x-z detector plane.

in the neck. Specifically, they were binned according to their value of  $\theta_{neck}$ , where

$$\cos \theta_{neck} = \frac{\hat{d}_{fit} \cdot (\vec{r}_{fit} + 650\hat{z})}{|\vec{r}_{fit} + 650\hat{z}|} \quad (\text{B.1})$$

Therefore,  $\theta_{neck} = 0$  is toward the neck at the reconstructed position and  $\theta_{neck} = \pi$  is away from the neck.

For each of the four  $\theta_{neck}$  bins, two 2D grids - one for MC and one for calibration data - are generated in the variables  $\rho_{fit} = \sqrt{(x_{fit}^2 + y_{fit}^2)} \sim |x_{fit}|$  and  $z_{fit}$ . The chosen grid spacing is 5  $\rho_{fit}$  points from 0 to 550 cm and 10  $z_{fit}$  points from -550 cm to 550 cm, corresponding to a 1.1 m spacing. Each grid point contains the mean of a Gaussian fit to the NHIT distribution of events reconstructing “near” the grid point. The value of “near” depends on the required statistics and the available calibration data. An event is added to a given grid point  $i$  if all of the following are true:

- $|y_{fit}| < 75$  cm (i.e. near the xz-plane)
- $28 < \text{NHIT} < 90$
- $|x_{fit} - \rho_i| < 40$  cm and  $|z_{fit} - z_i| < 40$  cm
- Reconstructed distance from the source is not “too large” (currently not implemented, but this would avoid outlying grid points containing large fractions of poorly reconstructed events)

The final output grids (one for each of the four  $\theta_{neck}$  bins) used in energy scale interpolation are created with the same spacing, however each grid point now contains the difference between the previous two grid sets (MC and data). Therefore, these new grids,  $\Delta^k$ , contain the difference in mean response between the MC and calibration

data at “discrete” points in  $\rho_{fit}$  and  $z_{fit}$  for the  $k^{th}$  bin in  $\theta_{neck}$ . As such, value at any grid point  $i$  and  $\theta_{neck}$  bin  $k$  is given by

$$\Delta_i^k = \overline{Nhit}_i^{k,MC} - \overline{Nhit}_i^{k,data}$$

Additionally, by explicit construction  $\Delta_i^k = 0$  if, and only if,

- The statistical error on the *fractional* difference,  $\frac{\Delta_i^k}{\overline{Nhit}_i^{k,data}}$ , is larger than 2.5%
- There are fewer than 150 entries in the grid point

These requirements are to get a statistically significant response at each grid point and avoid bad Gaussian fits to either NHIT distribution (data or MC). Figure B.2 shows the grid points which survive these two criteria for each of the four  $\theta_{neck}$  bins.

## B.2 Using the Grid

The  $\Delta^k$  grids, containing the average difference in response between data and MC at  $^{16}\text{N}$  energies, can now be used to adjust the MC response at different energies in the following way. An event is generated and reconstructed at a point  $(\rho_{fit}, z_{fit}, \theta_{neck})$ . The value of  $\theta_{neck}$  will fall into one of the  $\theta_{neck}$  bins, so we use the corresponding  $\Delta^k$  grid. The point  $(\rho_{fit}, z_{fit})$  is in general not on a grid point, so we use bicubic spline interpolation to get the value of  $\Delta_{N16}^k$ , which is the interpolated difference in response at an arbitrary point. The NHIT of the MC event is then adjusted according to the following transformation:

$$NHIT \rightarrow NHIT - \Delta_{N16}^k \times \frac{N_\gamma}{N_\gamma^{N16}}$$

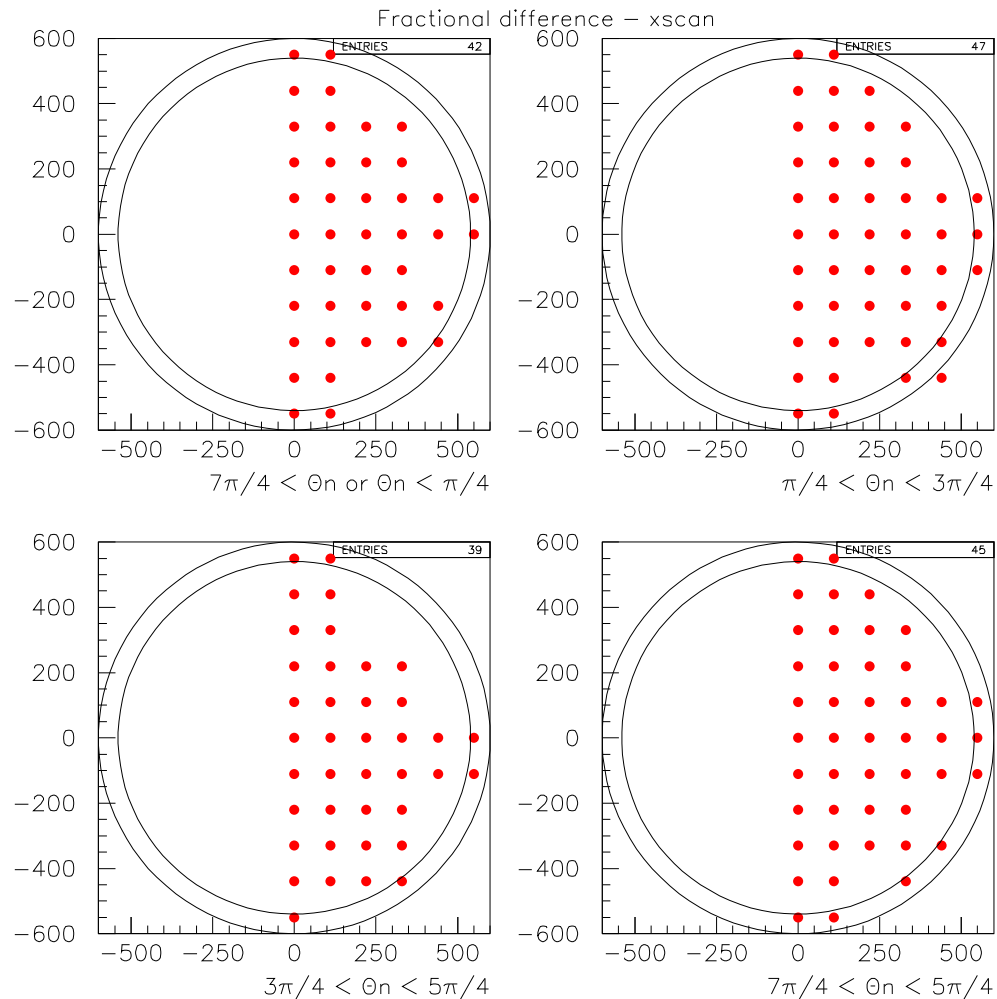


Figure B.2: Figure showing grid points with enough statistics to use in the energy scale interpolation scheme.

where  $N_\gamma$  is the number of Cerenkov photons generated in the event and  $\overline{N}_\gamma^{N^{16}}$  is the mean of the Cerenkov number distribution of simulated  $^{16}\text{N}$  source events. It should be noted that two primary assumptions that are implicit in this transformation are:

- The *difference* between MC and actual response from the  $^{16}\text{N}$  source is azimuthally symmetric.
- The difference between MC and actual response from the  $^{16}\text{N}$  source scale linearly with the number of Cerenkov photon generated relative to the mean number of Cerenkov photons from the  $^{16}\text{N}$

### B.3 Effect of Applying Response Corrections to Grid Data

To check that the interpolation scheme is able to correct the data upon which it is based, the effect of applying corrections to the data used to generate the grid is investigated. One expects the agreement between the xz-scan  $^{16}\text{N}$  data and MC energy scale to get better if corrections are applied, which is indeed the case (Figures B.3).

### B.4 Fitter Dependence

The Monte Carlo used to generate the interpolation grid was derived from  $^{16}\text{N}$  simulations and source data reconstructed with the Time Fitter. The reason for using the Time Fitter is for speed of grid generation, since a large amount of Monte Carlo is required. Neutrino data is reconstructed with the Path Fitter, so we need to check that the corrections are sensible using different fitters. Figures B.4, and B.5 show x

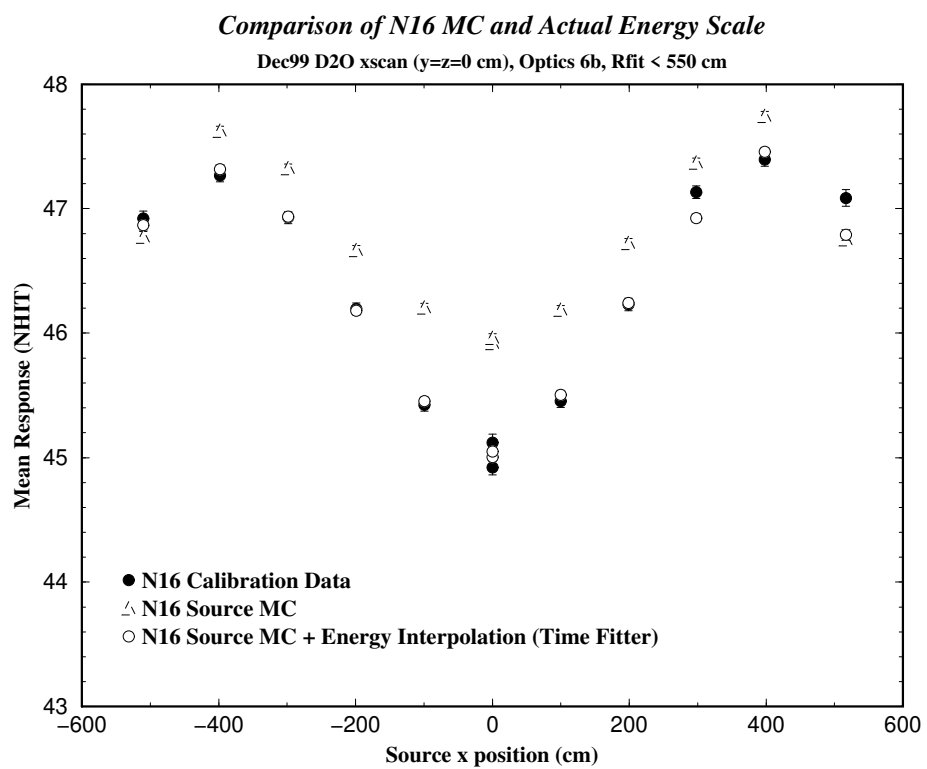


Figure B.3: Energy scale before and after energy interpolation for the Dec99  $^{16}\text{N}$  x-scan using the Time Fitter.

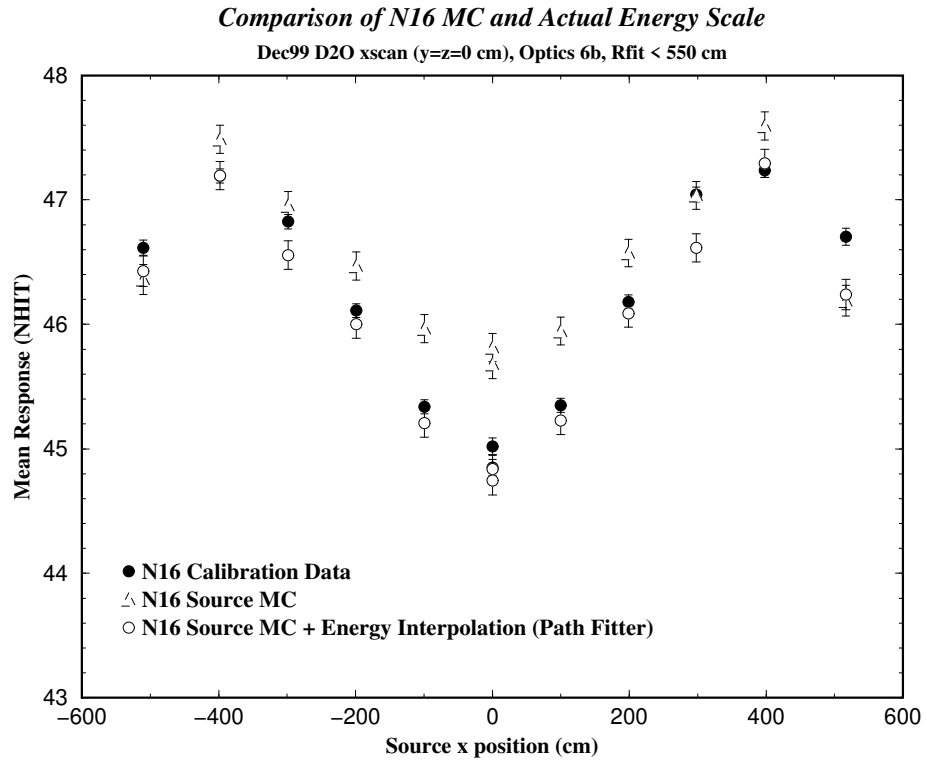


Figure B.4: Energy scale before and after energy interpolation for the Dec99  $^{16}\text{N}$  x-scan using the Path Fitter.

and z scan comparisons between corrected  $^{16}\text{N}$  Monte Carlo and source data used to generate the interpolation grids. Notice that the consistency of the correction is not compromised by using a different fitter (Path Fitter in this case).

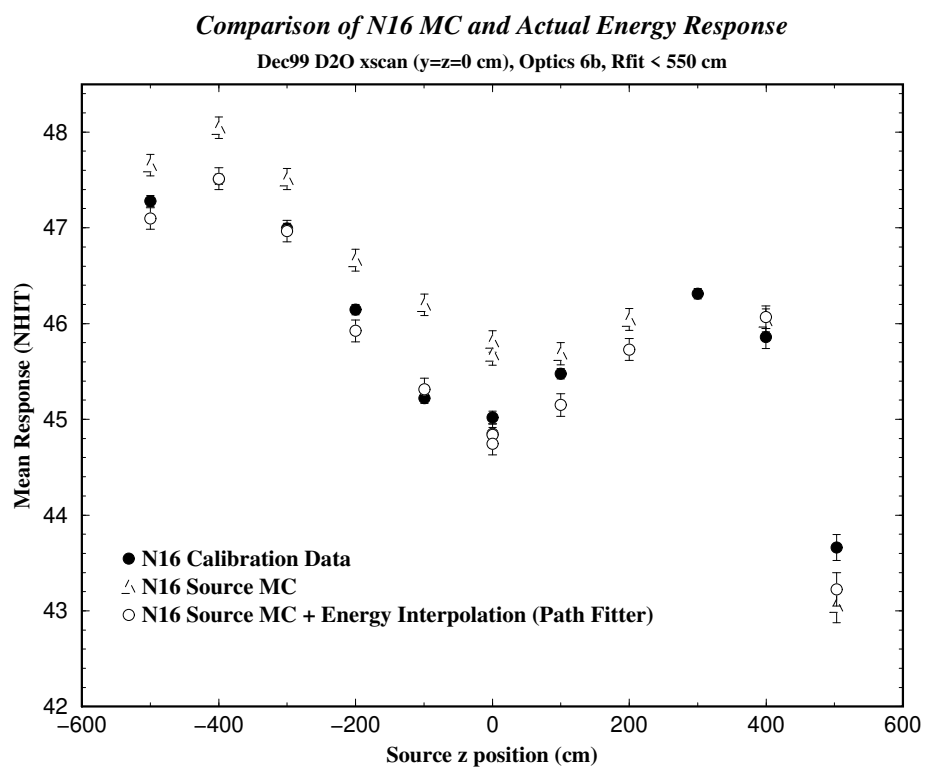


Figure B.5: Energy scale before and after energy interpolation for the Dec99  $^{16}\text{N}$  z-scan using the Path Fitter.

# Appendix C

## Trigger Efficiency Follow-up

This appendix provides a follow-up to the trigger efficiency discussion contained in the main text.

### C.1 Checks and Systematics

Numerous checks have been performed that support the validity of the trigger efficiency results. This section includes a brief description of these checks, as well as some discussion regarding how disabled channels can affect the trigger efficiency results. Additional details can be found in [61].

Early attempts to measure the trigger efficiency were performed using the MTC/D trigger word to determine how often the trigger thresholds fire in response to diffused light from the laser. In this method, the laser trigger timing is carefully tuned so that the majority of trigger firings get latched into the trigger word. The relatively narrow latching window - although useful for normal data taking - leads to uncertainties in the method which are greatly reduced in the FEC/D latch method. However, the

## Trigger Efficiency Using MTC/D Latch Method

Laserball Runs 5735–8, 5760–2 with  $x = y = z = 0$

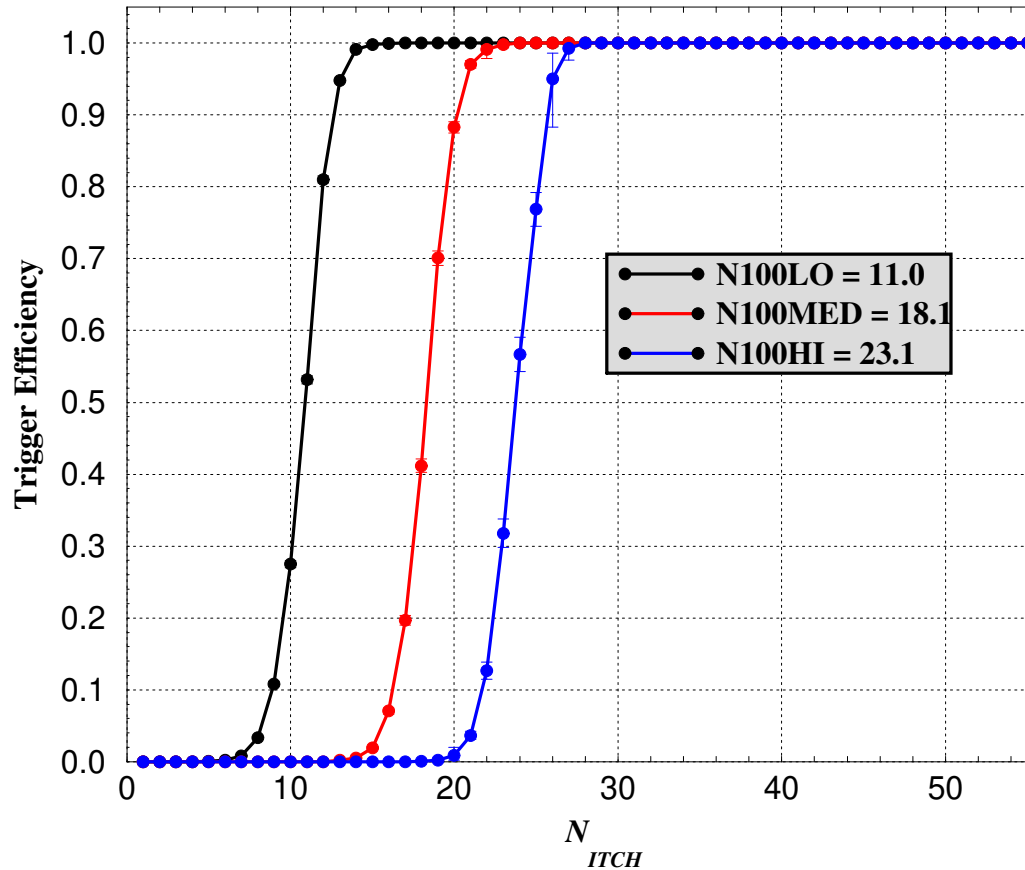


Figure C.1: Measured trigger efficiency using the laserball with the MTC/D as the trigger latch. The laserball position is  $x = y = z = 0$ .

method can still be used as an approximate check of the FEC/D results. The results of the MTC/D latch method are shown in Figure C.1 and are consistent with the results of the FEC/D latch method.

The NHIT triggered data can also be used to estimate the efficiency. The fact that the same trigger sum is discriminated with different thresholds allows one to use a lower threshold as a triggered source of correlated hits for a higher threshold for which the efficiency is estimated. Since the MTC/D trigger word is used to determine how often the higher threshold fires and because in order to count the number of in-time channels one needs to estimate the shape of the trigger sum from the PMT hit times, this method is considered even more approximate than the laserball MTC/D latch method. The trigger efficiency results are shown in Figure C.2. Note that the statistics are still poor above  $\tilde{N} = 30$ , so one needs to augment the data sample with more high NHIT data if a better limit is desired. However, the shape of the curve is reasonably consistent with the N100HI threshold results using the laser with MTC/D latch method presented in Section 5.6.5, with a trigger turn-on of  $\sim 3.8$  NHIT and a similar 100% efficiency value of  $\tilde{N}$  ( $\sim 28$ ).

Several systematic effects were investigated. Recall that a 93 ns sliding window was used to count the number of in-time channels. This is a convenient parameterization of the problem since this window corresponds to the width of the analog trigger primitives that determine the trigger coincidence time. Although not strictly a systematic on the measurement, the curves were compared when the window width was changed by  $\pm 10\%$  and little difference was found, demonstrating that there is no fine-tuning in the choice of parameterization. Timing calibrations can also affect the measurement, since the calibrated PMT times are used to estimate the number of in-time channels. This was checked by comparing the efficiency curves both with

## Trigger Efficiency Using NHIT Triggered data

Run 10237 (all) + 10000–10236 (NHIT=30–50); N100M = 18.1 Triggered

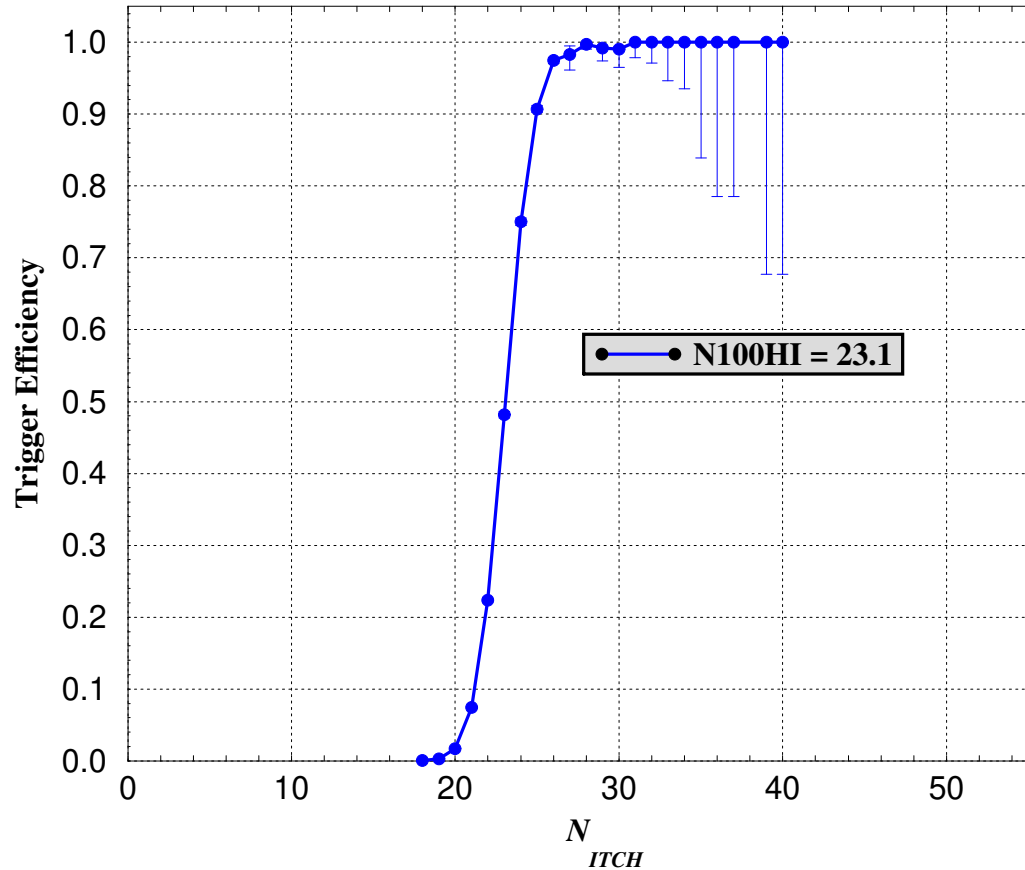


Figure C.2: Measured trigger efficiency using the NHIT triggered data from standard neutrino runs.

and without PCA calibrations applied, and essentially no difference was found. This checks timing errors of  $\sim 5$  ns, which is quite a bit larger than the expected error in the full timing calibration. Finally, the sensitivity of the efficiency results to changes in the FEC/D charge cut used in the method was investigated. The results were unchanged when the cut was changed by  $\pm 50\%$ , indicating the method is largely insensitive to the FEC/D charge used to determine how often the trigger thresholds fire in response to the laser light.

## C.2 Effect of Missing Channels on Trigger Efficiency

In Section 5.6.3, it was pointed out that channels which acquire data but do not contribute to the trigger sum are a source of inefficiency in the trigger system. At the time the trigger efficiency data was taken, there were a number of such channels in the system that smear out the efficiency curve (other sources of inefficiency described in Section 5.6.3 also contribute to a broadening of the efficiency curve). A large fraction of these channels had their triggers deliberately disabled due to excessive CMOS dropout, and some were simply dead because of some failure in the hardware. In this section, the effect of adding dead trigger channels on the full efficiency  $\tilde{N}$  point reported in Section 5.6.5 is estimate. This is important because the analyzer needs to know how the results presented in this report are modified by changes in the trigger hardware state corresponding to the data being analyzed.

The “dead trigger channels” relevant for studying changes in the trigger efficiency are channels which have their triggers disabled (i.e. do not contribute to the analog

trigger sum) but their sequencers *enabled* which allows them to acquire data. These channels reduce the efficiency because they are included in the count of in-time channels but lower the probability for the NHIT trigger to fire since they do not contribute to the analog trigger sum. Channels which have both their triggers *and* sequencers disabled are simply “dead channels” which are sources of inefficiency to the overall acceptance much like PMTs without high voltage applied.

In the trigger efficiency runs taken on 10/25 and 10/26/99, which comprise the data for this trigger efficiency analysis, there were 9719 channels enabled to acquire data (i.e. sequencers enabled) and 9307 of these channels also had their NHIT triggers enabled based on information extracted from the DQCH banks written by the DAQ. Therefore, the trigger efficiency results in this thesis correspond to a 9719 channel detector with 4.2% of the triggers disabled. To estimate how much the efficiency is reduced when additional trigger channels are disabled, consider the following. There are  $N_{trig}$  total trigger channels enabled in the system when the efficiency,  $\epsilon(\tilde{N})$ , is measured. An *additional* fraction,  $f_{dead}$ , of these channels then have their triggers disabled and the efficiency curve changes to  $\epsilon'(\tilde{N})$ . An estimate of the change in efficiency at a given number of in-time channels,  $\tilde{N}_o$ , is given by

$$\epsilon(\tilde{N}_o) - \epsilon'(\tilde{N}_o) = f_{dead}[1 - \epsilon(\tilde{N}_o - 1)] + f_{dead}^2[1 - \epsilon(\tilde{N}_o - 2)] + \dots$$

The  $i^{th}$  term in the sum is the probability for getting  $i$  trigger disabled hits in the event times the reduction of efficiency in having only  $\tilde{N}_o - i$  in-time channels in the analog trigger sum rather than  $\tilde{N}_o$ . This is actually not quite right, particularly when  $\tilde{N}_o$  is comparable to  $f_{dead}N_{trig}$ , the number of newly disabled trigger channels, which is the most likely case since this represents adiabatic changes in the detector configuration. In this case, one includes the fact that a channel can not be hit twice in

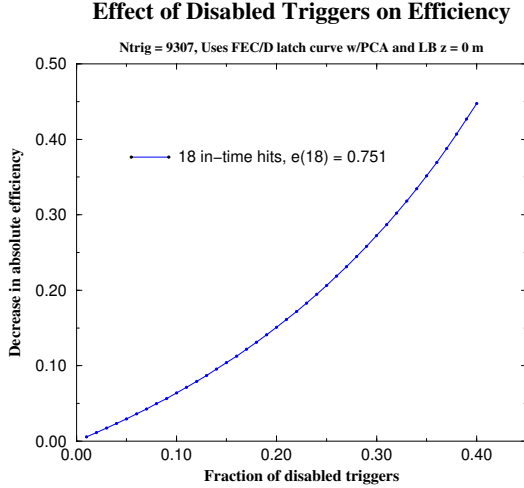


Figure C.3: Reduction in efficiency versus the fraction of newly disabled trigger channels for  $\tilde{N}_o = 18$  (left) and  $\tilde{N}_o = 23$  (right).

the same event (although a PMT can!) and a hit in a newly disabled trigger channel removes it from the population of dead trigger channels to be picked from. Therefore, one gets in the limit where the fraction of good trigger channels remains the same, the following modified series

$$\epsilon(\tilde{N}_o) - \epsilon'(\tilde{N}_o) = f_{dead}[1 - \epsilon(\tilde{N}_o - 1)] + f_{dead}(f_{dead} - \frac{1}{N_{trig}})[1 - \epsilon(\tilde{N}_o - 2)] + \dots,$$

which can be written in a more compact form as

$$\epsilon(\tilde{N}_o) - \epsilon'(\tilde{N}_o) = \sum_{i=1}^{\min(\tilde{N}_o, f_{dead}N_{trig})} \left\{ \prod_{j=1}^i \left( f_{dead} - \frac{j-1}{N_{trig}} \right) [1 - \epsilon(\tilde{N}_o - i)] \right\}$$

The  $\min(\tilde{N}_o, f_{dead}N_{trig})$  upper limit is included to terminate the sum when contributions from all the dead trigger channels have been included.

The results of calculating the previous sum with  $N_{trig} = 9307$  are shown in Figure C.3 for  $\tilde{N}_o = 18$  and  $\tilde{N}_o = 23$ . Note that while the reduction in efficiency is substantial at  $\tilde{N}_o = 18$  where the efficiency changes rapidly, the full efficiency is

nearly unaffected even with relatively large fractions of the triggers disabled. This is because at  $\tilde{N}_o = 23$  it takes several random chance hits of the dead trigger channels to make a substantial change in the efficiency which is unlikely when only a small fraction of the good trigger channels are disabled.

It should be noted that this approximation assumes that channels are hit at random. This would be a good approximation for isotropic light at the center of the detector and the dead trigger channels were distributed uniformly over the PSUP. However, in reality, dead trigger channels are strongly correlated to certain channels that are prone to excessive CMOS dropout and hence the PMTs connected to them have a non-uniform distribution on the PSUP which complicates the estimate. Still, the equation presented in this section should give a rough estimate of the effect of disabling trigger channels on the trigger efficiency.

# Bibliography

- [1] B. L. for the DONUT collaboration, *Status of DONUT*, Nuclear Physics B (Proc. Supplement) (2001), *XIX International Conference on Neutrino Physics and Astrophysics (Neutrino 2000)*.
- [2] P. Wittich, *First Measurement of the Flux of Solar Neutrinos from the Sun at the Sudbury Neutrino Observatory*, Ph.D. thesis, University of Pennsylvania (2000).
- [3] A. M. for the SNO Collaboration, *First neutrino observations at the sudbury neutrino observatory*, Nuclear Physics B (Proc. Supplement) (2001), *XIX International Conference on Neutrino Physics and Astrophysics (Neutrino 2000)*.
- [4] J. Bahcall, *Neutrino Astrophysics* (Cambridge University Press, Cambridge, 1989).
- [5] J. N. Bahcall, M. Pinsonneault, and S. Basu, *Solar models: current epoch and time dependences, neutrinos, and helioseismological properties*, astro-ph/0010346 (2001), this is BP2000 "modified" which has  $5.05 \times 10^6$  for B8 flux.
- [6] J. Bahcall, available at <http://www.sns.ias.edu/~jnb/>.
- [7] B. T. Cleveland, T. Daily, J. Raymond Davis, J. R. Distel, K. Lande, C. Lee, P. S. Wildenhain, and J. Ullman, *Astrophysical Journal* **496**, 505 (1998).

- [8] J. Abdurashitov *et al.*, Physical Review C **60** (1999).
- [9] W. Hampel *et al.*, Physics Letters B (447), 127 (1998).
- [10] M. Altmann *et al.*, Physics Letters B (490), 16 (2000).
- [11] Y. Fukuda *et al.*, Phys. Rev. Let. **77**(9), 1683 (1996).
- [12] S. Fukuda *et al.*, *Constraints on neutrino oscillations using 1258 days of super-kamiokande solar neutrino data*, hep-ex/0103033 (2001).
- [13] S. Fukuda *et al.*, *Solar  ${}^8\text{B}$  and hep neutrino measurements from 1258 days of superkamiokande data*, hep-ex/0103032 (2001).
- [14] N. Hata, S. Bludman, and P. Langacker, Phys. Rev. D **49**, 3622 (1994).
- [15] N. Hata and P. Langacker, Phys. Rev. D **56**(10), 6107 (1997).
- [16] M. Lusignoli, *Non-standard neutrino properties*, hep-ph/0101074 (2001).
- [17] H. Nunokawa, *Exotic solutions to the solar neutrino problem and some implications for low energy solar neutrino experiments*, hep-ph/0105027 (2001).
- [18] L. Wolfenstein, Phys. Rev. D **17**, 2369 (1978).
- [19] S. P. Mikheev and A. Y. Smirnov, Soviet Journal Nuclear Physics **42**(6), 913 (1985).
- [20] F. Boehm and P. Vogel, *Physics of Massive Neutrinos* (Cambridge University Press, Cambridge, 1992).
- [21] J. N. Bahcall, P. I. Krastev, and A. Y. Smirnov, *Solar neutrinos: Global analysis and implications for sno*, hep-ph/0103179 (2001).

- [22] M. Gonzalez-Garcia and C. Pena-Garay, *Global and unified analysis of solar neutrino data*, hep-ph/0009041 (2000).
- [23] H. H. Chen, Phys. Rev. Let. **55**(14), 1534 (1985).
- [24] J. Boger *et al.*, Nuclear Instruments and Methods **A449**, 172 (2000).
- [25] J. Cameron *et al.*, *Status of the SNO Connectors - Report to the EAC*, Tech. Rep., Oxford University, CRPP, Triumf, University of Pennsylvania (2000).
- [26] T. Ekenberg, F. M. Newcomer, R. Van Berg, A. Biman, and R. L. Stevenson, in *IEEE Transactions on Nuclear Science* (1995), vol. V0042, pp. 925–932.
- [27] F. M. Newcomer and R. Van Berg, in *IEEE Transactions on Nuclear Science* (1994), vol. V0042, pp. 745–749.
- [28] R. Stevenson *et al.*, in *Conference Issue of the 1994 Transactions on Nuclear Science* (1994).
- [29] D. S. McDonald, *Studies of the Sudbury Neutrino Observatory Detector and Sonoluminescence using a Sonoluminescent Source*, Ph.D. thesis, University of Pennsylvania (1999).
- [30] J. R. Klein, M. S. Neubauer, R. Van Berg, and F. M. Newcomer, *The SNO trigger system*, SNO technical report SNO-STR-97-036, University of Pennsylvania (1997).
- [31] J. R. Klein, *Design of the SNO timing system*, SNO technical report SNO-STR-95-007, University of Pennsylvania (1995).
- [32] The SNO Collaboration, *The SNOMAN User's Manual*, version 4.01 ed.

- [33] The SNO Collaboration, *The SNOMAN Programmer's Manual*, version 4.01 ed.
- [34] D. Cowen, G. Jonkmans, R. Komar, C. Okada, and R. Tafirout, *The SNO Database: SNODB v3.06.05*, Penn, Neuchatel, UBC, LBNL, Laurentian (1998).
- [35] CERN Program Library Long Writeup Q180, *HEPDB Database Management Reference Manual*.
- [36] W. Frati and R. G. Van de Water, *Quad Fitter Introduction: Reconstruction and Pattern Recognition*, SNO technical report SNO-STR-94-030, University of Pennsylvania (1994).
- [37] W. Frati, *Quad Fitter Update I*, SNO technical report SNO-STR-94-035, University of Pennsylvania (1994).
- [38] M. E. Moorhead, *Grid Fitter for Reducing Tails in Spatial Distributions*, SNO technical report SNO-STR-95-042, Oxford University (1995).
- [39] X. Chen, *An Improved Grid Fitter*, SNO technical report SNO-STR-00-004, Lawrence Berkeley National Laboratoy (2000).
- [40] S. J. Brice, *The Elastic Fitter*, SNO technical report SNO-STR-95-040, Oxford University (1995).
- [41] J. R. Klein and M. S. Neubauer, *Using Time and Angle Information in Reconstruction and the SNOMAN Path Fitter*, SNO technical report SNO-STR-00-022, University of Pennsylvania (2001).
- [42] J. R. Klein, *Maximum Likelihood Fitting to Both Time and Angle*, SNO technical Report SNO-STR-94-055, University of Pennsylvania (1995).

- [43] J. D. Jackson, *Classical Electrodynamics* (John Wiley & Sons, New York, 1975), 2nd ed.
- [44] S. J. Brice, *Monte Carlo and Analysis Techniques for the Sudbury Neutrino Observatory*, Ph.D. thesis, Balliol College, Oxford University, Oxford (1996).
- [45] D. F. Cowen, Personal Communication.
- [46] B. Heintzelman, Personal Communication.
- [47] W. H. Press, S. A. Teukolsky, W. T. Vetterling, and B. P. Flannery, *Numerical Recipes in Fortran* (Cambridge University Press, 1992), 2nd ed.
- [48] V. Rusu, *Post Reconstruction Cuts*, Tech. Rep., University of Pennsylvania (2001).
- [49] S. Biller *et al.*, *SNO Electronic Calibration Constants*, Tech. Rep., SNO Collaboration (2001).
- [50] G. McGregor, Personal Communication.
- [51] R. J. Ford, *Calibration of SNO for the detection of  $^8\text{B}$  neutrinos*, Ph.D. thesis, Queen's University, Kingston, Ontario (1998).
- [52] B. A. Moffat, *The Optical Calibration of the Sudbury Neutrino Observatory*, Ph.D. thesis, Queen's University, Kingston, Canada (2001).
- [53] M. G. Boulay, *Direct Evidence for Weak Flavor Mixing with the Sudbury Neutrino Observatory*, Ph.D. thesis, Queen's University (2001).
- [54] A. S. Hamer, *Energy Calibration of SNO for measurement of the Charged-Current Neutrino Reaction*, Ph.D. thesis, Queen's University, Kingston, Ontario (1999).

[55] S. Brice *et al.*, *First Generation Acrylic Encapsulated U/Th Sources*, SNO Technical Report SNO-STR-99-023, LANL, LBNL, Queens University (2000).

[56] A. W. P. Poon, *Energy Calibration of the Sudbury Neutrino Observatory using Monoenergetic Gamma-Ray Sources*, Ph.D. thesis, University of British Columbia, Vancouver, British Columbia (1998).

[57] G. Jonkmans, I. Towner, and B. Sur, Physical Review C **58**(2), 1278 (1998).

[58] N. Tagg, *The 8Li Calibration Source and Through-going Muon Analysis in the Sudbury Neutrino Observatory*, Ph.D. thesis, University of Guelph (2001).

[59] N. McCauley, *Sacrifice Update to Include Recent Li8 Data*, Tech. Rep., University of Oxford (2001).

[60] C. J. Jillings, *The Electron Scattering Reaction in the Sudbury Neutrino Observatory*, Ph.D. thesis, Queen's University, Kingston, Ontario (1999).

[61] M. S. Neubauer and J. R. Klein, *Measurement of the SNO Trigger Efficiency*, SNO technical report report, University of Pennsylvania (2000).

[62] J. Cameron *et al.*, *Study of High Voltage-Dependent Phenomena in the SNO Detector*, SNO technical report SNO-STR-99-038, Penn, Oxford and TRIUMF (1999).

[63] J. Cameron *et al.*, *The Gain and the Pain: A Study of Detector Response and Instrumental Backgrounds After the High Voltage Raise*, SNO technical report SNO-STR-99-039, University of Pennsylvania, Oxford University, TRIUMF, and Queens University (1999).

- [64] S. Brice *et al.*, *Sacrifice and Contamination in SNO Data Cleaning Cuts*, Tech. Rep., The SNO Collaboration (2000).
- [65] M. Neubauer, *Data Cleaning: The Fitterless Time Spread (FTS) Cut*, SNO Technical Report SNO-STR-2000-002, University of Pennsylvania (2000).
- [66] M. Neubauer, *Addendum to the FTS Report*, SNO Technical Report SNO-STR-2000-002-A, University of Pennsylvania (2000).
- [67] M. Neubauer, *Data Cleaning: The In-Time Channel (ITC) Cut*, SNO Technical Report SNO-STR-2000-012, University of Pennsylvania (2000).
- [68] W. Heintzelman, *Use of the Angular Correlation Function to Identify Background SNO Events*, SNO Technical Report SNO-STR-2000-032, University of Pennsylvania (2000).
- [69] J. Klein, *Time Dependent Systematic Uncertainties of QCluster (and FGC) Cut*, Tech. Rep., University of Pennsylvania (2001).
- [70] J. Klein, *Time Dependent Systematic Uncertainty of AMB Cut*, Tech. Rep., University of Pennsylvania (2001).
- [71] J. Klein, *Addendum to QvT Cut: Monitoring the Sacrifice*, Tech. Rep., University of Pennsylvania (2001).
- [72] G. Ewan *et al.*, *Sudbury Neutrino Observatory Proposal*, SNO technical report SNO-STR-87-12, Queen's University (1987).
- [73] P. Skensved and B. C. Robertson, *Summary of Backgrounds in SNO*, SNO technical report SNO-STR-94-13, Queens University (1994).

[74] M. Isaac, Y. Chan, *et al.*, *High Energy  $\gamma$ -ray Measurements in the SNO Cavity*, SNO technical report SNO-STR-97-009, LBL, Laurentian, UBC, Guelph (1997).

[75] M. Neubauer and V. Rusu, *Estimation of High Energy Backgrounds in SNO*, Tech. Rep., University of Pennsylvania (2001).

[76] M. Yuk, *Evidence for Solar Neutrinos at SNO*, SNO technical report SNO-STR-2000-xx, TOXENN (TRIUMF, Oxford, University of Pennsylvania) (2000).

[77] M. Neubauer and V. Rusu, *Estimation of High Energy Backgrounds in SNO*, Tech. Rep., University of Pennsylvania (2001).

[78] S. Nakamura, T. Sato, V. Gudkov, and K. Kubodera, Physical Review C **63** (2001).

[79] M. Butler, J.-W. Chen, and X. Kong, Physical Review C **63** (2001).

[80] G. Cowan, *Statistical Data Analysis* (Oxford University Press, 1998).

[81] E. Beier and W. Frati, *Analysis of Monte Carlo Events and Study of Systematic Effects for SNO*, Tech. Rep. SNO-STR-88-87, University of Pennsylvania (1988).

[82] E. Beier and W. Frati, *Extraction of CC, NC, and ES Signals II - Acrylic Radioactivity Three Parameter Maximum Likelihood Analysis*, Tech. Rep. SNO-STR-91-19, University of Pennsylvania (1991).

[83] E. Beier and W. Frati, *Extraction of CC, NC, and ES Signals III - Multi-year Three Parameter Maximum Likelihood Analysis*, Tech. Rep. SNO-STR-91-025, University of Pennsylvania (1991).

[84] S. Oser, *Extracting Neutral Current Results from Pure D<sub>2</sub>O*, Tech. Rep., University of Pennsylvania (2000).

[85] S. Brice, *A Roadmap for PMT Solar Neutrino Analysis*, Tech. Rep., LANL (2000).

[86] Ortiz *et al.*, *Shape of the <sup>8</sup>B alpha and neutrino spectra*, nucl-ex/0003006 (2000).

[87] R. Robertson, *Solar Neutrino Interactions with <sup>17</sup>O and <sup>18</sup>O in SNO*, Tech. Rep., University of Washington (2001).

[88] T. L. Committee, *Livetime Status Report III: The First Paper*, Tech. Rep., The SNO Collaboration (2001).

[89] T. L. Committee, *Livetime Status Report IV*, Tech. Rep., The SNO Collaboration (2001).

[90] M. Smith, Personal Communication.

[91] TOXENN, *Analysis for First Solar Neutrino Paper*, Tech. Rep., Triumf, Oxford Univeristy, Rutherford Appleton Laboratory, University of Pennsylvania (2001).

[92] G. Feldman and R. Cousins, Phys. Rev. D **57**, 3873 (1998).

[93] J. A. Aguilar-Saavedra, *Computation of confidence intervals for poisson processes*, hep-ex/9911024 (1999).

[94] I. Towner, Phys Rev C **58**(2), 1288 (1998).

[95] J. F. Beacom and S. J. Parke, *On the normalization of the neutrino-deuteron cross section*, hep-ph/0106128 (2001).